Characterization of the novel transcript P4 in human keratinocytes and epidermal homeostasis

DISSERTATION

zur Erlangung des Doktorgrades der Naturwissenschaften (Dr. rer. nat.)
der Fakultät für Biologie und Vorklinische Medizin
der Universität Regensburg

vorgelegt von Fabian Schabenberger

aus Neuburg an der Donau

im Jahr 2023

Das Promotionsgesuch wurde eingereicht am:

21. September 2023

Die Arbeit wurde angeleitet von:

Prof. Dr. Markus Kretz

Unterschrift:

Meiner Familie

Fata viam invenient.

Vergil

Table of contents

1. Abstract

The human epidermis is an essential part of the organism that prevents excessive loss of body water and provides protection of vulnerable tissues against environmental hazards such as pathogens, irradiation, chemicals or mechanical trauma. This is achieved by establishment of an impermeable, sturdy barrier of tightly linked cells in its uppermost layers. In order for these functions too be steadily carried out in a correct fashion, the epidermis undergoes a process of constant renewal which is referred to as epidermal homeostasis. During this, proliferatively active basal keratinocytes give rise to daughter cells that are committed to step into a fixed differentiation program on their way to the body surface which results in barrier formation in the final stages before they are ultimately shed off from the skin. Unsurprisingly, this complex process needs to be tightly controlled since even the occurrence of seemingly small disturbances in homeostasis may manifest in severe skin diseases. Hence, the role of multiple known signaling pathways in epidermal homeostasis has been well characterized. Yet, the probable prevalence of additional regulatory layers suggests the presence of more biomacromolecules such as proteins or non-coding RNAs that are involved in the upholding of epidermal functions.

In a screening for potential regulatory long non-coding transcripts in epidermal homeostasis, a novel RNA that we termed *P4* had been shown to be upregulated in proliferating compared to differentiated keratinocytes. In subsequent experiments, we had roughly investigated the transcript in terms of exonic architecture, polyadenylation status, localization and abundance. Moreover, initial phenotypical analyses upon *P4* depletion had shown striking changes related to keratinocyte differentiation. Due to the fact that *P4* was still widely uncharacterized apart from reported functions in cancer tissue, we attempted to shed further light on this RNA in human keratinocytes regarding basic transcript features, associated phenotypical alterations and possible interactors.

Our analyses showed shared differentiation-dependent *P4* expression patterns across multiple keratinocyte cell lines as well as elevated transcript levels in several types of cancer cells. At least one more *P4* isoform in addition to the originally identified full-length transcript was found to be present in keratinocytes. Furthermore, our experiments resulted in low probabilities of an open reading frame within the *P4* sequence to be translated into a functional protein, whereas association of the RNA with ribosomes was demonstrated. A secondary structure that was computed under consideration of experimental data exhibited modular organization into two independent domains.

While overexpression of the transcript did not result in any obvious changes, *P4* knockdown in organotypic tissue culminated in a plethora of associated phenotypical alterations. These included the occurrence of uncommon histological features, enhanced DNA replication, altered distribution of cytoskeletal proteins and variations in the lipidomic profile. Additionally, *P4* depletion in 2D-cultured primary keratinocytes revealed multiple related effects such as shift of cells towards the synthetic phase of cell cycle, reduced keratinocyte adhesion and migration as well as conditionally increased cell growth.

Three distinct screening approaches were employed to identify putative protein interactors of *P4*, of which some were validated in subsequent experiments. Hence, *P4* was shown to bind to phenylalanyl-tRNA-ligase subunit β (FARSB), the centrosome-associated centrin-2 (CETN2) and double-stranded RNA-binding protein Staufen homolog 2 (STAU2).

The detailed nature of *P4* binding to these proteins and downstream mechanisms that explain the observed phenotypes remain to be elucidated by subsequent experiments. Nevertheless, in the course of the here presented studies *P4*, a novel key element in human epidermal homeostasis, was extensively characterized in keratinocytes with regard to the transcript *per se*, related phenotypical manifestations and its protein interactome.

2. Zusammenfassung

Die menschliche Epidermis ist ein essenzieller Bestandteil des Körpers, der sowohl überschüssigen Wasserverlust verhindert als auch darunterliegende verwundbare Gewebe vor äußeren Gefahren wie Pathogenen, Strahlung, Chemikalien oder mechanischen Traumata beschützt. Bewerkstelligt wird dies durch die Bildung einer undurchlässigen, widerstandsfähigen Barriere aus eng miteinander verbundenen Zellen in den obersten Schichten. Damit ihre Funktionen durchgehend in korrekter Art und Weise ausgeführt werden, durchläuft die Epidermis einen Prozess der konstanten Erneuerung, auch epidermale Homöostase genannt. Währenddessen bilden proliferativ aktive basale Keratinozyten neue Tochterzellen, welche auf ihrem Weg zur Körperoberfläche in ein spezifisches Differenzierungsprogramm eintreten und in den letzten Schritten eine Barriere bilden, bevor sie letztendlich von der Haut abgeschuppt werden. Erwartungsgemäß bedarf dieser komplexe Prozess strenger Kontrolle, zumal sich selbst das Auftreten kleiner homöostatischer Unregelmäßigkeiten in ausgeprägten Hautkrankheiten widerspiegeln kann. Dementsprechend ist die Rolle vieler Signalwege in epidermaler Homöostase gut charakterisiert. Nichtdestotrotz lässt die wahrscheinliche Existenz zusätzlicher regulatorischer Ebenen auf das Vorkommen weiterer biologischen Makromoleküle wie etwa Proteine oder nichtkodierender RNAs schließen, die in der Aufrechterhaltung epidermaler Funktionen involviert sind.

In einem Screening-Verfahren zur Identifizierung potenziell regulatorischer, nichtkodierender Transkripte hatte eine neuartige RNA, die wir daraufhin *P4* nannten, höhere Expressionslevel in proliferierenden verglichen mit differenzierten Keratinozyten gezeigt. In Folgeexperimenten hatten wir das Transkript bereits grob in Bezug auf Exonarchitektur, Polyadenylierungsstatus, Lokalisierung und Abundanz untersucht. Zudem hatten erste phänotypische Analysen nach *P4*-Knockdown markante Veränderungen in Hinblick auf die Differenzierung von Keratinozyten aufgezeigt. Da *P4* abseits einiger bekannten Funktionen in Krebsgewebe noch weitgehend unerforscht war, strebten wir danach, jene RNA weiter bezüglich ihrer grundlegenden Transkripteigenschaften, assoziierten phänotypischen Veränderungen und möglichen Interaktionspartnern zu ergründen.

Unsere Analysen zeigten, dass *P4* in über Keratinozytenzelllinien hinweg ein ähnliches, vom Differenzierungsstatus abhängiges Expressionsmuster aufzeigt, zudem wurden in einigen Arten von Krebszellen erhöhte Transkriptmengen detektiert. Zusätzlich zum ursprünglich identifizierten langen Transkript wurde mindestens eine weitere *P4*-Isoform in Keratinozyten

nachgewiesen. Ein innerhalb der *P4*-Sequenz von befindlicher offener Leserahmen weist laut unserer Experimente nur eine geringe Wahrscheinlichkeit der Translation in ein funktionales Protein auf, jedoch wurde eine Assoziation des Transkripts mit Ribosomen gezeigt. Eine wahrscheinliche Sekundärstruktur von *P4*, die unter Einbezug experimenteller Daten berechnet wurde, zeigt eine modulare Organisation zweier unabhängiger Domänen.

Während die Überexpression von *P4* keine eindeutigen Unregelmäßigkeiten hervorbrachte, mündete Herunterregulierung der RNA in organotypischem Gewebe in einer Vielzahl damit verbundener phänotypischer Änderungen. Diese umfassten das Auftreten ungewöhnlicher histologischer Besonderheiten, angehobene DNA-Replikation, veränderte Verteilung struktureller Proteine und Abweichungen in der Lipidkomposition. Des Weiteren enthüllte Depletion von *P4* in 2D-kultivierten primären Keratinozyten mehrere damit einhergehende Effekte, darunter eine Verschiebung der Zellpopulationen hin zur Synthesephase des Zellzyklus, verminderte Zelladhäsion und Migration sowie erhöhtes Zellwachstum unter bestimmten Bedingungen.

Drei unterschiedliche Methoden wurden zur Identifikation von Proteinkandidaten mit potenzieller *P4*-Interaktion herangezogen, manche der resultierenden Proteine wurden wiederum in Folgeexperimenten validiert. Auf diesem Wege konnte eine Bindung von *P4* an die β-Untereinheit der Phenylalanyl-tRNA-Synthetase (FARSB), an das zentrosomenassoziierte Centrin-2 (CETN2) und an das Doppelstrang-RNA-Bindeprotein Staufen Homolog 2 (STAU2) gezeigt werden.

Der genaue Ablauf dieser Interaktionen sowie nachfolgende mechanistische Schritte, welche die beobachteten Phänotypen erklären, verbleiben Gegenstand künftiger Untersuchungen. Nichtsdestotrotz konnte *P4*, ein neuartiges Schlüsselelement humaner epidermaler Homöostase, im Laufe der hier präsentierten Studien umfassend in Hinblick auf das Transkript an sich, verwandte phänotypische Manifestationen und interagierende Proteine charakterisiert werden.

3. Introduction

3.1 The human skin

Life is one of the most versatile and therefore still not quite fully explored aspects of nature that, due to its fundamentality in enabling concepts such as consciousness itself, gives rise to a scientific branch harboring innate fascination for humanity. This is why some of the most basic and intuitive questions in this area, such as the search for defining characteristics that are required for the formation of organisms, are attempted to be answered not only by those explicitly labeling themselves as biologists, but also by persons originally stemming from other fields of science. In his short book *What is Life?*, Erwin Schrödinger formulated living beings to prevent "the rapid decay into the inert state of 'equilibrium'" by carrying out metabolism as a controlled exchange of material with the surrounding environment[1]. However, to guarantee that this essential process does indeed remain well-ordered and regulated, boundaries separating and protecting organisms from external conditions need to be established.

In single-celled creatures like bacteria, this delineation is generally accomplished by cell membranes that are in many cases mechanically supported by cell walls and, in order to enable metabolism, exhibit selective permeability for molecules and ions[2]. However, multicellular eukaryotes such as metazoans often require specialized, macroscopic structures to ensure proper compartment separation as well as guarding of vulnerable internal tissues against mechanical stress and environmental hazards[3]. In the early embryogenesis of eutherian mammalian species, multiple extraembryonic membranes play a major part in fulfilling such protective functions, with the amniotic-sac-derived placenta being the most prominent measure as it keeps the developing fetus safe from mechanical and pathogenic dangers[4]. Nonetheless, in order to enable autonomous protection of the developing body, a layer of ectoderm-derived cells grows to form the epidermis starting from day 9.5 of human embryonic development[5]. Subsequently, together with mesenchymal cells, morphogenesis of elements such as hair follicles and the basement membrane are initiated, the latter being an extracellular structure that divides the epidermis from the mesoderm-originated dermis, and both layers contribute to what we commonly refer to as skin[5].

3.1.1 Skin architecture and compartments

In general, the human skin can be divided into multiple substructures, each carrying out their own important tasks (Figure 1A). A deep lying compartment referred to as hypodermis separates the skin from connective tissues beneath and, due to its nature of comprising mainly adipocytes, carries out functions such as insulation, energy storage and padding from mechanical trauma, while also containing root parts of sweat glands as well as elements of vascular and nervous systems[6]. However, recently it has been found that some populations of the adipose tissue present in skin share a common precursor with dermal fibroblasts, promoting the idea that the border between hypodermis and dermis may be defined by subtle distinctions in functionality and morphology of dermal white adipose tissue (dWAT) and underlying subcutaneous WAT, both divided by the *panniculus carnosus* muscle in some vertebrates[7].

Apart from dWAT, dermal tissue can additionally be divided into the papillary dermis in close proximity to the epidermis that contains dense but disordered collagen fibers supporting the structure of the basement membrane, and the reticular dermis below that is composed of more organized and thicker collagen bundles with a lower overall density[8]. The dermis is mainly comprised of different subsets of fibroblasts, some of which form specialized structures such as the dermal papillae that, in communication with neighboring epithelial cells, coordinate formation of hair follicles with their adjacent sebaceous glands and *arrector pili* muscles[9]. These are only some of the many types of dermal appendages also including mechano- and thermoreceptors, sweat glands and underlying blood capillary networks, all of which being important for reception of, and adaptation to external stimuli[9].

Although it is common to strictly separate the skin into fixed compartments, it has to be noted that cells of these layers can still crosstalk with each other. This becomes particularly evident during skin wound repair when fibroblasts synthesize the extracellular matrix needed to form a niche for epithelial stem cells in order to regenerate the epidermis[10]. A similar, specialized matrix is the aforementioned basement membrane that is composed of proteins such as collagens, laminins or nidogens derived from either epidermal cells, dermal cells or both[11]. Located on top of the basement matrix and close to the body surface sits the epidermis, a skin layer that, compared to other mammalian species, demonstrates increased thickness in humans and forms expansions that extend downwards into the dermis and are called rete ridges[12]. The essential function of the epidermis is to provide a sturdy and impermeable barrier around the human body protecting it from excessive water loss as well as mechanical trauma, irradiation or pathogens.

3.1.2 Morphological changes during epidermal homeostasis

Apart from few additional cell types including melanocytes, Merkel cells and immune cells, interfollicular epidermis mainly consists of keratinocytes that uphold an important balance of proliferation and differentiation[9]. Unlike other skin compartments, the epidermis undergoes a dynamic process of keratinocyte division at the basal layers, differentiation of the cells as they are pushed upwards, and eventually cell death and desquamation once the skin surface is reached. This process that guarantees upholding of the epithelial barrier is termed epidermal homeostasis and one cycle of daughter cell generation to death lasts 30 to 40 days in humans[13].

Generally, the epidermis can be divided into four layers or *strata* (Figure 1B). The *stratum basale* is connected to the basement membrane through hemidesmosomes and consists of epidermal stem cells that secrete components of the bottom niche while undergoing symmetric cell divisions to maintain the progenitor cell pool, but also asymmetric divisions, giving rise to daughter keratinocytes that start the epidermal differentiation program as they move upwards[14]. Apart from their proliferative activity, characteristics of basal keratinocytes are the expression of keratins K5 and K14 as well as a flexible cytoarchitectural network of microtubules and actin filaments establishing contact to E-cadherin-mediated intercellular adherens junctions by interaction with catenins[12].

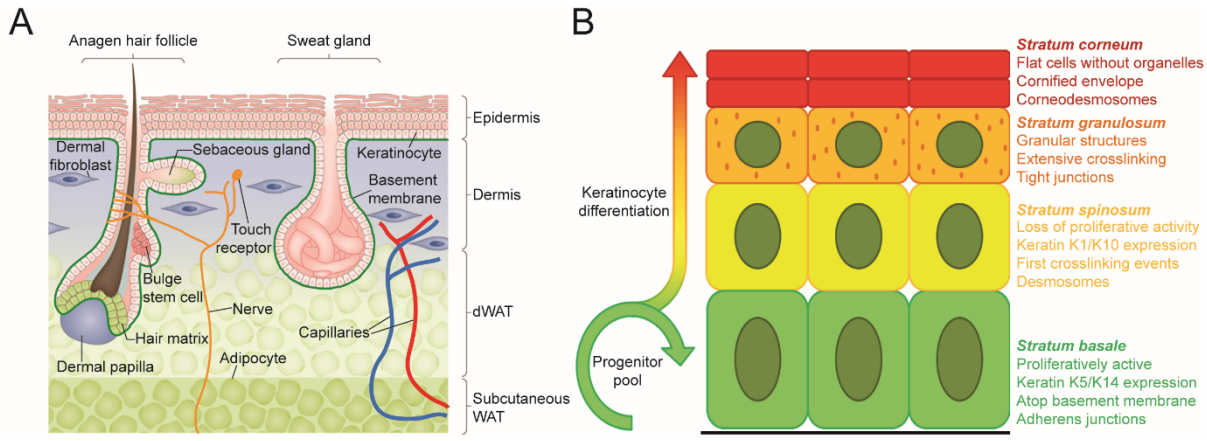

Figure 1: Organization of human skin compartments. (A) Schematic depiction of skin architecture. Human skin can be divided into a bottom layer containing mostly adipose tissue which provides insulation and energy storage, a dermal mid layer including several appendages with a broad variety of receptive and adaptive functions and, separated from the lower layers by the basement membrane, the uppermost epidermis that ensures protection from the surrounding environment (modified from [15]). **(B)** Overview of epidermal stratification during homeostasis. Epidermal stem cells in the *stratum basale* with contact to the basement membrane niche undergo symmetrical and asymmetrical cell divisions to either uphold the progenitor cell pool, or, in case of the latter, generate daughter cells stepping into the keratinocyte differentiation program. On their way towards the surface, the cells that are now devoid of proliferative capability experience multiple molecular biological and morphological changes. In the *stratum spinosum*, initiation of crosslinking events takes place which are intensified in the following *stratum granulosum* and *stratum corneum* layers, culminating in the formation of the sturdy and impermeable cornified envelope by flattened, organelle-less corneocytes with heavily crosslinked structure proteins on one hand and extracellular lipids on the other.

The suprabasal *stratum spinosum* is composed of daughter keratinocytes that have lost their proliferative activity and show multiple alterations in their expression pattern, such as a shift towards keratins K1 and K10, which are abundantly connected to desmosomes in order to provide a robust mechanical network[12]. In addition, structural proteins envoplakin and periplakin are crosslinked beneath the plasma membrane by transglutaminases TG1 and TG5, whereas other cornified-envelope proteins such as involucrin are being synthesized[16].

In the *stratum granulosum*, changes to cell morphology become more obvious as macroscopic structures like keratohyalin granules or lamellar bodies are discernible. In summary, the granular layer is mainly characterized by reinforcement of structures that were already initiated in the *stratum spinosum*, such as transglutaminase-mediated crosslinking of additional proteins including loricrin, involucrin and small proline-rich proteins to the cell membrane and desmosomes[16]. In later stages of the *stratum granulosum*, lipids including sphingomyelin and ceramides deriving from the lamellar bodies are secreted into intercellular spaces where they are modified and arranged to form what is known as the lipid envelope[17,18]. Moreover, transmembrane proteins such as claudins and occludin enable formation of an additional barrier by tight junctions which is hypothesized to provide impermeability to water and ions[19].

Ultimately, in the uppermost *stratum corneum*, profilaggrin that is the main component of keratohyalin granules is dephosphorylated and proteolytically cleaved into filaggrin which in turn causes aggregation of keratin filaments, a process that leads to flattening of the cells then termed corneocytes[20]. Further crosslinking of proteins in combination with the extracellular lipids secreted by granular keratinocytes results in the formation of the cornified envelope, a structure that replaces the plasma membrane and, together with corneodesmosomes, is responsible for the tight epidermal barrier that protects the human body[16,21]. Moreover, controlled disruption of organelles including mitochondria and nuclei as well as DNA degradation leaves corneocytes behind as lifeless husks that are eventually shed off in the process of desquamation which is mediated through the proteolysis of corneodesmosomes[22,23].

3.1.3 Regulation of keratinocyte proliferation and differentiation in epidermis

As epidermal homeostasis poses a highly complex process that needs to be carried out in an exact manner, tight regulation is necessary. Up to this point, many aspects of the employed signaling pathways have been elucidated. The first question one may ask is what the

determinants are that lead to the decision-making of cells towards either symmetrical or asymmetrical division, or to turn them from proliferative activity to committed differentiation.

One factor that appears to promote asymmetrical divisions is an increased cell density or height-to-width ratio of basal cells through mechanisms that may be mediated by not yet fully explored lateral and basal neighboring interactions, such as binding of basement membrane components by β1 integrin[24,25]. Downstream asymmetric cell division components such as LGN and NUMA1 promote reorientation of the mitotic spindle, enabling subsequent perpendicular divisions that also promote suprabasal Notch signaling as an important effector of differentiation[26]. In contrast, upon experiencing stretch-mediated mechanical stress, actomyosin cytoskeleton regulators such as non-muscle myosin are able to detect these stimuli and activate downstream nuclear translocation of transcriptional regulators such as MAL and YAP1 that promote a shift towards stem cell renewal rather than differentiation[27]. In general, the Hippo pathway effector YAP1 that exerts its function together with the TAZ transcriptional coactivator appears to be rather prevalent in inducing stem cell proliferation in response to mechanical cues[28]. This is also the case for basal keratinocytes responding to increased suprabasal contractility due to microtubule disruption, where augmented nuclear YAP1 localization and a concurring increase in proliferative activity are observed[29].

In addition, paracrine signaling plays a major role in controlling the balance of keratinocyte proliferation and differentiation. Many of these signals appear to be derived from dermal fibroblasts, including IGFs, FGFs and EGFR ligands[14]. The insulin growth factor receptor IGF-1R is shown to play a major part in both promoting skin proliferation and inhibiting differentiation-related effects as ablation of the receptor results in thin epidermis exhibiting pathologically facilitated differentiation; both the Ras/ERK MAPK pathway and the PI3K/Akt/mTORC1 axis seem to be active downstream mediators of this process[30]. In addition to response to paracrine signals, mTORC1 is also influenced by energy levels through the AMP-activated protein kinase and possibly by amino acid availability, suggesting an effect of both factors on skin homeostasis[31]. The Ras/ERK MAPK cascade alters expression of more than 140 target proteins and affects a broad spectrum of cellular functions such as proliferation, differentiation and migration which is why upholding of typical signaling levels is important for correct epidermal homeostasis[32]. Another upstream signal transmitter for Ras proteins is the epidermal growth factor receptor EGFR which is why many of the effects upon ligand binding are analogous to IGF-1R[32,33]. Fibroblast growth factor receptors FGFR1 and FGFR2 exhibit similar downstream targets and also mediate increased cellular proliferation upon binding of

FGFs; however, loss of specific receptor splice variants resulted in downregulation of tight junctions in the *stratum granulosum*, while wild-type keratinocytes treated with FGF7 demonstrated increased expression of responsible genes, indicating further, not yet characterized signaling pathways[34,35]. While TGF-β family proteins such as BMPs may act synergistically with FGFs in epidermal development to promote basal cell proliferation and subsequent tissue stratification, during tissue homeostasis TGF-β exerts its functions as inhibitor of epithelial growth[36,37]. Another family of majorly important signaling molecules in epidermal development is represented by WNT proteins as they determine the epidermal fate of ectoderm-derived cells by inhibiting the response to FGFs while also inducing the aforementioned BMP-FGF cascade for initial spinous layer formation[38]. In adult epidermal tissue, autocrine WNT signals are described to promote stem cell self-renewal while simultaneous secretion of WNT inhibitors may induce differentiation of distant progeny keratinocytes[39]. G-protein coupled receptors are a diverse protein family that, in the context of modulating keratinocyte proliferation and differentiation, play important roles in activating multiple mechanisms such as the already addressed Hippo YAP1 or WNT/β-catenin cascades, but also the Hedgehog GLI signaling pathway[40]. During epidermal homeostasis, while having several functions in hair follicle maintenance, Hedgehog is involved in crosstalk with other signaling components such as YAP1 and β-catenin[41].

Additionally, an aspect that plays a major role in epidermal homeostasis but was so far left unmentioned is the occurrence of calcium gradients. In human epidermis, Ca^{2+} concentrations steadily increase from the *stratum basale* up to the *stratum granulosum* but decline again in the *stratum corneum*; and this particular distribution is hypothesized to be caused by low transepidermal water loss paired with ion impermeability of the cornified envelope and tight junction barriers, whereas it is also suggested that calcium released from endoplasmic reticulum via Ca^{2+}-responsive channels contributes to the gradient[42]. The levels of multiple miRNAs, which generally pose a major type of regulating molecules in epidermal homeostasis, are increased in response to elevated calcium concentrations, including *miR-203* that in turn targets transcription factors such as SNAI2 and p63, thus promoting keratinocyte differentiation[43,44]. p63 is an immensely important protein in epidermal development and homeostasis and is often referred to as a master regulator since it controls individual up- or downregulation of a broad spectrum of genes involved in proliferation, adhesion and chromatin remodeling among others[45]. Loss of p63 appears to negatively affect both proliferative and differentiation potential of adult keratinocytes with distinctions between both occurring isoforms and via p53-dependent and -independent mechanisms[46]. While p63 may directly activate or repress expression of

chromatin remodeler genes, including BRG1 and SATB1 that rearrange the epidermal differentiation complex (EDC) gene cluster on chromosome 1, it can also interact with HDAC1/2, one of many histone modifying complexes that are relevant in epidermal homeostasis[45,47]. Little has been uncovered of possible upstream mechanisms in terminal differentiation, however involvement of cathepsins in the activation of transglutaminases is known, whereas organelle disruption may be in part carried out by caspase-14 and calpain-1, and nucleic acid degradation is suggested to be in part modulated via RNase7, DNase1L2, DNase2 and TREX2[48]. Desquamation, on the other hand, is controlled by a kallikrein proteolytic cascade that crosstalks with other types of proteases in the skin and is induced by elevated calcium levels[49].

Taken together, many factors are involved in the control and modulation of keratinocyte cell fate which act through several signaling pathways that are not necessarily strictly separated from each other, but altogether form an entire network of regulatory elements with the shared goal of epidermis maintenance.

3.1.4 Perturbance of epidermal homeostasis in chronic skin conditions

Anormal changes to regulatory components may lead to defects in the stratification of epidermal tissue. This is the case for two genetic skin disorders, namely Darier disease and Hailey-Hailey disease, which are characterized by mutations in endoplasmic reticulum and Golgi calcium ATPase genes, respectively[50]. In the autosomal dominant Darier disease with a low prevalence around 1 in 50,000, defects in the *ATP2A2* gene cause loss of intercellular adhesion and premature cornification, leading to keratotic papules that form crusty lesions on the skin prone to infection[51]. The similarly rare Hailey-Hailey disease is caused by mutations in the gene coding for the Golgi-Ca^{2+}-ATPase ATP2C1; patient epidermis presents with suprabasal cell separation that is suggested to be partly caused by effects on NOTCH1[52].

Inflammatory reactions caused by a dysregulated immune system are found in many chronic skin diseases with psoriasis posing one that is rather common[53]. It may be caused due to polymorphisms in the *HLA-C*, *CCHCR1* and corneodesmosin (*CDSN*) genes, all of them located within the major histocompatibility complex on chromosome 6, and is characterized by reddened, well-defined plaques covered with silvery scales that are result of early keratinocyte differentiation onset paired with impaired cornification and barrier formation; furthermore, basal cell hyperproliferation culminates in increased epidermal thickness with elongated rete

ridges[54]. T-cell hyperactivity and accompanying aberrant excretion of cytokines such as interleukins IL-17 and IL-22 result in keratinocyte downstream signaling including the NF-κB pathway; hence, affected keratinocytes, while further promoting inflammation by producing cytokines themselves, show dysregulated levels of keratins and cell junction proteins such as occludin, E-cadherin or connexin CX26[55]. Lichen planus on the other hand is a more uncommon inflammatory skin disease that manifests in purple, polygonal and flat-topped papules crossed by white lines and has a rather unexplored pathogenesis, however mutations within the human leukocyte antigen (HLA) system seemingly increase susceptibility for lichen planus[56]. Diseased epidermis is characterized by hyperkeratosis which means enhanced cornification, acanthosis referring to a broadened *stratum spinosum*, hypergranulosis that stands for increased occurrence of keratohyalin granules in the *stratum granulosum*, vacuolic alterations in the basal layer, changes in rete ridges and increased occurrence of apoptotic keratinocytes near the basal layer termed colloid bodies[56].

Due to causative mutations in their genes, keratins play a major role in the skin conditions of pachyonychia congenita and epidermolysis bullosa simplex[57,58]. The quite rare pachyonychia congenita is at least partly caused by autosomal dominantly mutated wound-repair-associated keratin genes accompanied by an imbalance of keratin levels, and often results in lesions on patient palms and soles termed palmoplantar keratoderma that exhibit hyperkeratosis and epidermal thickening[57]. Epidermolysis bullosa simplex patients often carry autosomal dominant mutations in their *KRT5* and *KRT14* genes, leading to protein misfolding that causes cytoskeletal defects combined with weakened intercellular junctions and by this a generally high predisposition of affected epidermis to rupture in response to mechanical trauma[58].

Mutations in genes encoding structural proteins are as well found in ichthyosis vulgaris, a common disease with a prevalence of around 1:200 that is characterized by a hyperproliferative epidermis demonstrating both thickening of the cornified layer and reduction of the *stratum granulosum* accompanied by smaller and less keratohyalin granules, all of which manifests in dry and scaly skin[59]. In ichthyosis vulgaris, the filaggrin gene *FLG* is mutated in a loss-of-function fashion, but other ichthyosis subtypes carry mutations on genes encoding keratins, transglutaminases or proteins related to formation of the lipid envelope[60]. Additionally, *FLG* null mutations are a predisposing factor for atopic dermatitis, a mostly pediatric disease with the typical symptom of persistent itching of the skin that is based on a complex pathophysiology combined of disturbed immune response and an impaired epidermal barrier due to genetic defects[61,62].

While many of the here addressed skin disorders are at least partly caused by preexisting genetic alterations, somatic skin cells can also acquire risky mutations by excessive interaction with environmental hazards in spite of the epidermis providing valuable protection. This is the case for actinic keratosis in which UV irradiation causes cytosine to thymine transitions within the gene encoding the p53 transcription factor that is responsible for cell arrest and apoptosis in response to DNA damage[63]. Basal cells often exhibit atypic morphology with changes in nuclear-to-cytoplasmic ratio, loss of polarity and frequent superposition, whereas abnormal keratinization and inflammation can be additionally observed; and while actinic keratosis often remains at this stage or sometimes even regresses, it can also develop into cutaneous squamous cell carcinomas (cSCCs)[64]. These malignancies present with uncontrolled keratinocyte proliferation and massively disturbed epidermal architecture, but unlike the more common basal cell carcinomas, cSCCs tend to invade surrounding tissue which increases mortality by a lot, resulting in approximately 350,000 deaths in the year 2019 alone[65–68]. With a median of 45.2 mutations per megabase, cSCC is the cancer type with the highest mutational burden which emphasizes the sturdiness of epidermal tissue against environmental damage, but also impedes the identification of individual cSCC drivers apart from classic candidates such as genes encoding the p53, Notch and Ras proteins, whereas in general many important pathways and effectors of epidermal homeostasis are dysregulated[67,69].

Summarized, the high complexity of regulation taking place in epidermal tissue comes with many potential attacking points which, if perturbed, can cause detrimental skin conditions. Therefore, a broad spectrum of regulatory elements is favorable since redundancy of single cogs in the whole homeostatic machinery may avert such scenarios. However, a large amount of mediators and effectors which remained unnoticed for a long time is just now steadily being discovered and characterized due to the realization that not only proteins, but also nucleic acids may participate in regulatory processes.

3.2 Long non-coding RNAs

In his aforementioned book that was published in 1944, Schrödinger additionally suggested an "aperiodic crystal forming the hereditary substance" to be the "material carrier of life"[1]. Coincidentally, both James Watson and Francis Crick were inspired by this work to enter the field of molecular biology which in 1953 famously culminated in them suggesting, based on Rosalind Franklin's and Maurice Wilkins' data, a double helical structure of this "aperiodic

crystal" that is desoxyribonucleic acid[70–72]. Only five years later, Crick described that ribonucleic acid might be produced to extract information carried by DNA, as well as a potential role of RNA in directing the correct amino acid arrangement for proteins in microsomal particles, those in turn consisting of both RNA and proteins, and that latter process of protein synthesis could be mediated by additional, nucleotide-containing adapter molecules[73]. Not only did Crick by this predict the quintessential processes of transcription and ribosomal translation in cells, but he also pointed out the existence of different functional RNA types.

While acting as a messenger RNA (mRNA) for the purpose of protein synthesis is one of the most prominent RNA functions, only approximately 1.2% of total bases in the genome carry actual information coding for annotated proteins, whereas at least 62% are actively transcribed into RNA[74]. This can be partially explained by untranslated regions at both ends of mRNAs and by introns that are subsequently spliced out of immature transcripts, but still a large fraction of RNA remains that may fulfil non-coding functions. Two types of these non-coding RNAs (ncRNAs) had already been implied in Cricks original hypothesis, on one hand ribosomal RNAs (rRNAs) which in fact constitute around 80% of total cellular RNA and are integral components of ribosomes responsible for catalysis of peptide bond formation during translation, and on the other hand transfer RNAs (tRNAs), heavily base-modified adapter molecules that exhibit a conserved cloverleaf secondary structure and form the link between mRNA codons and their corresponding amino acids[75,76]. Small nuclear RNAs (snRNAs) with high uridine content are mostly components of the major and minor spliceosomes that catalyze RNA splicing[77]. Small nucleolar RNAs (snoRNAs) are primarily responsible for directing post-transcriptional editing machinery towards other ncRNAs such as rRNAs and snRNAs, whereas some play important roles in pre-rRNA cleavage[78].

In contrast to these "housekeeping RNAs", small interfering RNAs (siRNAs), microRNAs (miRNAs) and piwi-interacting RNAs (piRNAs) are essential in providing sequence-specific regulation of gene expression and transcript levels by guiding proteins such as members of the Argonaute family to complementary base sequences[79]. This may result in endonucleolytic cleavage, translational repression and enhanced degradation of target RNAs, or in the case of piRNAs to histone modifications and DNA methylation[80,81]. Another class of RNAs with often regulatory functions that sparked major interest in the past few decades is represented by long non-coding RNAs (lncRNAs).

3.2.1 Characteristic features of lncRNAs

For a long time, lncRNAs were commonly defined as non-coding transcripts that are longer than 200 nucleotides (nt) which is a frequent size threshold in RNA purification protocols, though the existence of other non-coding RNAs such as the 305 nt long *7SL* supports a readjusted definition of lncRNAs as transcripts that are longer than 500 nt and mostly generated by RNA polymerase II[82]. Due to the latter fact, lncRNA transcription and processing often resembles that of mRNAs and results in the occurrence of co-transcriptional lncRNA modifications such as 5' m^7G-capping and polyadenylation[83]. However, lncRNAs also show distinctions from mRNAs in that they exhibit both decreased abundance levels and lower sequence conservation, whereas expression profiles appear to be comparably conserved across species[84,85]. Furthermore, lncRNA promoters are usually more devoid of histone marks apart from H3K9me3 and are bound by fewer different families of transcription factors than mRNA promoters[84,86]. Moreover, the most important factors that facilitate initiation of lncRNA transcription appear to be open chromatin regions and R-loop structures in which RNA-DNA hybrids are formed[87]. In addition, lncRNAs generally contain fewer exons as a result of weaker splicing, and termination differs from mRNA in that a wide variety of alternative mechanisms is employed[86,87]. Increased nuclear localization of lncRNAs may be partly caused by tethering to neighboring chromatin during transcription, or by sequence-based recruitment of nuclear factors[83]. Surprisingly, many of the cytosolic lncRNAs that may have been translocated through mechanisms similar to mRNA nuclear export demonstrate an association with polysomes, presumably promoted by cryptic open reading frames (ORFs), 5' methyl guanosine caps and long "pseudo-5'-UTRs"; and it is suggested that ribosome association and translation possibly triggers degradation as a general mechanism of lncRNA turnover[88,89]. Sequence- and structure-based features that occur favorably in lncRNAs include repetitive regions which may be derived from transposable elements, unusual secondary structure elements such as non-canonical base pairing, pseudoknots, G-quadruplexes or triple RNA helices, and a tendency of transcripts to form modular domains[90].

As can be seen, lncRNAs represent a very diverse category of RNAs which prompts a need for classification. A common approach to this problem is the subdivision of these transcripts based on their genomic location in respect to annotated regions. Hence, lncRNAs can be classified into enhancer, promoter-associated, genic sense- or antisense-orientated and intergenic RNAs (Figure 2A)[91]. However, it becomes more and more clear how the actual genetic landscape is far more fluent and complex than initially considered and that current gene annotations are still

a long way from drawing the whole transcriptomic picture[82]. Therefore, molecular mechanisms through which lncRNAs achieve their function may be more suitable as a parameter for categorization.

3.2.2 LncRNA modes of action

In general, lncRNA may be subdivided into three different *modi operandi* by which they execute their function, as they mostly act as guides, scaffolds or decoys for other molecules (Figure 2B). Guide lncRNAs usually direct bound effectors towards nucleic acid sites for which they demonstrate sequence- or structure-specific binding affinity, or towards regions that are in close proximity to their corresponding transcription units. These spatial distinctions relative to their original gene loci enable further subdivision of lncRNAs into those that accumulate or act in *cis* on the DNA nearby, transcripts operating in *trans* at distant regions on the same or another chromosome, or lncRNAs which are not post-transcriptionally interacting with DNA at all[92].

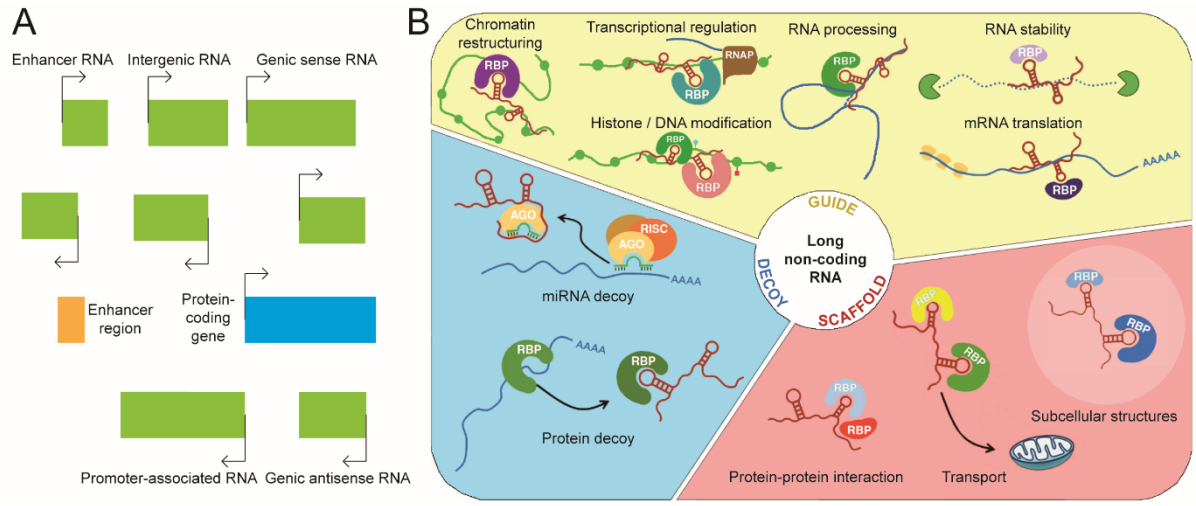

Figure 2: Different methods of lncRNA classification. (A) Categories of non-coding transcripts based on their genomic location. LncRNAs can originate from loci that overlap with annotated protein-coding genes or enhancer regions, are not covered by any of those genomic elements at all, or are transcribed in a divergent manner, using the same promoter as known genes. LncRNA genes are colored green, enhancer elements orange, and protein-coding genes blue; arrows indicate transcriptional direction. **(B)** Subdivision of lncRNAs in respect to their molecular mechanisms. Modes of action include guiding of effector molecules towards specific DNA and RNA regions, generating scaffolds to enable spatial and temporal concurrence of multiple interacting effectors, and posing as decoys by competitively titrating nucleic acids or proteins away from their usual targets. LncRNAs are colored in red, DNAs in dark green, miRNAs in light green and other RNAs in blue. RBP is short for RNA binding protein, RNAP for RNA polymerase, RISC for RNA-induced silencing complex, and AGO for member of the Ago protein subfamily (modified from [93]).

The most common functions of DNA-associated lncRNAs include effects on remodeling and spatial reorganization of chromatin, direct transcriptional regulation, histone modification and DNA methylation [94]. An exemplary non-coding transcript affecting chromatin structure is the mouse transcript *Evf2* which recruits the ATPase BRG1 to the enhancers of the *Dlx5* and *Dlx6* genes and similarly inhibits its activity[95]. Also in mice, the *Firre* lncRNA appears to modulate nuclear architecture by interacting with five distinct *trans*-chromosomal loci resulting in spatial proximity of these sites to the *Firre* gene[96]. Recruitment of transcription regulators is demonstrated by lncRNAs such as the p53-induced mouse transcript *lincRNA-p21* which inhibits expression of multiple genes by association with hnRNP-K, in turn component of a transcriptional repressing complex[97]. Likewise, the *Airn* lncRNA inhibits expression of its neighboring gene *Igf2r* in mice, but apparently achieves this by mere transcriptional overlap[98]. *HOTAIR* is a lncRNA recruiting Polycomb Repressive Complex 2 (PRC2) to the 40 kb distant *HOXD* locus in humans where it trimethylates lysine-27 residues of histone H3 which is a chromatin mark repressing transcription[99]. One of the first-discovered lncRNAs that is very well-known is the *H19* transcript that mediates genomic imprinting by DNA methylation of the *Igf2* gene that is 95 kb distant in mice[100,101]. Another long non-coding transcript that is known for quite some time by now is *Xist* that achieves dosage compensation by X-chromosome inactivation via crosstalk of multiple mechanisms involving histone modification[102].

Guide lncRNAs may also exhibit specific binding to RNAs and thereby exert posttranscriptional functions such as regulation of RNA processing, stability or translation[103]. LncRNAs may mediate transcript-specific alternative splicing as shown for the human non-coding transcript *EGOT* that hybridizes with the *IPTR1* pre-mRNA and recruits hnRNPH1 to regulate splicing of *pre-IPTR1*[104]. Exemplary for effects on RNA editing, interaction of the m^6A demethylase ALKBH5 with the nascent *FOXM1* transcript is shown to be promoted by the antisense lncRNA *FOXM1-AS*, resulting in enhanced levels of *FOXM1* gene products in human glioblastoma cells[105]. Both mural and human *Meg3* lncRNA binds to Ptbp1 and appears to guide it towards the *Shp* mRNA, promoting its decay[106]. In addition to its aforementioned function as a transcriptional regulator, *lincRNA-p21* targets the *CTNNB1* and *JUNB* mRNAs in humans and inhibits production of their corresponding proteins, likely by interacting with the translational repressor RCK[107].

A class with broad variety of functions are scaffolding lncRNAs that possess different binding domains, enabling tethering of multiple effector molecules at once[108]. This simultaneous binding of multiple partners may lead to the formation of subcellular structures as is the case

for *Neat1* which binds to the Fus, Sfpq, Nono and Pspc1 proteins in mice and is necessary for formation of paraspeckles, membrane-less nuclear bodies playing a role in mRNA sequestration[109]. The human lncRNA *NRON* is shown to regulate specific nuclear translocation of interacting NFAT family proteins by additionally binding to nuclear import factors such as importin β1[110]. *HOTAIR* demonstrates additional scaffolding functions in humans as it mediates interaction of the E3 ubiquitin ligases DZIP3 and MEX3B with their respective substrates ATXN1 and SNUPN, resulting in rapid decay of latter targets[111].

Lastly, lncRNAs can also titrate regulatory nucleic acids or proteins away from their canonical targets, thus acting as decoys and influencing the fate of remote molecules. *NORAD* is an abundant non-coding transcript in humans that sequesters PUMILIO proteins which in turn are repressors of stability and translation for a specific set of mRNAs coding for mitotic, DNA repair, and DNA replication factors; hence, interaction of *NORAD* with PUMILIO enables synthesis of those proteins[112]. *PTENP1* acts as a competing endogenous RNA that in humans prevents the *PTEN* and other mRNAs from being targeted by a specific set of miRNAs due to matching seed sequences within the transcript[113].

In summary, lncRNAs cover a wide spectrum of possible molecular mechanisms that may not always be clearly divisible into specific subclasses due to the intricacy of participating molecules. Furthermore, definite categorization of individual transcripts can be impeded by a plethora of potential functions as shown for *lincRNA-p21* and *HOTAIR*. Furthermore, downstream pathways are often complex and may potentially lead to multiple functions of lncRNAs in cellular processes.

3.2.3 Keratinocyte-linked lncRNAs in normal and disturbed epidermal homeostasis

Due to the high complexity of human epidermal homeostasis, it is not surprising that some affiliated regulatory functions are also fulfilled by lncRNAs. Some of the many differentially regulated transcripts have been additionally characterized to some degree as is the case for *BLNCR*, a lncRNA which is less expressed in keratinocytes during differentiation and appears to be regulated by p63 and AP-1, whereas its decrease in transcript levels precedes that of its neighboring gene *ITGB1*[114]. *PRANCR* is upregulated in proliferatively active epidermal layers and artificial depletion causes reduced proliferation and clonogenicity as well as cell phase shifts, whereas knockdown in organotypic tissue is accompanied by impaired stratification and global transcriptomic dysregulations in particular of genes containing a *CHR* promoter

element[115]. *LINC00941* also exhibits elevated levels in basal keratinocytes and cSCC while being downregulated in psoriasis, and its depletion in epidermis-like tissue results in transcriptome-wide upregulation of multiple genes involved in epidermal differentiation, moreover, its association with AGO2 points towards a potential mechanism as a miRNA decoy[116,117]. Similarly, the *ANCR* transcript exhibits decreased levels during epidermal differentiation and deficiency of the lncRNA in organotypic tissue results in premature onset of keratinocyte differentiation in basal layer, which is presumably achieved by recruitment of the EZH2 histone methyltransferase to the *MAF* and *MAFB* gene loci that in turn encode differentiation-related transcription factors[118,119]. Additionally, elevated *ANCR* levels are observed in psoriatic tissue[120].

Multiple lncRNAs demonstrate upregulation in differentiated tissue instead, for instance *H19* which regulates desmoglein-1 mRNA levels by acting as a competitive endogenous RNA for *miR-130b-3p*[121]. Moreover, miRNA-related mechanisms may also play a role in atopic dermatitis and psoriasis, where *H19* expression is decreased, and in cSCCs that exhibit elevated levels[120,122,123]. The *HOXC13-AS* transcript is increasingly found in suprabasal epidermal layers and its overexpression promotes differentiation of organotypic tissue, whereas knockdown reduces keratinocyte differentiation; furthermore, the lncRNA is upstream regulated by EGFR signaling and downstream interferes with molecular transport by sequestering the COPA protein[124]. LncRNA *uc.291* is downregulated both in basal epidermal tissues and in cSCC, and its depletion causes higher proliferative activity combined with impaired differentiation both in cultured keratinocytes and organotypic epidermal tissue; on a mechanistic level, *uc.291* is suggested to interact with the ACTL6A protein which otherwise inhibits induction of terminal differentiation genes by the chromatin remodeling BAF complex[125,126]. *NEAT1* is upregulated in differentiated tissue in a ΔNp63-dependent manner and binds, likely associated with paraspeckle proteins, to promoters of key epithelial transcription factors such as ZNF750 and KLF4, which may explain the observation of weaker differentiation in epidermal organotypic tissue models upon *NEAT1* knockdown[127]. Furthermore, *NEAT1* is abnormally overexpressed in psoriatic and cSCC tissue[120,128]. The lncRNA *SMRT-2* is downregulated in proliferative epidermal layers and squamous cell carcinomas, and its depletion in organotypic tissue causes global repression of genes associated with epidermal differentiation[129]. *TINCR* expression is reduced in undifferentiated epidermal layers, in SCCs in an ZNF750-dependent manner, as well as in atopic dermatitis and psoriasis; and *TINCR*-deficient epidermis exhibits lack of differentiation both on a morphological and transcriptomic level[120,130,131]. Mechanistically, *TINCR* binds to differentiation-related mRNAs such as *MAF*, *MAFB*, *KRT80* and *CALML5* via

a partially conserved sequence motif and, in complex with STAU1, mediates stabilization of those transcripts[119,130,132]. In addition, recent data suggest that *TINCR* encodes a small ubiquitin-like protein that is predominantly found in the *stratum corneum*, promotes cell cycle progression and acts as a tumor suppressor in squamous cell carcinomas[133–135].

Some lncRNAs are found to play roles in epidermal homeostasis under specific circumstances, for instance *SPRR2C* that is prevalently expressed in *stratum granulosum* and *stratum corneum* of middle-aged to old individuals as well as in tissues affected by atopic dermatitis and psoriasis; moreover, overexpression of this transcript causes upregulated expression of several late differentiation marker genes and a mode of action as a sponge for miR196a-5p and miR542-5p is assumed[120,136]. Wound repair is a particularly complex process in skin requiring an epithelial-to-mesenchymal transition (EMT) of keratinocytes and, to no surprise, lncRNAs also play regulatory roles in this context, such as *MALAT1* which is upregulated in skin wounds, psoriasis and cSCCs[137–139]. In diabetic wounds, changes in EMT-associated gene expression are observed upon *MALAT1* knockdown, presumably resulting from it usually binding to miR-205 that additionally targets *ZEB1*, a mRNA coding for a critical EMT transcription factor; besides, further miRNA sponging mechanisms of *MALAT1* in cutaneous wound healing-related WNT/β-catenin pathway activation are also reported.[140,141]. *WAKMAR1* is downregulated around chronic non-healing wounds in comparison to normal wounds and positively affects keratinocyte motility by interacting with multiple DNA methyltransferases and therefore inhibiting methylation of the *E2F1* promoter, affecting expression of a key transcription factor for several migratory genes[142]. TGF-β-induced *WAKMAR2* demonstrates a similar expression pattern in wounds and, proposedly by downregulation of NF-κB pathway activity, inhibits chemokine expression while similarly promoting cell migration; hence, its depletion is accompanied by impaired wound closing[143]. Defects in the skin barrier of chronic actinic dermatitis patients may be caused by decreased levels of *WAKMAR2* that targets transcription factor component c-Fos to the claudin-1 gene promoter[144]. Among its many functions, *lincRNA-p21* is also involved in induced apoptosis of UVB-exposed keratinocytes in which its levels are elevated in a p53-dependent manner, and knockdown of the transcript inhibits UVB-induced apoptosis[145]. Another lncRNA that is upregulated in response to UVB irradiation as well as other stress factors is *PRINS*, and keratinocytes with reduced transcript levels show lower viability in response to serum starvation; furthermore, based on its overexpression in involved as well as uninvolved psoriatic tissue *PRINS* appears to be a factor associated with psoriasis susceptibility[146]. Many more lncRNAs exhibit distinct regulation and characterized functions in psoriasis, such as *FABP5P3*, *KLHDC7B-DT*, *LINC00958*, *MEG3*, *MIR31HG*, and *RP6-*

65G23.1[147–149]. Moreover, non-coding transcripts with altered expression in cSCCs include *HOTAIR*, *LINC00319*, *LINC00520*, *LINC01048*, *PICSAR* and *THOR*[150,151].

Taken together, a broad variety of lncRNAs associated with proper and perturbed epidermal tissue maintenance have been found and characterized up until now, but far more are supposedly still undiscovered when assuming a similar diversity for regulatory nucleic acids as found for proteins in epidermal homeostasis.

3.3 Identification of *P4*, current knowledge and objective

Due to the high frequency of polymorphisms within non-coding genes and generally less severe phenotypes of regulatory mutations, identification of new lncRNAs occurs rarely via genetic screens but rather by detection of expression pattern changes in diseases or tissue-specific processes such as epidermal homeostasis[82]. This was also the case for a novel transcript that was, in collaboration with the FANTOM5 consortium, detected to be upregulated in proliferatively active keratinocytes when compared to differentiated cells[152]. Since the proposedly non-coding RNA had not been characterized at this point and only been genomically annotated based on predictions, we labeled it *P4* for future reference.

In commonly used human genome annotation databases, the *P4* gene is termed *AC004585.1*, *LOC105371773* or *ENSG00000266088* and is located between the C-C chemokine receptor type 7 and tensin-4 genes on the q-arm of chromosome 17, in close proximity to a keratin gene cluster[153–155]. *P4* expression is predicted to be influenced by three enhancer elements with a distance of 3.2, 15.0 and 40.2 kb from the transcription start site, respectively[156]. Moreover, according to published ChIP-sequencing data, parts of the gene body are enriched for the H3K9me3 mark, and the sequence is overall conserved within the eutherian clade[74,157,158]. In addition, while observed potentially pathogenic polymorphisms are only found in intron regions of predicted *P4* transcripts, publicly available ribosome profiling data suggests a 93 nucleotide long exonic small ORF to be occupied by ribosomes[159,160]. Human tissue expression data indicate enhanced *P4* levels in lymphocyte-containing parts of the organism, such as blood, bone marrow, lymph nodes, spleen, thymus and tonsils, while also being steadily expressed in organs involved in female reproduction including cervix, placenta and vagina, as well as parts of the digestive system such as appendix, colon, gall bladder and rectum, whereas modest *P4* expression is reported in other tissues including thyroid, skin and lung[161–163].

In a first published attempt at its characterization, *P4* expression levels are reported to correlate with metastasis in lung cancer, and depletion of *P4* or *lnc-IGFBP4-1*, as it is referred to in the publication, results in inhibition of proliferation and induced apoptosis, whereas overexpression promotes proliferative activity *in vitro* and *in vivo*[164]. Furthermore, *P4* appears to be associated with both ATP production levels and expression of transcripts originating from the *HK2*, *PDK1*, *LDHA* and *IGFBP4* genes[164]. Another report links high *P4* transcript levels to poor survival in bladder urothelial carcinoma, and its overexpression is shown to result in enhanced proliferation, reduced apoptosis and cell cycle progression, while depletion counteracts these phenotypes and suppresses tumor growth *in vivo*[165]. Mechanistically, *P4* appears to promote phosphorylation of STAT3, whereas JAK/STAT pathway inhibition rescues the phenotypes caused by *P4* overexpression[165]. Additionally, a further study reveals decreased *P4* levels in HeLa cells upon serum starvation and demonstrates that *P4* overexpression reverses autophagy-related alterations in protein levels and modifications, all of which having been priorly induced via *P4* depletion[166]. Binding of c-Myc close to the *P4* transcription start site reduces expression of the lncRNA, resulting in suppressed cell growth *in vitro*[166]. Many recent studies suggest *P4* as a potential predictive, diagnostic or prognostic biomarker for several types of cancer including breast carcinoma, clear cell renal cell carcinoma, endometrial cancer, esophageal adenocarcinoma, glioblastoma, hepatocellular carcinoma and melanoma[167–173].

Due to *P4* not having been characterized in human epidermis at all in spite of our internal preliminary experiments providing intriguing phenotypical results, aims of these doctoral studies were to continue with the transcript-centered characterization that had already began in our group, to reveal new *P4*-associated phenotypes in both organotypic epidermal tissue models and cultured primary keratinocytes additional to those that we had initially discovered, and to elucidate possible mechanisms by which *P4* functions, in particular by identifying and validating protein interaction partners.

4. Characterization of the *P4* transcript

At the point of time in which *P4* had been identified as a potential regulator of epidermal homeostasis, the transcript had neither been reliably annotated in common genome browser sites nor characterized regarding exonic structure, polyadenylation status or localization. Therefore, first analyses had been carried out in order to elucidate keratinocyte-specific properties of this RNA.

RACE experiments and cDNA sequencing that had been performed by Michaela Pöppel and Dr. Sonja Hombach had shown that the full-length isoform detected in keratinocytes comprises five exons of which the third exon includes a sequence not to be found in the GRCh38 human reference genome[174]. However, a new reference genome released by the telomere-to-telomere (T2T) consortium contains this particular sequence, indicating gaps in previous reference genomes (unpublished data, Figure 3A)[175].

Furthermore, polyadenylation of the transcript had been investigated by Bianca Förstl and Dr. Sonja Hombach via enrichment of poly(A)-positive RNAs using immobilized oligo(dT) followed by RT-qPCR analysis. For the *P4* transcripts which were targeted by the qPCR primers, these results had indicated 3' polyadenylation which is common for mRNAs and many lncRNAs (unpublished data, Figure 3B)[83].

Subcellular location of the *P4* RNA in keratinocytes had been specified by Bianca Förstl and Dr. Sonja Hombach via nuclear fractionation experiments with subsequent RT-qPCR measurements. These data had shown that the targeted isoforms localize mainly towards compartments enriched in the nuclear fraction (unpublished data, Figure 3C). Additional qPCR analyses normalized to *in vitro*-transcribed *P4* which had been carried out by Bianca Förstl and Dr. Sonja Hombach resulted in an approximate copy number for targeted *P4* transcripts of 60 molecules per keratinocyte (unpublished data).

While these initial experiments had already covered multiple characteristics of the *P4* RNA, little was known about possible isoforms, protein coding potential and secondary structure. Hence, in order to shed light upon these aspects, corresponding analyses were to be performed during doctorate studies.

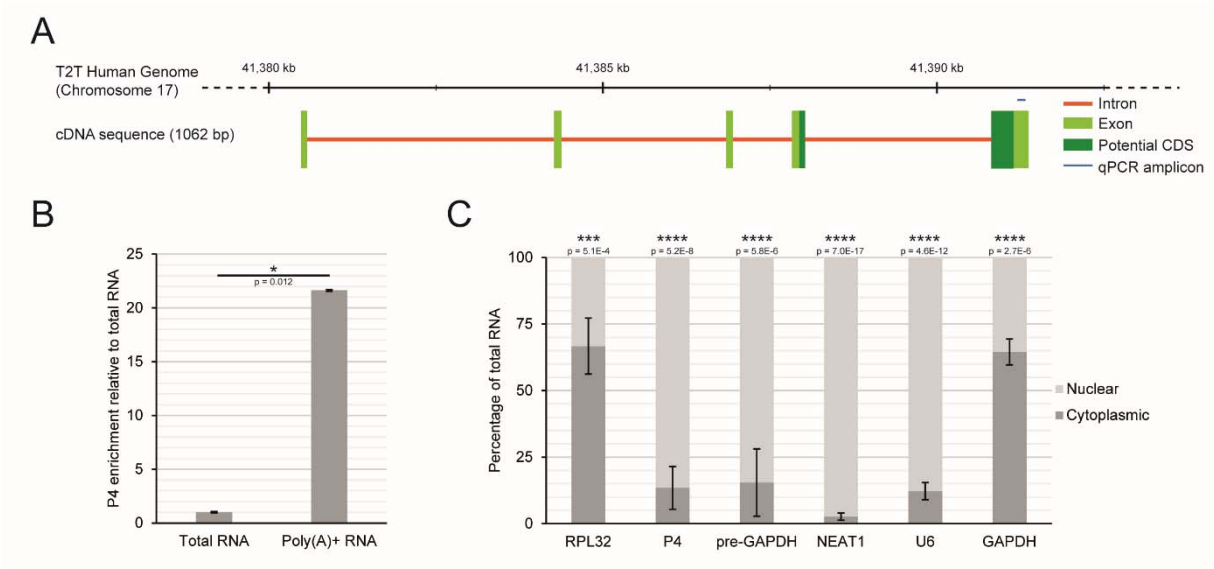

Figure 3: Known characteristics of *P4* transcripts in primary neonatal keratinocytes. (A) Genomic location and exon structure of the full-length *P4* isoform as identified by cDNA sequencing analysis. The *P4* locus spanning 10,892 base pairs on the q21.2 region of chromosome 17 is transcribed into an RNA containing five exons with a potentially protein-coding sequence on exons 4 and 5. With a length of 559 base pairs, the last exon constitutes a major part of the full-length transcript. **(B)** Polyadenylation status of *P4* transcripts. Isoforms targeted by the qPCR primers depicted in (A) show significant enrichment in the polyadenylated RNA fraction (N = 2). **(C)** Subcellular localization of *P4* RNA. Similar to known nuclear transcripts such as lncRNA *NEAT1* or snRNA *U6*, isoforms of *P4* covered by the qPCR primers indicated in (A) are mainly found in nuclear fractions (N = 6). P-value indicators across figures are ns (> 0.05), * (< 0.05), ** (< 0.01), *** (< 0.001) and **** (< 0.0001).

4.1 Results

4.1.1 Expression and isoforms of *P4*

4.1.1.1 P4 is steadily expressed in keratinocytes and several carcinoma cell lines

While *P4* expression changes in the differentiation of primary neonatal foreskin keratinocytes (NKCs) had already been investigated, little was known about its RNA levels in immortalized cell lines. Hence, corresponding RT-qPCR analyses with normalization to the housekeeping gene *RPL32* were performed to compare relative expression levels. Gastrointestinal cancer cell and melanoma cell lines as well as HeLa and HepG2 cDNAs were supplied by Kevin Heizler and Michaela Bauer from the group of Prof. Dr. Gunter Meister (Department of Biochemistry I, University of Regensburg). For the tested keratinocyte cell lines, 2D differentiation was induced and RNA purified at several points in time. The immortalized keratinocyte cell lines N/TERT1 and N/TERT2G showed an expression pattern during differentiation that resembles that of NKCs, whereas increased *P4* levels could also be detected in leukemia, colorectal cancer and melanoma cell lines (Figure 4)[176].

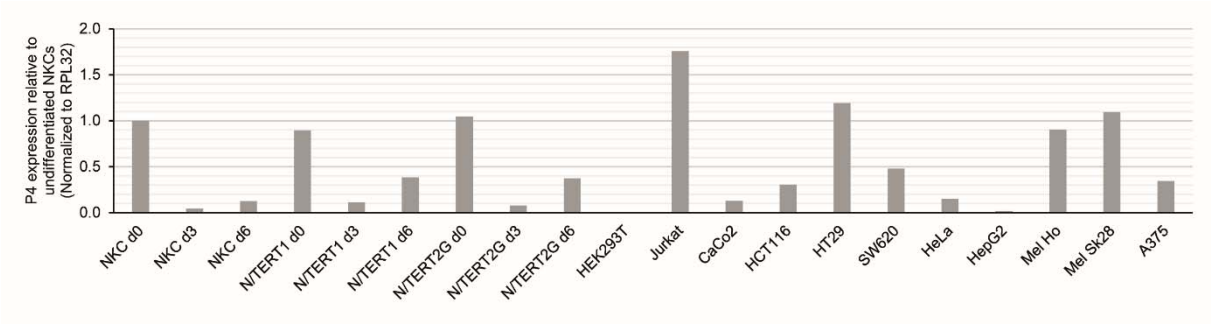

Figure 4: Expression of *P4* transcripts in different cell types. In primary as well as immortalized N/TERT keratinocytes *P4* levels are highest before initiation of differentiation (d0; day 0 time point). Noteworthy *P4* RNA levels could also be detected in Jurkat lymphocyte cells; HCT116, HT29 and SW620 colon cancer cells; as well as in Mel Ho, Mel Sk28 and A375 melanoma cell lines. No expression of *P4* can be seen in human embryonic kidney 293T cells or hepatocellular carcinoma cell line HepG2. The employed RT-qPCR analysis targeted *P4* transcripts containing the region indicated in Figure 3A.

4.1.1.2 Nanopore sequencing data indicate two dominant transcript variants

In order to get more information about additional isoforms of the *P4* transcript in keratinocytes, Daniela Strauß and Dr. Sonja Hombach performed nanopore sequencing on poly(A)-enriched RNA purified from NKCs. During nanopore sequencing, changes in electric current are detected as nucleic acids pass through specific protein nanopores and the electric signal can be read out in order to gather information about whole transcript isoforms as they are endogenously present in the cell[177]. Eight of the resulting reads could be assigned to *P4* by Johannes Graf and were subsequently aligned to the T2T reference genome. In addition to the full-length transcript, these alignments indicated the existence of at least one more polyadenylated isoform in keratinocytes (Figure 5A).

4.1.1.3 Exon-specific RT-qPCR investigations point towards presence of additional isoforms

In order to validate the previous results from nanopore sequencing, RT-qPCR analyses with primer pairs targeting each exon individually were performed Therefore, cDNAs were generated from undifferentiated keratinocyte as well as from early differentiated organotypic tissue RNAs and then measured with each primer set. The obtained values were subsequently normalized using dilutions of *in vitro*-transcribed full-length *P4*, enabling comparison of exon abundancy for all transcripts containing the full exons. These data suggested additional isoforms in non-differentiated keratinocytes, some of which seeming to contain exons 3 and 5 but not exons 1 and 4. In the organotypic tissue, exon distribution appeared more uniform,

hinting towards the full-length transcript being the most prevalent isoform at this stage of differentiation (Figure 5B).

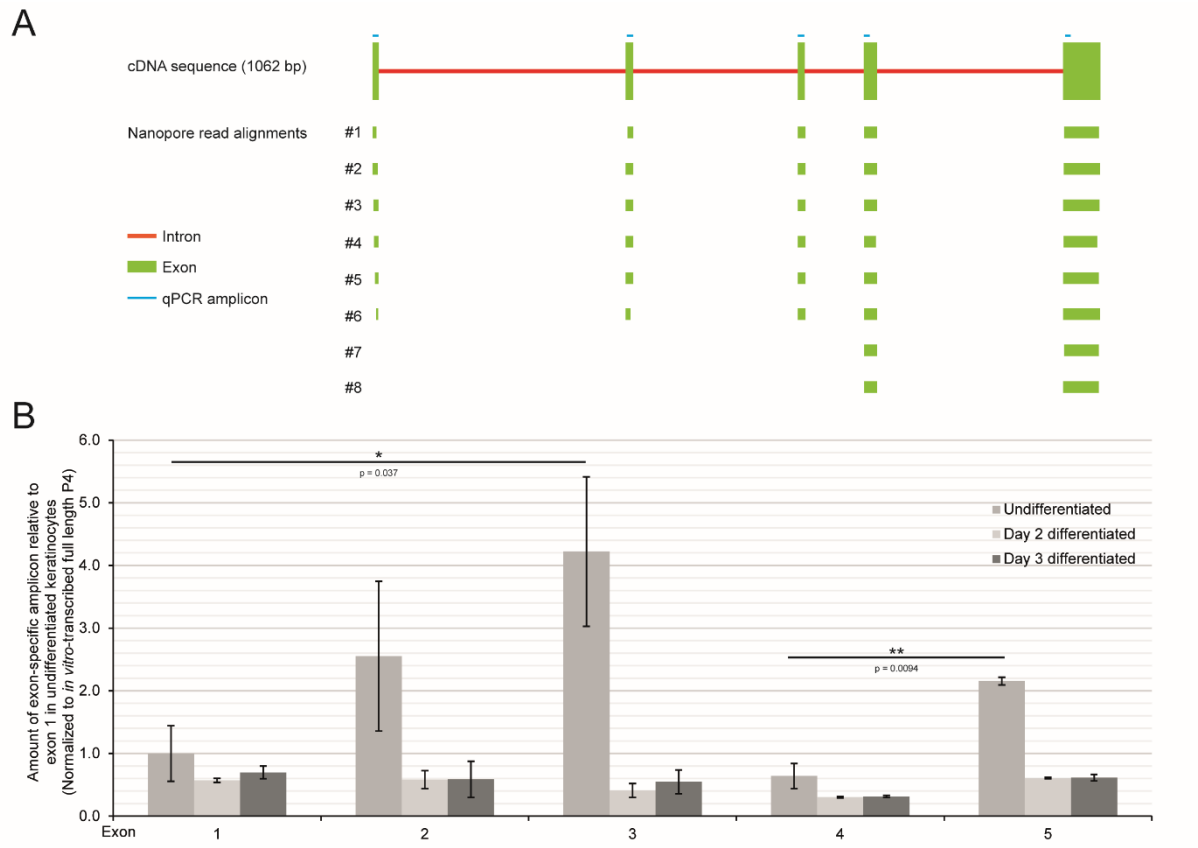

Figure 5: Isoforms of *P4* in primary neonatal keratinocytes. (A) *P4* Nanopore sequencing reads aligned to the T2T reference genome. A total of eight reads could be identified for *P4*, six of which covering the entire full-length transcript. The remaining two reads contain only the last two exons. Nanopore sequencing was performed on poly(A)-enriched RNA. **(B)** RT-qPCR analysis of undifferentiated and differentiated keratinocytes using exon-specific *P4* primers depicted in (A). In comparison to Nanopore sequencing, exon-specific quantification of *P4* in undifferentiated keratinocytes indicates the presence of additional isoforms not containing exons 1 and 4 but other parts of the full-length *P4* transcript, in particular exons 3 and 5. Differentiated organotypic tissue shows a more equal distribution of exons among analyzed *P4* transcripts (N = 3).

4.1.2 Protein-coding potential of the *P4* transcript

4.1.2.1 In silico *and mass spectrometric analyses predict low protein-coding potential*

While the *P4* transcript was initially discovered in a screening for regulatory lncRNAs in epidermal homeostasis, it was unclear whether the functional *P4* gene product is in fact an RNA or if a potentially protein-coding sequence on the last two exons is translated into a 139 amino acids (aa) long protein (Figure 3A). Hence, the protein-coding potential of the full-length transcript was analyzed using multiple publicly available, sequence-based *in silico* tools, most of which predicting *P4* to be a non-coding RNA (Table 1)[178–184].

Table 1: Software-based *P4* coding potential predictions

Prediction software	Score	Interpretation
Coding-Potential Assessment Tool (CPAT)[178]	0.1379	Non-coding
iSeeRNA[179]	0.6459	Non-coding
Coding-Potential Calculator 2 (CPC2)[180]	0.9109	Coding
Coding-Non-coding Identifying Tool (CNIT)[181]	-0.3417	Non-coding
ORF Length and GC content (LGC)[182]	-0.287	Non-coding
RNAsamba[183]	0.8265	Coding
RNAmining[184]	0.9999	Non-coding

In addition to this, multiple sequence alignment was performed for the potential P4 proteins of twelve mammalian species using MAFFT[185]. Due to two nucleotide sequences not containing the corresponding start codon, only ten protein sequences were ultimately aligned. While inside of the *Hominidae* clade the putative protein appeared to be rather conserved, the remaining species exhibited early interruptions of the peptide, mostly after eight amino acids (Figure 6A). Alignments of the predicted peptide against known proteins using the blastp algorithm showed no significant matches; furthermore, searching for conserved domains within the amino acid sequence yielded no results[186,187]. Moreover, crude lysate from wildtype NKCs was subjected to mass spectrometric analysis carried out by the group of Dr. Astrid Bruckmann (Department of Biochemistry I, University of Regensburg) in order to detect the putative protein. However, in spite the potential protein sequence containing several possible tryptic peptides of optimal length, none of these could be identified in the mass spectrometry data.

4.1.2.2 Polysome fractionation experiments point towards association of P4 with ribosomes

After these first analyses had pointed towards low protein-coding potential of the *P4* full-length transcript, polysomal fractionation experiments were performed together with Daniela Strauß and with support of Dr. Sébastien Ferreira-Cerca's group (Department of Biochemistry III, University of Regensburg) in order to get insight about a possible association of *P4* with ribosomes. Therefore, the translation of cultured primary NKCs was stalled by addition of cycloheximide to the cell medium. Cycloheximide inhibits eEF2-mediated translocation at the ribosome and therefore blocks translational elongation in eukaryotes[188]. Cytoplasmic lysates of these pretreated cells were separated using density gradient centrifugation. Spike-in of *in vitro*-transcribed *GFP* RNA into the collected fractions previous to RNA purification enabled normalization in subsequent RT-qPCR analyses of different transcripts. Furthermore, control runoff experiments without translational inhibition of cells were carried out.

As shown in the RT-qPCR data, major parts of targeted *P4* transcripts were detected in the tetrasome-containing fraction but also in other polysome fractions (Figure 6B). In comparison with known non-coding and coding RNAs, the fractionation pattern of *P4* resembled that of the *GADD45A* transcript, an mRNA with high expression levels in our keratinocyte RNA sequencing data which contains a slightly longer ORF than *P4* and is translated into a protein related to DNA repair[189]. The mostly nuclear lncRNA *NEAT1*[190] on the other hand was mostly detected in fractions containing 60S subunits and monosomes (Figure 6B). Moreover, upon runoff more *P4* transcripts were found in fractions of lower density, proving at least parts of the initially observed fractionation pattern to be caused by association with ribosomes (Figure S1).

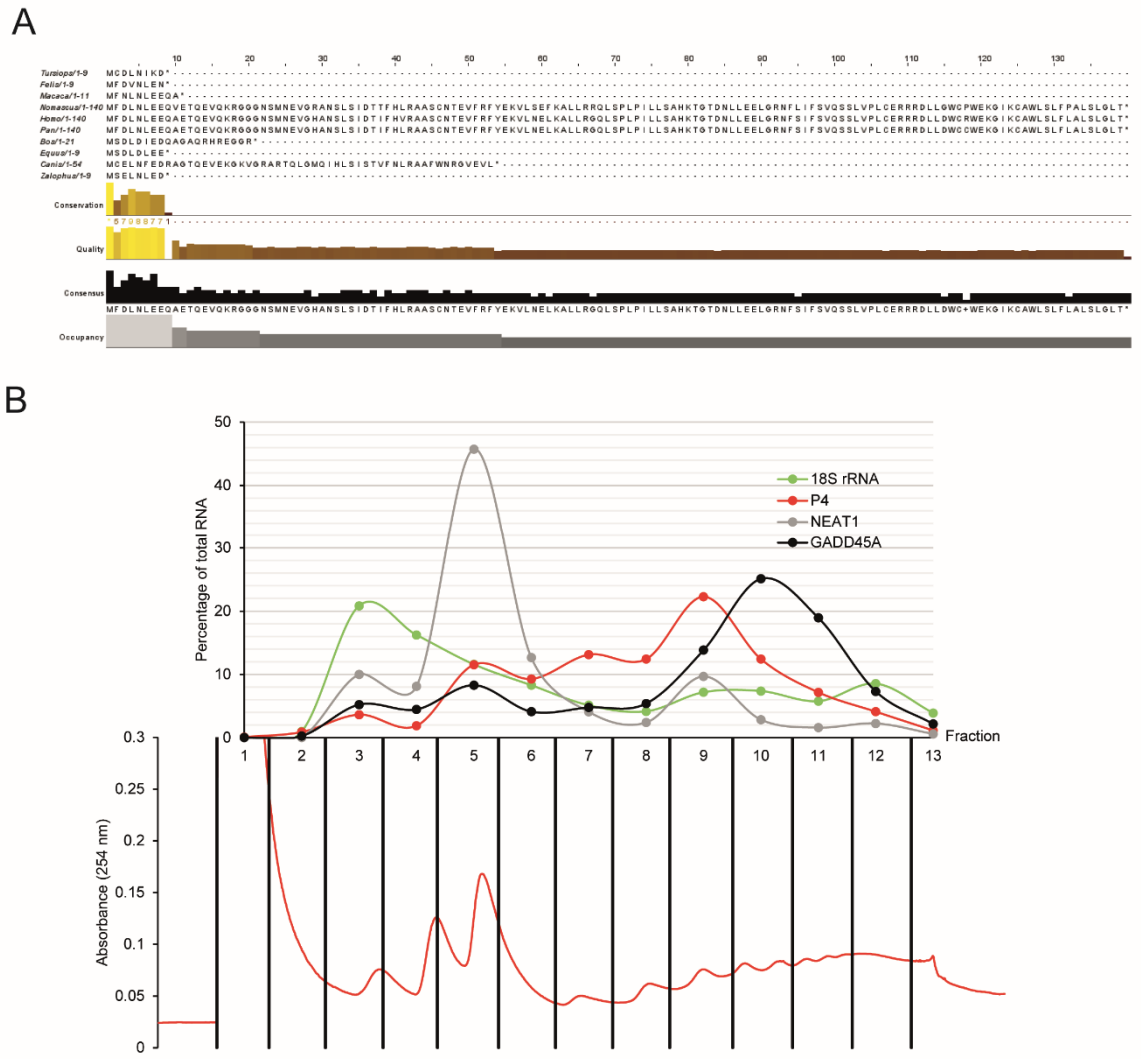

Figure 6: Analysis of *P4* protein-coding potential. (A) Multiple sequence alignment of ten putative mammalian P4 protein sequences[185]. While *Homo*, *Pan* and *Nomascus* exhibit 139 aa long protein sequences with only few substitutions in between, for the remaining nine species either no corresponding start codon is found, or an early stop codon leads to shorter peptides. **(B)** Polysome fractionation of cycloheximide-treated primary NKCS. Cytoplasmic *P4* transcripts containing the amplicon region depicted in Figure 3A show enrichment in fractions containing one or more ribosomes. The overall fractionation pattern is similar to the *GADD45A* mRNA which codes for a 165 aa long protein. The lncRNA *NEAT1* is mostly found in fractions containing monosomes or the large ribosomal subunit. Shown here is one of two fractionation analyses with similar outcome.

4.1.3 Features of *P4* RNA structure

4.1.3.1 Computational algorithms agree on few probable secondary structure elements

Although the sequence of full-length *P4* had been studied quite well up to this point, little was known about its secondary structural features, which may be functionally important in terms of interaction with RNA-binding proteins[90]. Hence, a sequence-dependent structure was predicted using the SSRTool which runs and compares several publicly available algorithms[191]. Thus, a meta-stable structure containing the most prevalent secondary structure elements was created. While in the first three exons this consensus structure contained sporadic features such as short double strands and hairpins, exons 4 and 5 exhibited multiple areas of higher structural complexity with long helices, multiple internal loops, bulges, hairpins and some multi-branched loops (Figure 7). In addition, no sequence-based indications for formation of G-quadruplexes could be identified[192].

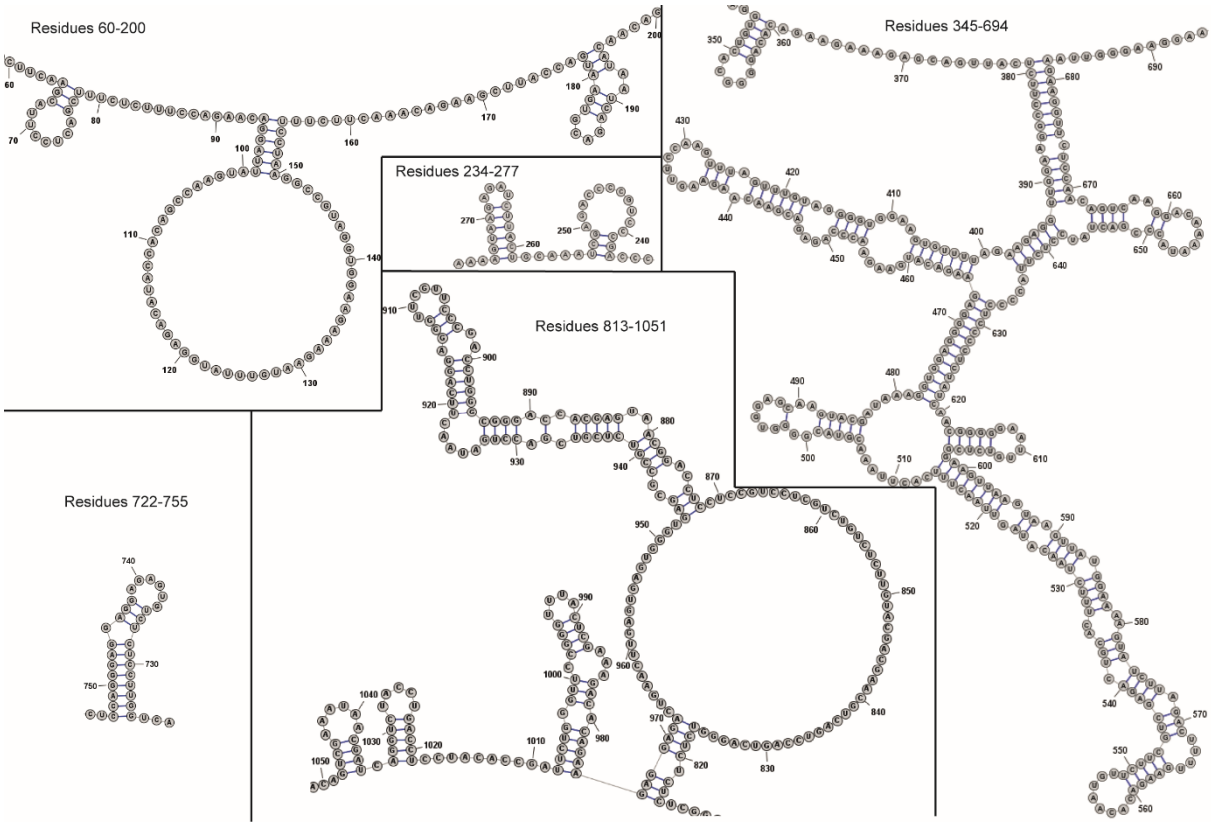

Figure 7: *In silico P4* consensus secondary structure[191]. The most prevalent *P4* folding patterns across multiple algorithms are displayed. While for the first three exons only occasional simple helix-loop motifs can be agreed on (top left, top mid), several secondary structure elements of higher complexity including several multi-branched loops and extended helices with multiple internal loops are collectively predicted in exons 4 and 5 (right, bottom left and bottom mid).

4.1.3.2 SHAPE experiments point towards modular secondary structural architecture

In order to provide experimental evidence for already predicted features and to obtain structural information for the remaining regions of *P4*, Selective 2′ Hydroxyl Acylation analyzed by Primer Extension (SHAPE) experiments on the *in vitro*-transcribed full-length isoform was performed together with Daniela Strauß and Johanna Gizler with assistance from the group of Dr. Sébastien Ferreira-Cerca (Department of Biochemistry III, University of Regensburg). SHAPE analysis utilizes the inability of some reverse transcriptases to continue their catalytic process once they encounter nucleotides that are specifically modified at their 2' hydroxyl group; and when RNA is treated with corresponding chemicals, it is mostly unpaired bases exhibiting higher flexibility that are reactive for such modifications[193]. Reverse transcription of the chemically changed transcript then results in cDNA fragments of different length which can subsequently be read out and normalized to unmodified controls in order to get base pairing information. In this approach, N-methylisatoic anhydride (NMIA) was used as a modifying reagent and reverse transcription was performed using six fluorescent primers distributed throughout the full-length *P4* transcript, enabling detection and, in combination with respective sequencing ladders, determination of nucleotide accessibility on a base resolution scale.

Modification of *P4* with the chosen reagent proved to be successful compared to the control, whereas the sequencing gels themselves were either too short to reach sufficient resolution or showed complications during gel electrophoresis resulting in uneven running behavior (Figure S2). Nonetheless, a rough SHAPE reactivity pattern for the whole *P4* transcript was determined and implemented into secondary structure prediction using the RNAstructure software[194].

Strikingly, this resulted in a structure composed of two large, independently folded modules in which almost two thirds of nucleotides demonstrated base pairing probabilities higher than 80% (Figure 8), in contrast to other tested *in silico* algorithms without the context of experimental data that had calculated different architectures with generally lower Gibbs free energies, but also low hybridization likelihoods. Furthermore, formation of H pseudoknots at the ends of exons 3 and 5 was predicted to be possible, though with a rather low likelihood. Looking at the structure in more detail, both the 5' domain, comprising exons 1 to 3 and a major part of exon 4, and the 3' domain appear to be connected by two helical segments which are only interrupted between the third and the last nucleotide of *P4*, leading to the first and the final bases of the RNA being in close proximity to each other. Furthermore, while the 5' module of the prediction can be further subdivided into two major structural components, the 3' region contains a wide variety of multibranch loops, resulting in high complexity for this part of the transcript.

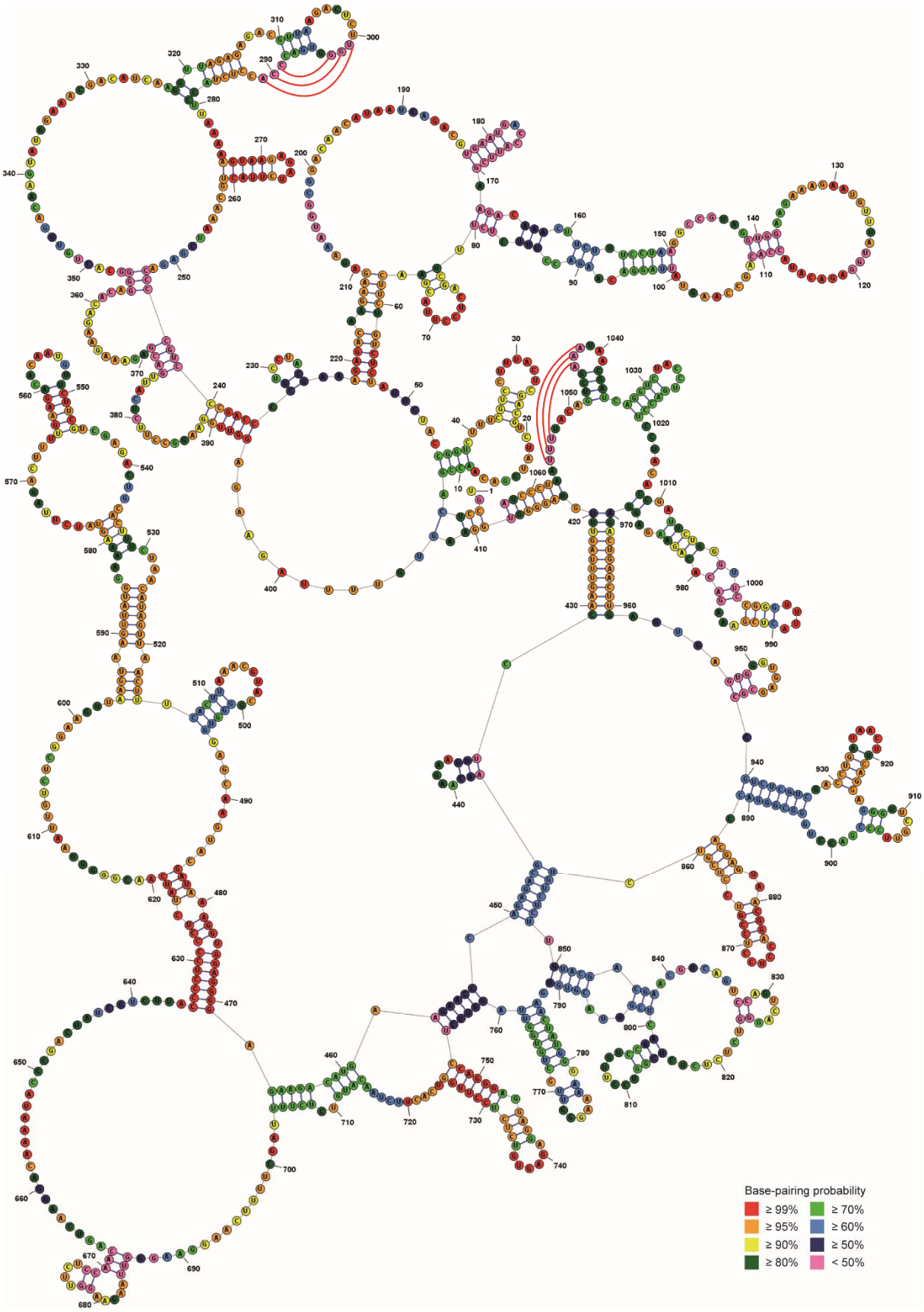

Figure 8: SHAPE reactivity-based secondary structure prediction for full-length *P4*[194]. The proposed structure contains 57 helical segments, 22 terminal loops, 26 internal loops and 11 multi-way junctions. Two potential H pseudoknot structure elements are depicted by red lines. 670 of 1063 nucleotides are predicted with probabilities higher or equal to 80%. The calculated Gibbs free energy of the structure is -240.9 kcal/mol.

4.1.3.3 Conserved structure-involved nucleotides encourage tertiary structure prediction

As a quality determinant of aforementioned structure prediction, a multiple sequence alignment of the estimated *P4* gene loci was carried out for twelve mammalian species using MAFFT[185]. For each individual nucleotide of the full-length *P4* transcript, the percentage of identity was calculated. When assigned to their predicted secondary structure status, bases that paired with a probability higher than or equal to 90% showed significantly higher conservation than those that were reliably computed to remain unpaired, while the combined remaining bases with lower likelihood scores demonstrated intermediate identity values (Figure 9A).

Taking the putative secondary structure of full-length *P4* into account, as a next step tertiary structure prediction was performed using the 3dRNA tool[195]. The best-scoring structures resembled each other with the most prominent features being visible separation into the less condensed 5' domain and a tightly packed 3' domain, in addition to the presence of three isolated, surface-oriented helix-loop motives in exons 2, end of exon 3 and beginning of exon 4, as well as early on in exon 5 (Figure 9B). However, inclusion of the predicted pseudoknots in the computation led to major differences in the accessibility of some motifs (Figure S3).

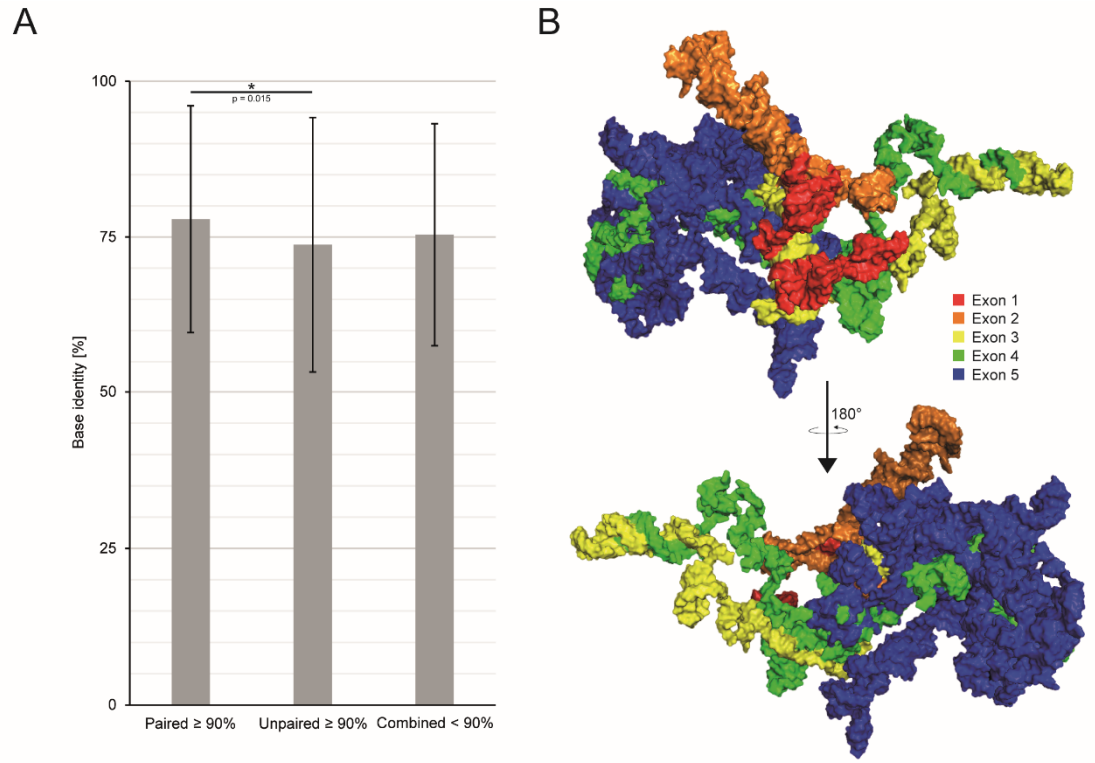

Figure 9: *P4* secondary structure conservation and tertiary structure prediction. (A) Identity of putatively paired and unpaired *P4* nucleotides in twelve mammalian species[185]. Bases predicted to pair with a high probability are significantly more conserved than analogical unpaired bases. **(B)** Tertiary structure prediction for full-length *P4*[195]. Taking the assumed secondary structure into account, the division into two domains becomes also apparent in a three-dimensional model. Three helix-loop motifs composed of residues 80-168, 281-322 and 515-596 are directed outwards to the periphery. Shown here is the best scoring out of five predicted structures.

4.2 Discussion and Outlook

The shared *P4* expression patterns between primary neonatal keratinocytes and immortalized keratinocyte cell lines during calcium treatment (Figure 4) indicate that differentiation-related downregulation of this lncRNA is a stable hallmark observable even in genetically altered keratinocytes. Furthermore, *P4* transcript levels in other tested cell lines roughly reflect publicly available data, as Jurkat leukemic lymphocytes, similarly to lymphatic tissues, show high *P4* expression[161–163]. Likewise, elevated *P4* levels in the HCT116, HT29 and SW620 colorectal cancer cell lines are coherent with the modest expression of the lncRNA observed in human colon tissue[162]. In relation to a reported association of *P4* with high-risk melanoma, increased transcript levels are found in the corresponding Mel Ho, Mel Sk28 and A375 cell lines[173]. Contrary to this, no *P4* was detected in HEK293T and HepG2 cells, consistent with low levels in kidney and liver tissues[161–163]. However, it has to be kept in mind that the expression patterns of cancer cell lines usually deviate far from their healthy tissue counterparts, and discrepancies may also be found for other immortalized cell lines[196,197]. Nonetheless, knowledge about *P4* abundancies in various cell lines may prove useful for future mechanistical studies.

While the *P4* reads resulting from nanopore sequencing give valuable information about isoforms that are most prevalent in keratinocytes, only eight reads could ultimately be assigned to *P4*. Two of these indicate the occurrence of another isoform consisting of the last two exons of the full-length sequence that is in turn represented by six reads (Figure 5A). Hence, it may be possible that additional existing isoforms were not detected due to the generally low *P4* abundancy in keratinocytes. Moreover, it is possible that some reads were not assignable to *P4* due to inclusion of unexpected genomic sequences as a result of alternative splicing.

Furthermore, the presence of other *P4* isoforms is implied by exon-specific RT-qPCR analyses that reveal rather high levels of transcripts containing exons 2 and 3 but not exon 4 in undifferentiated NKCs (Figure 5B). The emerging inconsistency in regard to the abundancies reflected by nanopore data could be explained by the fact that, prior to the sequencing, enrichment for polyadenylated RNA had been carried out. Therefore, it may well be that non-polyadenylated *P4* isoforms that had not been targeted by primers in initial RT-qPCR polyadenylation analyses had been excluded from subsequent experiments. Considering this possibility, an additional nanopore sequencing analysis with rRNA depletion instead of poly(A)+ transcript enrichment may deliver more conclusive results. Aside from that, the performed RT-qPCR approach only covered one particular region per exon that may not necessarily be included in *P4* transcripts, for instance in the case of alternative splicing. Hence,

it would be valuable to extend this analysis by RT-qPCR measurements with other exon- and intron-targeting primer pairs or by northern blots with corresponding probes. Shifted exon abundancies in differentiated keratinocyte on the other hand may be a hint towards isoform-specific expression level changes in the course of epidermal stratification but also require further investigations.

Full-length *P4* contains three small ORFs shorter than 200 nt and one longer potentially protein-coding sequence of 420 nt length. Sequence-based *in silico* tools predicted overall low coding potential for the entire full-length transcript. For the subsequent analyses that were focused on putative protein sequences, only the peptide originating from the longest ORF was considered due to the assumption that larger proteins may be more probable to act in a functional manner. However, it has also be reported that small micropeptides can carry out important functions as well, such as the 34 aa long DWORF which enhances SERCA calcium pump activity by displacing its inhibitors[198]. Nevertheless, for the longest potential *P4*-originating peptide of 139 aa, no conservation apart from the first few amino acids could be seen outside of the *Hominidae* clade in spite of reported nucleotide sequence conservation throughout eutherian species, indicating that a functional P4 peptide from this ORF could have only emerged in recent evolutionary history (Figure 6A)[158]. Mass spectrometric analysis on keratinocyte lysate was unable to detect possible fragments of the putative P4 protein, pointing towards the absence of a stable peptide. Again, the low abundancy of the *P4* transcript in keratinocytes has to be mentioned which may also result in protein amounts too small to be reliably measured by mass spectrometry. In addition, it would be interesting to analyze conservation and potential peptide presence for the other ORFs within *P4* transcripts, especially for the one on exon 2 that had already been shown to be ribosome-associated in publicly available data[160].

In contrast to these preliminary results, density-based fractionation of lysates derived from translationally stalled keratinocytes in combination with runoff experiments pointed towards an association of cytosolic *P4* transcripts with polysomes (Figure 6B and Figure S1). Importantly, the employed analysis focused on cytoplasmic transcripts and therefore the majority of nuclear transcripts was ignored. However, in our laboratory full-length *P4* had been majorly detected in nuclear fractions (Figure 3C), indicating that main functions of the transcript may still be independent of mature ribosomes. As previously mentioned, association of cytoplasmic lncRNAs with polysomes is rather common and may be, apart from potential translation of functional proteins, involved in transcript turnover via nonsense-mediated decay[89]. The observed fractionation patterns for both *P4* and *NEAT1* with substantial occurrence in ribosomal

fractions (Figure 6B) could hence have similar reasons, since *NEAT1* also contains multiple short ORFs. Prevalently cytoplasmic lncRNAs that are known not to be associated with ribosomes at all might therefore pose a helpful additional control, as clearer distinctions to ribosome-associated transcripts could be made. Furthermore, additional fractionation experiments on total lysates also containing nuclear transcripts would perhaps clarify how prevalent the association of full-length *P4* with ribosomes actually is in the whole cellular context. All in all, persisting uncertainties regarding a putative functional P4 protein may be solved by rescue experiments which investigate phenotype restoration in *P4*-depleted keratinocytes upon ectopic expression of start codon mutants or standalone ORFs. In spite of its association with ribosomes, our aggregated results prompted us to assume a majorly non-coding function of the *P4* RNA.

Pure *in silico* approaches to predict the secondary structure of the *P4* lncRNA resulted in a wide plethora of differently folded arrangements, and only few secondary structure elements could be agreed on across multiple algorithms (Figure 7). This may be caused by difficulties of these prediction tools to operate with long input sequences; moreover, most algorithms are based on finding structures with minimum free energy, which are probable to differ from those that actually occur in complex *in vivo* environments[199]. This is why experimental approaches are needed in order to determine the often functionally relevant secondary structure of lncRNAs[90].

Hence, SHAPE was employed as a means to gather information about accessible nucleotides within the *P4* transcript. However, the overall low levels of *P4* in keratinocytes impeded *in vivo* SHAPE analyses, which is why full-length *P4* was *in vitro*-transcribed and used for the subsequent reactions. Therefore, structures identified by this approach may not necessarily reflect the actual RNA folding in actual biological surroundings. Although it was the method of choice when the method was firstly established, gel-based analysis of synthesized fluorescently marked cDNAs may bring some difficulties[200]. This is especially true when gel electrophoresis does not happen flawlessly as it was the case for us (Figure S2), thus preventing automatized evaluation of the gel images and necessitating a rather inaccurate manual interpretation approach with limited consideration of the unmodified controls for the determination of accessibility values. Due to this reason, high throughput sequencing which became the method of choice for downstream analysis of synthesized cDNAs may be more suitable for this purpose[201]. Considering this, the resulting secondary structure for *P4* should be treated with caution and may be a product of imprecise evaluation. Nonetheless, the predicted intramolecular arrangement fits together quite well with what is known about published

lncRNA structures since similar ratios of secondary structure elements as well as a modular architecture can be observed (Figure 8)[90]. If compared to the pure *in silico* prediction (Figure 7), only some of the consensus features are found in the exact same fashion in the SHAPE-based structure while few exhibit slightly changed base pairings and several are not found at all, emphasizing the necessity of experimental evidence for accurate determination of long transcript secondary structures. Moreover, the prediction is coherent with what was known so far about the *P4* transcript as the individually folded 3' domain contains major parts of exon 4 and the entire last exon, which suggests a similar structure for the short isoform identified by nanopore sequencing. Interestingly, the ORF that was previously analyzed regarding its coding potential is fully located within the 3' domain of the predicted folding. All in all, this coherence with other known transcript features supports validity of the SHAPE-based *P4* structure prediction.

As another layer of quality control, the detected higher conservation of paired in comparison to unpaired nucleotides (Figure 9A) may be indicative of a meaningful secondary structure prediction, though sequence conservation does not necessarily infer structural or even functional homologies[202]. Nevertheless, this observation was taken as a rationale to initiate computational tertiary structure prediction for the *P4* lncRNA. However, the resulting three-dimensional elements are purely hypothetical which becomes even more apparent when contemplating the substantial differences in the calculated tertiary structures that are caused only by minor changes such as consideration of predicted pseudoknots (Figure 9B and Figure S3). Hence, experimental means are required in order to obtain conclusive tertiary structures, including approaches based on solvent accessibility and RNA duplex formation, or high-resolution methods such as cryogenic electron microscopy[203–205].

5. Phenotypical changes caused by *P4* level modulation

While *P4* had initially been considered for continued examination due to its expression changes during keratinocyte differentiation, in the case of stronger involvement of the transcript with epidermal homeostasis regulation additional phenotypes were to be expected. This is why further analyses had been carried out in order to identify differentiation-related changes associated with *P4* level alterations.

Therefore, organotypic epidermal tissue had been created by Bianca Förstl and Dr. Sonja Hombach, using *P4*-depleted keratinocytes. In order to do this, NKC RNA levels were modulated by electroporation with pools of siRNAs before seeding them onto devitalized human dermis acting as a matrix. High cell density and addition of a specialized differentiation medium containing high calcium levels and differentiation-promoting constituents such as epidermal growth factor then induced stratification into *in vivo*-like epidermal tissue at the air-liquid interface. At time points of early differentiation, both RNA and protein levels of typical differentiation markers had been investigated. Interestingly, diminishing *P4* levels to a quarter of those observed in control tissue had led to upregulation of early as well as late differentiation marker transcripts (unpublished data, Figure 10A). Moreover, *P4*-deficient tissue had been characterized by earlier onset in stratification as well as generally higher levels of differentiation marker proteins (unpublished data, Figure 10B).

In addition to that, Bianca Förstl and Dr. Sonja Hombach had performed RNA deep sequencing on early differentiated organotypic tissue with or without *P4* knockdown. The data had then been aligned to the human genome and analyzed by Dr. Uwe Schwartz from the group of Prof. Dr. Gernot Längst (Department of Biochemistry III, University of Regensburg). Strikingly, the *P4*-depleted samples had presented severe transcriptome-wide changes with 1434 genes being differentially regulated to a significant extent with $|\log_2(\text{fold change})| > 1$, many of which associated with processes of epidermal homeostasis (unpublished data, Figure 10C). Gene ontology analyses had also shown highly significant upregulation of keratinocyte differentiation-related genes; upregulated genes were additionally associated with processes going hand in hand with epidermal homeostasis such as intermediate filament organization, fat metabolism or cation channeling, while downregulated genes were mostly related to cell adhesion and migration (unpublished data, Figure 10D).

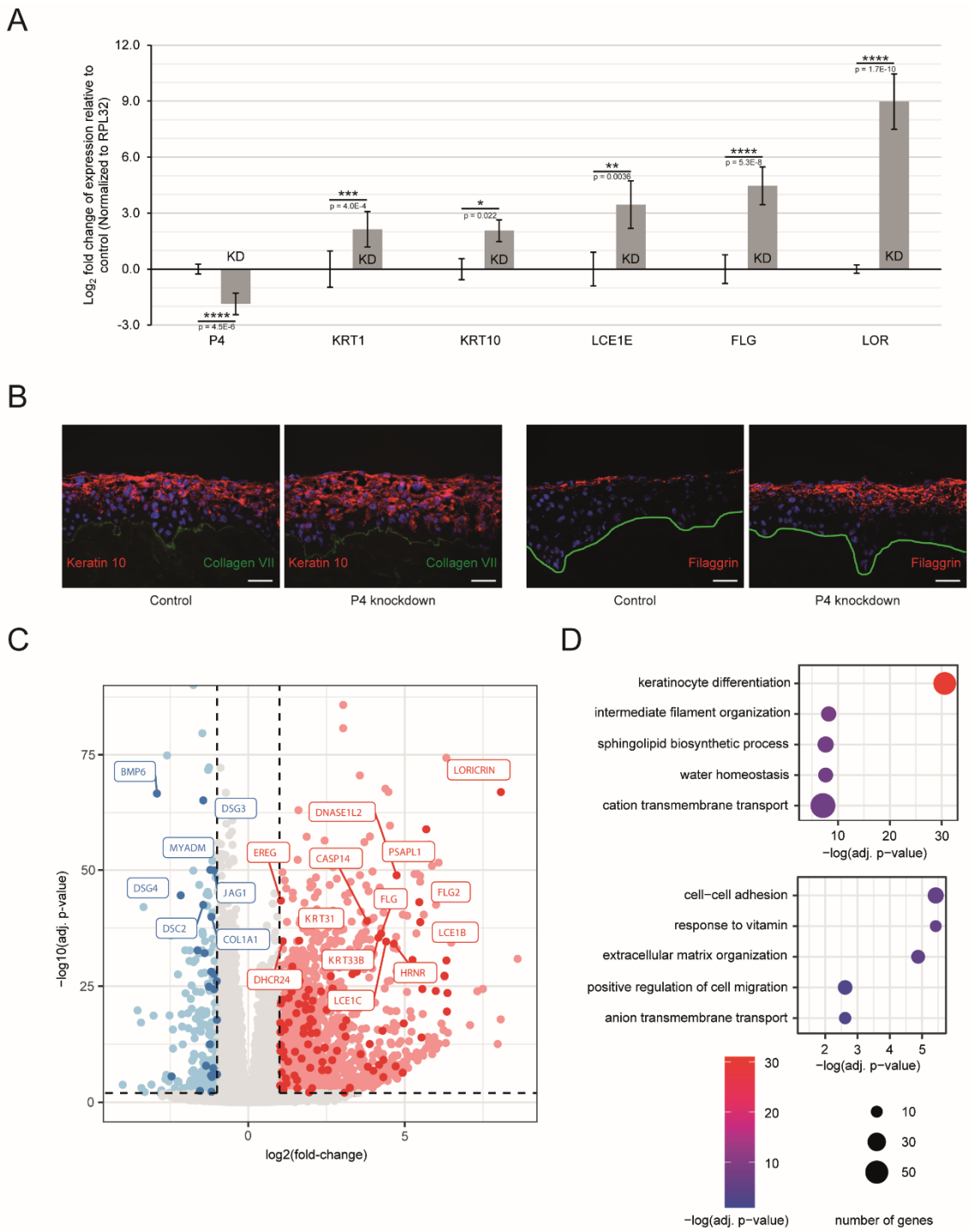

Figure 10: Differentiation-related changes in *P4*-depleted, early differentiated epidermal organotypic tissue. **(A)** RT-qPCR analysis on selected differentiation marker transcripts. Knockdown of *P4* results in upregulated expression of early differentiation marker genes such as keratins 1 and 10 and in particular of later differentiation markers such as late cornified envelope 1E, filaggrin and loricrin (N = 3-9). **(B)** Immunofluorescent stains of keratin 10 and filaggrin in tissue with or without *P4* knockdown. In *P4*-deficient tissue, earlier onset and higher levels of these differentiation-associated proteins are observed. Nuclei are stained blue (Hoechst 33342), green lines represent basement membrane, scale bars are 50 µm. **(C)** Volcano plot of globally differentially regulated genes upon *P4* depletion. A large number of genes associated with epidermal differentiation (highlighted in darker tone) are up- or downregulated, the 20 most significant are additionally labeled. Red genes are upregulated, blue genes downregulated, black dashed lines represent thresholds for consideration as significantly up- or downregulated ($-\log_{10}$(adj. p-value) > 2; $|\log_2$(fold change)| > 1). **(D)** Gene ontology analysis of significantly up- (top) or downregulated (bottom) genes. The most significant associated processes of upregulated genes are keratinocyte differentiation followed by related pathways such as cytoskeletal organization and lipid catabolism.

Since epidermal homeostasis is a complex process, presentation of additional phenotypes other than increased differentiation was suspected in *P4*-depleted tissue which is why epidermal morphology and basal cell proliferative activity that is known to be coregulated with keratinocyte differentiation[46,206] were to be investigated. Furthermore, RNA sequencing data suggested changes in the cytoskeleton as well as epidermal lipidomic profile upon *P4* depletion which were meant to be looked into. Aside from that, effects of *P4* overexpression in organotypic tissue were to be analyzed in the course of doctoral studies. Finally, effects of *P4* level modulation on 2D-cultured cell characteristics such as cell growth, tendency towards apoptosis, cell cycle population shifts and migrational capacity were planned to be looked into.

5.1 Results

5.1.1 *P4*-associated phenotypes in organotypic tissue

5.1.1.1 P4 overexpression does not alter differentiation marker expression patterns

Due to the first phenotypical analyses exhibiting strong changes in differentiation marker levels between *P4*-depleted and control tissues, contrary effects were assumed when comparing *P4*-overexpressing tissue with control samples. Hence, primary keratinocytes were virally transduced in order to continuously overexpress either the full-length *P4* transcript or a *LacZ* control and were subsequently seeded onto devitalized dermis for generation of organotypic epidermal tissue.

However, while overexpression itself was successful, leading to a 100- to 1000-fold increase in comparison to endogenous *P4* transcript levels, no significant differences could be observed regarding the tested differentiation marker RNAs at time points of both early (day 3) and late differentiation (day 5, Figure 11A). When immunostaining the corresponding late differentiated organotypic tissue for insight into keratin 10 and filaggrin protein levels, in a similar fashion no change regarding onset or amount of protein presence could be seen, though morphology-wise the *P4*-overexpressing tissue appeared to show decreased overall epidermal thickness in comparison to the controls (Figure 11B).

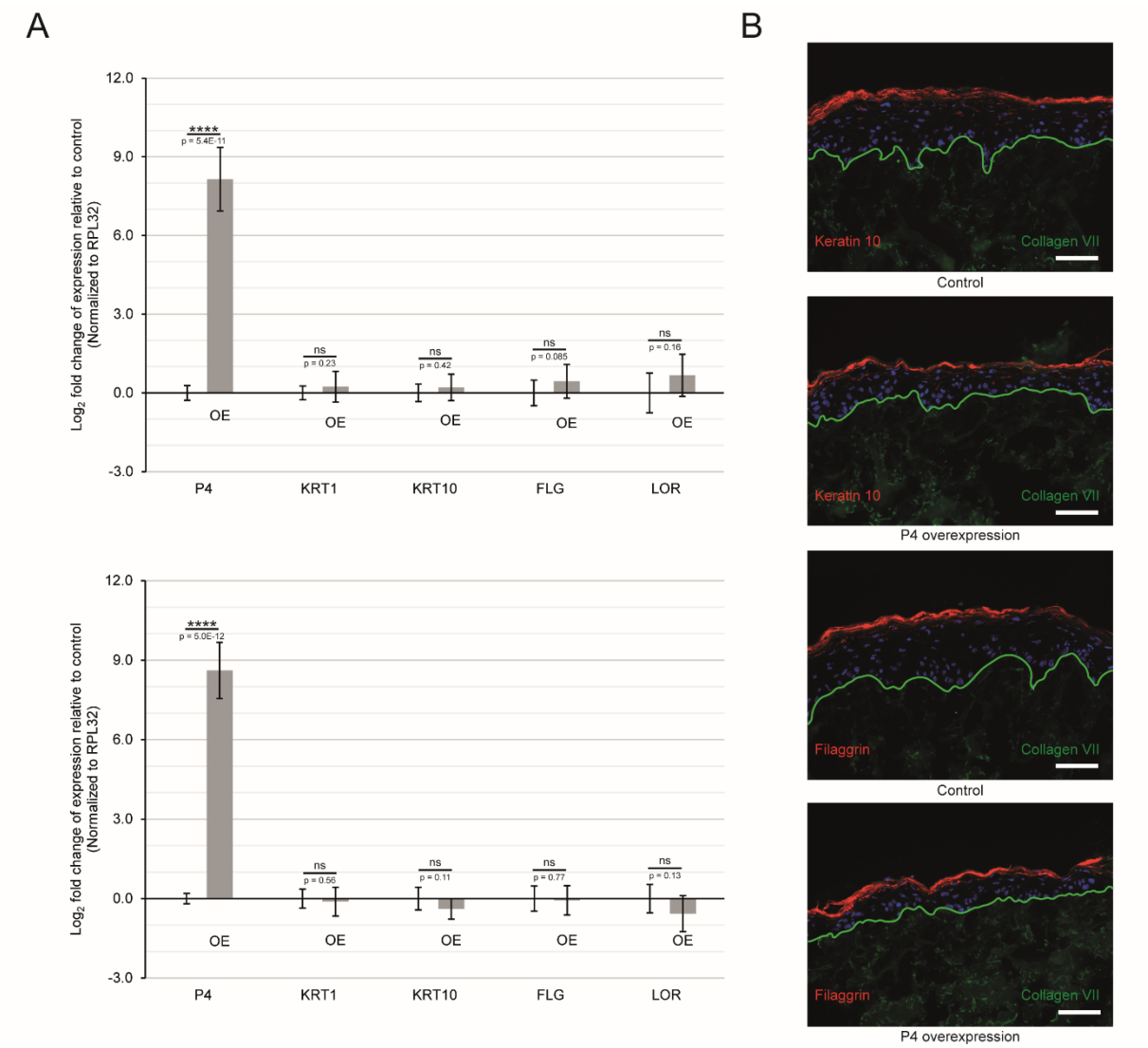

Figure 11: Effects of *P4* overexpression in organotypic tissue. (A) RT-qPCR analyses on selected differentiation marker transcripts at early (day 3, top) and late (day 5, bottom) differentiation time points. While overexpression is proven to be successful, no significant changes in differentiation marker expression are observed (N = 7-13). **(B)** Exemplary immunofluorescent stains of keratin 10 and filaggrin in late differentiated tissue (day 5) with or without *P4* overexpression. While protein levels are not visibly altered between both conditions, *P4*-overexpressing tissue appears to be thinner than the control counterparts. Nuclei are stained blue (Hoechst 33342), green lines represent basement membrane, scale bars are 100 µm.

5.1.1.2 P4 depletion causes severe changes in tissue morphology

In order to identify histological changes that might go along with *P4* deficiency, during her master's thesis in the laboratory Carolin Molthof created organotypic tissue with or without knockdown of *P4* which was subsequently harvested and stained with hematoxylin and eosin. While hematoxylin in complex with metal ions such as aluminum stains nuclei in a blue color, eosin is an anionic dye which preferably stains cytoplasm and the extracellular matrix pink; and due to the varying affinity of certain organelles to bind the dyes and also because of pre-existing

pigmentation, this stain results in broad spectra of tissue coloration, allowing detailed insights into tissue structure[207].

Strikingly, at time points of early differentiation (day 3), the *P4*-depleted tissue exhibited a perturbed epidermal architecture with several uncommon morphological features such as hypergranulosis which means increased occurrence of keratohyalin granules in the *stratum granulosum*, but also generally earlier onset of granulation was observed as well as vacuolar changes, acanthosis and general thickening of the epidermis, whereas none of these could be observed in later differentiated tissues (day 5); instead, the *stratum corneum* appeared to be disorganized at this time point (Figure 12A).

5.1.1.3 P4-deficient tissue exhibits increased proliferation in basal cell layers

The increased size in epidermal thickness upon *P4* depletion that was visible in aforementioned histological stains led to the assumption that this might be caused by dysregulated proliferative activity in tissue with low *P4* levels. Therefore, as part of her master's thesis Carolin Molthof performed bromodeoxyuridine (BrdU) incorporation assays. BrdU acts as a thymidine analog and is in a similar fashion incorporated into newly synthesized DNA; and pulsing of cells with this component followed by immunostaining utilizing BrdU-directed antibodies allows highlighting of cells which are undergoing the process of DNA replication, an indicator of proliferative activity[208].

Intriguingly, *P4*-deficient, early differentiated (day 3) organotypic tissue presented significantly more BrdU-positive keratinocytes in the proliferatively active basal cell layer indicating that, in addition to the previously observed disturbances in differentiation-related processes, proliferation or at least DNA synthesis appears to be enhanced upon *P4* knockdown while still being restricted to the *stratum basale* (Figure 12B).

5.1.1.4 P4 reduction leads to perturbations in microtubule organization

Since many genes that were dysregulated in the RNA sequencing data were shown to be associated with processes such as cytoskeletal organization, adhesion or cell migration (Figure 10D), in an attempt to identify corresponding phenotypes, α-tubulin, which is one of the two main microtubule components, was fluorescently immunostained in early differentiated (day 2) organotypic tissue with or without prior depletion of *P4*.

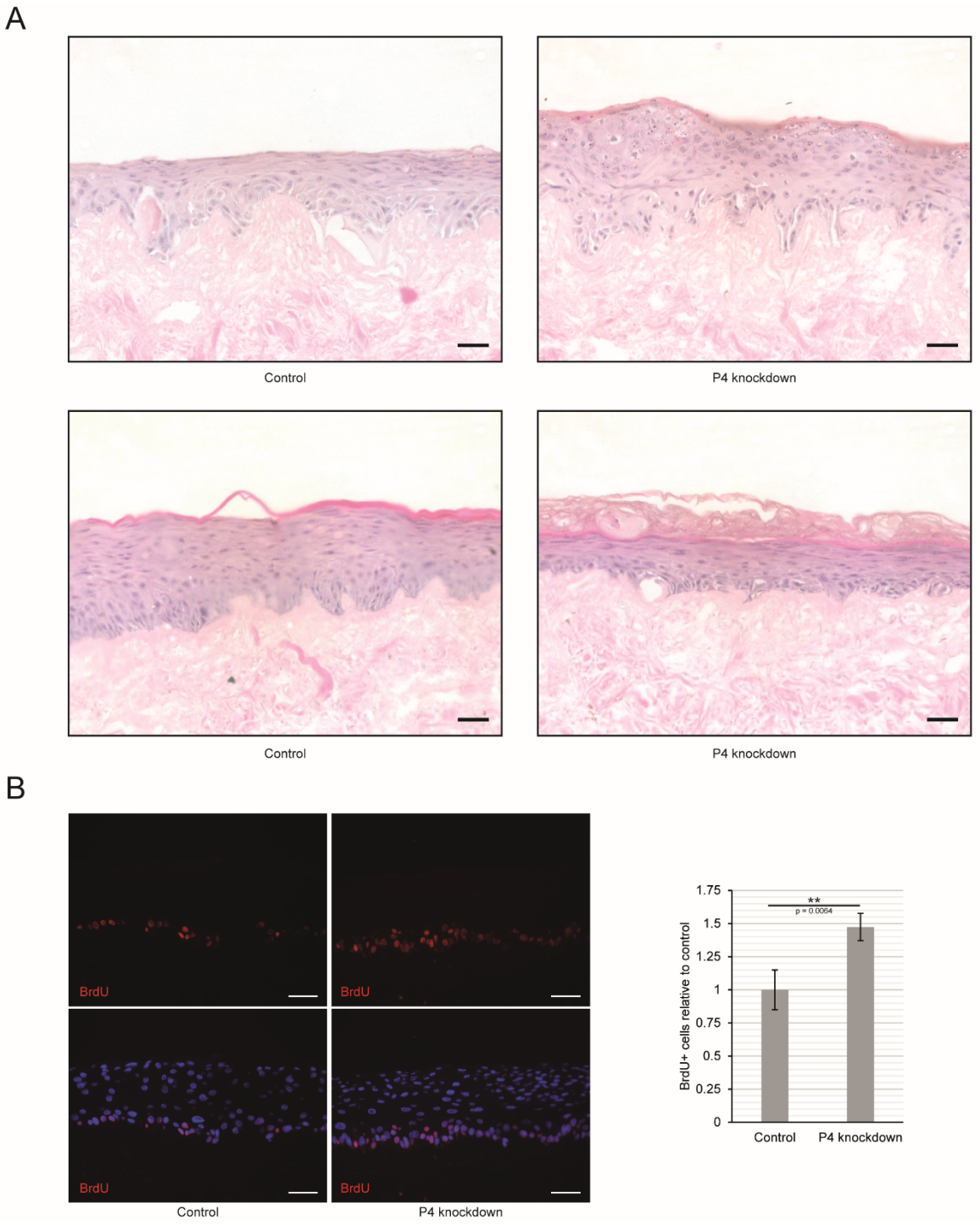

Figure 12: Histological and proliferative changes in organotypic tissue upon *P4* knockdown. (A) Hematoxylin and eosin stains of early (day 3, top) and late (day 5, bottom) differentiated tissue with normal or decreased *P4* levels. During early differentiation, *P4*-depleted tissue exhibits uncommon features such as early onset of the *stratum granulosum* and increased amount of granules, occurrence of perinuclear vacuoles as well as thickening of epidermis. In later time points of differentiation, only the *stratum corneum* is increased in size. **(B)** Representative BrdU immunostainings (left) and comparative analysis (right) of BrdU incorporation assays on *P4*-depleted and control organotypic tissue. Keratinocytes in the *stratum basale* show higher DNA replication activity. No changes are observed regarding the cells in suprabasal layers (N = 16). Nuclei are stained blue (DAPI), scale bars are 50 µm.

While overall α-tubulin levels were not visibly changed between control or *P4*-deficient tissue, distribution of the protein appeared to be altered in that knockdown tissue demonstrated increased condensation of α-tubulin in the cell periphery but also patterns of absence at intercellular contacts, particularly in the bottom layers (Figure 13A).

5.1.1.5 Differences in the epidermal lipidomic profile following P4 depletion

Given the circumstance that many transcripts involved in lipid metabolism had been shown to be upregulated in *P4*-deficient organotypic tissue (Figure 10D), it was investigated whether any accompanying phenotypical changes could be detected. Hence, epidermis-like tissue models were generated under the use of *P4*-depleted or control keratinocytes followed by homogenization of the tissues at a time point of early differentiation (day 3). Mass-spectrometry-based lipidomic analysis on the homogenates was subsequently performed by the group of Prof. Dr. Gerhard Liebisch (Institute of Clinical Chemistry and Laboratory Medicine, University Hospital of Regensburg).

The detected absolute amount of whole lipids within the epidermal organotypic tissues was not substantially altered between both conditions. However, *P4* knockout resulted in a significant shift of lipid composition from phospholipids towards ceramides and triglycerides, whereas the ratio of sterol lipids to the total measured lipidome remained unaffected (Figure 13B).

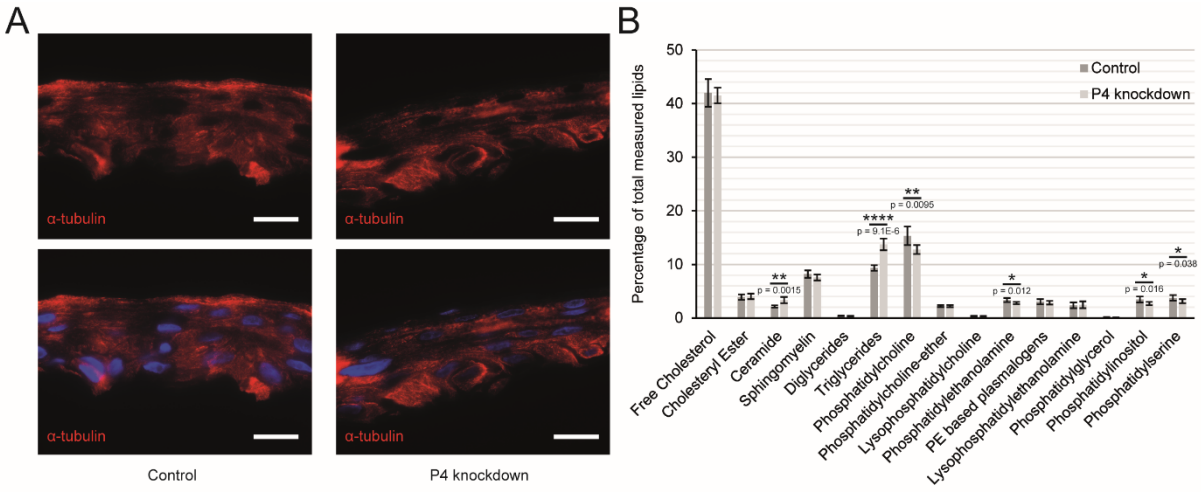

Figure 13: Cytoskeletal and lipidomic changes in *P4*-deficient organotypic epidermal tissue. (A) Exemplary immunofluorescent stains of α-tubulin in early differentiated *P4*-depleted and control tissue. While in tissues with normal *P4* levels a more uniform distribution throughout the cytosol can be observed, the *P4* knockdowns demonstrate higher α-tubulin density in peripheral cell regions but absence close to the cell membrane. Nuclei are stained blue (Hoechst 33342), scale bars are 20 µm. **(B)** Changes in lipid composition for *P4*-deficient epidermis-like tissue. Upon *P4* knockdown, overall detected lipids are less constituted by phospholipids including phosphatidylcholines, phosphatidylethanolamines, phosphatidylglycerols and phosphatidylserines. Instead of this, larger proportions of ceramides and triglycerides are found (N = 7). PE abbreviates phosphatidylethanolamine.

5.1.2 Alterations in 2D-cultured primary keratinocytes

5.1.2.1 Keratinocytes shift towards the S phase upon P4 knockdown

As increased incorporation of BrdU and therefore elevated DNA replication had been shown in basal cells of *P4*-depleted organotypic tissue (Figure 12B), it was investigated together with the group of Prof. Dr. Gero Brockhoff (Department of Gynecology and Obstetrics, University Hospital of Regensburg) whether related effects could be seen in primary keratinocytes cultivated on common plastic cell culture dishes. Hence, cells were modified to either enhance or suppress *P4* expression, and static cell cycle analyses employing DAPI staining with subsequent flow cytometry measurements were performed in comparison to corresponding controls. As cells in G2/M phases contain double the amount of total DNA than those in the G1 phase while cells in the S phase are somewhere between, this allows classification into different cell phase populations[209].

P4-overexpressing cells showed no different behavior from the *LacZ*-overexpressing controls (Figure S4A), whereas keratinocytes with decreased *P4* levels demonstrated a shift of populations from the G1 and G2/M phases towards the S phase when compared to control cells (Figure 14A).

5.1.2.2 Cell viability remains unaffected by P4 level changes

Since cell death is a process required to be tightly regulated particularly in the context of tissue homeostasis, flow cytometric apoptosis analyses based on combined DAPI and annexin V stains were carried out for *P4*-overexpressing and -depleted keratinocytes as well as corresponding controls in collaboration with the group of Prof. Dr. Gero Brockhoff (Department of Gynecology and Obstetrics, University Hospital of Regensburg)[20]. Accessibilities of phosphatidylserine, a lipid which is prevalently located on the cytoplasmic side of the membrane, for fluorescently conjugated annexin V, as well as of normally membrane-protected DNA for DAPI give information about the state of viability that the cells are currently in[210].

Analogically to the cell cycle assay, cells overexpressing full-length *P4* did not behave differently from the *LacZ* controls (Figure S4B). Interestingly, also the keratinocytes with *P4* knockdown were as viable as their control counterparts, showing no signs of increased apoptosis (Figure 14B).

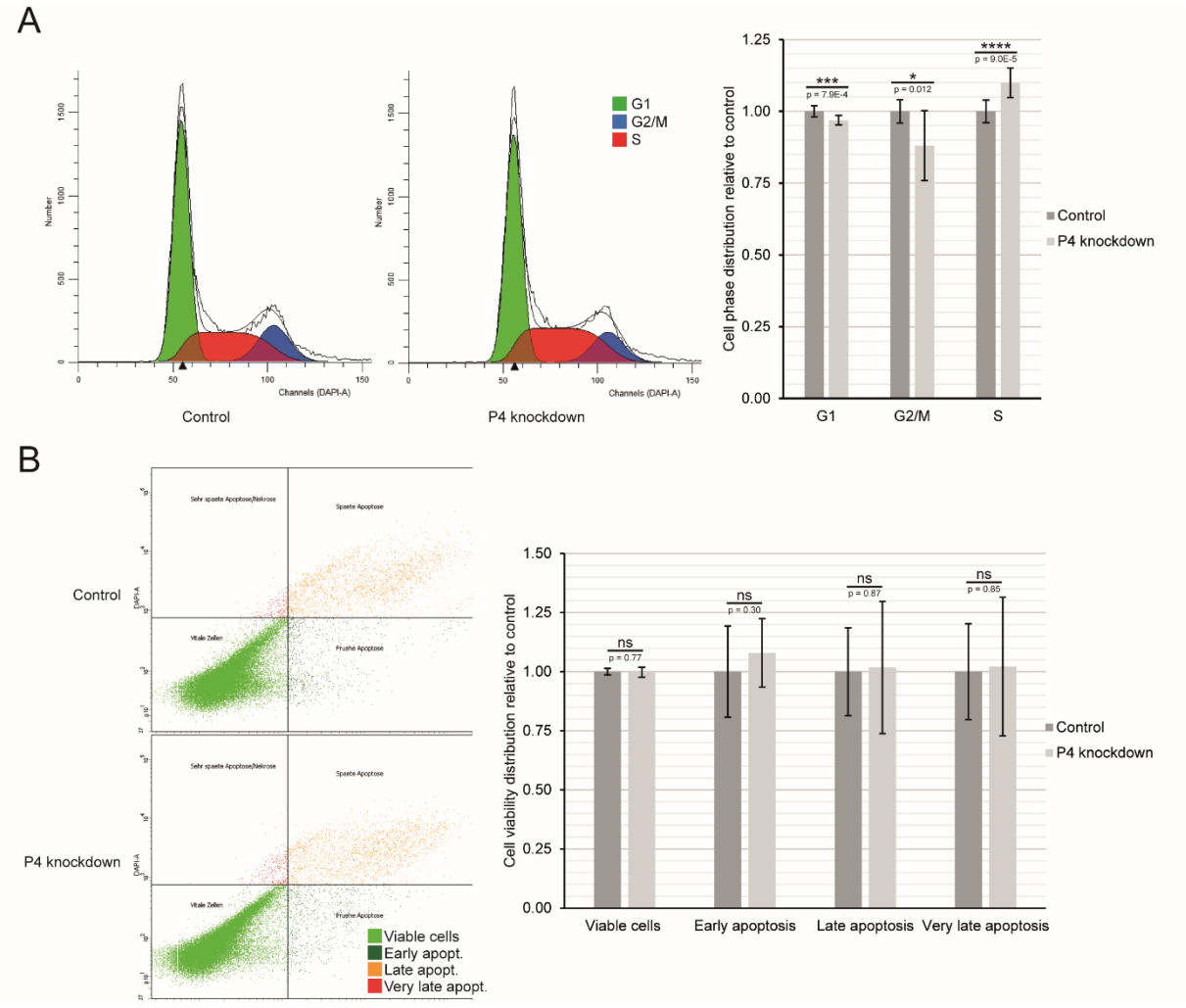

Figure 14: Effects of *P4* knockdown on cell cycle distribution and cell viability. (A) Representative fitted DAPI fluorescence intensity histograms (left) and cell cycle analysis (right) on *P4*-depleted and control keratinocytes. Decreased levels of *P4* are associated with a population shift of cells from the G1 and G2/M phases towards the S phase (N = 11-12). **(B)** Exemplary DAPI/FITC fluorescence intensity plots (left) and evaluation of cell viability (right) for keratinocytes with or without *P4* knockdown. No significant differences regarding apoptotic behavior are observed (N = 10-13). Apopt. abbreviates apoptosis.

5.1.2.3 Cell growth is situationally altered by P4 depletion

Keratinocytes with altered *P4* levels were seeded at low numbers and live-cell imaging was performed to observe area occupancy during 2D cultivation together with Dr. Ayse-Nur Menevse from the group of Prof. Dr. Philipp Beckhove (Department for Interventional Immunology, Leibniz Institute for Immunotherapy Regensburg) to analyze their proliferation.

When comparing relative changes in area occupancy over 24 hours, as expected the *P4*-depleted cells exhibited an overall increased growth rate and significance was observed for time points soon after seeding and then again for the last measured time points in which the cells had reached mediocre confluencies (Figure 15A).

Strikingly, although cells were meticulously counted prior to seeding in order to guarantee identical starting parameters for both conditions, *P4*-deficient cells occupied a smaller amount of the observed area than corresponding controls from measurement start on, and while the significance of this effect decreased over time due to the proliferative differences, the cell-covered area was at all time points higher for the control keratinocytes (Figure 15B). On the other hand, keratinocytes overexpressing full-length *P4* showed no significant changes in area occupancy or growth rates when compared to control cells overexpressing *LacZ* (Figure S5).

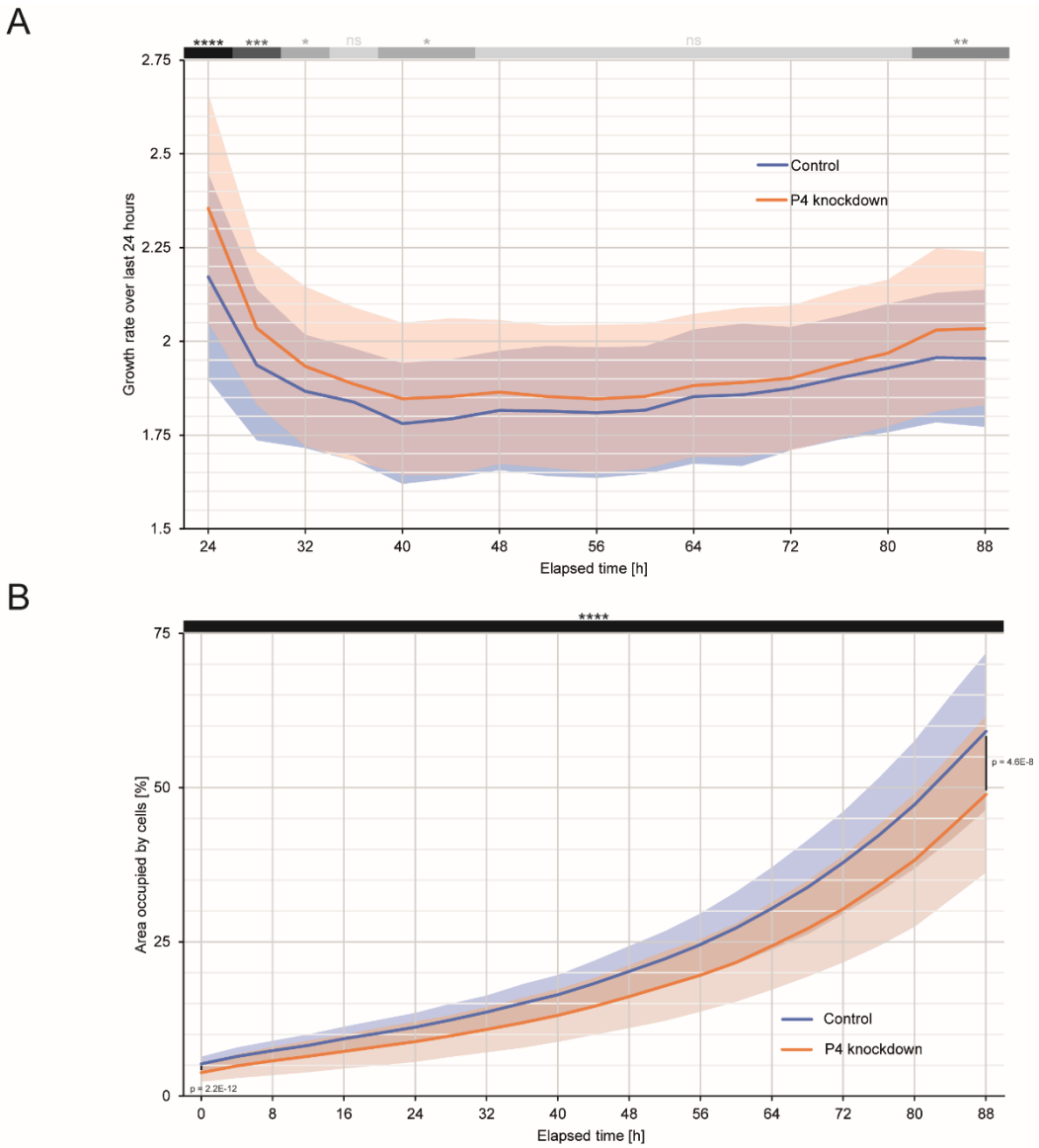

Figure 15: Alterations in cell growth following *P4* depletion as shown by live-cell imaging. (A) 24-hour growth rates for *P4*-depleted versus control cells. Keratinocytes with *P4* knockdown show an increased growth rate in general. Significancy is observed for time points close to the start of the assay as well as those in which the covered cell dish area is at least above 20% at begin of the interval **(B)** Absolute cell dish area covered by cells over the course of multiple days. Despite even seeding numbers, *P4*-deficient keratinocytes occupy less of the analyzed area from the start of the assay on. The observed difference to control keratinocytes becomes less significant over time (N = 99-102). Lightly colored areas denote standard deviations.

5.1.2.4 Scratch assays of P4-depleted cells show defects in migration

In order to analyze the proliferative activity of 2D-cultured keratinocytes at higher confluencies, scratch-wound assays were performed in which cells with normal or decreased expression of *P4* were seeded at very high confluency and a scratch of uniform width was applied amidst the culture dish area. Collaborating with Dr. Ayse-Nur Menevse from the group of Prof. Dr. Philipp Beckhove (Department for Interventional Immunology, Leibniz Institute for Immunotherapy Regensburg), live-cell imaging was subsequently used to document the velocity of gap closure upon subsequent cultivation.

While in the immediate time points after scratch performance and assay start the gap appeared to close significantly faster for *P4*-deficient keratinocytes, this effect was attenuated over time and while the p-value remained low, significance was only reached again for time points at which the scratch was almost completely grown over (Figure 16A).

Hence, a concurring effect in gap closure was suspected and since cytoskeletal architecture had been shown to be disturbed in *P4*-deficient organotypic tissue (Figure 13A), migrational capacity of cells was to be investigated. In order to negate proliferative effects, the capability of mitomycin C, a DNA-crosslinking drug[211], to inhibit keratinocyte growth was tested for different concentrations using an MTT assay (Figure 16B). Subsequently, *P4*-depleted and control cells which were pretreated with optimized amounts of mitomycin C were used for scratch assays.

As it had been assumed, proliferatively inhibited keratinocytes demonstrated significantly slower closure of the applied gap when *P4* levels were reduced for mid to late time points of the assay, whereas p-values were higher during the first 16 hours and eventually when wound confluency approached a steady state (Figure 16C).

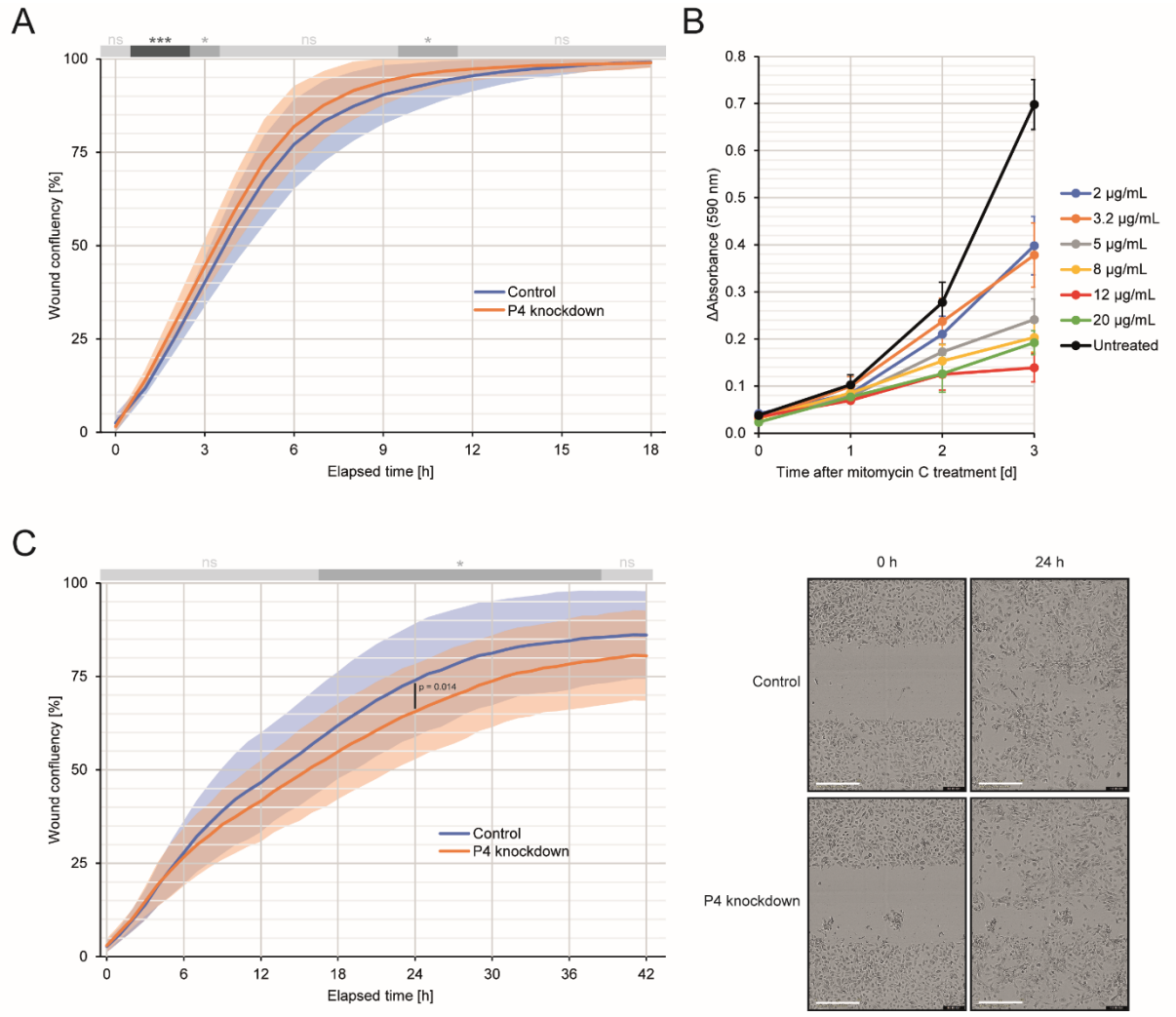

Figure 16: Scratch-wound assays in order to analyze high-confluency proliferation and migration. (A) Live-cell imaging of gap closure process for *P4*-deficient and control keratinocytes. Cells with *P4* knockdown show faster closing of the applied scratch, particularly for early time points (N = 33). **(B)** Effect of different mitomycin C concentrations on keratinocyte proliferation as measured via MTT assay. Cells treated with 12 µg/mL mitomycin C for 4 hours demonstrate the least change in absorbance over time, indicating slower growth (N = 8). **(C)** Comparative analysis (left) and representative images (right) for closing of scratch wounds by *P4*-depleted and control keratinocytes pretreated with 12 µg/mL mitomycin C as measured by live-cell imaging. Proliferatively inhibited cells exhibit slower closing of applied gaps when *P4* levels are low, indicating impeded migrational ability (N =32-40). Lightly colored areas mark standard deviations, scale bars are 400 µm.

5.2 Discussion and Outlook

Although major differences in several aspects of differentiation had been observed in *P4*-deficient organotypic epidermal tissue (Figure 10), neither in such tissue models nor in 2D-cultured keratinocytes a relevant phenotype could be identified in the scenario of *P4* overexpression (Figure 11, Figure S4 and Figure S5). This is possibly caused by multiple circumstances, one of them being that, in order to achieve overexpression, lentiviral

transduction was employed due to keratinocytes being rather resistant to conventional transfection methods[212,213]. However, viral treatment puts a lot of stress on keratinocytes which results in cellular changes such as increased size or impaired growth rate as discernible in the analysis of the performed proliferation assays (Figure 15 and Figure S5). Hence, it may well be that potential phenotypical alterations upon ectopic expression were concealed by gravely perturbed cellular homeostasis. Moreover, overexpression of lncRNAs can result in far deviations from the endogenous situation because of altered transcript localization or neglected importance of the original gene locus for some lncRNA functions[214]. Thus, it requires further investigations whether the observed thinner organotypic epidermis contrasting the increased thickness upon knockdown was specifically caused by overexpression of *P4* (Figure 11B). All in all, transcript depletion remains the favorable approach for lncRNA-dependent phenotypical studies and was therefore applied for most of these experiments.

Histological analysis of *P4*-deficient epidermis-like tissue made it clear that keratinocyte differentiation-related changes not only occur on a molecular level, but also that the epidermal architecture as a whole gets disturbed (Figure 12). This becomes particularly obvious for time points of early differentiation, in which several features reminiscent of known skin disorders were visible. Intriguingly, many of the observed morphologic changes such as hypergranulosis, acanthosis and vacuolar alterations also occur in the epidermis of lichen planus patients[56]. Moreover, in our RNA sequencing data, slight but significant downregulation of multiple genes within the HLA system was observed, those being reported to be associated with lichen planus susceptibility (data not shown)[215]. Analysis of *P4* expression in affected patient epidermis would be helpful to gain insight into a possible association with lichen planus. The absence of these morphological changes in later-differentiated *P4*-depleted organotypic tissue may be explained by possibly decreased knockdown efficiency over time or potential recovering mechanisms within the epidermis. Latter may also be probable with respect to the added *stratum corneum* structures at this time point which could be a sign for epidermal disposal of dysfunctional tissue.

Interestingly, *P4*-deficient epidermis-like tissue demonstrated elevated incorporation of BrdU which indicates enhanced DNA replication and therefore proliferative activity in the absence of *P4*. However, keratinocyte proliferation did not appear to be completely deregulated as the BrdU signal stayed restricted to the basal epidermal layers (Figure 12B). Therefore, potential proliferation-associated mechanisms of *P4* may be partially controlled by cell-matrix and intercellular interactions. Nevertheless, elevated keratinocyte proliferation is counterintuitive

with respect to the also observed upregulation of differentiation since induction of one of both is usually associated with repression of the other, although some regulators such as p63 are known to directly control both processes[216]. However, it is also possible that, due to the complex regulatory networks in epidermal homeostasis, only one of both aspects is caused directly by *P4* depletion and that the other process is subsequently induced in response to the original changes as some sort of compensatory mechanism to maintain epidermal function. Something similar can be seen in skin lesions such as keratoacanthomas which exhibit rapid cell growth but, in contrast to poorly differentiated cSCCs, the upper layers of the epidermis appear to achieve upholding of epidermal barrier functions by reactive upregulation of differentiation[217]. Keratoacanthomas may be referred to as a subtype of well-differentiated cSCCs and are hard to distinguish from the latter based on histopathological analysis, but they often tend to regress which suggests a categorization as benign tumors[218]. A potential connection of *P4* with keratoacanthomas or cSCCs is subject of current investigations in collaboration with Dr. Carolyn Lee's group (Department of Dermatology, Stanford University).

Strikingly, the detected relocation of α-tubulin especially in the *stratum basale* of *P4*-deficient organotypic models (Figure 13A) is coherent with changes in cytoskeletal organization that were implied in the gene ontology analysis of our RNA sequencing data (Figure 10D). The detailed nature of these alterations and how they manifest in the structure of epidermal tissue requires additional analyses, though the lack of α-tubulin at intercellular contacts hints at a possible deregulation of cell-cell adhesion which would also be consistent with aforementioned RNA sequencing analysis. For further studies, immunofluorescent staining of catenins or E-cadherin could give more detailed information in this regard since those proteins are critical components involved in adherens junctions of the basal epidermal layer[219]. In addition, quantitative methods for measurement of cell-cell adhesion such as single-cell force spectroscopy or dual micropipette aspiration may provide conclusive results[220].

Likewise, the observed alterations in the lipidomic profile of *P4*-depleted epidermis-like tissue (Figure 13B) are concordant with the transcriptome sequencing data since multiple genes associated with lipid biosynthesis were shown to be dysregulated (Figure 10D). The shift in lipid composition towards higher proportions of ceramides may be in part explained by the previously mentioned changes in differentiation as both lamellar bodies within the *stratum granulosum* and the lipid envelope in the cornified layer majorly consist of ceramides[221]. Detected accumulations of triglycerides on the other hand could be a sign of disturbed lipid metabolism since excess fatty acids in non-adipose tissue are channeled to be incorporated into

triglycerides to prevent lipotoxicity-induced apoptosis[222]. Whether lipid metabolism is in fact dysregulated upon *P4* knockdown and, if so, which exact enzymatic steps are affected remains to be uncovered by subsequent lipidomic analyses.

The measured cell cycle population shift of *P4*-depleted primary keratinocytes from the G1, G2 and M phases towards the S phase (Figure 14A) can be associated with a general increase in proliferative activity, whereby cell phase distribution also contains kinetic information since more cells in the corresponding population translate into extended time of phases[223]. Intriguingly, longer synthesis phases as accordingly observed following *P4* knockdown are suggested to stabilize self-renewal states in cell fate decisions[224]. Hence, keratinocytes with reduced *P4* levels may exhibit either enhanced proliferation, reduced tendency of commitment towards differentiation, or both. However, for a detailed analysis of cell cycle kinetics and additional information about the amount of quiescent keratinocytes, dynamic flow cytometric analyses utilizing base analog incorporation could provide valuable insights[223].

Due to apoptosis being a critical means for balancing keratinocyte proliferation in epidermal homeostasis, one could expect upregulated cell death in response to the probable increase of proliferative activity in *P4*-deficient keratinocytes[225]. In contrast to this, no significant changes in cell viability were detected (Figure 14B), indicating a potential uncoupling of proliferation and apoptosis as observed in hyperplasia-associated diseases including psoriasis or skin cancers[225]. While this would concur with the previously observed epidermal thickening upon *P4* knockdown (Figure 12A), definite statements in this regard may necessitate detailed in-tissue investigations of known apoptosis-associated pathway molecules such as BCL2 or MDM2[226,227].

In accordance with previous analyses that indicated elevated proliferation in *P4*-depleted keratinocytes (Figure 12B and Figure 14A), a corresponding cell growth phenotype was also confirmed in the employed live-cell imaging assays since a significant increase in the 24-hour growth rate of cells with *P4* knockdown was observed at early and late measured time points (Figure 15A). As keratinocytes were possibly still adapting to the new seeding environment, the observed alterations at earlier time points have to be interpreted with care as many other effects apart from growth may also play a role there. On the other hand, although counterintuitive at first glance, cell-cell contacts can promote proliferation under certain conditions which might explain why growth is significantly increased in the later time points[228]. Whether increased confluency is in fact a prerequisite for manifestation of *P4*-dependent cell growth alterations remains subject to further investigations, for instance by repetition of the

previous assay with higher starting cell numbers. The unexpected absolute differences in cell dish area covered by keratinocytes that persisted from the start point until the final measurement point in spite of equal seeding numbers (Figure 15B) may be the result of reduced adhesion capability of cells upon *P4* knockdown and thus lower cell dish occupancy. Therefore, significant changes in the 24-hour growth rate that were observed at early time points may in fact be a result of delayed adherence interfering with actual proliferative measurements. This hypothesis could also be feasible with respect to the α-tubulin staining which indicated cytoskeletal changes around the plasma membrane (Figure 13A), yet performance of specific cell adhesion assays would be needed for conclusive results[229].

Concordantly with the aforementioned higher growth rate at higher confluencies (Figure 15A), *P4*-depleted keratinocytes exhibited faster closing of the gap in standard scratch-wound assays initially, though the significance of this effect was lost at later time points (Figure 16A). Since gap closure under these conditions is mediated by an interplay of proliferative and migratory effects, pre-treatment with mitomycin C was performed as a common method to block proliferation and focus solely on keratinocyte motility[230]. Using optimized concentrations of mitomycin C (Figure 16B), cells showed attenuated recolonization of the applied scratch wound upon *P4* knockdown, indicating an impact of the lncRNA on migrational capacity of keratinocytes (Figure 16C). Subsequently, it would be of major interest to identify potential related phenotypes in epidermal tissue, for instance in the scenario of epithelial wound healing.

6. Protein interaction partners of the *P4* RNA

The *P4* transcript itself and phenotypes associated with its depletion had been well investigated up to this point, but little was known about how both these aspects are linked in terms of mechanism. However, due to previous analyses leaning against its active translation, it was assumed that *P4* exerts its function as a lncRNA.

While interactions of lncRNAs with multiple types of macromolecules, including DNAs, RNAs and proteins, are possible, our focus lied on the protein interactome of the *P4* transcript[231]. This decision was influenced by the broad spectrum of observed phenotypes, for which at least some kind of protein interaction was hypothesized. For many lncRNA interactions with other nucleic acids that lead to transcriptome-wide changes, effector or mediator proteins such as chromatin remodelers are present[232]. Furthermore, the additionally observed phenotypes might not implicitly be caused by modes of action that require interaction with nucleic acids but by other lncRNA mechanisms in which the transcript acts as a protein scaffold or decoy, for instance[233].

In general, most common procedures for RNA-centric identification of interacting proteins are quite similar in their experimental concept. They usually involve some kind of direct or indirect pulldown of proteins that are either associated or in close proximity to the transcript of interest with corresponding experimental controls, followed by mass spectrometry measurements[234]. On the other hand, subsequent validation of putative interaction partners can be carried out in many distinct ways, for example by RNA or protein pulldowns with quantitative readout of the other interacting molecule, or by a wide range of biophysical binding assays[231,235].

During these doctorate studies, three different published methods for identification of *P4* protein interactors were tested, those being ChIRP-MS, CARPID, and S1 aptamer-based pulldowns (Figure 17A)[236–238]. For each approach a subset of proteins identified by mass spectrometric analyses was considered for validation by pulldown experiments, and for some of these candidates further specification of interaction by thermophoretic measurements was performed (Figure 17B).

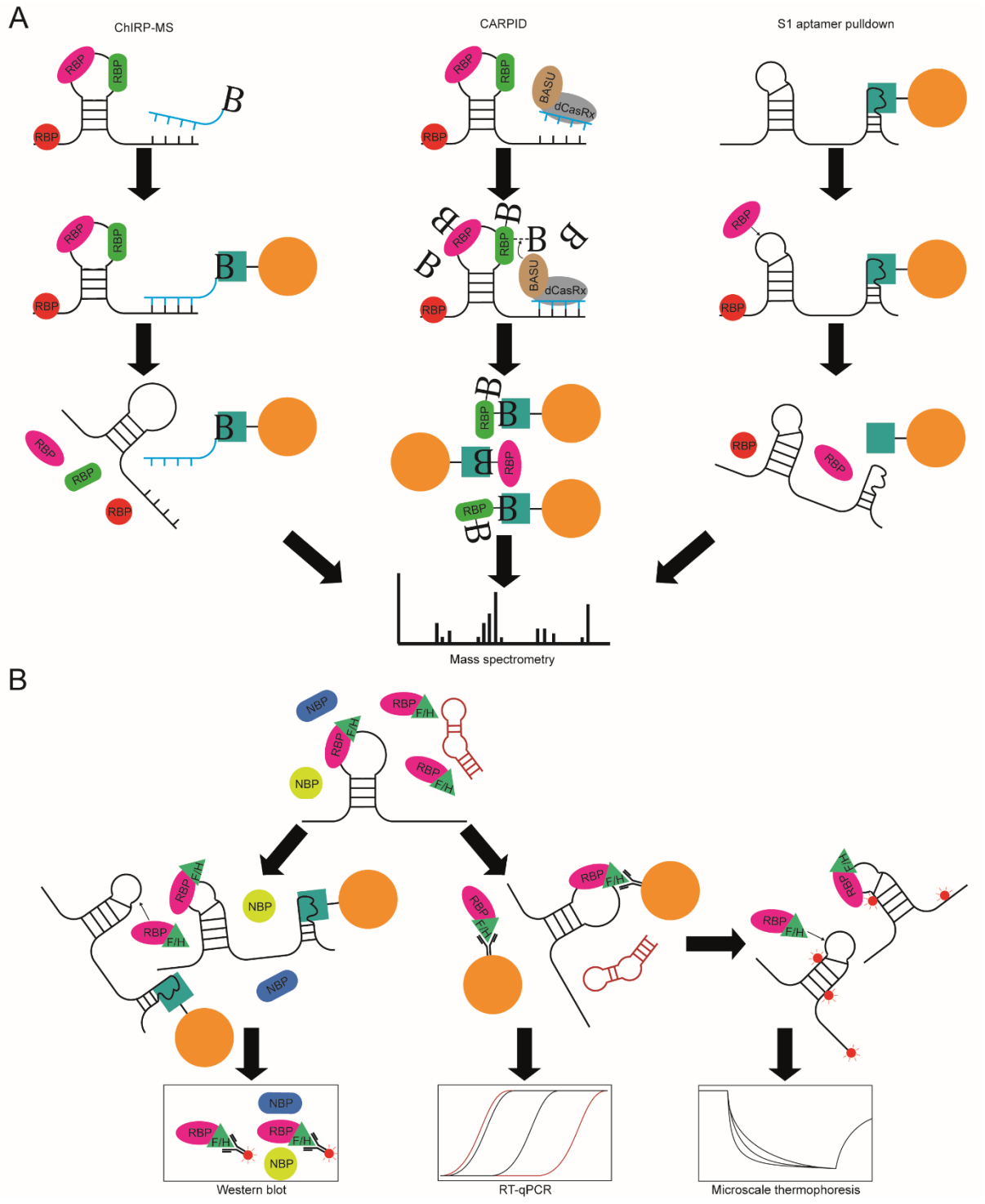

Figure 17: Strategies for identification and validation of RNA-interacting proteins. (A) Schematic illustration of tested screening approaches for *P4*-binding proteins. All methods involve interaction of bead-fixed streptavidin (blue rectangles) with biotin (capital B's) or S1 aptamers. ChIRP-MS targets endogenous transcripts and associated proteins via biotinylated and complementary oligonucleotides. During CARPID, endogenous RNAs of interest are targeted by gRNAs guiding a catalytically inactive nuclease fused to a biotin ligase that, after addition of biotin, biotinylates proteins in close proximity. On the other hand, S1 aptamer-fused *in vitro*-transcribed RNAs bind to streptavidin and can be pulled down after interacting with endogenous proteins present in cell lysate. **(B)** Simplified depiction of applied interactor validation assays. Protein candidates fused to a FLAG/HA or 3xHA tag (green triangles) are overexpressed in cells, and RNA pulldown via S1 aptamers or protein immunoprecipitation is carried out with subsequent quantitative readout of associated proteins by western blot or of RNAs by RT-qPCR. Immunopurified candidate proteins and fluorescently marked *in vitro*-transcribed RNAs are measured using microscale thermophoresis in order to determine binding affinities. NBP abbreviates non-binding protein.

6.1 Results

6.1.1 Screening approaches for identification of *P4* interactors

6.1.1.1 Chromatin isolation by RNA purification-mass spectrometry (ChIRP-MS)

In an attempt to reliably capture *P4*-associated proteins while still staying close to the native context, ChIRP-MS was employed. In this method, pools of 3'-biotinylated ChIRP probes with lengths of 18 to 20 nt were applied to wildtype lysate (Figure 17A)[236]. Here, two distinct pools of four probes complementary to different regions of the *P4* transcript were utilized to enable purification of multiple isoforms and their associated proteins, while pools of eight *LacZ*-directed or seven transcriptomically unique, randomly scrambled probes were used as controls.

When comparing the amounts of RNA present in the pulled down fraction, specific enrichment of *P4* compared to other transcripts was confirmed with the *P4* probe pools, furthermore, significantly more *P4* was pulled down with the corresponding probes than with the control probe pools (Figure 18A). However, when performing SDS-PAGE and Coomassie staining with the pulldown samples, no difference in band pattern could be detected (Figure S6A). Nonetheless, whole gel lanes were analyzed via mass spectrometry by the group of Dr. Astrid Bruckmann (Department of Biochemistry I, University of Regensburg).

When using the DAVID tool to perform GO term analysis on 50 putative interacting candidates that were picked based on score differences between the *P4* pulldown and control samples, no specific enrichment of pathway-related proteins was detected with tRNA aminoacylation and protein folding being the processes closest to the significance threshold (Figure 18B)[239].

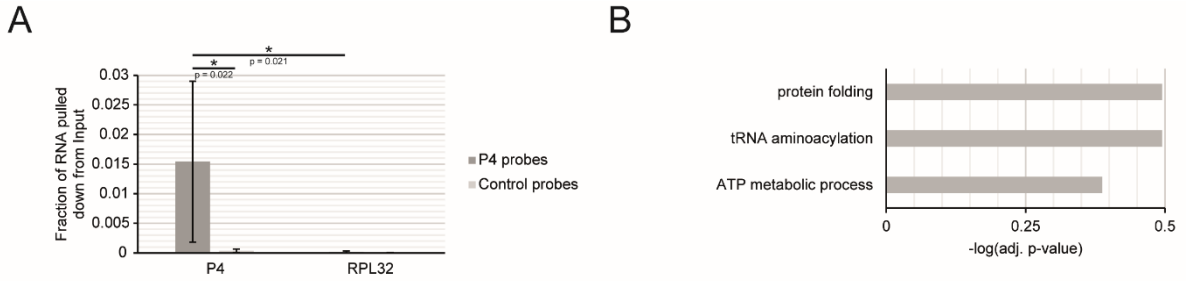

Figure 18: ChIRP-MS verification and classification of resulting protein candidates. (A) Analysis of enrichment specificity with utilized ChIRP probes. *P4* shows significantly more enrichment with the two pools of probes complementary to the transcript compared to the *LacZ* and scrambled probe pools. *P4* probes also exhibit specificity to the target RNA as the *RPL32* transcript is pulled down less efficiently in a significant manner (N = 8). **(B)** Gene ontology term enrichment analysis of 50 proteins present in *P4* ChIRP-MS samples with Mascot scores at least 1.5 times higher than in corresponding controls[239,240]. The three terms with the lowest adjusted p-values are included. No annotated process is found to be represented by the identified proteins in a significant manner with protein folding and tRNA aminoacylation coming closest.

6.1.1.2 CRISPR-assisted RNA-protein interaction detection (CARPID)

Another approach that targets proteins associated with endogenous transcripts is CARPID. For this method, cells are double transfected or transduced in order to express arrays of two gRNAs complementary to the RNA of interest as well as a fusion protein consisting on one hand of the RNA-targeting, catalytically inactive endonuclease dCasRx and on the other of the genetically engineered biotin ligase BASU; and gRNA-directed recruitment of this protein to the desired transcript followed by supplementation of biotin enables biotinylation of proteins in next proximity to the gRNA binding sites (Figure 17A)[237].

For *P4*, two different gRNA arrays with the first one targeting exon 2 and the beginning of exon 3 and the second one exon 4 and the beginning of exon 5 were designed to include a high proportion of unpaired bases as predicted by RNAfold[241]. As controls, cells were single transduced either with one of the gRNA array constructs or with the fusion protein construct.

When testing the biotinylation efficiency of the fusion protein, cells that were successfully double transduced exhibited strong and specific incorporation of biotin after 15 minutes of supplementation, especially in the nuclear region of the cells (Figure 19A). Specificity of the gRNA arrays for *P4* was tested by double transduction together with catalytically active CasRx and comparison of *P4* levels to the controls which expressed dCasRx-BASU instead. Keratinocytes that expressed CasRx and one of the two gRNA arrays showed significantly reduced *P4* expression in comparison to cells expressing the catalytically inactive mutant (Figure 19B). Although after pulldowns with two different washing buffers no distinct bands but only intensity changes were detected when analyzing parts of the fraction via SDS-PAGE with subsequent Coomassie stain (Figure S6B), all samples for both conditions were digested on-beads and subjected to mass spectrometric measurements by the group of Dr. Astrid Bruckmann (Department of Biochemistry I, University of Regensburg).

Since a wide spectrum of ribosomal large and small subunit proteins was detected in the pulldown fractions but not in the controls, translation resulted as the most significantly enriched GO term when analyzing 49 candidates meeting the required criteria, followed by actin organization, actin-based movement and ribosome small subunit biogenesis (Figure 19C)[239].

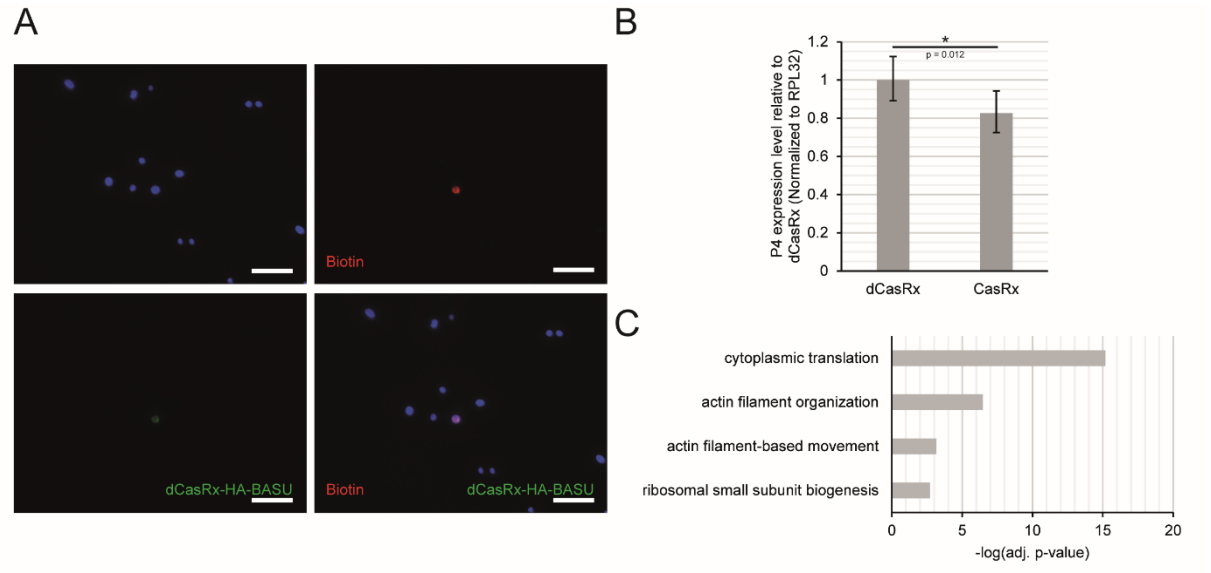

Figure 19: CARPID quality control and enrichment analysis of mass spectrometric readout. (A) Fluorescent staining of biotin incorporation into keratinocytes expressing dCasRx-HA-BASU and a *P4*-targeting gRNA array. Cells were treated with 200 µM biotin for 15 minutes prior to fixation. Biotin signals show colocalization with dCasRx-HA-BASU in the nuclear regions of keratinocytes. Nuclei are stained blue (DAPI), scale bars are 100 µm. **(B)** Specificity of gRNA array for targeting *P4*. Cells double transduced to express catalytically active CasRx and either of the gRNA arrays demonstrate a significant decrease in *P4* levels compared to keratinocytes expressing the mutated nuclease instead (N = 8). **(C)** GO term analysis for 49 proteins either present only in double transduced samples or exhibiting higher emPAI scores than the corresponding single transduced controls for either gRNA array under both applied washing conditions[239,242]. Terms with adjusted p-values lower than 0.05 are shown. Multiple proteins associated with ribosome- or cytoskeleton-related processes were identified to be possible interaction partners of *P4*.

6.1.1.3 Pulldown of endogenous proteins binding to S1 aptamer-tagged RNA

As opposed to aforementioned strategies that focus on targeting endogenous transcripts, in a further experiment, pulldowns based on *in vitro*-transcribed S1 aptamer-fused RNAs were carried out. This method utilizes an increased binding affinity of specific aptamers towards streptavidin[243]. The aptamer is attached to the 3' end of the RNA of interest in order to interfere as little as possible with potential binding sites, in contrast to randomly incorporated biotin-tagged ribonucleotides; and coupling of synthesized transcripts to streptavidin beads followed by incubation with cell lysate enables pulldown of RNA-binding proteins (Figure 17A)[238].

In the case of *P4*, the DNA sequence of the full-length transcript was amplified with primers adding the streptavidin-binding sequence to the 3' end in order to enable subsequent *in vitro* transcription of the aptamer-fused RNA. In addition, a truncated version of *LacZ* that matches the length of *P4* as well as the *mCherry* transcript, both with added aptamer, were synthesized as controls in order to rule out proteins that bind to RNA unspecifically, additionally, yeast tRNAs were added prior to the pulldown procedure as an unspecific competitor.

In order to make sure that the affinity tag works properly, the entire pulldown procedure was performed and the ultimately streptavidin-associated RNA was compared to the input via RT-qPCR, indicating that, even though the major fraction of the used *P4* was lost in the course of washing, detectable amounts remained bound to the beads while still being distinguishable from the background signal (Figure 20A). Hence, despite the absence of prominent new bands in the protein gel (Figure S6C), pulldown fractions were submitted for analysis via mass spectrometry that was carried out by the group of Dr. Astrid Bruckmann (Department of Biochemistry I, University of Regensburg).

Significant amounts of the 64 proteins that were eventually selected for GO term analysis based on the comparison of *P4* pulldown and control mass spectrometric data showed association with cytoskeletal processes such as intermediate filament organization, but also epithelial-specific keratinization (Figure 20B)[239,244].

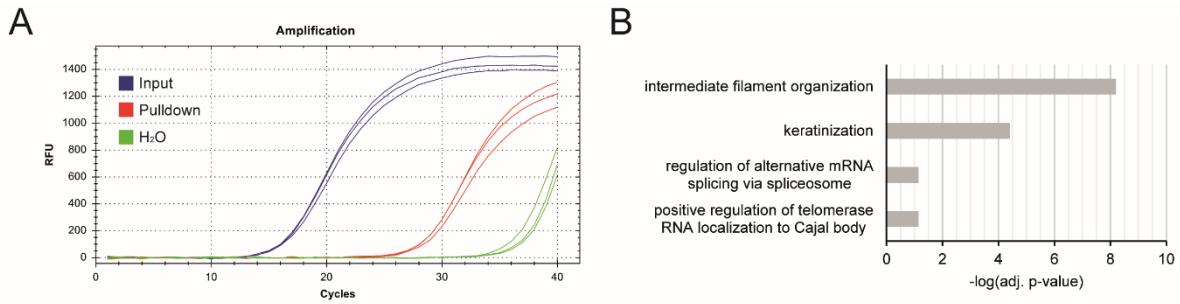

Figure 20: S1 aptamer binding control and categorization of pulled down proteins. (A) Raw fluorescence data of *P4*-targeting RT-qPCR on cDNAs transcribed from *in vitro*-transcribed aptamer input and the eluted fraction after pulldown as well as a template-less control. While only a small fraction of the originally used RNA remains attached to the beads, the fluorescence signal is distinct from the water control. **(B)** Analysis of GO term enrichment for 64 proteins detected in the *P4* aptamer pulldown with iBAQ scores at least twice as high as in both controls[239,245]. The four terms with the lowest adjusted p-values are displayed. Significant fractions of putative interactors are found to be related to cytoskeletal pathways.

Summarized, the proteins that were identified by the varying screening methods demonstrated hardly any overlap when comparing the filtered sets that were previously used for GO term analyses, with IGF2BP2 emerging as single protein present in both ChIRP-MS and aptamer pulldown results, and ACTBL2 being the only shared candidate between the CARPID and the aptamer pulldown data.

6.1.2 Strategies for validation of putative interaction partners

6.1.2.1 Aptamer pulldowns not suitable for validation of specific RNA-protein interactions

As a prerequisite to validate some selected interaction partners resulting from the previous mass spectrometric analyses, those were cloned into lentiviral or nonviral vectors designed to enable mammalian expression with the addition of an N- or C-terminal FLAG/HA- or 3xHA-tag. Transduction of NKCs with previously generated virus allowed overexpression of the respective candidates. In order to gather insight about potential protein binding to *P4*, the corresponding aptamer already used for screening pulldowns was *in vitro*-transcribed, coupled to beads and incubated with NKC lysate containing the overexpressed proteins. As controls, F/H-GFP was used for proteins and *LacZ* aptamers on the RNA side. After pulldown, eluted fractions and inputs were used for SDS gel electrophoresis with subsequent western blot targeting the overexpressed proteins via their tags, followed by comparison of band signal intensities.

While a small fraction of the aptamers remained attached to the beads after the pulldown procedure as it already had been shown during the aptamer screening approach, hardly any signal could be detected in most eluted fractions, whereas in some cases protein-specific bands were visible but no difference in band intensities between *P4* pulldowns or controls was discernible (Figure S7).

6.1.2.2 α-HA immunoprecipitation confirms multiple interactors of P4

In a reverse approach, putative FLAG/HA- or 3xHA-tagged protein interactors were as well abundantly expressed in primary keratinocytes by viral transduction. Immunoprecipitations targeting the tagged proteins were carried out on the lysates and total RNA was purified from the pulled down as well as from input fractions to be afterwards analyzed by RT-qPCR, enabling detection of endogenous RNA binding to the overexpressed proteins. Again, F/H-GFP was used as a protein control, and in addition to *P4*, *RPL32* transcripts levels were also analyzed by RT-qPCR as an unspecific RNA binding control.

The immunoprecipitation was shown to be successful for most proteins, as corresponding signals could be detected for pulldown fractions that were analyzed by SDS-PAGE and subsequent semi-dry western blot, with the exception of the putative band for NHP2 overlapping with the light chain of the utilized HA-directed antibody (Figure 21A). Out of two

tested candidates that had been identified via ChIRP-MS, FARSB but not ANXA6 showed significant enrichment, whereas for neither GELS nor TPM4 that had both resulted from the CARPID analysis an increased *P4* abundance in the IP fraction was detected. Moreover, with CETN2 and STAU2, two of three considered proteins that had been indicated by the S1 aptamer pulldown analysis exhibited relevant association with *P4* in comparison to the GFP control, while the same trend was not significant for NHP2 (Figure 21B). In contrast to *P4*, no RT-qPCR signals distinct from water controls could be detected for the *RPL32* transcript in the pulldown fractions.

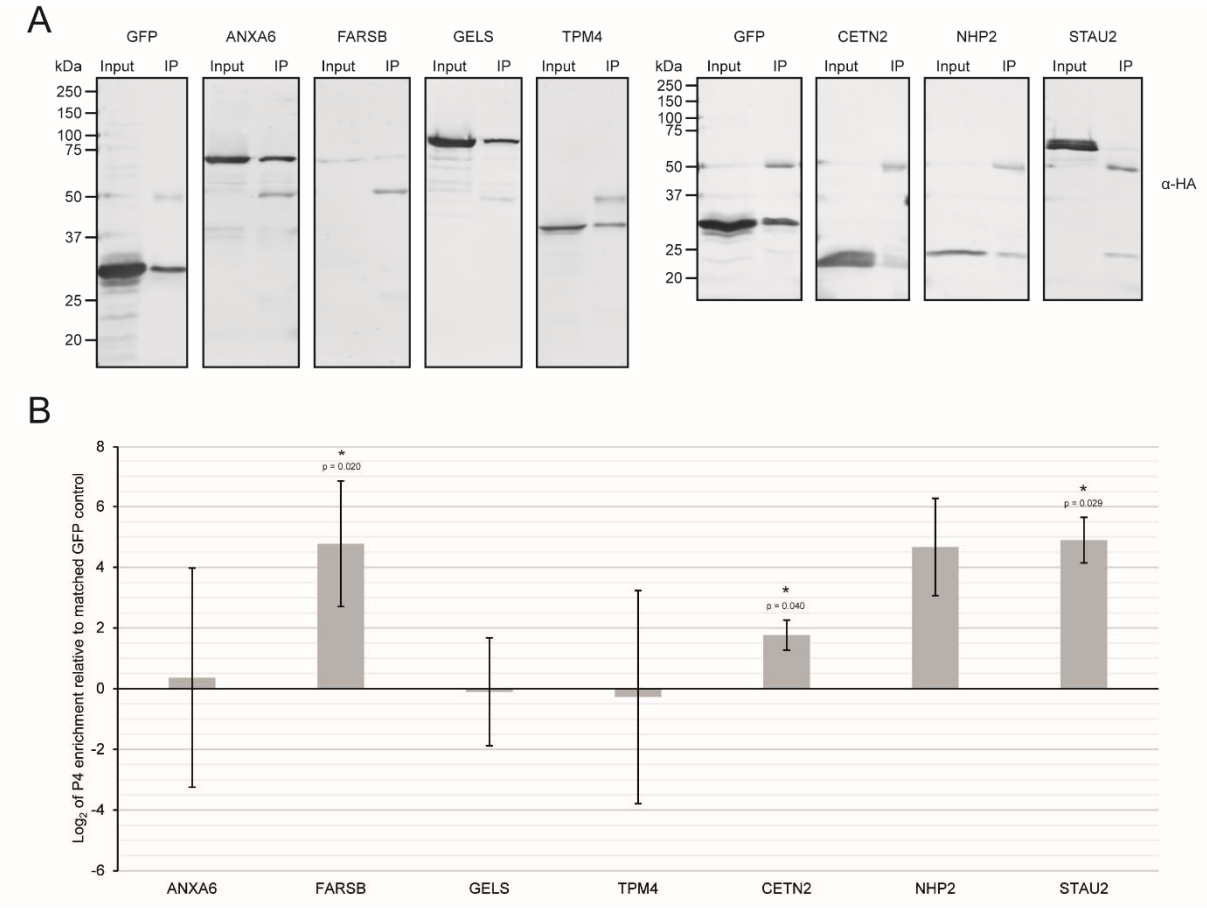

Figure 21: Protein immunoprecipitation for validation of *P4* interactors. (A) Verification of successful immunoprecipitation by western blot. Two of the cloned candidates each for ChIRP-MS and CARPID (left) as well as three proteins resulting from the aptamer-based pulldown (right) demonstrate a signal at the correct molecular weight range both in input and IP fractions when targeted by an HA-directed antibody. Bands for heavy and light antibody chains are detected at 50 kDa and 25 kDa, respectively. **(B)** RT-qPCR-based analysis of *P4* association with immunoprecipitated putative interaction partners compared to GFP control. While ANXA6, GELS and TPM exhibit no signs of *P4* binding, significant enrichment is detected for FARSB, CETN2 and STAU2 (N = 2-3).

6.1.2.3 Microscale thermophoresis measurements deliver inconclusive results

As a means to gather detailed information about binding affinity of *P4* towards some of the tested proteins, microscale thermophoresis measurements were carried out at the MST facility of Prof. Dr. Gernot Längst's group (Department of Biochemistry III, University of Regensburg). In this method, even when no intrinsic fluorescence is present, interaction of two molecule types can be observed by fluorescently labeling one of them and adding the other in high purity. Induction of local temperature changes by usage of an infrared laser results in fluorescence changes which occur due to thermophoretic movement along the temperature gradient which is affected by molecular properties such as size, charge or conformation, meaning that binding events can result in quantifiable alterations of this effect by adding the second interacting component in different dilutions[246].

In the case of *P4*, fluorescent full-length transcript as well as five fragments of approximately 200 nt were *in vitro*-transcribed by adding an Cy5-labeled uridine analog to the reaction mixture, furthermore, fluorescent truncated *LacZ* (*LacZt*) and the reverse complementary *P4* antisense (*P4-AS*) transcripts as well as randomly scrambled fragments of different GC-content and 200 nt in length were synthesized as control RNAs. Out of the putative interactors, FARSB, S100A8, a protein identified in the aptamer pulldown data which had shown *P4* enrichment in a singly performed HA-IP (data not shown), and GELS as a negative control were overexpressed in HEK cells, immunopurified and concentrated prior to usage in MST assays. RNA synthesis was successful in that fluorescent transcripts of the correct size were detected in RNA gels with the exception of the two of the shorter fragments that exhibited an additional signal at an approximate length of 400 nt (Figure 22B). For the tested proteins, specific purification was achieved; however, further bands believed to be caused by binding partners of the proteins were present in the purified fraction, and in the case of GELS the additional signal could indeed be identified as actin (Figure 22B and C).

Unfortunately, none of the investigated proteins were purified in sufficient concentrations to enable fitting of a binding affinity curve and therefore no dissociation constant could be determined; and although the relative difference of the fluorescence intensity signal for the highest concentration from the remaining data points in terms of standard deviation units was in general larger for *P4*-related transcripts than for the controls except *P4-AS* (Figure 22D), the total amplitude change of normalized fluorescence between highest concentration and mean was rather low, reaching a maximum of 0.89 percentage points for the measurement of full-length *P4* with S100A8.

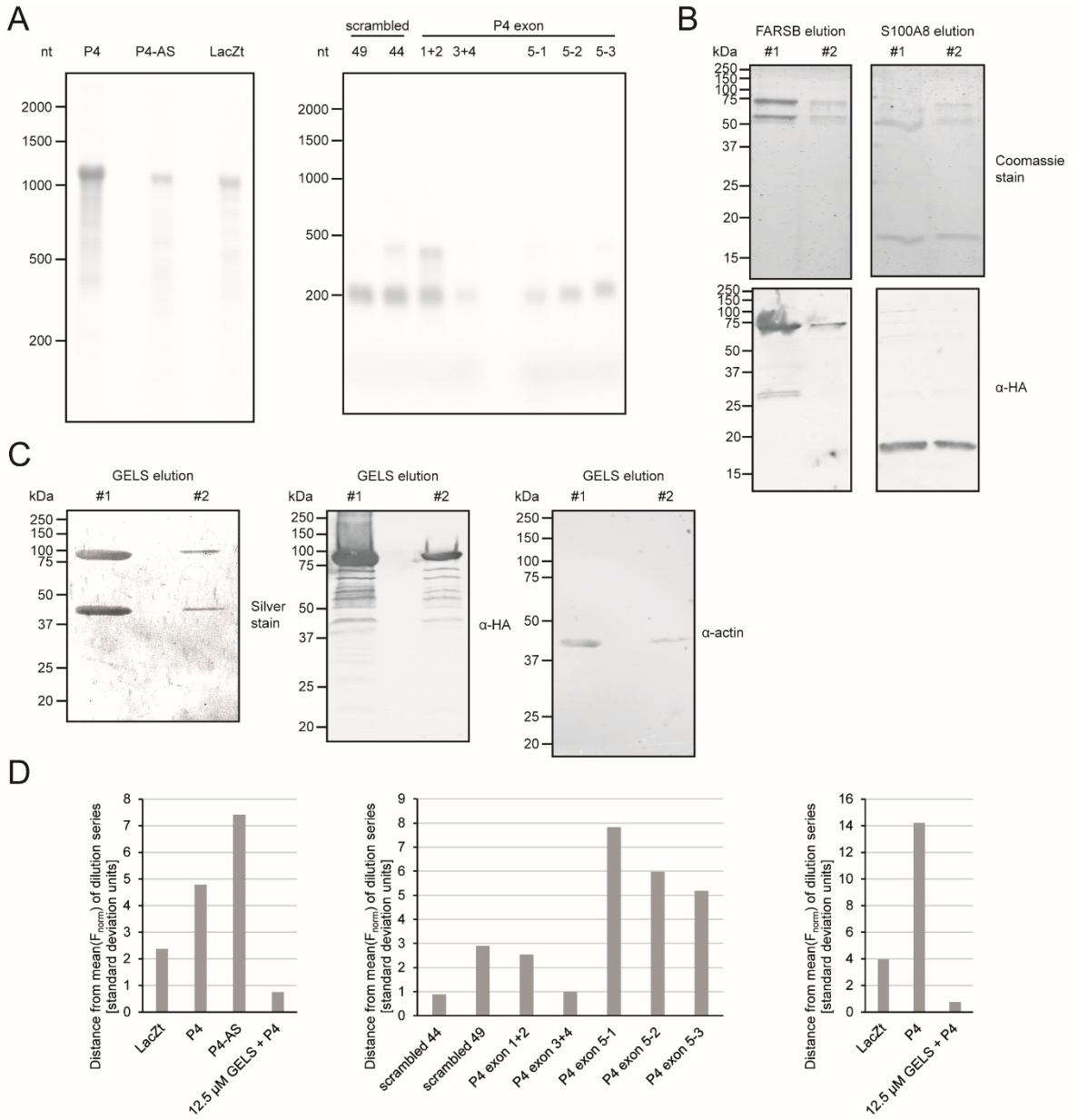

Figure 22: Preliminary experiments and results of MST measurements. (A) Verification of correct *in vitro* transcription and incorporation of Cy5-labeled nucleotides for MST-intended RNAs by performing agarose gel electrophoresis followed by fluorescence imaging. Synthesized RNAs exhibit emission signals at the expected wavelength of 700 nm and at the correct lengths except for scrambled 44 and *P4* exon 1+2 that demonstrate additional bands at 400-500 nt. **(B)** Coomassie stains (top) and western blots targeting the HA-tag (bottom) for eluted fractions of FARSB and S100A8 immunopurifications. In addition to the signal assignable to the protein at 70 kDa, elutions for FARSB shows one further band at 55 to 60 kDa, while S100A8 elutions exhibit additional signals at 50 and 75 kDa aside from the protein-specific band between 15 and 20 kDa. **(C)** Silver stain (left) and western blots targeting the HA-tag (mid) or actin (right) for immunopurified GELS elutions. Other than the expected signal at a molecular weight range of 80 to 90 kDa, another protein band not targeted by the HA-directed antibody is present between 40 and 45 kDa. Western blot incubation with an antibody targeting actin reveals that the signal can be assigned to this protein. **(D)** MST measurement distance of highest concentration datapoints from dilution series mean at MST laser power of 20% and excitation time of 15 seconds for 4 µM (left) and 1.85 µM FARSB (mid) as well as 8.3 µM S100A8 (right). Measurements point towards slightly higher affinities of FARSB towards full-length *P4* and *P4-AS* in comparison to the truncated *LacZt* control, whereas fragments of exon 5 tend towards a clearer discrimination of the highest concentration datapoint from the rest of the dilution series as compared to fragments covering exons 1 to 4 or scrambled controls. Similar to FARSB, binding events of S100A8 at the highest concentration appear more probable for full-length *P4* than for the *LacZt* transcript, whereas the datapoint for 12.5 µM GELS shows no clear deviation from the dilution series mean.

6.2 Discussion and Outlook

Out of the tested screening methods, ChIRP-MS stays closest the endogenous keratinocyte context, and specific purification of *P4* transcripts was indeed shown (Figure 18A). However, neither were any distinct bands detected on the stained gels of pulldown fractions (Figure S6A) nor did the identified proteins group into specific functional categories (Figure 18B) which possibly hints at disruption of the *P4*-protein interactions during applied washing steps. Crosslinking with reagents such as formaldehyde as it was performed in the initially published approach could prevent this but requires thorough optimization to find the best conditions regarding crosslinker concentration and incubation time[236].

While CARPID also targets endogenous transcripts, the procedure requires lentiviral transduction which drastically disturbs keratinocyte behavior, therefore relativizing similarity to the wildtype *in vivo* environment. Nevertheless, the results of preliminary CARPID analyses indicated correct functioning of the method since both dCasRx-BASU-dependent biotinylation as well as specific gRNA-mediated targeting of the fusion protein, two core prerequisites for a successful experiment, were detected (Figure 19A and B). The overall poor knockdown efficiency that was seen upon targeting of catalytically active CasRx to *P4* may be the result of generally low double transduction rates around 30% (data not shown). Thus, for the final CARPID approaches it could be that too little total cell material was used as no prominent new bands were present following gel electrophoresis and staining of pulldown fractions, although differences in band intensities were discernible (Figure S6B). *P4*-specific pulldown of multiple proteins associated with ribosomes and actin structures (Figure 19C) fits together with the previously discovered polysomal occupancy of cytoplasmic *P4* (Figure 6B) as well as with the observation of cytoskeleton-related changes upon *P4* modulation (Figure 13A, Figure 15A and Figure 16C), respectively. However, it is unclear why biotinylation was prevalently observed in the nucleus (Figure 19C) while most of these proteins mainly localize to the cytoplasm. Yet, the possibility exists that *P4* indeed interacts with actins, myosins or ribosomal proteins within the nucleus, for instance in the context of ribosome biogenesis[247,248]. Still, potential for optimization of the CARPID procedure is given as new gRNA arrays could be designed with respect to the SHAPE-based *P4* structure (Figure 8). Moreover, instead of singly transduced controls, double transduction of cells with dCasRx-BASU as well as empty gRNA vectors as performed in the original publication may be the preferable choice[237].

It is uncertain how much the *in vitro*-transcribed S1-aptamers resemble endogenous transcripts which may exhibit altered properties due to post-transcriptional modifications and existence of

multiple isoforms. Regardless, affinity of the synthesized aptamers to streptavidin beads was confirmed (Figure 20A), and while no obvious differences were visible upon gel analysis (Figure S6C), mass spectrometric measurement of pulldown fractions resulted in a plethora of potential interactors associated with cytoskeletal changes including keratinization (Figure 20B). This is coherent with the observed alterations in keratinocyte differentiation (Figure 10 and Figure 12A), though it has to be kept in mind that the assessment was predominantly based on the detection of keratins which are common contaminants in mass spectrometry[249]. Moreover, the absolute amount of *P4*-aptamers in the final pulldown fraction was calculated to be as low as in the femtomolar range (data not shown). Therefore, it cannot be stated with certainty whether the identified proteins actually stem from an interaction with *P4* or from contamination during the procedures of pulldown and mass spectrometry preparation. Repetition of the experiment with larger quantities of RNA and streptavidin beads, gentler washing steps or quantitative proteomic analysis as applied in the original approach could yield more conclusive outcomes[238].

Each of these screening methods resulted in distinct sets of putative *P4* interactors with almost no overlap. While this may be in part caused by the stringent filtering of mass spectrometric output, one would expect at least some candidates to occur across multiple approaches. What has to be additionally considered, however, is that the performed experiments exhibit substantial differences regarding their basic concepts, since some methods are closer to the endogenous situation than others, whereas protein pulldown can be dependent either on direct interaction with the transcript of interest or on proximity to specific target regions.

While the amount of *P4*-aptamer remaining to streptavidin beads was perhaps high enough for subsequent mass spectrometric analysis, it was probably too low to enable application of the assay as a validation method. Accordingly, aptamer-based pulldown followed by gel electrophoresis and western blot analysis of tagged interaction partners resulted in the total absence of signal or no distinct differences between *P4*- and *LacZt*-aptamers (Figure S7). Hence, more efficient coupling of transcripts to streptavidin beads may be achieved by utilizing 3'-biotinylated instead of S1-aptamer-fused *in vitro* transcripts[250].

HA-immunoprecipitation and RT-qPCR analysis validated the interaction of *P4* with FARSB, CETN2 and STAU2, whereas for some other protein candidates additional replicates are required (Figure 21). Thereby, one of the validated interactors was identified via ChIRP-MS, the other two through the aptamer-based approach. However, the total number of tested candidates is too low to allow definite statements regarding the individual performance of

applied screening methods. Cytosolic phenylalanine-tRNA ligase is a tetramer comprised of two catalytically active α- (FARSA) and two regulatory β-subunits (FARSB), the latter having additional functions by which misaminoacylations of $tRNA^{Phe}$ are corrected[251]. Intriguingly, the α-subunit possesses three DNA binding domains in humans and reportedly antagonizes Notch signaling in *Drosophila*[252,253]. Possible influences of the *P4*-FARSB interaction on $tRNA^{Phe}$ aminoacylation or putative FARSA signaling and further downstream effects remain to be elucidated. Centrin-2 (CETN2) is a multifunctional member of the calcium-binding EF-hand protein superfamily and is associated with centrosomes and basal bodies in which it is required for ciliogenesis, potentially through mechanisms of Ca^{2+}-regulated self-aggregation[254–256]. Moreover, CETN2 demonstrates SUMO-dependent translocation to the nucleus where it interacts with the XPC protein and stimulates nucleotide excision repair[257,258]. In *Xenopus laevis*, the protein is found to localize to nuclear pores and mediate both mRNA and protein export[259]. While interaction of CETN2 with centrosomes and the microtubule-organizing center is coincident with the observed perturbances in α-tubulin distribution (Figure 13A), the presumably nuclear localization of *P4* points towards CETN2-mediated functions in nuclear transport or nuclear excision repair. The versatile Staufen2 protein (STAU2) contains four double-stranded RNA binding domains and is well characterized in mammalian neurons where Stau2 influences stabilization and microtubule-dependent transport of target mRNAs, supposedly by interacting with their 3'-UTRs[260–262]. Interestingly, in rat neurons one of the Staufen2 RNA-binding domains is involved in nuclear export of both isoforms and is even required in case of the longer isoform[263]. Furthermore, Staufen2 functions in regulation of mammalian neuronal proteomes and transcriptomes and achieves the latter through effects on Argonaute assembly or by directly promoting Staufen1-mediated mRNA decay[264–266]. In human retinal hTERT-RPE1 cells, STAU2 depletion results in facilitated proliferation, and the protein is shown to interact with nucleolar proteins involved in DNA damage response and ribosome biogenesis, hinting at a possible involvement of *P4*, particularly in the latter process, due to its nuclear localization and enriched proteins in the CARPID experiment (Figure 19C)[267].

Given the several potential functions of these validated *P4* protein interactors in combination with a broad spectrum of *P4*-related phenotypes, it is difficult to hypothesize on which downstream effect may be caused by which interaction. Strikingly, both CETN2 and STAU2 are linked to microtubular processes, nuclear transport and response to DNA damage, which suggests associated functions of *P4*, but detailed mechanistical analyses are required. Especially the putative effect of *P4* on microtubule organization encourages further pursue due to multiple matching phenotypes (Figure 13A, Figure 15A and Figure 16C) and the fact that microtubules

play many additional important roles in the epidermis including spindle orientation, cilia-mediated signaling and reinforcement of the epithelial barrier[268].

While the fluorescent transcripts for MST measurements were synthesized in sufficient quality and quantity (Figure 22A), preparation of the proteins turned out to be problematic. Only low levels of both FARSB and S100A8 were effectively purified from mammalian cells. S100A8, a calcium-binding protein which usually dimerizes with S100A9, was considered for this assay due to promising results in an initial HA-IP experiment (data not shown) and because of its epidermal context as it is induced in stress and inflammatory responses as well as linked to keratinocyte proliferation and differentiation[269–272]. Moreover, gelsolin (GELS), a Ca^{2+}-dependent actin filament regulator, was chosen as a negative control due to the previous results of HA immunoprecipitation (Figure 21B)[273]. However, additional bands were observed in the purified fractions of all three proteins, suggesting potential copurification of interacting proteins and indeed, in the case of GELS, the unexpected signal was shown to be caused by bound actin (Figure 22C). Analogically, the unidentified signal in the FARSB purification could be assigned to FARSA which exhibits a molecular weight of around 58 kDa, whereas for S100A8 multiple bands of unknown origin were detected (Figure 22B). The resulting mixture of proteins in the purified fractions in combination with generally low protein concentrations may be the reasons for the ineffectiveness of MST measurements in predicting K_D values for *P4* binding. Thus, large-scale purification of the recombinant proteins from bacterial cells may yield more conclusive results. Furthermore, employment of additional methods such as electrophoretic mobility shift assays could also provide detailed information about binding affinities. When contemplating fluorescence shifts at the highest protein concentrations, vague differences were found between putative interactor and control pairings, weakly hinting at structure-based binding of *P4* to FARSB since both the sense and the antisense transcripts exhibited rather distinct shifts compared to the controls, as well as preferential binding at exon 5, while S100A8 also showed clearer shifts than corresponding controls (Figure 22D). However, with respect to the available data, this is purely speculative and requires proper experimental evidence.

7. Material

7.1 Antibodies, conjugates and beads

7.1.1 Antibodies and conjugates

Table 2: Utilized primary antibodies and conjugates

Name	Source	Dilution (Fixative)	Application	Supplier
Alexa Fluor 555 streptavidin conjugate	-	1:300 (PFA)	IF staining	Thermo Fisher Scientific, S21381
annexin V FITC-conjugated	-	1:25	Apoptosis FACS assay	ImmunoTools, 31490013
α-actin (I-19)	goat, polyclonal	1:200	WB	Santa Cruz Biotechnology, sc-1616
α-bromodeoxyuridine	rat, monoclonal BU1/75 (ICR1)	1:500 (PFA)	IF staining	Abcam, ab6326
α-collagen VII	rabbit, polyclonal	1:400 (dependent on diff. marker)	IF staining	Merck Millipore, 234192
α-filaggrin	mouse, monoclonal AKH1	1:50 (ethanol)	IF staining	Santa Cruz Biotechnology, sc-66192
α-HA.11 epitope	mouse, monoclonal 16B12	1:1000 (PFA), 1:100 for IP	IF staining, IP, WB	BioLegend, previous Covance MMS-101R
α-keratin 10	mouse, monoclonal DE-K10	1:400 (methanol)	IF staining	Thermo Fisher Scientific, MS-611-P
α-tubulin alpha	mouse, monoclonal DM1A	1:500 (PFA)	IF staining	Sigma-Aldrich, T9026

Table 3: Utilized secondary antibodies

Name	Source	Dilution	Application	Supplier
Alexa Fluor 488 goat α-mouse IgG	goat, polyclonal	1:300	IF staining	Thermo Fisher Scientific, A11001
Alexa Fluor 488 goat α-rabbit IgG	goat, polyclonal	1:300	IF staining	Thermo Fisher Scientific, A11008
Alexa Fluor 555 goat α-mouse IgG	goat, polyclonal	1:300	IF staining	Thermo Fisher Scientific, A21422
IRDye 680RD goat α-mouse IgG	goat, polyclonal	1:15000	WB	LI-COR Biosciences, 926-32220
IRDye 680RD donkey α-goat IgG	donkey, polyclonal	1:15000	WB	LI-COR Biosciences, 926-68074

7.1.2 Beads

Table 4: Utilized covalently coupled magnetic beads

Name	Application	Supplier
Dynabeads MyOne Streptavidin C1	Aptamer pulldown, CARPID, ChIRP-MS	Thermo Fisher Scientific, 65001
Dynabeads Protein G	IP	Thermo Fisher Scientific, 10004D
Pierce α-DYKDDDDK Magnetic Agarose	Immunopurification	Thermo Fisher Scientific, A36797

7.2 Buffers and solutions

All buffers and solutions were prepared in deionized water unless stated otherwise.

Table 5: Utilized buffers and solutions

Buffer/Solution	Composition	
10% APS	10% (w/v)	ammonium persulfate
Aptamer binding buffer	50 mM	HEPES/HCl pH 7.4
	100 mM	sodium chloride
	10 mM	magnesium chloride
	0.5% (v/v)	NP-40
Aptamer wash buffer	50 mM	HEPES/HCl pH 7.4
	250 mM	sodium chloride
	10 mM	magnesium chloride
	0.5% (v/v)	NP-40
	1 mM	AEBSF, added freshly
	1x	cOmplete protease inhibitor (Roche), added freshly
	100 U/mL	RiboLock RNase inhibitor (Thermo Fisher Scientific), added freshly
CARPID elution buffer 1	50 mM	Tris/HCl pH 8.0
	2 M	urea
	1 mM	dithiothreitol
	0.001%	trypsin
CARPID elution buffer 2	50 mM	Tris/HCl pH 8.0
	2 M	urea
	5 mM	iodoacetamide
CARPID lysis buffer	50 mM	Tris/HCl pH 7.4
	150 mM	sodium chloride
	1 mM	EDTA
	0.5% (v/v)	Triton X-100
	1 mM	AEBSF, added freshly
	1x	cOmplete protease inhibitor (Roche), added freshly
CARPID wash buffer	50 mM	Tris/HCl pH 7.4
	500 mM	sodium chloride
	1 mM	EDTA
	0.5% (v/v)	Triton X-100
	1 mM	AEBSF, added freshly
	1x	cOmplete protease inhibitor (Roche), added freshly

Buffer/Solution	Composition	
ChIRP-MS hybridization buffer	50 mM	Tris/HCl pH 7.0
	750 mM	sodium chloride
	15% (v/v)	formamide
	1 mM	EDTA
	1% (w/v)	SDS
	1 mM	AEBSF, added freshly
	1x	cOmplete protease inhibitor (Roche), added freshly
	100 U/mL	RiboLock RNase inhibitor (Thermo Fisher Scientific), added freshly
ChIRP-MS wash buffer	2x	SSC
	0.5% (w/v)	SDS
	1 mM	AEBSF, added freshly
	1x	cOmplete protease inhibitor (Roche), added freshly
Demasking buffer	10 mM	sodium citrate
		pH 6.0 with hydrochloric acid
	0.05% (v/v)	polysorbate 20
6x DNA loading dye	30% (v/v)	glycerol
	0.25% (w/v)	bromophenol blue
FACS binding buffer	140 mM	sodium chloride
	10 mM	HEPES
	2.5 mM	calcium chloride
		pH 7.4 with sodium hydroxide
FACS fixing buffer	70% (v/v)	methanol
		in PBS
FACS wash buffer	1% (v/v)	FBS
		in PBS
FLAG elution buffer	0.075% (w/v)	3x DYKDDDDK peptide (Thermo Fisher Scientific)
		in PBS
3.3x Folding buffer	333 mM	HEPES/NaOH pH 8.0
	333 mM	sodium chloride
	33 mM	magnesium chloride
Hoechst buffer	4 µg/mL	Hoechst 33342
		in PBS
IF blocking buffer	10% (v/v)	BCS
		in PBS
IF stopping buffer	100 mM	glycine
		in PBS
IF wash buffer	1% (v/v)	BCS
		in PBS
IP wash buffer	50 mM	Tris/HCl pH 7.5
	750 mM	sodium chloride
	10% (v/v)	glycerol
	5 µM	EDTA
	0.5% (v/v)	NP-40
	1 mM	AEBSF, added freshly
	1x	cOmplete protease inhibitor (Roche), added freshly
5x Laemmli buffer	300 mM	Tris/HCl pH 6.8
	62.5% (v/v)	glycerol
	10% (w/v)	SDS
	0.1% (w/v)	bromophenol blue
	10% (v/v)	β-mercaptoethanol, added freshly

Buffer/Solution	Composition	
LB medium	1% (w/v)	sodium chloride
	1% (w/v)	tryptone
	0.5% (w/v)	yeast extract
		pH 7.4 with sodium hydroxide, autoclaved
LB-Amp	0.01% (w/v)	ampicillin
		in LB medium
LB-Amp agar	1.5% (w/v)	agar
		in LB medium, autoclaved
	0.01% (w/v)	ampicillin
LDS elution buffer	50 mM	dithiothreitol
		4x NuPAGE LDS buffer (Thermo Fisher Scientific)
10x MOPS buffer	200 mM	MOPS
	50 mM	sodium acetate
	10 mM	EDTA
		pH 7.0 with sodium hydroxide
MS carbamidomethylation solution	50 mM	ammonium bicarbonate
	0.5% (w/v)	iodoacetamide
MS digestion solution	50 mM	ammonium bicarbonate
	0.002% (w/v)	trypsin
MS reduction solution	50 mM	ammonium bicarbonate
	0.1% (w/v)	dithiothreitol
MS wash solution 1/1	25 mM	ammonium bicarbonate
	50% (v/v)	acetonitrile
MS wash solution 3/1	37.5 mM	ammonium bicarbonate
	25% (v/v)	acetonitrile
MST binding buffer	0.01% (w/v)	poloxamer 407
		in PBS
PBS	140 mM	sodium chloride
	6.5 mM	disodium hydrogen phosphate
	2.7 mM	potassium chloride
	1.5 mM	potassium dihydrogen phosphate
		pH 7.4 with hydrochloric acid
PFA buffer	4% (w/v)	paraformaldehyde
		in PBS
Polysome fractionation lysis buffer	20 mM	Tris/HCl pH 7.5
	100 mM	sodium chloride
	10 mM	magnesium chloride
	0.01% (w/v)	cycloheximide
	0.4% (v/v)	NP-40
	1x	cOmplete protease inhibitor (Roche)
	100 U/mL	RiboLock RNase inhibitor (Thermo Fisher Scientific)
Protein lysis buffer	50 mM	Tris/HCl pH 7.5
	150 mM	sodium chloride
	5%	glycerol
	1 mM	EDTA
	1 mM	dithiothreitol, added freshly
	1 mM	AEBSF, added freshly
	1x	cOmplete protease inhibitor (Roche); added freshly
4x Resolving gel buffer	1.5 M	Tris
	0.4% (w/v)	SDS
		pH 8.8 with hydrochloric acid

Buffer/Solution	Composition	
2x RNA loading dye	45% (v/v)	formamide
	6% (v/v)	formaldehyde
	6% (v/v)	glycerol
	0.01% (w/v)	bromophenol blue
	1x	MOPS buffer
RNA running buffer	2%	formaldehyde
	1x	MOPS buffer
SDWB blocking buffer	5% (w/v)	powdered milk
		in TBS-T
2x SHAPE loading dye	95% (v/v)	formamide (deionized)
	20 mM	EDTA
	0.05% (w/v)	bromophenol blue
Silver stain developing solution	2% (w/v)	sodium carbonate
	0.04% (v/v)	formaldehyde
Silver stain fixing solution	50% (v/v)	ethanol
	5% (v/v)	acetic acid
Sodium borate buffer	100 mM	sodium borate
		pH 8.5 with sodium hydroxide
20x SSC	3 M	sodium chloride
	300 mM	sodium citrate
		pH 7.0 with hydrochloric acid
4x Stacking gel buffer	500 mM	Tris
	0.4% (w/v)	SDS
		pH 6.8 with hydrochloric acid
10% Sucrose gradient buffer	20 mM	Tris/HCl pH 7.5
	100 mM	sodium chloride
	5 mM	magnesium chloride
	0.005% (w/v)	cycloheximide
	10% (w/v)	sucrose
50% Sucrose gradient buffer	20 mM	Tris/HCl pH 7.5
	100 mM	sodium chloride
	5 mM	magnesium chloride
	0.005% (w/v)	cycloheximide
	50% (w/v)	sucrose
TAE	40 mM	Tris
	20 mM	acetic acid
	1 mM	EDTA
10x TBE	890 mM	Tris
	890 mM	boric acid
	20 mM	EDTA
TBS-T	10 mM	Tris/HCl pH 7.5
	150 mM	sodium chloride
	0.05% (v/v)	polysorbate 20
TFBI	100 mM	rubidium chloride
	50 mM	manganese chloride
	30 mM	potassium acetate
	10 mM	calcium chloride
		pH 5.8 with hydrochloric acid
	15% (v/v)	glycerol
		sterile filtered

Buffer/Solution	Composition	
TFBII	75 mM	calcium chloride
	10 mM	MOPS sodium salt
	10 mM	rubidium chloride
		pH 7.0 with hydrochloric acid
	15% (v/v)	glycerol
		sterile filtered
TGS	192 mM	glycine
	25 mM	Tris
	0.1% (w/v)	SDS
Towbin transfer buffer	192 mM	glycine
	25 mM	Tris
	20% (v/v)	methanol
YT++ medium	0.8% (w/v)	tryptone
	0.5% (w/v)	sodium chloride
	0.5% (w/v)	yeast extract
		pH 7.5 with sodium hydroxide, autoclaved
	20 mM	magnesium sulfate, added freshly
	10 mM	potassium chloride, added freshly

7.3 Chemicals, enzymes and peptides

Unless stated differently, chemicals, enzymes and peptides were purchased from Abcam (Cambridge, UK), Bio-Rad (Hercules, USA), Carl Roth (Karlsruhe, Germany), Jena Bioscience (Jena, Germany), Merck (Darmstadt, Germany), New England Biolabs (Ipswich, USA), Promega (Fitchburg, USA), Roche (Basel, Switzerland), Sakura Finetek (Torrance, USA), Sigma-Aldrich (St. Louis, USA), Thermo Fisher Scientific (Waltham, USA) and VWR International (Radnor, USA).

7.4 Commercial kits

Commercial kits were used according to their respective manuals unless stated otherwise.

Table 6: Utilized commercially available kits

Name	Supplier	Catalog Number
Amersham MicroSpin G-25 Columns	Cytiva (Marlborough, USA)	27532501
Cell Proliferation Kit I (MTT)	Roche (Basel, Switzerland)	11465007001
Human Keratinocyte Nucleofector Kit	Lonza (Basel, Switzerland)	VPD-1002
iScript cDNA Synthesis Kit	Bio-Rad (Hercules, USA)	1708891
Lipofectamine 3000 Transfection Reagent	Thermo Fisher Scientific (Waltham, USA)	L3000008
NucleoBond Xtra Midi	Macherey-Nagel (Düren, Germany)	740410
NucleoBond Xtra Midi EF	Macherey-Nagel (Düren, Germany)	740420
NucleoSpin Gel and PCR Clean-up	Macherey-Nagel (Düren, Germany)	740609

Name	Supplier	Catalog Number
NucleoSpin Plasmid Kit	Macherey-Nagel (Düren, Germany)	740588
QIAshredder	Qiagen (Venlo, Netherlands)	79656
RevertAid H Minus First Strand cDNA Synthesis Kit	Thermo Fisher Scientific (Waltham, USA)	K1631
RNeasy Plus Mini Kit	Qiagen (Venlo, Netherlands)	74136
Takyon No ROX SYBR 2X MasterMix blue dTTP	Eurogentec (Seraing, Belgium)	UF-NSMT-B0701
USB Thermo Sequenase Cycle Sequencing Kit	Affymetrix (Santa Clara, USA)	78500
Vivaspin 500 Centrifugal Concentrators, MWCO 10 kDa	Sartorius (Göttingen, Germany)	VS0101
Vivaspin 500 Centrifugal Concentrators, MWCO 30 kDa	Sartorius (Göttingen, Germany)	VS0121

7.5 Consumables

Consumables were, if not stated otherwise, obtained from Bio-Rad (Hercules, USA), Carl Roth (Karlsruhe, Germany), Corning (Corning, USA), Eppendorf (Hamburg, Germany), Eurogentec (Seraing, Belgium), MP Biomedicals (Irvine, USA), NanoTemper Technologies (Munich, Germany), PluriSelect (Leipzig, Germany), Sakura Finetek (Torrance, USA), Sarstedt (Nümbrecht, Germany), Sartorius (Göttingen, Germany), Sigma-Aldrich (St. Louis, USA), Thermo Fisher Scientific (Waltham, USA) and VWR International (Radnor, USA).

7.6 Eukaryotic cell cultivation

Dermis for organotypic cultures was prepared from frozen human skin obtained from Biopredic International (Saint-Grégoire, France). Utilized primary cells, cell lines, media components and compositions are listed below.

Table 7: Utilized eukaryotic primary cells and cell lines

Name	Details	Supplier
HEK293T cells	gift from the Meister group	University of Regensburg (Regensburg, Germany)
Jurkat E6.1 cell line	from ECACC, catalog number 88042803	Sigma-Aldrich (St. Louis, USA)
Normal Human Epidermal Keratinocytes (NHEK), juvenile foreskin, pooled	lot numbers 459Z009 and 466Z002	PromoCell (Heidelberg, Germany)
NTERT1 cells	gift from the van den Boogard group	Radboud University (Nijmegen, Netherlands)
NTERTG2 cells	gift from the van den Boogard group	Radboud University (Nijmegen, Netherlands)

Table 8: Utilized reagents for eukaryotic cell culture

Name	Supplier	Catalog Number
3,3',5'-Triiodo-L-thyronine	Sigma-Aldrich (St. Louis, USA)	T0281
Adenine hydrochloride hydrate	Sigma-Aldrich (St. Louis, USA)	A9795
Amikacin disulfate	Sigma-Aldrich (St. Louis, USA)	A1774
Antibiotic-Antimycotic (100x)	Thermo Fisher Scientific (Waltham, USA)	15240062
Biotin	Sigma-Aldrich (St. Louis, USA)	B4501
Bovine Pituitary Extract	Thermo Fisher Scientific (Waltham, USA)	13028014
BrdU (5-bromo-2'-deoxyuridine)	Abcam (Cambridge, UK)	ab142567
Calcium chloride	Carl Roth (Karlsruhe, Germany)	CN93.1
Cholera Toxin from *Vibrio cholerae*	Sigma-Aldrich (St. Louis, USA)	C8052
Dimethyl sulphoxide	Carl Roth (Karlsruhe, Germany)	A994.2
di-Sodium hydrogen phosphate dihydrate	Carl Roth (Karlsruhe, Germany)	4984.1
DMEM, high glucose, pyruvate	Thermo Fisher Scientific (Waltham, USA)	41966029
DPBS, no calcium, no magnesium	Thermo Fisher Scientific (Waltham, USA)	14190094
ECM Gel from Engelbreth-Holm-Swarm murine sarcoma	Sigma-Aldrich (St. Louis, USA)	E1270
Ethanol	Carl Roth (Karlsruhe, Germany)	9065.1
Ethylenediamine tetraacetic acid disodium salt dihydrate	Carl Roth (Karlsruhe, Germany)	8043.1
Fetal Bovine Serum, qualified, Brazil	Thermo Fisher Scientific (Waltham, USA)	10270106
Ham's F12 medium with L-glutamine	Lonza (Basel, Switzerland)	BE12-615F
hEGF	Sigma-Aldrich (St. Louis, USA)	E9644
HEPES	Carl Roth (Karlsruhe, Germany)	9105.3
Hexadimethrine bromide	Sigma-Aldrich (St. Louis, USA)	107689
holo-Transferrin bovine	Sigma-Aldrich (St. Louis, USA)	T1283
holo-Transferrin human	Sigma-Aldrich (St. Louis, USA)	T0665
Human Keratinocyte Growth Supplement	Thermo Fisher Scientific (Waltham, USA)	S0015
HyClone Calf Serum, U.S. origin	Cytiva (Marlborough, USA)	SH30073.04
HyClone Characterized Fetal Bovine Serum, U.S. Origin	Cytiva (Marlborough, USA)	SH30071.03
Hydrocortisone-Water Soluble	Sigma-Aldrich (St. Louis, USA)	H0396
Insulin-like Growth Factor-I human	Sigma-Aldrich (St. Louis, USA)	I3769
Insulin solution human	Sigma-Aldrich (St. Louis, USA)	I9278
Keratinocyte-SFM Supplement	Thermo Fisher Scientific (Waltham, USA)	37000015
Keratinocyte-SFM, with L-glutamine	Thermo Fisher Scientific (Waltham, USA)	17005059
Matrigel Basement Membrane Matrix, LDEV-free	Corning (Corning, USA)	354234
Medium 154	Thermo Fisher Scientific (Waltham, USA)	M154500
Mitomycin C from *Streptomyces caespitosus*	Sigma-Aldrich (St. Louis, USA)	M4287
Opti-MEM I Reduced Serum Medium	Thermo Fisher Scientific (Waltham, USA)	31985047
Penicillin-Streptomycin (10000 U/mL)	Thermo Fisher Scientific (Waltham, USA)	15140122
Puromycin dihydrochloride	Carl Roth (Karlsruhe, Germany)	0240.3
RPMI 1640 Medium	Thermo Fisher Scientific (Waltham, USA)	21875034
Sodium azide	Carl Roth (Karlsruhe, Germany)	K305.1
Sodium chloride	Carl Roth (Karlsruhe, Germany)	0601.1
Sodium hydroxide	Carl Roth (Karlsruhe, Germany)	9356.1
Trypsin-EDTA (0.05%) phenol red	Thermo Fisher Scientific (Waltham, USA)	25300054
Vancomycin hydrochloride	Carl Roth (Karlsruhe, Germany)	0242.3

Table 9: Composition of utilized cell culture media and solutions

Medium/Solution	Composition	
50:50 medium	49.4% (v/v)	Keratinocyte-SFM
	49.4% (v/v)	Medium 154
	0.494x	Antibiotic-Antimycotic
	one of both	
	(0.494% (v/v)	Human Keratinocyte Growth Supplement)
	(0.142% (v/v)	self-made keratinocyte supplement)
	either	
	(1	Keratinocyte-SFM Supplement)
	or both	
	(24,7 µg/mL	bovine pituitary extract)
	(0.025% (v/v)	EGF stock solution)
Adenine stock solution	10 mM	Adenine hydrochloride hydrate in DMEM, pH 7.5 with sodium hydroxide, sterile filtered
Basic buffer	200 mM	sodium chloride
	3 mM	sodium azide
	1 mM	EDTA
Biotin stock solution	1 mM	biotin sterile filtered
BrdU stock solution	50 mM	BrdU sterile filtered
Calcium chloride stock solution 1	2 M	calcium chloride sterile filtered
Calcium chloride stock solution 2	120 mM	calcium chloride sterile filtered
Cholera toxin stock solution	0.1% (w/v)	cholera toxin in basic buffer, sterile filtered
Cycloheximide stock solution	2% (w/v)	cycloheximide sterile filtered
DMEM+BCS	10% (v/v)	BCS
	100 U/mL	Penicillin-Streptomycin in DMEM
DMEM+FBS	10% (v/v)	FBS (Thermo Fisher Scientific)
	100 U/mL	Penicillin-Streptomycin in DMEM
DPBS+2xA/A	2x	Antibiotic-Antimycotic in DPBS
EGF stock solution	0.001% (w/v)	hEGF sterile filtered
2x HEPES buffer	274 mM	sodium chloride
	54.6 mM	HEPES
	1.5 mM	disodium hydrogen phosphate
		pH 7.1 with sodium hydroxide, sterile filtered
HEPES stock solution	1 M	HEPES sterile filtered
Hydrocortisone stock solution	4% (v/v)	ethanol
	0.02% (w/v)	hydrocortisone
		sterile filtered

Medium/Solution	Composition	
Keratinocyte-SFM+	0.5x	Antibiotic-Antimycotic
	either	
	(1	Keratinocyte-SFM Supplement)
	or both	
	(25 µg/mL	bovine pituitary extract)
	(0.025% (v/v)	EGF stock solution)
		in Keratinocyte-SFM
KGM	22% (v/v)	Ham's F12
	10% (v/v)	FBS (Cytiva)
	1x	Antibiotic-Antimycotic
	1% (v/v)	Vancomycin/Amikacin
	0.2% (v/v)	adenine stock solution
	0.2% (v/v)	hydrocortisone stock solution
	0.1% (v/v)	cholera toxin stock solution
	0.1% (v/v)	EGF stock solution
	0.1% (v/v)	T/T_3 stock solution
	5 µg/mL	insulin
		in DMEM
Mitomycin C stock solution	0.05% (w/v)	mitomycin C
		sterile filtered
Polybrene stock solution	0.1% (w/v)	hexadimethrine bromide
		in DPBS, sterile filtered
Puromycin stock solution	0.1% (w/v)	puromycin dihydrochloride
		sterile filtered
RPMI+	10% (v/v)	FBS (Cytiva)
	1% (v/v)	HEPES stock solution
	100 U/mL	Penicillin-Streptomycin
		in RPMI 1640
Self-made keratinocyte supplement	69.4% (v/v)	bovine pituitary extract
	3.47 µg/mL	insulin-like growth factor-I
	62.5 µg/mL	hydrocortisone
	0.174% (w/v)	holo-transferrin bovine
	69.4 ng/mL	hEGF
T/T_3 stock solution	0.5%	holo-transferrin human
	100 µM	3,3',5'-triiodo-L-thyronine
		in DPBS, sterile filtered
Vancomycin/Amikacin	0.6% (w/v)	amikacin
	0.4% (w/v)	vancomycin
		sterile filtered

7.7 Instruments

General laboratory instruments were acquired from Bio-Rad (Hercules, USA), Eppendorf (Hamburg, Germany), NeoLab (Heidelberg, Germany), Sartorius (Göttingen, Germany) and Thermo Fisher Scientific (Waltham, USA). Specific devices are listed in the table below.

Table 10: Utilized laboratory instruments

Name	Supplier
74900-00 Single Syringe Pump	Cole-Parmer (Vernon Hills, USA)
All-in-One Fluorescence Microscope BZ-X810	Keyence (Osaka, Japan)
Alpha 1-4 LDplus	Martin Christ Gefriertrocknungsanlagen (Osterode am Harz, Germany)
Amersham Ultrospec 3300 pro	GE Healthcare (Chicago, USA)
Axio Imager.D2m	Carl Zeiss (Oberkochen, Germany)
BD FACSCanto-II Flow Cytometer	BD Biosciences (San José, USA)
BioLogic LP System	Bio-Rad (Hercules, USA)
CASY Cell Counter	OMNI Life Science (Bremen, Germany)
Centrifuge 5424 R	Eppendorf (Hamburg, Germany)
Centrifuge 5810	Eppendorf (Hamburg, Germany)
Concentrator 5301	Eppendorf (Hamburg, Germany)
Cryostat Microm HM 500 OM	Thermo Fisher Scientific (Waltham, USA)
D1008 Palm Micro Centrifuge	DLAB Scientific (Beijing, China)
Electrophoresis Chamber Mini horizontal	NeoLab (Heidelberg, Germany)
Electroporation Device Nucleofector II	Lonza (Basel, Switzerland)
EPS 500/400 Electrophoresis Power Supply	Pharmacia (Uppsala, Sweden)
EV202 Power Supply	Consort (Turnhout, Belgium)
FastPrep-24 Classic Instrument	MP Biomedicals (Irvine, USA)
Gradient Master IP Model 107	BioComp Instruments (Fredericton, Canada)
Heracell 240i CO 2 Incubator	Thermo Fisher Scientific (Waltham, USA)
Heraeus T6060	Thermo Fisher Scientific (Waltham, USA)
Heraeus Megafuge 40R	Thermo Fisher Scientific (Waltham, USA)
Heraeus Multifuge 1S	Thermo Fisher Scientific (Waltham, USA)
Herasafe KS	Thermo Fisher Scientific (Waltham, USA)
Incucyte SX5 Live Cell Imaging Instrument	Sartorius (Göttingen, Germany)
Inverted microscope Axiovert 200 M	Carl Zeiss (Oberkochen, Germany)
Inverted microscope Diavert	Leitz (Wetzlar, Germany)
Mastercycler nexus	Eppendorf (Hamburg, Germany)
MaXis plus UHR-QTOF	Bruker (Billerica, USA)
MilliQ Q-Pod	Merck (Darmstadt, Germany)
Mini-PROTEAN Tetra Cell	Bio-Rad (Hercules, USA)
Mithras LB 940	Berthold Technologies (Bad Wildbad, Germany)
Mixer 5432	Eppendorf (Hamburg, Germany)
Monolith NT.115 Blue/Red	NanoTemper Technologies (Munich, Germany)
NanoDrop 1000 Spectrophotometer	Thermo Fisher Scientific (Waltham, USA)
New Brunswick Innova 44 Shaker	Eppendorf (Hamburg, Germany)
Odyssey Classic Imaging System	LI-COR Biosciences (Lincoln, USA)
Optima LE-80K	Beckman Coulter (Brea, USA)
Polymax 1040	Heidolph Instruments (Schwabach, Germany)
PowerPac HC High-Current Power Supply	Bio-Rad (Hercules, USA)
PURA 22 Water Bath	Julabo (Seelbach, Germany)
Q Exactive Orbitrap	Thermo Fisher Scientific (Waltham, USA)
Real-Time PCR Cycler CFX96	Bio-Rad (Hercules, USA)
RM2265 Automated Microtome	Leica Biosystems (Wetzlar, Germany)
Thermomixer comfort	Eppendorf (Hamburg, Germany)
Trans-Blot SD Semi-dry transfer cell	Bio-Rad (Hercules, USA)
Transilluminator Quantum ST4	Peqlab (Erlangen, Germany)

Name	Supplier
UltiMate 3000 RSLCnano System with Acclaim PepMap100 C18 Nano-Trap column and Acclaim PepMap100 C18 column	Thermo Fisher Scientific (Waltham, USA)
Vortex-Genie 2	Scientific Industries (Bohemia, USA)
XCell SureLock Mini-Cell Electrophoresis System	Thermo Fisher Scientific (Waltham, USA)
Xevo TQ-S micro	Waters Corporation (Milford, USA)

7.8 Oligonucleotides

DNA oligonucleotides were ordered from Sigma-Aldrich (St. Louis, USA), siRNA Pools (mixture of 11-30 different siRNAs per target, exact sequences are available from siTools upon request) were designed and ordered from siTools (Munich, Germany).

Table 11: Utilized sequencing primers

Name	Sequence (5' to 3')
ANXA6_seq850	TAGTGAGTTGGACATGCTCG
BASU_R	TTCGGTAAGTATCCCTACTG
CMV-F	CGCAAATGGGCGGTAGGCGTG
dCasRx_R2	TAGCTTCATCGTAGTAGAGG
dCasRx_R3	AAGTTTCGTAGTACCTGTCG
dCasRx_R4	GTTGGAAGTAGGAATTGACC
FARSB_seq850	CGGGAACTGACTTTACTAAGG
GELS_seq_F1	AGTGCACGTGTCTGAGGAGG
GFP_R2	AAGTCGTGCTGCTTCATGTG
IRES_R	ATATAGACAAACGCACACCG
PGKseq	TGTTCCGCATTCTGCAAGCC
SP6	ATTTAGGTGACACTATAG
T7	TAATACGACTCACTATAGGG
U6 Seq F	GACTATCATATGCTTACCGT
VP5-F	CGAAATTAATACGACTCACTATAG
VP5-R	CCCAACAGCTGGCCCTCGCAGA

Table 12: Utilized RT-qPCR primers

Name	Sequence (5' to 3')
18s_F	GCAATTATTCCCCATGAACG
18s_R	GGCCTCACTAAACCATCCAA
FLG_F	AAAGAGCTGAAGGAACTTCTGG
FLG_R	AACCATATCTGGGTCATCTGG
GADD45 RT fwd	CCATGCAGGAAGGAAAACTATG
GADD45 RT rev	CCCAAACTATGGCTGCACACT
KRT1_F	TGAGCTGAATCGTGTGATCC
KRT1_R	CCAGGTCATTCAGCTTGTTC
KRT10_F	GCAAATTGAGAGCCTGACTG
KRT10_R	CAGTGGACACATTTCGAAGG
L32_F	AGGCATTGACAACAGGGTTC

Name	Sequence (5' to 3')
L32_R	GTTGCACATCAGCAGCACTT
T7_LacZt1_F	CGTTAATACGACTCACTATAGGA TGATAGATCCCGTCGTTTT
LacZ-HincII_R2	ACCCAGGGTTTTCCCAGTC
LOR_F	CTCTGTCTGCGGCTACTCTG
LOR_R	CACGAGGTCTGAGTGACCTG
mCherry_F1	AGCTGAAGGTGACCAAGGGT
mCherry_R1	TCAAGTAGTCGGGGATGTCG
NEAT1_fwd	TTGCATAGCTGAGCGAGCCC
NEAT1_rev	CTGCTGCGGCCTATTCCTCC
P4_L2	GTCCAGCCCTTGCTTGGGAG
P4_R2	GTGGCTAAGACCCAAGGCCC
P4-g1_F1	TGAACCGACACCATACAGAGG
P4-g1_R1	ATGACGTTTAGCTCTGGGGC
P4-g2_F1	TTGTGAAGGTGGGGATGTTTG
P4-g2_R1	CAAGAAGCAGCTCTGACGTGAA
qP4_E1-S_F	CAGCCAACAGCTATCTGCAGC
qP4_E1-S_R	CCTGTTCTGGAAAGAGAAAGC
qP4_E2-S_F	CACCATACAGAGGTATTTG
qP4_E2-S_R	CCTGTTGTATTAGTCTGCAC
qP4_E3-S_F	CTCAGAATTGCAGAGAGATTG
qP4_E3-S_R	CTCCAACCTTCCGGAAGAG
qP4_E4-S_F	ACGTCAGAGCTGCTTCTTGT
qP4_E4-S_R	GCCCCCTTAACAGAGCCTTC
qP4_ins-S_F	GCGGTAAAGAGAAGAACAGAG
qP4_ins-S_R	CCACTGGGTGGAGATGGAAT

Table 13: Utilized primers for cloning PCRs

Name	Sequence (5' to 3')
AgeI-3xHA_R	ATTTATACCGGTTCAGGCGTAATCGGGCACGT
AgeI-CasRx_GFP_R	GACTACACCGGTTTACTTGTACAGCTCGTCCA
AgeI-P4new_R	GGCAGAACCGGTTAGGGATTAAAATGTCAGCT
AscI-CETN2-Ctr_R	ATTATAGGCGCGCCATAGAGGCTGGTCTTTTTCA
AscI-FARSB_R	CAAGACGGCGCGCCCAAAAAGGGTCCAACATTGA
AscI-GELS-Ctr_R	ATTATAGGCGCGCCGGCAGCCAGCTCAGCCATGG
AscI-NHP2-Ctr_R	ATTATAGGCGCGCCTAGGGGTAGGGGCAGGGACT
AscI-S100A8-Ctr_R	ATTATAGGCGCGCCCTCTTTGTGGCTTTCTTCAT
AscI-STAU2-Ctr_R	ATTATAGGCGCGCCGACGGCCGAGTTTGATTTCT
BamHI-CasRxgRNA_R	GACTACGGATCCAAAAAAAGTTTCAAACCCCGACCAGTT
BsmBI-CasRxgRNA_F	ATTTATACACCTGAGACGAACCCCTACCAACTGGTCGG
FseI-FARSB_F	ATTATAGGCCGGCCGCCACCATGCCGACTGTCAG
FseI-GELS_F	ATATTTGGCCGGCCGCCACCATGGTGGTGGAACACCCCGA
FseI-S100A8_F	ATATTTGGCCGGCCGCCACCATGTTGACCGAGCTGGAGAA
HincII-gRNA2--1_R	GGCGCGGTAGGGGTTAACCTTGAAGA
HincII-gRNA2--2_F1	GGCGCGTTCAAGGTTAACCCCTACCA
HindIII-gRNA1--1_R	GGCGCGTCTTCAAACAGAAGCTTACC
HindIII-gRNA1--2_F	GGCGCGAACGGTAAGCTTCTGTTTGA
HpaI-CARPID_R	GACTCCGTTAACTTACTTGTACAGCTCGTCCA

Name	Sequence (5' to 3')
SpeI-ANXA6_F	ACTATTACTAGTGCCACCATGGCCAAACCAGC
SpeI-FARSB_F	ACTTATACTAGTGCCACCATGCCGACTGTCAG
SpeI-dCasRx-BASU_F	GACTCCACTAGTATGAGCCCCAAGAAGAAGAG
SpeI-KS-CETN2_F	ATTGCTACTAGTGCCACCATGGCCTCCAACTTTAAGAA
SpeI-KS-MAL-F/H_F	ATTTATACTAGTGCCACCATGGCCCCCGCAGC
SpeI-KS-NHP2_F	CACGCCACTAGTGCCACCATGACCAAAATAAAGGCAG
SpeI-KS-S100A8_F	ATTGCTACTAGTGCCACCATGTCTCTTGTCAGCTGTCT
SpeI-KS-STAU2_F	CACAACACTAGTGCCACCATGGCAAACCCAAAAGAGAA
SpeI-P4new_F	GACTACACTAGTTGCCTCAGCCAACAGCTATC

Table 14: Utilized primers for IVT-PCRs

Name	Sequence (5' to 3')
Aptamer_LacZt1_R	CATGGCCCGGCCCGCGACTATCTTACGCACTTGCATGATTCTGG TCGGTCCCATGGATCCGCTCGTGACGGTTAACGCCT
Aptamer_mCherry_R	CATGGCCCGGCCCGCGACTATCTTACGCACTTGCATGATTCTGG TCGGTCCCATGGATCCTTACTTGTACAGCTCGTCCA
Aptamer_P4_R	CATGGCCCGGCCCGCGACTATCTTACGCACTTGCATGATTCTGG TCGGTCCCATGGATCCTAGGGATTAAAATGTCAGCT
IVT-P4_R	TAGGGATTAAAATGTCAGCTTTATTGCTAG
IVT-P4AS_R	TGCCTCAGCCAACAGCTATCTGCA
P4Exon12T7-R	CCTGTTGTATTAGTCTGCACTTACTGGTAA
P4Exon34T7-F	CGTTAATACGACTCACTATAGGCGGTAAAGAGAAGAACAGAG
P4Exon34T7-R	CATCCCCACCTTCACAAAATCTTCTCCAAC
P4Exon51T7-F	CGTTAATACGACTCACTATAGGTTTGATTTGAACCTTGAAGA
P4Exon51T7-R	GGGGAGGGGAGATAGTTGCCCCCTTAA
P4Exon52T7-F	CGTTAATACGACTCACTATAGGATTCTCCTATCAGCCCATAA
P4Exon52T7-R	ATGCTGCTTGCAGTCAGGTCAGTCC
P4Exon53T7-F	CGTTAATACGACTCACTATAGGGTTCTCTGTCTGCTCCTGCC
P4Exon53T7-R	TAGGGATTAAAATGTCAGCTTTATTGCTAGTCCAGATGGACTGG
scr44T7-F	CGTTAATACGACTCACTATAGGCTTCTCGACAGCATTTCTTT
scr44T7-R	GGAGAGATAGGGACTTATTCCCGTACTGATACCTACAATC
scr49T7-F	CGTTAATACGACTCACTATAGGCGACGTGGAGCTTAACTCTC
scr49T7-R	GATCCTCCGAGTGTGGTACATACGCCAGC
T7_LacZt1_F	CGTTAATACGACTCACTATAGGATGATAGATCCCGTCGTTTT
T7_mCherry_F	CGTTAATACGACTCACTATAGGATGGTGAGCAAGGGCGAGGA
T7_P4_F	CGTTAATACGACTCACTATAGGTGCCTCAGCCAACAGCTATC
T7_P4AS_F	CGTTAATACGACTCACTATAGGTAGGGATTAAAATGTCAGCT

Table 15: Utilized oligonucleotides for PCR template generation

Name	Sequence (5' to 3')
P4_gRNA1--1_F	AACCCCTACCAACTGGTCGGGGTTTGAAACGGTAAGCTTCTGTTT
P4_gRNA1--1_R	AAACAGAAGCTTACCGTTTCAAACCCCGACCAGTTGGTAGGGGTT
P4_gRNA1--2_F	GGTAAGCTTCTGTTTGAAGAAAGGATTCCGAACCCCTACCAACTGGTCGG GGTTTGAAACTCTCTGTTCTTCTCTTTACCGCCTGTTGTAAACCCCTACC AACTGGTCGGGGTTTGAAAC

Name	Sequence (5' to 3')
P4_gRNA1--2_R	GTTTCAAACCCCGACCAGTTGGTAGGGGTTTACAACAGGCGGTAAAGAGA AGAACAGAGAGTTTCAAACCCCGACCAGTTGGTAGGGGTTCGGAATCCTT TCTTCAAACAGAAGCTTACC
P4_gRNA2--1_F	AACCCCTACCAACTGGTCGGGGTTTGAAACTTCTTGGGTCTCTGCTTGTT CTTCAAGGTTAACCCCTAC
P4_gRNA2--1_R	GTAGGGGTTAACCTTGAAGAACAAGCAGAGACCCAAGAAGTTTCAAACCC CGACCAGTTGGTAGGGGTT
P4_gRNA2--2_F	TTCAAGGTTAACCCCTACCAACTGGTCGGGGTTTGAAACTTTGCATGCCC CACCTCGTTCATGCTATTTAACCCCTACCAACTGGTCGGGGTTTGAAAC
P4_gRNA2--2_R	GTTTCAAACCCCGACCAGTTGGTAGGGGTTAAATAGCATGAACGAGGTGG GGCATGCAAAGTTTCAAACCCCGACCAGTTGGTAGGGGTTAACCTTGAA
scr44FL-F	CTTCTCGACAGCATTTCTTTTTTCAGAATGATATGCACACAAGTGCTAAT CGAGTACACACGACGTTCTCCCCTGCAATCAAGTGGGGGTTCAGATTACT TCATACCAGTCTTTTAGTGC
scr44FL-R	GGAGAGATAGGGACTTATTCCCGTACTGATACCTACAATCGTTACATGTC ATGCGGAATCAATTACAATTCGCCTCGATGTTAACGACGTCCGCACTAAA AGACTGGTATGAAGTAATCT
scr49FL-F	CGACGTGGAGCTTAACTCTCCTGAGTCGGGGCTCATATACGGGAATAGCT CTATGGAATTAAGTTGGAAAAGAATGCAATCCATGCGGTAGCACTTAGGA GCCGCTGATACCTACCATCA
scr49FL-R	GATCCTCCGAGTGTGGTACATACGCCAGCCGTCATTGCGTTCTTAAGGCT CTGGGTTCATTGATAACTTTCTTAGGCGCTTAGAACTCTCCGTGATGGTA GGTATCAGCGGCTCCTAAGT

Table 16: Utilized primers for SHAPE

Name	Sequence (5' to 3')
o-p4 E1 R	CTGGAAAGAGAAAGCTGAGGA
o-p4 E2 R	CCTGTTGTATTAGTCTGCACT
o-p4 E3 R	TTCTGAGAACCCACTGGGTG
o-p4 E4 R	CATGCCCCACCTCGTTCATG
o-p4 E5 R1	TAGGGATTAAAATGTCAGCT
o-p4 E5 R2	GATACCCTTTTCCCAACGAC

Table 17: Utilized ChIRP probes

Name	Sequence (5' to 3')
LacZ_ChIRP_1	TGCAAGGCGATTAAGTTGGG
LacZ_ChIRP_2	GAGACGTCACGGAAAATGCC
LacZ_ChIRP_3	TAACGCCTCGAATCAGCAAC
LacZ_ChIRP_4	GGATCGACAGATTTGATCCA
LacZ_ChIRP_5	GTTGCCGTTTTCATCATATT
LacZ_ChIRP_6	AATTGCCAACGCTTATTACC
LacZ_ChIRP_7	GTCAAAACAGGCGGCAGTAA
LacZ_ChIRP_8	ACACCAGACCAACTGGTAAT
lncP4_ChIRP_1	AGATAGCTGTTGGCTGAGG
lncP4_ChIRP_2	CTGTTGTATTAGTCTGCAC
lncP4_ChIRP_3	CCACTGGGTGGAGATGGAA
lncP4_ChIRP_4	AGAAGCAGCTCTGACGTGA
lncP4_ChIRP_5	GAGCCTTCAATTCATTCA

Name	Sequence (5' to 3')
lncP4_ChIRP_6_o3	GATAGTTGCCCCCTTAAC
lncP4_ChIRP_7	GGTTGTCAGTTCCTGTTTTA
lncP4_ChIRP_8	CTTCCCAATTCTTCCAAGA
scram_ChIRP_1	CATCCATCTAATTGGGTCTT
scram_ChIRP_2	AGAGAGTCCGAGACTATGTT
scram_ChIRP_3	GTTCACTCGTTTGTGCGTTC
scram_ChIRP_4	ATTCGCGTGCCTAACGTTAC
scram_ChIRP_5	TGCTACGGTTGCTGACTGAC
scram_ChIRP_6	ATCTGGTGTCCTAAAGAGTG
scram_ChIRP_7	GAATCTGCTGGTCATATACC

7.9 Plasmids

Table 18: Utilized plasmids

Name	Properties	Origin
CARPID dCasRx-BASU	Viral transfer vector containing the NLS-dCasRx-NLS-HA-BASU-T2A-EGFP cassette	Addgene, #153303
pcDNA3.1-ANXA6 (Isoform 3)-3xHA	Mammalian expression vector containing the KS-ANXA6-3xHA cassette	AG Kretz/Manuel Schidlmeier (supervised student, University of Regensburg)
pcDNA3.1-FARSB-3xHA	Mammalian expression vector containing the KS-FARSB-3xHA cassette	AG Kretz/Manuel Schidlmeier (University of Regensburg)
pcDNA3.1_KZ_GFP-3xHA	Mammalian expression vector containing the KS-GFP-3xHA cassette	AG Kretz/Christian Ziegler (University of Regensburg)
pCMV dR8.91	Packaging plasmid for generation of lentiviral particles, encodes the viral gag, rev, tat and pol proteins under control of the CMV promoter	gift from the Khavari group (Stanford, USA)
pLARTA-LacZ	Lentiviral transfer vector containing the *LacZ* sequence under control of the hPGK promoter, flanked by LTR sequences for stable genomic integration	AG Kretz/Johannes Graf (University of Regensburg)
pLARTA-P4_new	Lentiviral transfer vector containing the full-length *P4* sequence under control of the hPGK promoter, flanked by LTR sequences for stable genomic integration	AG Kretz/Manuel Schidlmeier (University of Regensburg)
pLEX-ANXA6 (Isoform 3)-3xHA	Lentiviral transfer vector containing the KS-ANXA6-3xHA cassette under control of the CMV promoter, containing a puromycin resistance cassette	this work
pLEX-CasRx-EGFP	Lentiviral transfer vector containing the NLS-CasRx-NLS-HA-T2A-EGFP cassette under control of the CMV promoter, containing a puromycin resistance cassette	this work
pLEX-CETN2-F/H	Lentiviral transfer vector containing the KS-CETN2-F/H cassette under control of the CMV promoter, containing a puromycin resistance cassette	this work

Name	Properties	Origin
pLEX-dCasRx-BASU	Lentiviral transfer vector containing the NLS-dCasRx-NLS-HA-BASU-T2A-EGFP cassette under control of the CMV promoter, containing a puromycin resistance cassette	this work
pLEX-FARSB-3xHA	Lentiviral transfer vector containing the KS-FARSB-3xHA cassette under control of the CMV promoter, containing a puromycin resistance cassette	this work
pLEX_FLAG HA_GFP	Lentiviral transfer vector containing the F/H-GFP cassette under control of the CMV promoter, containing a puromycin resistance cassette	AG Kretz/Christian Ziegler (University of Regensburg)
pLEX-GELS-F/H	Lentiviral transfer vector containing the KS-GELS-F/H cassette under control of the CMV promoter, containing a puromycin resistance cassette	AG Kretz/Kira Mangold (supervised student, University of Regensburg)
pLEX-LY-IRES-Puro N3	Lentiviral transfer vector containing the Luciferase-YFP cassette under control of the CMV promoter, containing a puromycin resistance cassette	gift from the Khavari group (Stanford, USA)
pLEX-MAL-F/H	Lentiviral transfer vector containing the KS-MAL-F/H cassette under control of the CMV promoter, containing a puromycin resistance cassette	AG Kretz/Manuel Schidlmeier (University of Regensburg)
pLEX_msGFP2 N3	Lentiviral transfer vector containing the KS-msGFP2 cassette under control of the CMV promoter	AG Kretz/Daniela Strauß (University of Regensburg)
pLEX-NHP2-F/H	Lentiviral transfer vector containing the KS-NHP2-F/H cassette under control of the CMV promoter, containing a puromycin resistance cassette	this work
pLEX-P4new	Lentiviral transfer vector containing the full-length *P4* sequence under control of the CMV promoter, containing a puromycin resistance cassette	this work
pLEX-S100A8-F/H	Lentiviral transfer vector containing the KS-S100A8-F/H cassette under control of the CMV promoter, containing a puromycin resistance cassette	this work
pLEX-STAU2-F/H	Lentiviral transfer vector containing the KS-STAU2-F/H cassette under control of the CMV promoter, containing a puromycin resistance cassette	this work
pLEX-TPM4-F/H	Lentiviral transfer vector containing the KS-TPM4-F/H cassette under control of the CMV promoter, containing a puromycin resistance cassette	AG Kretz/Kira Mangold (University of Regensburg)
pUC-MDG	Envelope plasmid for generation of lentiviral particles, encodes the viral VSV-G envelope protein under control of the CMV promoter	gift from the Khavari group (Stanford, USA)
pXR001: EF1a-CasRx-2A-EGFP	Viral transfer vector containing the NLS-CasRx-NLS-HA-T2A-EGFP cassette	Addgene, #109049
pZEX-GUIDE-CMV-PuroT2AmCherry N3	Lentiviral transfer vector for U6 promoter-mediated gRNA expression, containing a puromycin resistance-T2A-mCherry cassette	gift from the Khavari group (Stanford, USA)

Name	Properties	Origin
pZEX-P4gRNA1	Lentiviral transfer vector containing the sequence of P4gRNA array 1 under control of the U6-promoter, containing a puromycin resistance-T2A-mCherry cassette	this work
pZEX-P4gRNA2	Lentiviral transfer vector containing the sequence of P4gRNA array 1 under control of the U6-promoter, containing a puromycin resistance-T2A-mCherry cassette	this work
VP5-F/H empty	Mammalian expression vector containing a FLAG/HA cassette under control of the CMV promoter	gift from the Meister group (University of Regensburg)
VP5-FARSB-F/H	Mammalian expression vector containing the KS-FARSB-F/H cassette under control of the CMV promoter	this work
VP5-GELS-F/H	Mammalian expression vector containing the KS-GELS-F/H cassette under control of the CMV promoter	this work
VP5-S100A8-F/H	Mammalian expression vector containing the KS-S100A8-F/H cassette under control of the CMV promoter	this work

7.10 Prokaryotic cells

Table 19: Utilized *Escherichia coli* strains

Name	Genotype	Details
DH5α	F^- Φ80*lac*ZΔM15 Δ(*lac*ZYA-*arg*F) U169 *rec*A1 *end*A1 *hsd*R17(r_k^-, m_k^+) *pho*A *sup*E44 *thi*-1 *gyr*A96 *rel*A1 λ^-	Propagation of plasmids
Stbl3	F^-*mcr*B *mrrhsd*S20(r_B^-, m_B^-) *rec*A13 *sup*E44 *ara*-14 *gal*K2 *lac*Y1 *pro*A2 *rps*L20(Str^R) *xyl*-5 λ^-*leumtl*-1	Propagation of lentiviral plasmids
XL1 blue	F^-*rec*A1 *end*A1 *gyr*A96 *thi*-1 *hsd*R17 *sup*E44 *rel*A1 *lac*F'[*pro*AB *lac*I *q*ZΔM15 *Tn*10 (Tet^R)]	Propagation of plasmids

7.11 Software

Table 20: Utilized software programs

Name	Source of supply
Adobe Creative Suite 5	Adobe (San José, USA)
ALEX	University of Southern Denmark (Ejsing group)[274] http://mslipidomics.info/contents/?page_id=133
Analyst	SCIEX (Framingham, USA)
ApE	University of Utah (Jorgensen group)[275] https://jorgensen.biology.utah.edu/wayned/ape/
AxioVision 4.9.1.0	Carl Zeiss (Oberkochen, Germany)
BZ-X800 Analyzer	Keyence (Osaka, Japan)
BZ-X800 Viewer	Keyence (Osaka, Japan)
CFX Manager 3.1	Bio-Rad (Hercules, USA)

Name	Source of supply
FACSDiva 7.0	BD Biosciences (San José, USA)
Incucyte 2020B	Sartorius (Göttingen, Germany)
Jalview	University of Dundee (Barton group)[276] https://www.jalview.org/
LP Data View	Bio-Rad (Hercules, USA)
MASCOT 2.5.1	Matrix Science (London, UK)
Microsoft Office	Microsoft (Redmond, USA)
MikroWin 2000	Labsis (Neunkirchen-Seelscheid, Germany)
MO.Affinity Analysis	NanoTemper Technologies (Munich, Germany)
MO.Control	NanoTemper Technologies (Munich, Germany)
ModFit LT	Verity Software House (Topsham, USA)
ND-1000 3.81	Thermo Fisher Scientific (Waltham, USA)
Odyssey 3.0.30	LI-COR Biosciences (Lincoln, USA)
ProteinScape 3.1.3	Bruker (Billerica, USA)
PyMOL	Schrödinger (New York, USA)
QUANTUM-Capt	Peqlab (Erlangen, Germany)
RNAstructure Software Package	University of Rochester (Mathews group)[194] https://rna.urmc.rochester.edu/RNAstructure.html
SnapGene Viewer 4.1.4	GSL Biotech (Chicago, USA)
TraceFinder	Thermo Fisher Scientific (Waltham, USA)
Windows Notepad	Microsoft (Redmond, USA)
ZEN 3.4 (blue edition)	Carl Zeiss (Oberkochen, Germany)
Zotero	https://www.zotero.org

8. Methods

8.1 Bioinformatical data analysis

8.1.1 Coding potential analyses

For sequence-based *in silico* predictions of *P4* coding potential, the full-length sequence was converted into FASTA file format and either pasted or uploaded to the corresponding tool websites of Coding-Potential Assessment Tool (CPAT), Coding Potential Calculator 2 (CPC2), Coding-Non-Coding Identifying Tool (CNIT), ORF Length and GC content (LGC), RNAsamba and RNAmining[178,180–184]. For analysis via iSeeRNA, a gtf file of the *P4* exons that could be annotated to the GRCh38 human reference genome was created and subsequently uploaded to the respective website[174,179]. For each of aforementioned analyses, default settings were used. Homology search for a hypothetical P4 protein was performed by entering the putative peptide sequence in FASTA format into the blastp suite and NCBI Conserved domain Search webtools[186,187]. For the blastp analysis, an expect threshold of 10 was applied.

8.1.2 GO term analysis of putative protein interactors

Proteins detected in the mass spectrometric measurements were filtered for downstream analyses based on varying criteria. Putative candidates resulting from the ChIRP-MS experiment were determined to exhibit Mascot scores at least 1.5 times higher in the *P4* pulldown samples than in both controls[240]. For CARPID, only those proteins were picked that demonstrated higher emPAI scores in one of both double transductions if compared to corresponding singly transduced cells[242]. In the case of the aptamer-based screening approach, only those proteins with iBAQ scores at least twice as high as for both controls were considered for subsequent investigations[245]. GO term analysis was performed by pasting the respective lists of filtered proteins to the DAVID web tool and selecting the GOTERM_BP_DIRECT chart option of the Functional Annotation Tool[239].

8.1.3 Mapping of Nanopore sequencing reads to the human genome

T2T genomic sequences on chromosome 17 surrounding the *P4* gene were extracted using the UCSC gene browser[153,175]. Nanopore reads were manually compared to the cDNA sequencing results and accordingly subdivided into exons. Those exonic sequences were singularly aligned to the T2T reference sequence using the blastn algorithm and whole reads subsequently mapped to the genome by hand[175,186].

8.1.4 Multiple sequence alignments

Mammalian sequences believed to contain the homologous *P4* gene with lengths of 11,500-15,500 nt between the annotated *Ccr7* and *Tns4* genes were extracted from the Ensembl genome browser for *Bos taurus*, *Canis lupus familiaris*, *Equus caballus*, *Felis catus*, *Macaca mulatta*, *Mus musculus*, *Nomascus leucogenys*, *Pan troglodytes*, *Sus scrofa*, *Tursiops truncatus* and *Zalophus californianus*[155]. Sequences were subsequently aligned using the EMBL-EBI MAFFT web tool and further analyzed in Jalview[185,276]. ORFs corresponding to the 420 nt one in human *P4* were manually identified and respective peptide sequences were generated using ApE[275]. These putative proteins sequences were again aligned with the MAFFT tool followed by downstream analysis in Jalview[185,276].

8.1.5 RNA structure analyses

For the initial *in silico* secondary structure meta-prediction of *P4*, the full length nucleotide sequence was entered in SSRTool with default parameters and the meta-stable structure was obtained from the results page[191]. G-quadruplex search was performed by submitting the full-length *P4* sequence to the G4Hunter web application[192]. For SHAPE-based secondary structure prediction, a file in shape format was manually generated in Windows Notepad by applying nucleotide-specific accessibility values based on the sequencing gel images, ranging from 0 for no signal, over 0.5 for weak signals and 1 for medium signals, to 1.5 for strong signals. The shape file was, along with the full-length *P4* FASTA file, loaded into RNAstructure 6.4 for secondary structure prediction, and probability annotation as well as structure rearrangement were performed in StructureEditor[194]. Analysis of structure element conservation was manually performed by taking individual base identities in previously generated multiple sequence

alignments (see page 98) into account. Tertiary structure prediction was performed by converting the SHAPE-based ct file into dot bracket format using the ct2dot command in RNAstructure 6.4 and submitting the dot bracket annotation to the 3dRNA web tool employing the Optimization Procedure and default settings for remaining parameters[194,195]. The resulting 3D structure was visualized and sequence features were highlighted in PyMOL.

8.1.6 Statistical interpretation

P values were calculated by performing either one-sample T-tests or two-sample T-tests with unequal variance in Microsoft Excel. Null hypothesis rejections with p values lower than 0.05 were considered significant.

8.2 Cell culture methods

All cell culture methods were performed in a biological safety cabinet under sterile conditions achieved by laminar air flow. Lentiviral procedures were performed under biosafety level 2 precautions whereas remaining methods were carried out under biosafety level 1 standards. Cell cultivation and stopping media, as well as DPBS and trypsin were pre-warmed to 37 °C in a water bath prior to use. For cultivation, cells were incubated in humidified incubators at 37 °C and 5% carbon dioxide atmosphere.

8.2.1 Apoptosis analysis

For annexin-based apoptosis assays, NKCs that were either electroporated for knockdown (see page 102) four days in advance or lentivirally transduced for overexpression (see page 104) beforehand were trypsinized from their cell culture dishes (see page 102) whereas old medium and DPBS for washing where not discarded but pooled with the stopped trypsinized cell suspension in one 50 mL reaction tube per sample. Approximately 20% of this mix were washed once with DPBS and stored in TRIzol reagent (Thermo Fisher Scientific, Waltham, USA) for subsequent RNA purification (see page 119). The rest of the suspension was supplied with 15 mL DPBS and centrifuged for 3 min at 300 rcf and 4 °C. The supernatant was discarded and 70 µL FACS binding buffer as well as 5 µL FITC-conjugated annexin V (ImmunoTools,

Friesoythe, Germany) were added and resuspended with a vortex mixer. After 20 min of incubation at 4 °C in the dark, another 200 µL FACS binding buffer were added, cells resuspended with a pipet, transferred to 5 mL round-bottom tubes and further incubated in the dark on ice. Immediately before measurement, 10 µL of 5 µg/mL DAPI (Sigma-Aldrich, St. Louis, USA) were added to the suspension, once again mixed at a vortex mixer and measured at a BD FACSCanto-II Flow Cytometer using a pre-set program in the FACSDiva 7.0 software.

8.2.2 BrdU incorporation assay

BrdU assays were performed by Carolin Molthof. KGM medium of organotypic tissue cultures (see page 103) was supplemented with 50 µM BrdU (Abcam, Cambridge, UK) 12 h prior to harvest. FFPE tissue sections on slides were incubated for 30 min at RT with 1 M hydrochloric acid and subsequently neutralized by removal of the acid and 10 min of incubation at RT in sodium borate buffer. Following that, slides were washed three times for 10 sec in PBS before being immunofluorescently stained with a BrdU-targeting antibody (see page 108).

8.2.3 Calcium phosphate transfection

For calcium phosphate transfection, HEK293T cells were grown to a confluency of 30% on 15 cm cell culture dishes. For each plate, 860 µL water, 122 µL of 2 M calcium chloride and 15 µg of the corresponding plasmid DNA were mixed before 1 mL per plate of 2x HEPES buffer were added dropwise under constant vortex mixing. The resulting solution was pipetted into the HEK293T culture medium and gently mixed. Two days following the transfection, cells were harvested and lysed (see page 126) for downstream analyses.

8.2.4 Cell cycle analysis

For cell cycle assays, NKCs were trypsinized from their culture dishes and counted three days after electroporation for depletion (see page 102) or any time after lentiviral transduction for overexpression (see page 104). 500,000 cells per sample in 50:50 medium were pipetted into 15 mL reaction tubes. Suspensions were centrifuged for 5 min at 300 rcf and RT and pellets washed once with 2 mL DPBS followed by repeated centrifugation for 5 min at 300 rcf and RT.

The supernatant was discarded and 500 µL FACS fixing buffer were added under constant vortex mixing. Cell suspensions were stored overnight at 4 °C. On the next day, 2 mL of FACS wash buffer were added to the suspension and spun down for 5 min at 400 rcf and RT. Supernatants were discarded and the washing step repeated once more with 2 mL FACS wash buffer. Cell pellets were resuspended in 440 µL FACS wash buffer and 50 µL of 1 mg/mL RNAse A (Sigma-Aldrich, St. Louis, USA) before being transferred to 5 mL round-bottom tubes. The tubes were incubated in a water bath for 20 min at 37 °C before 10 µL of 50 µg/mL DAPI (Sigma-Aldrich, St. Louis, USA) were added and vortex mixed. After 30 min of incubation in the dark and at RT, cell suspensions were once again mixed directly before being measured at a BD FACSCanto-II Flow Cytometer under the use of a pre-set program in the FACSDiva 7.0 software. FACS raw data were subsequently fitted for determination of cell phase populations by using the ModFit LT software.

8.2.5 Cultivation of HEK293T cells

HEK293T cells were cultivated in DMEM+FBS. Once full confluency was observed with a microscope, trypsinization and passaging of cells was performed. For this, the old culture medium was carefully aspirated, cells were washed once with DPBS and a fifth medium volume of 0.05% trypsin-EDTA was added on top of the cells before being incubated for 4 min at 37 °C. Cells in trypsin solution were collected in a reaction tubes and dishes rinsed once more with the cell suspension. Subsequently, 1.5 volumes of DMEM+FBS were added and cells were directly seeded onto new cell culture dishes in the required dilutions.

8.2.6 Cultivation of Jurkat cells

Jurkat cells were grown in RPMI+ in suspension culture flasks with vent caps. Suitable time points for cell passaging were determined by measuring cell numbers at a CASY cell counter following the manufacturer's protocol. Old cell suspensions were diluted either in the old culture vessel or in new flasks with pre-warmed RPMI+ to concentrations of 500,000 to 750,000 cells per mL of medium for further cultivation.

8.2.7 Cultivation of keratinocytes

Primary NKCs or immortalized keratinocyte cell lines were cultivated in 50:50 medium or Keratinocyte-SFM+. At observed confluencies of 80% to 90% under the microscope, cells were trypsinized and passaged. Therefore, old culture medium was aspirated and cells washed once with DPBS before a fifth medium volume of 0.05% trypsin-EDTA was added to the keratinocytes. Plates with trypsin solution were incubated at 37 °C for 4 min before the suspension was added into prepared reagent tubes with 1.5 trypsin volumes of DMEM+BCS stopping medium, and plates once again rinsed with the resulting mixture. Cell suspensions were spun down for 5 min at 200 rcf and RT, the supernatant was discarded and pellets resuspended in culture medium before being counted utilizing a Neubauer counting chamber (see page 102 below). Required cell amounts were seeded onto new culture dishes and diluted in fresh culture medium for further cultivation.

8.2.8 Determination of keratinocyte numbers

10 µL of cell suspension each were pipetted into top and bottom parts of a Neubauer counting chamber mounted with a coverslip. Multiple corner quadrants were manually counted out under a microscope and average cell numbers per quadrant ($n_{quadrant}$) were determined. Keratinocyte concentration (c_{cell}) was calculated using the formula $c_{cell} = n_{quadrant} \times 10{,}000 \ \frac{cells}{mL}$.

8.2.9 Electroporation of keratinocytes

For electroporation of NKCs with siPools (siTools, Munich, Germany), electroporation buffer of the Human Keratinocyte Nucleofector Kit (Lonza, Basel, Switzerland) was equilibrated to RT and aliquots with 1 nmol of respective siPools were thawed on ice. Reaction tubes with 500 µL 50:50 medium each were prepared and kept at 37 °C. Cultivated keratinocytes were trypsinized and counted (see page 102 above), and 6 million cells each were transferred into reaction tubes. Latter were centrifuged for 5 min at 200 rcf and RT before aspirating the supernatant. Cell pellets were resuspended in 90 µL of electroporation buffer and 95 µL of the resulting suspension were pipetted into the tubes containing siPools. After pipetting up and down twice, the entire mixture was transferred into the kit-included electroporation cuvettes and electroporated with the Electroporation Device Nucleofector II using program T-018.

Immediately after electroporation, the suspension was carefully pipetted into the prepared reaction tubes containing pre-warmed 50:50 medium and incubated at 37 °C for 25 min. Afterwards, cells were carefully resuspended and evenly distributed on cell culture dishes containing fresh pre-warmed 50:50 medium for further cultivation. On the next day, cells were trypsinized, counted (see page 102) and used for downstream applications. Successful knockdown was in each case verified by RNA purification (see page 119), cDNA synthesis (see page 111) and RT-qPCR analysis (see page 119).

8.2.10 Freezing and thawing of cells

For long-term storage of cells, appropriate amounts of cells were carefully resuspended in culture medium containing 10% DMSO in cryogenic vials, immediately placed on ice and the temperature was slowly (-1 °C/min) lowered to -80 °C. On the next day, cryo-stocks were transferred to the vapor phase of liquid nitrogen. For reuse of stored cells, those were thawed in a water bath at 37 °C and transferred to 9 mL of pre-warmed culture medium before being spun down for 5 min at 200 rcf and RT. The supernatant was discarded, cell pellets resuspended in fresh culture medium and pipetted onto cell culture dishes for further cultivation. After one day, the medium was exchanged in order to remove last traces of DMSO.

8.2.11 Generation of organotypic epidermal tissue

In order to obtain a suitable matrix for organotypic tissue models, human skin (Biopredic International, Saint-Grégoire, France) was thawed on ice and transferred into a culture dish washed twice with DPBS+2xA/A and incubated at 37 °C with the epidermal side down in DPBS+2xA/A. Following that, the epidermis was carefully removed using tweezers. The remaining dermis was washed twice with DPBS+2xA/A and kept in KGM medium at 37 °C for several days before being transferred into DPBS+2xA/A and stored at 4 °C for further usage.

In order to set up the tissue models, inserts that were designed by Eva Morgenstern and 3D-printed using Clear Resin (Formlabs, Somerville, USA) in collaboration with Raphael Malka from the group of Prof. Dr. Stefanie Sprunck (Department of Cell Biology and Plant Biochemistry, University of Regensburg) were sterilized in 70% ethanol. Following that, previously prepared dermis was cut with a scalpel into pieces with a size of 1 cm x 1 cm. Those

pieces were placed on top of the insert openings and dried at RT under laminar air flow. Next, ECM gel (Sigma-Aldrich, St. Louis, USA) or Matrigel (Corning, Corning, USA) was thawed on ice and 90 µL were pipetted into the bottom side of insert openings onto the dermis. After another 15 min of drying at RT, inserts were placed in 6 cm cell culture dishes containing 7 mL KGM medium and incubated overnight at 37 °C. On the next day, keratinocytes that were either electroporated (see page 102) the day ago or lentivirally transduced (see page 104 below) any time before were trypsinized and counted (see page 102), and aliquots with 500,000 cells each were spun down for 5 min at 200 rcf and RT, the supernatant was discarded and pellets resuspended in 30 µL pre-warmed KGM medium. Keratinocyte suspensions were subsequently pipetted on top of the dermis of previously prepared inserts and incubated at 37 °C in a humidified atmosphere with 5% carbon dioxide. KGM medium in the 6 cm dishes was exchanged every second day until the organotypic was harvested for downstream analyses.

8.2.12 Keratinocyte differentiation cultures

In order to achieve 2D differentiation of keratinocytes, cells were trypsinized, counted (see page 102) and seeded with a theoretical confluence of 300% onto culture dishes in culture medium supplied with 1.2 mM calcium chloride. Cells were further cultivated and the differentiation medium was exchanged every day until cells were harvested for subsequent experiments.

8.2.13 Lentivirus production and transduction of keratinocytes

In order to produce lentivirus, HEK293T cells were transfected using the Lipofectamine 3000 Transfection Reagent (Thermo Fisher Scientific, Waltham, USA). Kit components, Opti-MEM medium and endotoxin-free viral plasmids were equilibrated to RT. For viral production on a 15 cm culture dish, the solutions in Table 21 were produced under sterile conditions.

Table 21: Transfection mixtures for production of lentivirus

Solution	Composition	
DNA mixture	3.5 mL	Opti-MEM
	1.44 ng/nt	transfer plasmid
	17.5 µg	pCMV dR8.91
	8.68 µg	pUC-MDG
	81 µL	P3000 enhancer reagent
Lipofectamine mixture	3.5 mL	Opti-MEM
	95 µL	Lipofectamine 3000 reagent

Both solutions were pipetted together and vortex mixed before being transferred onto a 15 cm culture dish. HEK293T cells were trypsinized (see page 101) and the equivalent of 1.5 confluent plates was pipetted to the transfection mix. Subsequently, 3 mL fresh culture medium were added and the cells cultivated under biosafety 2 precautions. Old medium was aspirated and exchanged with 25 mL of new culture medium 6 h and 24 h after transfection, and virus was harvested 48 h and 72 h after transfection. For this, the old culture medium was passed through 0.45 µm filters into reaction tubes that were subsequently stored at -80 °C for further usage. After the first virus harvest, new culture medium was added to the HEK293T cells.

For lentiviral transduction, NKCs were seeded to a confluency of 5% into 6-well plates. The day after, previously prepared virus was pre-warmed to 37 °C in a water bath. And polybrene stock solution was thawed at RT. In accordance to biosafety level 2 regulations, NKCs in the 6-well plates were treated with a mixture of culture medium and virus using maximal virus-to-medium ratios of 1:2 with a final volume of 2.5 mL per well. Furthermore, 12.5 µL of the polybrene solution were pipetted into each well. The plates were centrifuged for 1 h at 1200 rpm and 32 °C, afterwards washed twice with DPBS and 2 mL of fresh 50:50 medium were added to each well. On the following day, the culture medium was exchanged. Once confluency was reached, keratinocytes were trypsinized and further cultivated under biosafety level 1 conditions (see page 102). Efficiency of overexpression was in case of fluorescent constructs investigated at a BZ-X810 fluorescent microscope or otherwise analyzed by RNA purification (see page 119), cDNA synthesis (see page 111) and RT-qPCR experiments (see page 119).

8.2.14 Live cell growth assay

For analysis of cell growth by live-cell imaging, NKCs that were electroporated the previous day (see page 102) or lentivirally transduced beforehand (see page 104) were trypsinized and meticulously counted (see page 102) before being seeded onto well plates with a theoretical confluency of 5%. After 4 h of cultivation at 37 °C, plates were transferred to an Incucyte SX5 Live Cell Imaging Instrument and dish area coverage ($area_{occ}$) was, with support of Dr. Ayse-Nur Menevse from the group of Prof. Dr. Philipp Beckhove (Department for Interventional Immunology, Leibniz Institute for Immunotherapy Regensburg), determined for every 4 h using the Incucyte 2020B software, whereas 24 h cell growth rates (GR_{24}) were calculated via $GR_{24}(t[h]) = \frac{area_{occ}(t[h])}{area_{occ}(t[h]-24)}$.

8.2.15 MTT assay

MTT assays on NKCs were performed using the Cell Proliferation Kit I (Roche, Munich, Germany) in 96-well plates with at least 8 wells per keratinocyte condition and 8 empty wells. To each well containing 100 µL culture medium, 10 µL of filtered MTT Labeling Reagent were pipetted and 4 h later, 100 µL of Solubilization Reagent were added. On the next day, absorbance at a wavelength of 590 nm was measured for each well using a Mithras LB 940 plate reader with MikroWin 2000 software and blanked absorbance was obtained by subtracting the absorbance of empty wells from the cell-containing wells.

8.2.16 Preparation of cells for CARPID

For CARPID, 6-well plates with NKCs were lentivirally transduced (see page 104) with pZEX-P4gRNA1 virus, pZEX-P4gRNA2 virus or centrifuged without addition of virus and recovered in culture medium overnight. On the next day, selection of P4gRNA-positive cells was performed by treating transduced wells with 1 µg/mL puromycin in culture medium for two full days with one medium exchange in between. Following selection, wells were washed three times with DPBS, fresh culture medium was added and half of the transduced plates as well as the mock-transduced plates were lentivirally transduced with pLEX-dCasRx-BASU virus. After multiple days of recovery and cultivation (see page 102), cells were incubated with 200 µM biotin in culture medium at 37 °C for 30 min before being harvested and lysed (see page 126) for subsequent CARPID pulldown experiments (see page 122).

8.2.17 Scratch wound assay

For scratch assays, NKCs were trypsinized and counted one day after electroporation (see page 102) and seeded onto Incucyte ImageLock 96-well plates (Sartorius, Göttingen, Germany) with 40,000 cells per well either in normal culture medium or medium containing 12 µg/mL mitomycin C. After 4 h, mitomycin C-treated cells were washed twice with DPBS, fresh culture medium was added. Scratches were applied utilizing an Incucyte Woundmaker 96-Tool (Sartorius, Göttingen, Germany), plates were transferred into an Incucyte SX5 Live Cell Imaging Instrument and several parameters related to gap closure were, with help from Dr. Ayse-Nur Menevse from the group of Prof. Dr. Philipp Beckhove (Department for

Interventional Immunology, Leibniz Institute for Immunotherapy Regensburg), recorded every hour using the Incucyte 2020B software.

8.3 Histological analysis

8.3.1 Hematoxylin and eosin staining of sections from FFPE epidermal tissue

Hematoxylin and eosin staining was performed by Carolin Molthof. As a prerequisite to prepare tissue sections, pieces of generated organotypic tissue (see page 103) were placed in embedding cassettes, incubated on a shaker in the order indicated in Table 22, transferred in embedding forms with molten paraffin and subsequently stored at 4 °C.

Table 22: Steps of paraffin embedding procedure

Solution	Duration	Temperature	Number of steps
PFA buffer	overnight	4 °C	1x
Water	30 min	RT	1x
70% Ethanol	1 h	RT	1x
80% Ethanol	30 min	RT	1x
96% Ethanol	30 min	RT	1x
96% Ethanol	45 min	RT	1x
Ethanol	30 min	RT	2x
Xylene	30 min	RT	2x
Paraplast (Leica Biosystems, Wetzlar, Germany)	24 h	60 °C	2x

Using an RM2265 Automated Microtome, 7 µm sections were prepared, incubated at 42 °C in a water bath and placed on Polysine Adhesion Microscope Slides (Epredia, Portsmouth, USA). Excess water was carefully removed with a paper towel and slides were dried at 42 °C before being stored at 4 °C until further usage.

For hematoxylin and eosin staining, slides with paraffin-embedded tissue sections were incubated at RT for 5 min each in xylene, absolute ethanol and 70% ethanol in this exact order. Afterwards, slides were rinsed for 30 sec in water and stained by shaking 5 min in Mayer's hematoxylin. Slides were washed twice for 1 min in water and incubated under shaking in 1% eosin Y solution for 10 min. Subsequently, sections were dehydrated by incubating them twice for 30 sec each in 95% ethanol and 100% ethanol. Remaining ethanol was removed by performing two changes with xylene. Two drops of Entellan mounting medium (Sigma Aldrich, St. Louis, USA) were used for mounting, slides were dried overnight at 4 °C and analyzed at an Axio Imager.D2m microscope.

8.3.2 Immunofluorescence analysis of sections from organotypic tissue

For immunofluorescent staining of paraffin sections, slides were rehydrated by incubating them at RT in the order listed in Table 23.

Table 23: Rehydration procedure for immunofluorescent staining

Solution	Duration	Number of steps
Xylene	5 min	2x
Ethanol	2 min	1x
96% Ethanol	2 min	1x
80% Ethanol	2 min	1x
60% Ethanol	2 min	1x
Water	5 min	1x

A vessel with demasking buffer inside of a small water bath was brought to a boil in a microwave, the slides were inserted and incubated for 10 min. This step was repeated once and afterwards, the vessel was taken out of the water bath and cooled down to RT. After 3 washing steps of 2 min in PBS, slides were blocked in IF blocking buffer for 30 min under constant shaking. Primary antibodies were diluted in IF wash buffer, pipetted on top of the section, covered with Parafilm (Carl Roth, Karlsruhe, Germany) and incubated for 1 h at RT in a humidified chamber. Following this, sections were washed three times for 5 min in IF wash buffer, before secondary antibodies were diluted in IF wash buffer and applied to the sections. Again, Parafilm was positioned on top and the sections were incubated for 1 h in RT in a dark, humidified chamber. Subsequently, slides were washed three times for 5 min with PBS, incubated for 5 min in Hoechst buffer and again washed three times for 5 min in PBS with all of these steps being performed in the dark. Slides were carefully dried with a paper towel and mounted using ProLong Gold Antifade Mountant (Thermo Fisher Scientific, Waltham, USA). Slides were stored at 4 °C for downstream microscopic analysis.

For generation of cryosections, pieces of organotypic tissue were embedded in Tissue-Tek O.C.T. Compound (Sakura Finetek, Torrance, USA) and frozen on dry ice before being stored at -80 °C. Tissue blocks were subsequently cut at a Cryostat Microm HM 500 OM into 7 µm sections and immediately mounted onto Polysine Adhesion Microscope Slides (Epredia, Portsmouth, USA). Those were stored for further analyses at -20 °C. In order to immunofluorescently stain cryosections, those were incubated for 10 min at -20 °C in ethanol or methanol for fixation. Fixatives were diluted out by 3 changing steps with PBS before blocking was performed in IF blocking buffer. The remaining steps are identical to those found above in the protocol for immunofluorescent staining of paraffin-embedded sections.

Subsequent microscopic analysis was performed at Axiovert 200 M or BZ-X810 fluorescence microscopes.

8.4 Microbiological techniques

8.4.1 Cultivation of *Escherichia coli*

For colony formation, bacteria were grown overnight at 37 °C on LB-agar plates with or without antibiotics. Liquid cultures for amplification of plasmid DNA were inoculated overnight at 37 °C and with shaking at 200 rpm either in 13 mL plastic tubes or Erlenmeyer flasks with LB-Amp medium.

8.4.2 Preparation of chemically competent *Escherichia coli*

In order to generate competent *E. coli* cells for transformation, single colonies were grown by spreading out corresponding glycerol bacteria stocks on LB-agar plates with an inoculation needle and incubating overnight at 37 °C. On the next day, single colonies were picked, transferred to 2 mL YT++ medium and shaken overnight at 37 °C and 200 rpm. The overnight culture was diluted 1:100 in new YT++ medium to a final volume of 5 mL and further incubated with shaking at 37 ° for 90 min. The preculture was once again diluted 1:20 in YT++ medium and shaking incubated at 37 °C until an OD_{600} of 0.4-0.5 could be measured at an Amersham Ultrospec 3300 pro photometer. The bacteria suspension was transferred to reaction tubes, spun down for 5 min at 2,500 rcf and 4 °C and the supernatant was discarded. The pellet was resuspended on ice in 20 mL of cold TFBI, incubated at 4 °C for 10 min and once again centrifuged for 5 min at 2,500 rcf and 4 °C. The supernatant was removed and the pellet carefully resuspended in 4 mL cold TFBII before being rapidly pipetted into aliquots of 100 µL at 4 °C which were subsequently snap-frozen in liquid nitrogen and stored at -80 °C.

8.4.3 Transformation of chemically competent *Escherichia coli*

For transformation, aliquots of chemically competent *E. coli* strains (see page 109 above) were thawed on ice and 200 ng plasmid DNA or 10 µL of ligation reactions (see page 113) were

pipetted to the cells and mixed by swirling. The mixture was incubated for 30 min at 4 °C before a heat shock at 42 °C was performed. This lasted 45 sec for *Stbl3* cells, 60 sec for *XL1 blue* bacteria and 90 sec for *DH5α* cells. Afterwards, cells were incubated on ice for 2 min in order to recover. 900 µL of LB medium were added to the mixture and shaking incubated for 1 h at 37 °C and 800 rpm. Afterwards, the suspension was centrifuged for 1 min at 8000 rcf and the pellet, resuspended in 100 µL of the remaining supernatant, was plated on LB-Amp plates utilizing sterile glass beads. Following that, plates were incubated overnight at 37 °C for formation of bacterial colonies.

8.5 Molecular biological methods

8.5.1 Annealing of complementary single-stranded DNA oligonucleotides

In order to form linear double-stranded DNA templates for subsequent cloning PCRs (see page 116), synthesized complementary oligonucleotides were pipetted together to a final concentration of 50 µM each. The mixture was incubated at 95 °C for 5 min before cooling the samples down to room temperature with a rate of -0.5 °C/min. Template samples were stored at -20 °C for further downstream applications.

8.5.2 Aptamer-based RNA pulldown

As prerequisites for S1-aptamer pulldowns, the necessary RNAs were synthesized by PCRs on plasmid templates with corresponding primer pairs (see page 116) followed by *in vitro* transcription on the resulting amplicons (see page 113). Quality of the generated transcripts was controlled by RNA gel electrophoresis (see page 119). Furthermore, wildtype or, in case of validation assays, protein-overexpressing NKCs were harvested and lysed (see page 126) and the protein concentrations measured via Bradford assays (see page 122).

For the pulldown itself, 25 µg, or 2 µg for validation assays, of aptamer-fused RNAs were filled up with aptamer binding buffer to 1 mL final volume and 50 µL of this mixture were stored as input sample. 50 µL MyOne Streptavidin C1 Dynabeads (Thermo Fisher Scientific, Waltham, USA) per sample were washed twice with 500 µL aptamer binding buffer on a rotator at 4 °C for 30 min each and separation of beads from supernatant was achieved also for subsequent steps by fixing the beads under usage of a magnetic rack. Washed beads were added to the RNA

mix and coupling was achieved by rotating for 30 min at 4 °C. Coupled beads were washed twice by rotating 10 min at 4 °C with 1 mL of aptamer binding buffer each. The supernatant was discarded and beads resuspended in amounts of keratinocyte lysate corresponding to 500 µg total protein, whereas additional 60 µg, or 25 µg for validation assays, were taken aside as input samples. Furthermore, 20 µg of yeast tRNA (Thermo Fisher Scientific, Waltham, USA) were pipetted to the bead suspension and aptamer wash buffer was added to reach a final volume of 1 mL. The mixture was rotated 30 min at 4 °C and afterwards washed three times by rotating for 10 min at 4 °C with 200 µL aptamer wash buffer each. At the last washing steps, beads were transferred into a new reaction tube.

10% of beads as well as RNA input samples were stored in TRIzol (Thermo Fisher Scientific, Waltham, USA) for RNA purification (see page 119), cDNA synthesis (see page 111) and RT-qPCR analysis (see page 119). 4x NuPage LDS Sample Buffer (Thermo Fisher Scientific, Waltham, USA) and DTT were added to the remaining beads and protein input samples to concentrations of 1x and 100 mM, respectively, and mixtures shaken for 10 min at 70 °C and 1400 rpm. The samples were then used for SDS-PAGE (see page 127) followed by western blot (see page 128) for validation assays, or Coomassie stain (see page 123) and preparation for mass spectrometric analysis (see page 125).

8.5.3 cDNA synthesis

For generation of cDNAs as templates for cloning PCRs (see page 116), phenol-chloroform-extracted total RNA (see page 119) was used with the RevertAid H Minus First Strand cDNA Synthesis Kit (Thermo Fisher Scientific, Waltham, USA) according to the manufacturer's protocol and using oligo-dT primers. In order to synthesize cDNA for subsequent RT-qPCR analyses (see page 119), RNA that was either *in vitro*-transcribed (see page 113), extracted from cells with the phenol-chloroform method or purified from organotypic tissue (see page 118) was reverse transcribed by using the iScript cDNA Synthesis Kit (Bio-Rad, Hercules, USA), following the manufacturer's manual and using halved amounts. Ahead of cDNA synthesis for RT-qPCR analyses, phenol-chloroform extracted RNA was additionally subjected to DNase I digestion with 1x DNase I buffer and 0.5 units DNase I (both Thermo Fisher Scientific, Waltham, USA) in a final volume of 5 µL and incubated at 37 °C for 30 min. The DNase digestion was stopped by addition of 50 mM EDTA (Thermo Fisher Scientific, Waltham, USA) and incubating for 10 min at 65 °C.

8.5.4 ChIRP-MS

Biotinylated ChIRP probes that had been previously designed by Sonja Hombach were mixed in equimolar ratios to create pools with a total probe concentration of 100 µM. NKCs were harvested, lysed (see page 126) and protein concentration was determined (see page 122).

Per sample, 30 µL MyOne Streptavidin C1 Dynabeads were washed three times by rotating at RT for 10 min with 300 µL of ChIRP-MS wash buffer each. Beads were separated from supernatant by use of a magnetic rack for these and subsequent steps. Preclear was performed by adding 3 mg of protein lysate to the beads and filling up with one volume of ChIRP-MS hybridization buffer. After 1 h of rotating at RT, 10 µL were taken as input, the remaining supernatant was mixed with 2 µL of the 100 µM probe pools and incubated overnight at RT on a rotator. Additionally, 50 µL of streptavidin beads per sample were rotated in 500 µL ChIRP-MS wash buffer at RT overnight. On the next day, the washed beads were carefully resuspended in the probe-lysate-mixture and rotated for 2 h at RT. Afterwards, three washing steps were carried out by rotating the beads for 10 min at RT in 500 µL ChIRP-MS wash buffer each.

Beads and inputs were either used for RNA purification (see page 119), cDNA synthesis (see page 111) and RT-qPCR analysis (see page 119), or brought to 1x NuPAGE LDS Sample Buffer (Thermo Fisher Scientific, Waltham, USA) and 50 mM DTT, incubated for 10 min at 70 °C and used for SDS-PAGE (see page 127) with Coomassie stain (see page 123) and tryptic gel digestion for mass spectrometry (see page 125).

8.5.5 DNA agarose gel electrophoresis

In order to separate DNA fragments based on their size, for preparation of agarose gels 1% to 2% (w/v) agarose were dissolved in varying volumes of TAE buffer by heating in a microwave and subsequent addition of 250 ng/mL ethidium bromide. The gel solution was poured into a closed tray with inserted comb and solidified by cooling down to room temperature. Solid gels were transferred to horizontal gel chambers and covered in TAE buffer. DNA samples were brought to 1x DNA loading dye and pipetted into gel pockets along with 1 kb Plus DNA Ladder (New England Biolabs, Ipswich, USA). Gel electrophoresis was performed for 30 to 60 min at a voltage of 90 to 120 V. Gels were analyzed on a Transilluminator Quantum ST4 with the Quantum-Capt software and, if necessary, pieces cut out with a scalpel for DNA purification via the NucleoSpin Gel and PCR Clean-up kit (Macherey-Nagel, Düren, Germany).

8.5.6 Generation of plasmids

For ligation of multiple DNA fragments to one final plasmid, one or multiple inserts with digested sticky ends (see page 118) were mixed with 100 ng correspondingly digested vector to a minimal molar insert-to-vector ratio of 3:1. Ligation was started in 1x T4 DNA Ligase Reaction Buffer with 400 units T4 DNA Ligase (both New England Biolabs, Ipswich, USA) in a final volume of 10 µL. The reaction was incubated overnight at 4 °C or 1 h at RT before being used for transformation of chemically competent *E. coli* cells (see page 109), and integrity of constructs was analyzed by downstream colony PCR (see page 116).

8.5.7 *In vitro* transcription

Templates for *in vitro* transcription were generated either by restriction digest of vectors (see page 118) containing respective constructs under control of a T7 promoter or PCR on plasmid templates with suitable primer pairs (see page 116), both followed by DNA gel electrophoresis (see page 112) and DNA purification via the NucleoSpin Gel and PCR Clean-up kit (Macherey-Nagel, Düren, Germany) following the provided manual and eluting twice with 30 µL water. The volume of the eluted fractions was reduced using a Concentrator 5301 to a volume of less than 11 µL. Using general components purchased from Promega (Fitchburg, USA), RiboLock RNase inhibitor (Thermo Fisher Scientific, Waltham, USA) and optionally Aminoallyl-UTP-Cy5 (Jena Bioscience, Jena, Germany), the reaction shown in Table 24 was pipetted together.

Table 24: Composition of *in vitro* transcription reaction

Component	Volume
5x Transcription buffer	10 µL
100 mM DTT	5 µL
10 mM rATP	5 µL
10 mM rCTP	5 µL
10 mM rGTP	5 µL
10 mM rUTP	5 µL (4 µL)
(1 mM Aminoallyl-UTP-Cy5)	(2 µL)
40 U/µL RiboLock RNase inhibitor	1.25 µL
DNA template	variable
10-20 U/µL T7 RNA polymerase	1 µL
Water	ad 50 µL

The mixture was incubated for 2 h at 37 °C before addition of 2 units DNase I (Thermo Fisher Scientific, Waltham, USA) and further incubation for 15 min at 37 °C. The reaction was cleaned

over Amersham MicroSpin G-25 Columns (Cytiva, Marlborough, USA) following the manufacturer's instructions, and sodium acetate was added to a concentration of 300 mM and a final volume of 150 µL. The same volume ROTIAqua-P/C/I (Carl Roth, Karlsruhe, Germany) was added, vortex mixed and centrifuged for 5 min at 20,000 rcf and 4 °C. The upper aqueous layer was extracted, an equal volume of chloroform was added, and once more vortex mixed and spun down for 5 min at 20,000 rcf and 4 °C. Again, the aqueous layer was extracted and vortex mixed with 2.5 volumes of ethanol before being incubated for at least 1 h at -20 °C for precipitation. Afterwards, the mixture was centrifuged for 10 min at 20,000 rcf and 4 °C and the supernatant was removed. The RNA pellet was dried at RT, dissolved in 40 µL water and measured at a NanoDrop 1000 Spectrophotometer. RNA quality was analyzed by subsequent RNA gel electrophoresis (see page 119).

8.5.8 Lipidomic analysis of organotypic tissue

In order to determine lipid profiles, pieces of previously generated organotypic tissue (see page 103) were transferred into Lysing Matrix D tubes (MP Biomedicals, Irvine, USA) containing 800 µL 0.2% (w/v) SDS and homogenized using a FastPrep-24 Classic Instrument for 45 sec with a speed of 6 m/s. Protein concentration of the homogenous mixture was determined at a NanoDrop 1000 Spectrophotometer before samples were submitted to the group of Prof. Dr. Gerhard Liebisch (Institute of Clinical Chemistry and Laboratory Medicine, University Hospital of Regensburg) for lipidomic analysis.

In short, internal standards were added prior to lipid extraction and a Xevo TQ-S micro triple quadrupole mass spectrometer with Analyst software was used for quantification of ceramides, lysophosphatidylcholines, lysophosphatidylethanolamines, phosphatidylethanolamines, phosphatidylglycerols and phosphatidylinositols. For quantitative analysis of cholesterol esters, diglycerides, free cholesterol, phosphatidylcholines, sphingomyelins and triglycerides, samples were measured at a Q Exactive Orbitrap mass spectrometer and analyzed using TraceFinder and ALEX software[274].

8.5.9 Microscale thermophoresis

In preparation for MST measurements, HEK293T cells were transfected to overexpress proteins of interest (see page 100) before being harvested and lysed. Lysates were subsequently used for FLAG-immunopurification of the respective proteins (see page 123) and the concentration of purified proteins determined by Bradford assays (see page 122). Furthermore, success of purification was verified by SDS-PAGE (see page 127) with subsequent Coomassie staining (see page 123), silver staining or western blot (see page 127). Following this, proteins were concentrated using Vivaspin 500 Centrifugal Concentrators (Sartorius, Göttingen, Germany) according to the manufacturer's manual. Scrambled controls were designed by using the Shuffle DNA webtool on exon fragments of *P4*[277]. RNAs for MST analysis were fluorescently *in vitro*-transcribed (see page 113) and their integrity evaluated by RNA gel electrophoresis (see page 119) and additional detection with the 700 nm channel of an Odyssey Classic Imaging System.

For MST measurements themselves, capillary scans for different concentrations of the synthesized RNAs in MST binding buffer were performed at a Monolith NT.115 Blue/Red device using the MO.Control software in order to determine optimal parameters enabling fluorescence levels between 500 and 1,500 units. Next up, series of 16 1:1 dilutions of purified proteins were performed in MST binding buffer and fluorescent RNAs were added in their optimal concentrations to a final volume of 10 µL per dilution. These dilutions were transferred to capillaries and measured at aforementioned instrument with MST laser powers of 20%, 40%, 60% and 80% as well as a MST power-on time of 30 sec and a power-off time of 5 sec. Further analysis was performed using the MO.Affinity Analysis software and data points at 20% MST power at 15 sec excitation time were extracted for more detailed evaluation.

8.5.10 Plasmid purification

Depending on the required quantities of plasmid DNA, different volumes of *E. coli* liquid cultures were prepared overnight (see page 109), and on the next day DNA was purified using the NucleoSpin Plasmid, NucleoBond Xtra Midi or, in case of viral plasmids, NucleoBond Xtra Midi EF kits (all Macherey-Nagel, Düren, Germany) following the manufacturer's protocol. DNA was eluted or dissolved in water and concentration was measured at a NanoDrop 100 Spectrophotometer. In order to verify contained construct sequences, 500 ng of DNA were

mixed with 5 µM sequencing primers in a final volume of 10 µL and sent to Macrogen Europe, Amsterdam, Netherlands, for Sanger sequencing analysis.

8.5.11 Polymerase chain reaction

PCRs were performed at a Mastercycler nexus device and were performed using components and enzymes from New England Biolabs (Ipswich, USA). General cloning PCRs were performed using Phusion High-Fidelity DNA Polymerase and reactions were pipetted as listed in Table 25, using either 1 µL of cell cDNA (see page 111), 200 ng of plasmid or 5 picomoles of annealed linear double-stranded DNA (see page 110) as a template.

Table 25: Composition of cloning PCRs

Component	Volume
5x Phusion Buffer (HF or GC)	10 µL
10 mM dNTPs	1 µL
10 µM Forward primer	2.5 µL
10 µM Reverse primer	2.5 µL
DMSO	1.5 µL
DNA template	variable
2 U/µL Phusion High-Fidelity DNA Polymerase	0.5 µL
Water	ad 50 µL

In general, programs following the protocol in Table 26 were used for cloning PCRs, with hybridization temperature and elongation time dependent on amplicon properties.

Table 26: Protocol for cloning PCRs

Temperature	Time	
98 °C	30 sec	
98 °C	10 sec	35x
50-72 °C	30 sec	
72 °C	30 sec/kb	
72 °C	5 min	
10 °C	Storage	

For colony PCRs and generation of templates for *in vitro* transcription (IVT), Taq DNA Polymerase was used. In case of colony PCRs, colonies grown on LB-Amp plates after transformation (see page 109) were picked with a sterile tip, stricken out on a replica LB-Amp plate for overnight incubation and 37 °C, and subsequently dipped and swirled in the PCR mix containing one insert- and one vector-specific primer instead of a DNA template. The general

composition of Taq PCRs is listed in Table 27, with 200 ng of plasmid DNA or 1 picomole each of partially overlapping primers being used as templates in PCRs for *in vitro* transcription.

Table 27: Composition of Taq PCRs

Component	Volume for IVT-PCRs	Volume for colony PCRs
10x ThermoPol Reaction Buffer	5 µL	2.5 µL
10 mM dNTPs	1 µL	0.5 µL
10 µM Forward primer	1 µL	0.5 µL
10 µM Reverse primer	1 µL	0.5 µL
DNA template	variable	- (bacterial colony)
5 U/µL Taq DNA Polymerase	0.25 µL	0.125 µL
Water	ad 50 µL	20.875 µL

The protocol listed in Table 28 was used for Taq PCRs, whereas in case of PCRs for generation of scrambled templates, 4 cycles with a hybridization temperature of 68 °C followed by one cycle with a hybridization temperature 64 °C were added prior to the standard cycles.

Table 28: Protocol of Taq PCRs

Temperature	Time	
95 °C	30 sec	
95 °C	15 sec	30x
60 °C	15 sec	
68 °C	1 min/kb	
68 °C	5 min	
10 °C	Storage	

After PCR, amplicons were mixed with loading dye and DNA agarose gel electrophoresis (see page 112) was performed ahead of other downstream experiments.

8.5.12 Polysome fractionation

Polysome fractionation analysis was performed together with Daniela Strauß. For this, sucrose gradients were prepared by transferring 10% sucrose gradient buffer with a syringe into round-bottom centrifuge tubes up until a beforehand drawn mark was reached. Then, 50% sucrose gradient buffer was carefully injected underneath the first layer with a syringe until a second pre-applied mark was reached. Gradients were mixed with a Gradient Master IP Model 107 using a 6-step program for 10-50% (w/v) SW40 gradients. Except for runoff experiments, NKCs were treated with 100 µg/mL cycloheximide in culture medium and incubated for 10 min at 37 °C before plates were put on ice and washed twice with ice-cold DPBS. Cells were

scraped off in 1 mL of chilled polysome fractionation buffer per culture dish and the suspension was passed through a 23x gauge needle for 10 times. After 10 min incubation at 4 °C, the suspension was spun down for 10 min at 8,000 rcf and 4 °C, the supernatant was collected and its RNA concentration measured at a NanoDrop 1000 Spectrophotometer. 200 µg of RNA were carefully pipetted on top of the prepared gradients and centrifuged for 2.5 h at 4 °C and 39,000 rpm using a Optima LE-80K ultracentrifuge with SW40 rotor. Gradients were divided based on their density into 13 fractions of equal volume with a BioLogic LP System and the corresponding LP Data View software. To 250 µL of each fraction, 2.5 ng of *in vitro*-transcribed *GFP* RNA (see page 113) were spiked in for normalization before phenol-chloroform extraction of RNA was performed (see page 119) with the addition of 0.1% (v/v) glycogen (Thermo Fisher Scientific, Waltham, USA) at the precipitation step. Equal volumes of RNA were used for subsequent cDNA synthesis (see page 111) and RT-qPCR analysis (see page 119).

8.5.13 Restriction enzyme digest

In order to generate linear DNA fragments with sticky ends, 5 µg of plasmid DNA or entire purified PCR products (see page 116) were digested with suitable enzymes and in buffers by New England Biolabs (Ipswich, USA). Digestions were performed in a volume of 50 µL with 1-2 µL of each restriction enzyme with buffers and incubation conditions recommended by the New England Biolabs guidelines. Following heat inactivation, vector digests were separated on a DNA agarose gel (see page 112) and fragments of correct length were cut out for purification with the NucleoSpin Gel and PCR Clean-up kit (Macherey-Nagel, Düren, Germany).

8.5.14 RNA extraction from organotypic tissue

For purification of RNA from previously generated organotypic tissue models (see page 103), the tissue itself was cut into small pieces and transferred into Lysing Matrix D tubes (MP Biomedicals, Irvine, USA) containing 800 µL RLT Plus Buffer (Qiagen, Venlo, Netherlands) with 1% (v/v) β-mercaptoethanol. Tissues were disrupted using a FastPrep-24 Classic Instrument for 45 sec at 6 m/s, followed by centrifugation for 1 min at 11,000 rcf. The supernatant was transferred into QIAshredder tubes (Qiagen, Venlo, Netherlands), spun down for 2 min at 11,000 rcf, and the flow-through was used for further RNA purification with the RNeasy Plus Mini Kit (Qiagen, Venlo, Netherlands) according to the manufacturer's protocol.

RNA was eluted in 30 µL water and a NanoDrop 1000 Spectrophotometer used for measuring concentration prior to cDNA synthesis (see page 111) and RT-qPCR analysis (see page 119).

8.5.15 RNA extraction with phenol and chloroform

For RNA isolation with the phenol-chloroform method, washed cells or beads were transferred to 0.5-1 mL TRIzol reagent (Thermo Fisher Scientific, Waltham, USA) and a fifth volume of chloroform was added. The emulsion was vortex mixed for 15 sec and incubated at RT for 3 min before being centrifuged for 15 min at 10,000 rcf and 4 °C. The upper aqueous phase was transferred to a new reaction tube and the chloroform extraction step was repeated once. Afterwards, isopropanol of half the original TRIzol volume was added to the aqueous phase, inverted for multiple times and precipitated overnight at -20 °C. On the next day, the mixture was spun down for 10 min at 13,000 rcf and 4 °C, the pellet washed once in 500 µL 70% ethanol and centrifuged for 8 min at 10,000 rcf and 4 °C. The supernatant was removed and the pellet air dried at RT before dissolving in varying amounts of water and storing samples at -80 °C.

8.5.16 RNA agarose gel electrophoresis

In order to prepare a small RNA gel, 1 g agarose was dissolved in 85 mL water by heating in a microwave and cooled down before adding 10 mL of 10x MOPS buffer and 5.4 mL of 37% formaldehyde. Next, the gel was poured into a prepared closed tray with inserted comb at 4 °C. RNA samples were brought to the same volume and, along with RiboRuler High Range RNA Ladder (Thermo Fisher Scientific, Waltham, USA), mixed 1:1 with 2x RNA loading dye. Samples and marker were incubated for 10 min at 65 °C and put on ice immediately afterwards before adding ethidium bromide to a concentration of 80 µg/mL. At 4 °C, RNA gels were loaded and run in RNA running buffer for 10 min at 150 V, followed by 2 h at 90 V. Subsequently, gels were analyzed on a Transilluminator Quantum ST4 with the Quantum-Capt software.

8.5.17 RT-qPCR analysis

For RT-qPCR analyses, RNAs were reverse transcribed into cDNAs (see page 111) and in most cases diluted with water. 2 µL of those cDNAs were mixed in the wells of 96-well plates with

4.5 µL water, 1 µL of a primer mix containing 5 µM of both forward and reverse primers, and 7.5 µL of Takyon Mix (Eurogentec, Seraing, Belgium). Plates were sealed and analyzed at a Real-Time PCR Cycler CFX96 with the CFX Manager 3.1 software using the program listed in Table 29. Samples were run in duplicates or triplicates, and target specificity was determined by melt curve analysis. Prior to this, suitability of primers for quantitation was for each pair evaluated by dilution series.

Table 29: Protocol for RT-qPCR

Step	Time	
95 °C	3 min	
95 °C	15 sec	30x
60 °C	30 sec	
72 °C	30 sec	
plate read		
95 °C	10 sec	
65 °C to 95 °C, + 0.5 °C/step	5 sec	melt curve
plate read		

Fold changes for genes of interest (goi) in samples related to reference samples were calculated by using regression for Cq-value determination and using the $2^{-\Delta\Delta Cq}$ method[278]. If possible, normalization to housekeeping or spiked-in transcript controls (tc) was performed, using the formula $Fold\ change = 2^{-\{[Cq\ sample(goi) - Cq\ reference\ (goi)] - [Cq\ sample(tc) - Cq\ reference(tc)]\}}$. In case of HA-IPs (see page 124), normalization was carried out to dilution-corrected levels of same transcripts in the input and pulldown GFP samples. Hence, the formula applied here was $Fold\ change = 2^{-\{[Cq\ pulldown(goi) - Cq\ input(goi)] - [Cq\ GFP\ pulldown(goi) - Cq\ GFP\ input(goi)]\}}$.

8.5.18 SHAPE

SHAPE experiments were performed by Daniela Strauß and Johanna Gizler. As a prerequisite, full length *P4* RNA was *in vitro*-transcribed (see page 113) from PCR-synthesized template DNA (see page 116). In order to achieve correct folding, 4 µg of RNA in 12 µL water were incubated for 2 min at 95 °C, chilled on ice for 2 min prior to addition of 6 µL of 3.3x folding buffer and incubation for 30 min at 37 °C. Modification of RNA was performed by adding 10 mM NMIA to 9 µL of folded RNA and incubating for 75 sec at 37 °C, followed by storage on ice. For the unmodified control, the same procedure was applied without addition of NMIA. RNA purification was performed using the RNeasy Plus Mini Kit (Qiagen, Venlo, Netherlands)

according to the manufacturer's protocol and elution was performed in 40 µL of water before measuring the concentration at a NanoDrop 1000 Spectrophotometer. For reverse transcription, the reaction shown in Table 30 was pipetted with 0.5-10 µg of RNA template and 5' DY682-labeled primers, using components supplied by Thermo Fisher Scientific (Waltham, USA).

Table 30: Composition of reverse transcription reaction for SHAPE

Component	Volume
RNA	variable
10 mM dNTPs	1 µL
5 µM 5' DY682-labeled primer	0.2 µL
Water	ad 13 µL
Incubation for 5 min at 65 °C and 1 min on ice	
5x First Strand Buffer	4 µL
1 M DTT	1 µL
40 U/µL RiboLock RNase inhibitor	1 µL
200 U/µL SuperScript III Reverse Transcriptase	1 µL

The mixture was incubated for 1 h at 55 °C and inactivation was carried out for 15 min at 70 °C. 100 mM sodium hydroxide and 12.5 mM EDTA were added and incubated for another 30 min at 65 °C, before neutralizing with 100 µM hydrochloric acid. Samples were brought to 1x SHAPE loading dye afterwards. Sequencing ladders were synthesized using the USB Thermo Sequenase Cycle Sequencing Kit (Affymetrix, Santa Clara, USA) following the manufacturer's instruction for radiolabeled primer cycle sequencing while using the same DY682-labeled primers previously utilized for reverse transcription and 1 µg of plasmid DNA in 12.5 µL water as template. No overlaying with oil was performed, elongation was carried out for 1 min and the reaction was stopped by addition of 4 µL of 2x SHAPE loading dye to each tube. For sequencing gel electrophoresis, different sizes of gels with the composition listed in Table 31 were poured.

Table 31: Composition of sequencing gels

	Component
6 M	urea
1x	TBE
33-67% (v/v)	ROTIPHORESE Gel 30 (Carl Roth)
1% (v/v)	10% APS, added last
0.1% (v/v)	TEMED, added last

The polymerized gels were pre-run for 30 min at 20 W in 1x TBE buffer. Samples were denatured for 3 min at 65 °C and loaded into gel pockets along with sequencing ladder, and

electrophoresis was performed at 25 W. Subsequently, gels were imaged using the 700 nm channel of an Odyssey Classic Imaging System with corresponding software.

8.6 Protein biochemistry

8.6.1 Bradford assay for protein quantification

For determination of protein concentration by Bradford assay, 5x ROTIQuant (Carl Roth, Karlsruhe, Germany) was diluted to 1x with water and 900 µL were mixed in cuvettes with 100 µL of bovine serum albumin solutions ranging from 0 to 150 mg/mL. Furthermore, 10 µL of diluted or undiluted protein lysates were mixed with 990 µL 1x ROTIQuant in cuvettes. After 5 min at RT, all samples were measured at an Amersham Ultrospec 3300 pro photometer at a wavelength of 595 nm and a standard curve was created by plotting the absorbances against the respective concentrations for the bovine serum albumin samples. Using this curve and the measured protein lysate absorbances, corresponding concentrations were calculated while also taking possible dilution factors into account.

8.6.2 CARPID

In order to design *P4*-specific gRNAs, rough regions of the *P4* full-length transcript suitable for RNA-mediated targeting were identified using the web-based siMAX siRNA Design Tool (Eurofins Scientific, Luxembourg City, Luxembourg) and siRNA Target Finder (GenScript Biotech, Piscataway, USA)[279,280]. Based on this, pairs of *P4*-complementary sequences with GC-content between 40% and 60%, a length of 22 nt and a distance of 16-20 nt from each other were manually picked[237]. Sequences with both the highest percentage of non-pairing bases in full-length *P4* as predicted by RNAfold and least potential off-targets as identified by the blastn algorithm were considered favorable gRNAs for further downstream experiments[186,237,241]. Pre-gRNA sequences with a length of 30 nt were obtained by adding eight more *P4*-complementary bases to the 3' end of the respective gRNAs[281]. Arrays of paired pre-gRNAs were designed by fusing 30 nt CasRx direct repeats to the 5' end, between both pre-gRNAs and to the 3' end[281].

NKCs were doubly transduced with the necessary constructs and treated with biotin (see page 106) before they were harvested and lysed (see page 126) in CARPID lysis buffer and protein concentration was determined (see page 122 above). 40 µL of MyOne Streptavidin C1

Dynabeads (Thermo Fisher Scientific, Waltham, USA) were washed three times by rotating for 10 min at 4 °C with 400 µL CARPID lysis buffer and supernatant was for these and subsequent separated and discarded by fixing the beads with a magnetic rack. Washed beads were incubated with 2 mg of the protein lysates in 1 mL for 2 h at 4 °C on a rotator followed by four further washing steps for 10 min at 4 °C, either with 1 mL of CARPID lysis buffer or CARPID wash buffer. At the last washing step, beads were transferred into a new reaction tube and 25% of beads were put aside for SDS-PAGE (see page 127) with subsequent Coomassie stain (see page 123 below). The remaining beads were rotated three times for 10 min at 4 °C with 1 mL of 50 mM ammonium bicarbonate. Next, beads were shaken for 1 h at 30 °C and 400 rpm in 50 µL of CARPID elution buffer 1, the supernatant saved and the beads eluted twice more for 1 h at 30 °C and 400 rpm in 25 µL CARPID elution buffer 2. 250 ng trypsin were added to the pooled eluates and incubated overnight at 37 °C. On the next day, the tryptic digest was stopped by addition of 4 µL 10% formic acid before samples were submitted for mass spectrometric analysis (see page 125).

8.6.3 Coomassie staining

To achieve unspecific Coomassie staining of proteins, gels were rinsed three times for 10 min in water after SDS-PAGE (see page 127). Next, gels were covered with SimplyBlue SafeStain (Thermo Fisher Scientific, Waltham, USA) and shaking incubated for 1 h at RT. Gels were destained by discarding the Coomassie dye and shaking incubating them in 200 mL water for 1 h at RT, followed by another destaining step in water overnight at 4 °C. At the next day, gels were scanned using the 700 nm channel of an Odyssey Classic Imaging System.

8.6.4 FLAG-immunopurification

As prerequisite for purification of FLAG-tagged proteins, HEK293T cells were transfected to overexpress corresponding proteins (see page 100) ahead of cell lysis (see page 126). 50 µL of Pierce α-DYKDDDDK Magnetic Agarose beads (Thermo Fisher Scientific, Waltham, USA) per mL of protein lysate were washed twice for 20 minutes at 4 °C with 10 volumes of protein lysis buffer and supernatant was removed in these and following steps by fixing the beads with a magnetic rack. Protein lysates were added to the washed beads and incubated for 2 h at 4 °C on a rotating wheel. Next, beads were washed three times by rotating for 10 min at 4 °C with 1

mL IP wash buffer each. Bound proteins were eluted from the beads by adding one bead volume of FLAG elution buffer and shaking for 30 min at 4 °C on a Mixer 5432 at full speed. The eluate was collected and the elution step repeated once more before pooling both eluted fractions and determining their total protein concentration (see page 122).

8.6.5 HA-immunoprecipitation

In order to obtain material for subsequent HA-IP experiments, NKCs were lentivirally transduced (see page 104) to ectopically express HA-tagged proteins of interest. Following that, cells were lysed (see page 126) and protein concentration was determined (see page 122). For HA-IP, α-HA.11 epitope antibody (BioLegend, San Diego, USA) was diluted 1:100 in 10 µg to 1.5 mg of protein lysate in final volumes of 500 µL to 1 mL of protein lysis buffer and mixtures were rotated for 1 h at 4 °C. As input samples, 1-30 µg of respective protein lysate were stored in duplicate. Per sample, 30 µL of Protein G Dynabeads (Thermo Fisher Scientific, Waltham, USA) were washed by rotating for 30 min at 4 °C in protein lysis buffer. For removal of supernatant in these and following steps, beads were fixed using a magnetic rack. The antibody-lysate mix was added to the washed beads and rotated for 1 h at 4 °C. Following this, beads were washed three times with 1 mL of IP wash buffer by incubating for 10 min at 4 °C on a rotator, and at the last washing steps beads were transferred into a new reaction tube. 10% of beads and one half of input samples were used for SDS-PAGE (see page 127) followed by western blot analysis (see page 128), whereas the remaining beads and other half of input samples were mixed with TRIzol reagent (Thermo Fisher Scientific, Waltham, USA) for RNA purification (see page 119). At the last washing step of purification, small volumes of ethanol were left in the reaction tube and evaporated using a Concentrator 5301. The remaining pellet was dissolved in 4 µL water and used for subsequent cDNA synthesis (see page 111) and RT-qPCR analyses (see page 119).

8.6.6 Immunofluorescent staining of keratinocytes

For immunofluorescent staining, NKCs were grown on round sterile coverslips with a diameter of 13 mm that were inserted into the wells of a 24-well plate. When cells reached sufficient confluency, they were washed once with DPBS before being incubated for 10 min at 37 °C in PFA buffer. Fixation was stopped by replacing the solution with IF stopping buffer and

incubating for another 5 min at 37 °C. Cells were washed twice with PBS before incubating them for 15 min at RT with IF wash buffer supplemented with 0.2% (v/v) Triton X-100. After three more washing steps under agitation for 5 min at RT with IF wash buffer and additional 0.05% (v/v) Triton X-100, cells were incubated on a shaker for 1 h at RT with IF blocking buffer supplemented with 0.05% Triton X-100. Again, the same three washing steps as before blocking were performed and primary antibodies were diluted to suitable concentrations in the detergent-containing IF wash buffer. 200 µL of antibody solution were added to each well and shaking incubated for 2h at RT. Four more washing steps similar those before and after blocking were performed, and dilutions of secondary antibodies in detergent-supplemented IF wash buffer were prepared. 40 µL volumes of these antibody solutions were pipetted on top of Parafilm pieces (Carl Roth, Karlsruhe, Germany), and coverslips were taken out of the wells with tweezers and placed bottom-side up on top of the diluted antibodies. The cells were incubated with the antibodies overnight at 4 °C in a humidified chamber. On the next day, coverslips were transferred back to the well-plate and one more washing step with detergent-containing IF wash buffer was performed, followed by three washes with PBS for 5 min at RT. 40 µL of DAPI Fluoromount-G mounting medium (Thermo Fisher Scientific, Waltham, USA) were pipetted onto microscope slides, and the coverslips were placed bottom-side up on top of the mounting medium. Slides were dried overnight at RT in the dark before being analyzed at a BZ-X810 fluorescent microscope.

8.6.7 Mass spectrometry-based proteomic analyses

In order to prepare protein samples for mass spectrometry, tryptic in-gel digests were performed with the exception of CARPID where proteins were digested on-beads (see page 122). Samples in 1x LDS Sample Buffer (Thermo Fisher Scientific, Waltham, USA) and 50-100 mM DTT were loaded on NuPAGE 4 to 12% Bis-Tris 1.0 mm Mini Protein Gels in 1x NuPAGE MOPS SDS Running Buffer (both Thermo Fisher Scientific, Waltham, USA) and run for 45 min at 50 V and 2 h at 90 V before Coomassie staining was performed (see page 123). Whole lanes were cut out and sliced into small pieces which were transferred to reaction tubes filled with 1mL of 50 mM ammonium bicarbonate and shaken at RT for 1 h. Subsequently, gel pieces were washed once or multiple times for 1 h at RT in 1 mL MS wash solution 3/1 until blue stain was completely removed. Next, the gel slices were washed for 30 min at RT in 1 mL MS wash solution 1/1, and for 10 min at RT in 200 µL acetonitrile. Gel pieces were lyophilized at an

Alpha 1-4 LDplus device for 1 h before adding 200 µL of MS reduction solution to each sample and incubating for 35 min at 56 °C. The supernatant was removed and 200 µL MS carbamidomethylation solution were pipetted to the gel pieces, followed by 35 min of incubation at RT in the dark. The washing steps with 50 mM ammonium carbonate, MS wash solutions 3/1 and 1/1 as well as acetonitrile were repeated and gel pieces again lyophilized for 1 h. 40 µL of MS digestion solution were added to the gel pieces, incubated at RT for 20 min, and another 40 µL added before incubating overnight at 37 °C. The supernatant was transferred to a fresh reaction tube, and proteins were extracted by incubating samples twice for 1 h at 37 °C with 100 µL of 50 mM ammonium carbonate followed by incubation at RT for 30 min with 100 µL MS wash solution 1/1. All supernatants were collected and pooled into reaction tubes suitable for lyophilization, which was performed overnight.

Subsequent mass spectrometric measurements were performed by the group of Dr. Astrid Bruckmann (Department of Biochemistry I, University of Regensburg). In short, submitted tryptic digests were run through C18 HPLC columns before being measured at a MaXis plus UHR-QTOF mass spectrometer. The resulting data was transferred to MASCOT with the ProteinScape software. Using MASCOT, reads were aligned to proteins annotated in the Swiss-Prot database with or without the addition of a putative P4 peptide[282].

8.6.8 Preparation of protein lysates from mammalian cells

Using culture dishes with high cell confluency, the medium was aspirated and cells washed once with cold DPBS. Next, 125-500 µL protein lysis buffer per 15 cm plate were added, cells scraped off and incubated in a reaction tube on ice for 20 min. Subsequently, mixtures were transferred into a Dounce homogenizer and homogenized by moving the loose pestle up and down 25 times on ice. The suspensions were spun down for 10 min at 20,000 rcf and 4 °C and supernatants were collected. Pellets were resuspended in suitable amounts of protein lysis buffer and incubated for another 20 min on ice before being mechanically disrupted with a Dounce homogenizer using the tight pestle. The homogenized mixture was pooled with the previously saved supernatant and protein concentration was determined (see page 122).

8.6.9 SDS-PAGE

For preparation of SDS protein gels, as a first step resolving gels with polyacrylamide concentrations of 10-14% containing the components listed in Table 32 were poured between two spaced glass plates up to two thirds, overlayed with isopropanol and polymerized at RT.

Table 32: Composition of protein resolving gels

	Component
1x	resolving gel buffer
33-47% (v/v)	ROTIPHORESE Gel 30 (Carl Roth)
0.6% (v/v)	10% APS, added last
0.06% (v/v)	TEMED, added last

Next, the isopropanol on top was removed and stacking gels with the composition shown in Table 33 were poured on top, a comb was inserted and the gel was polymerized at RT.

Table 33: Composition of protein stacking gels

	Component
1x	stacking gel buffer
13% (v/v)	ROTIPHORESE Gel 30 (Carl Roth)
0.6% (v/v)	10% APS, added last
0.13% (v/v)	TEMED, added last

Ahead of electrophoresis, protein samples were brought to 1x Laemmli buffer and incubated for 5 min at 95 °C before being loaded into gel pockets along with Precision Plus Protein Dual Color Standard (Bio-Rad, Hercules, USA). Gels were run in TGS for 30 min at 90 V, followed by 45 min at 150 V.

8.6.10 Silver staining

Fixation for silver staining after protein gel electrophoresis (see page 127) was achieved by immersing gels in silver stain fixing solution for 30 min followed by 10 min of washing in 50% ethanol and two more washing steps for 10 min in water. Next, gels were placed in 0.02% (w/v) sodium thiosulfate for 3 min which was removed before adding 0.1% (w/v) silver nitrate and incubating for 30 min at RT. The gel was rinsed for 10 sec in water and subsequently immersed in silver stain developing solution for up to 5 min, and the reaction was stopped by replacing the solution with 5% acetic acid. Gels were scanned and afterwards stored in 1% acetic acid.

8.6.11 Western Blot analysis

Semi-dry western blots were performed after SDS-PAGE (see page 127) by placing gels on top of an accordingly cut piece of Amersham Hybond-ECL Nitrocellulose Membrane, with three pieces of Whatman Filter Paper (both Cytiva, Marlborough, USA) soaked in Towbin transfer buffer on top and bottom of gel-membrane layers. Blot setups were placed in a Trans-Blot SD Semi-dry transfer cell and western blot was performed for 45 min at 0.25 A before membranes were blocked by shaking in SDWB blocking buffer for 30 min at RT. Next, membranes were shaking incubated for 1 h at RT with primary antibodies diluted in SDWB blocking buffer. After three membrane washes of 5 min each with TBS-T at RT, secondary antibodies were diluted in SDWB blocking buffer and membranes were incubated with agitation in the resulting mixtures for 1 h at RT or overnight at 4 °C. Following this step, membranes were again washed three times with TBS-T for 5 min each at RT and signals were subsequently detected using a Odyssey Classic Imaging System with corresponding software.

9. Appendix

9.1 Supplementary figures

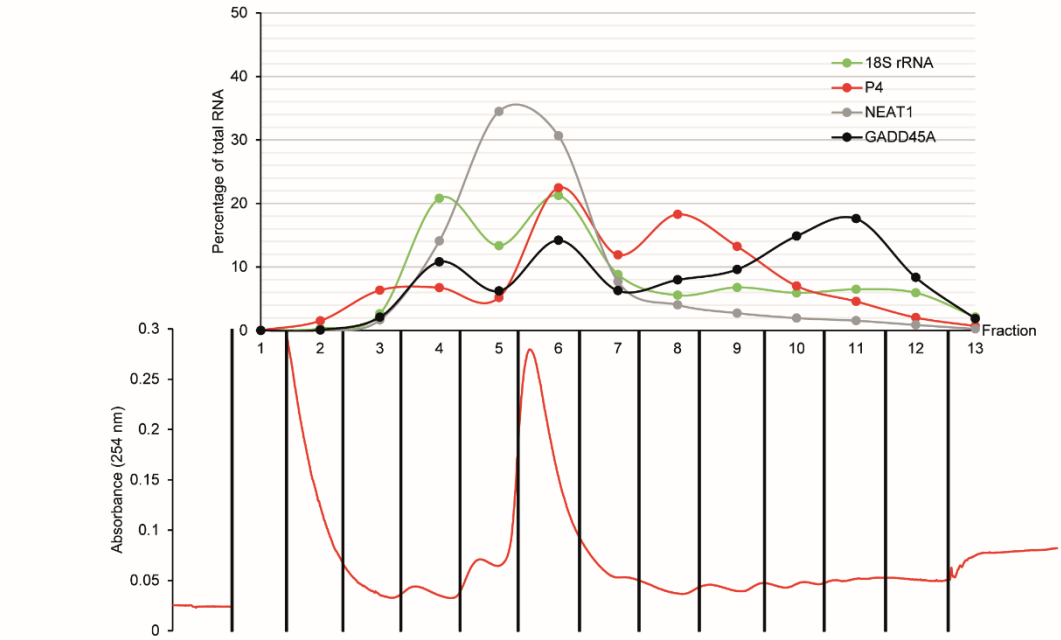

Figure S1: Runoff control for ribosome fractionation experiment. In the lysate of cells not treated with cycloheximide prior to harvest, *P4* transcripts targeted by the primers illustrated in Figure 3A are most prevalent in the fraction containing monosomes and not so much in fractions of higher density like in cycloheximide-treated keratinocytes (Figure 6B).

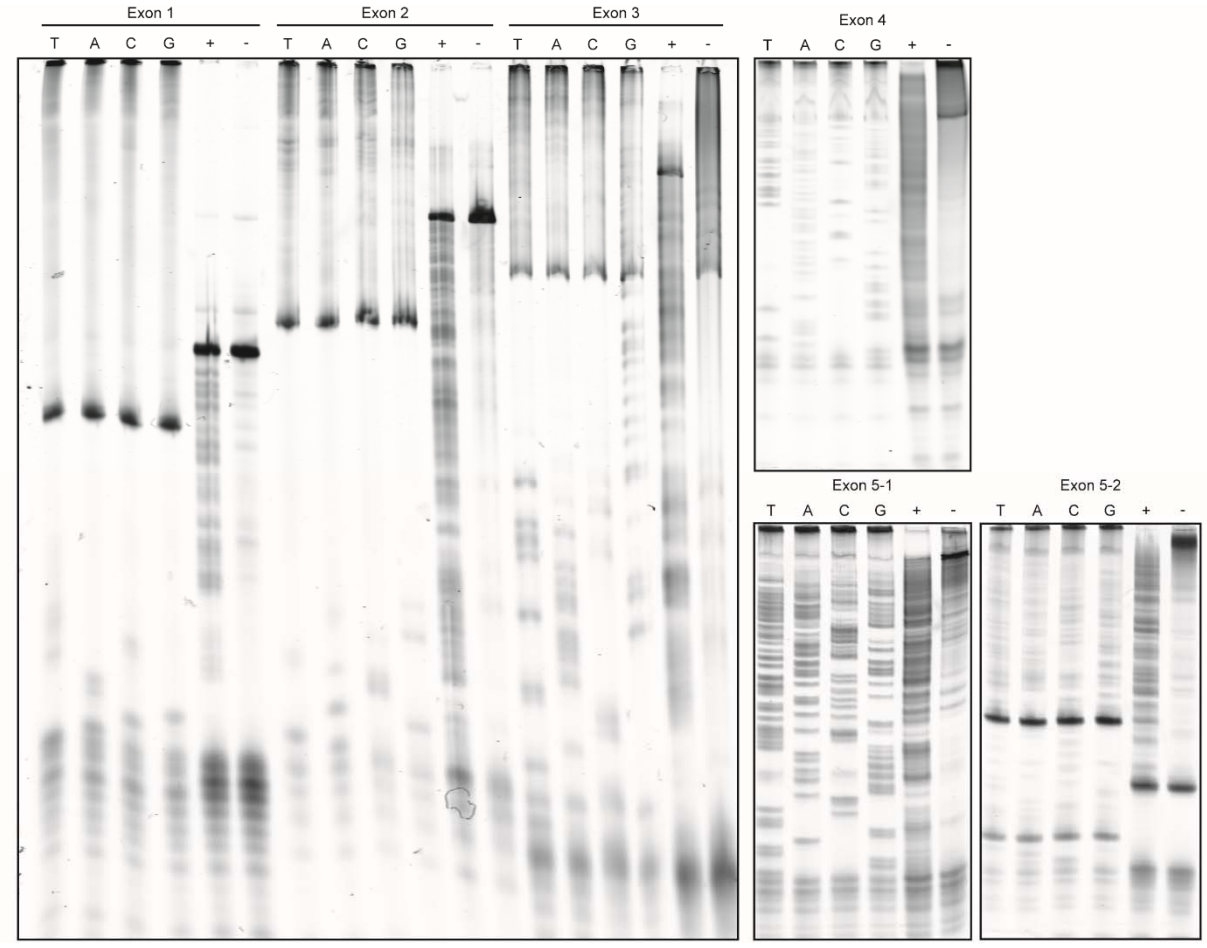

Figure S2: Sequencing gels of SHAPE reactions. A sequencing ladder composed of the 4 DNA nucleotide types enables approximate assignment of the SHAPE accessibility signals of RNA treated with NMIA (+) to the correct position in the *P4* transcript. RNA that was instead incubated only with DMSO (-) demonstrates hardly any early termination of reverse transcription.

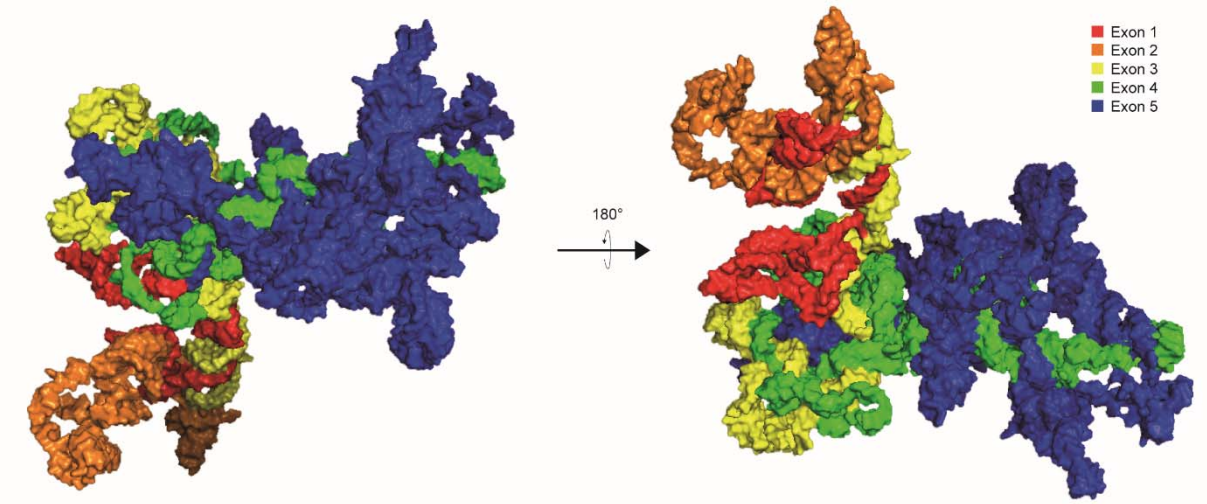

Figure S3: Predicted tertiary structure of *P4* under consideration of pseudoknots[195]. Including pseudoknots into the calculation changes the computed structure in terms of specific motifs being differently exposed towards the surface, whereas a general separation into a spread out 5' domain and a more condensed 3' region originally observed in the prediction without pseudoknots (Figure 9B) is maintained.

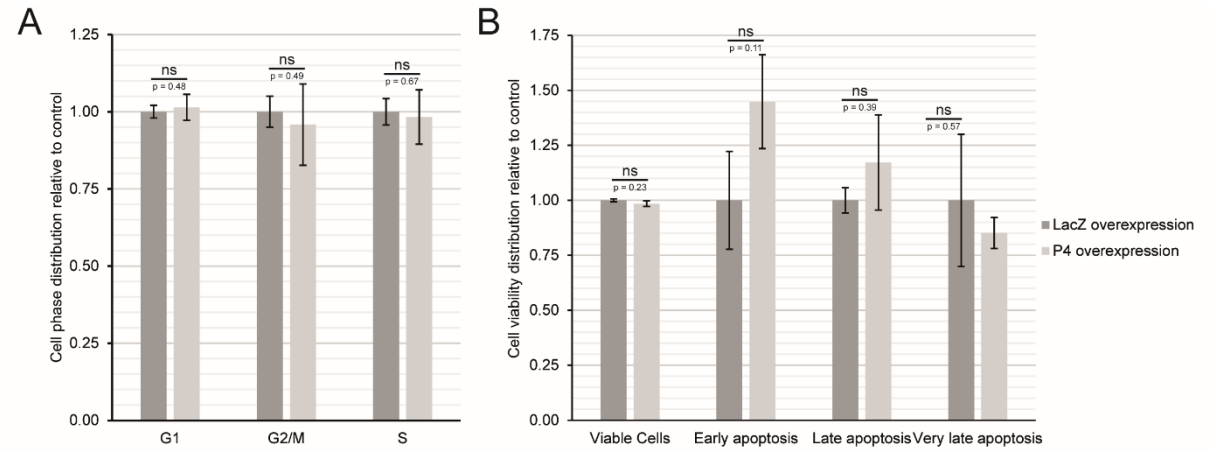

Figure S4: Effects of *P4* overexpression on cell cycle distribution and cell viability. (A) Analysis of cell phase population changes in keratinocytes with increased levels of full-length *P4*. No significant differences indicating phase shifts can be observed (N = 7-8). **(B)** Investigation of apoptotic behavior in *P4*-overexpressing cells. In comparison to the *LacZ* controls, no significant alterations are seen (N = 3).

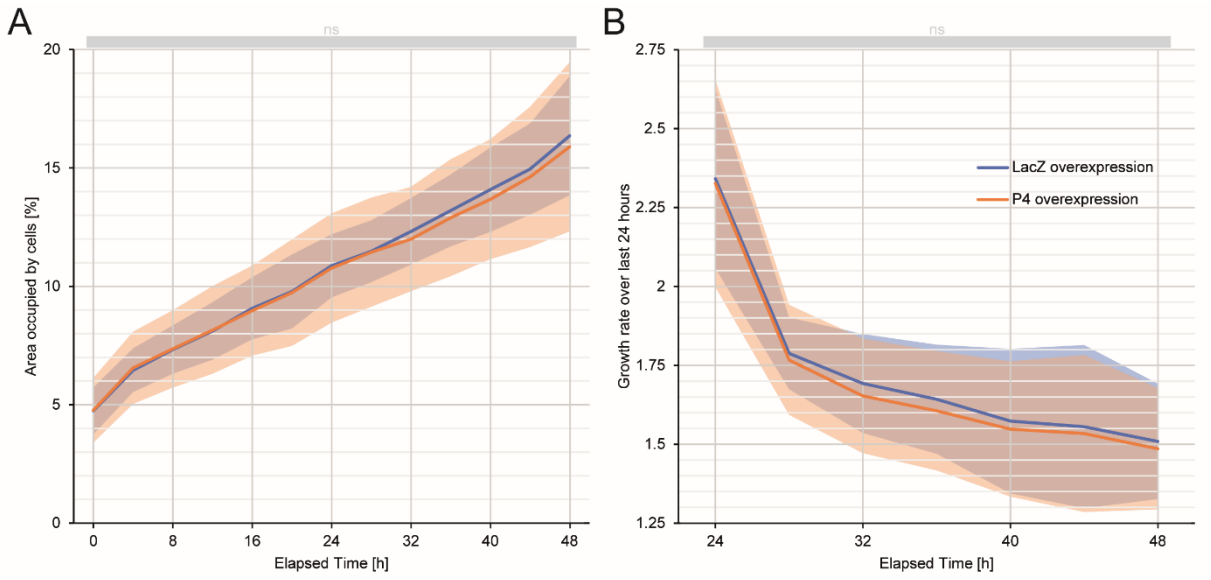

Figure S5: Live-cell-imaged growth assay of keratinocytes overexpressing full-length *P4*. (A) Absolute cell dish area covered by cells. No significant differences between *P4* and *LacZ* overexpression can be detected. **(B)** 24-hour growth rate calculated by using the formula $Area_{occ}$(hours)/$Area_{occ}$(hours-24). Similar to absolute occupancies, the slight differences that are observed between keratinocytes with high *P4* levels and the *LacZ*-overexpressing controls are insignificant (N = 21-22).

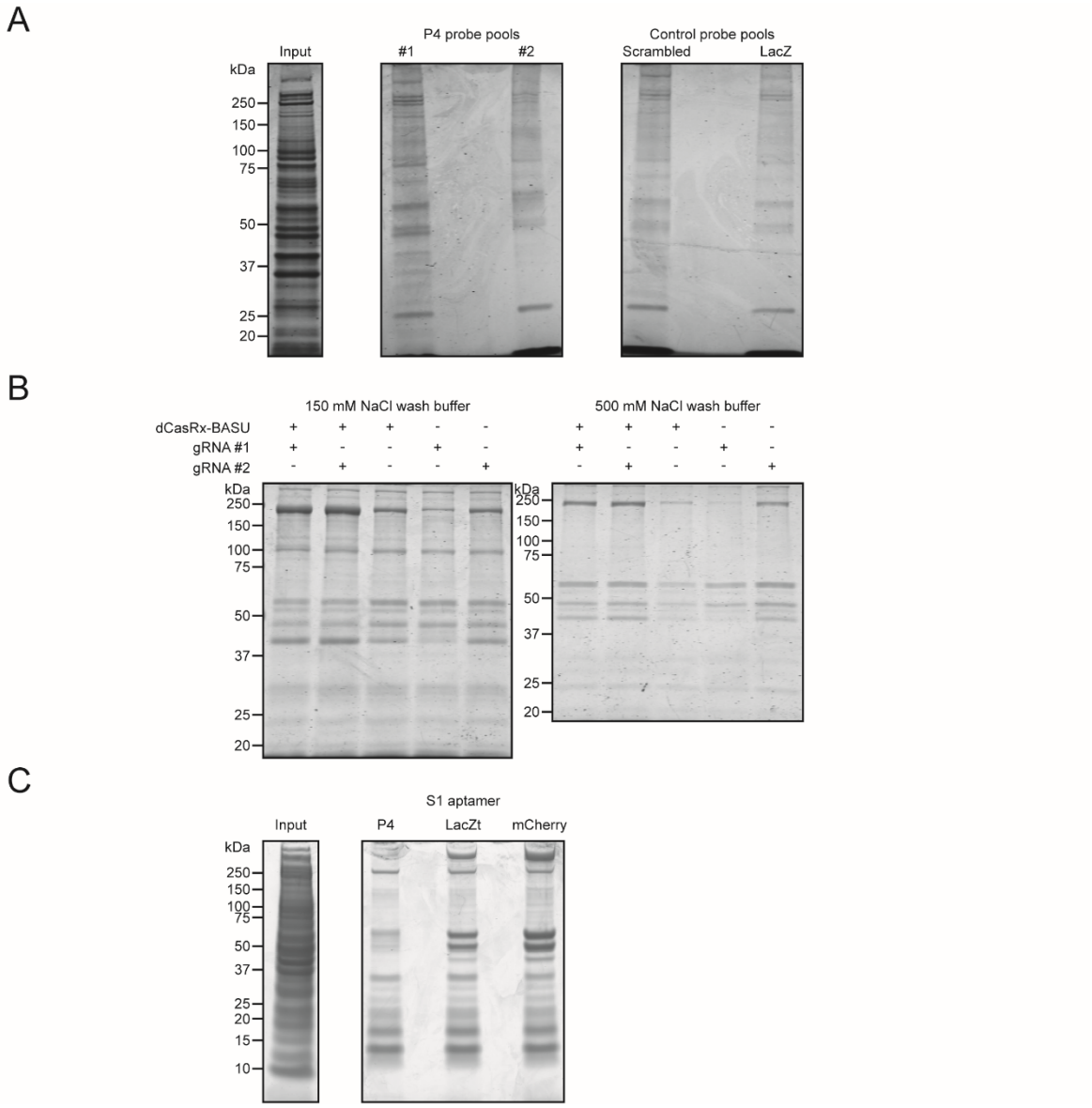

Figure S6: Gel analyses of pulldowns for *P4* interaction partner identification. (A) Coomassie stain of gel with samples resulting from ChIRP-MS pulldown. For both *P4*-complementary as well as the control probe pools, the band patterns resemble each other. Whole lanes were cut out and submitted to mass spectrometry. **(B)** SDS-PAGE followed by Coomassie stain for parts of the CARPID fractions. While no unique bands are visible for any sample, band intensities appear to be altered in some cases. The main part of the pulled down fractions was digested on-beads prior to mass spectrometric analysis. **(C)** Analysis of S1-aptamer based pulldown samples via SDS gel electrophoresis and subsequent Coomassie stain. No clear differences regarding bands between *P4*-directed and control pulldowns are detected. Entire gel lanes were cut out and used for mass spectrometric measurements.

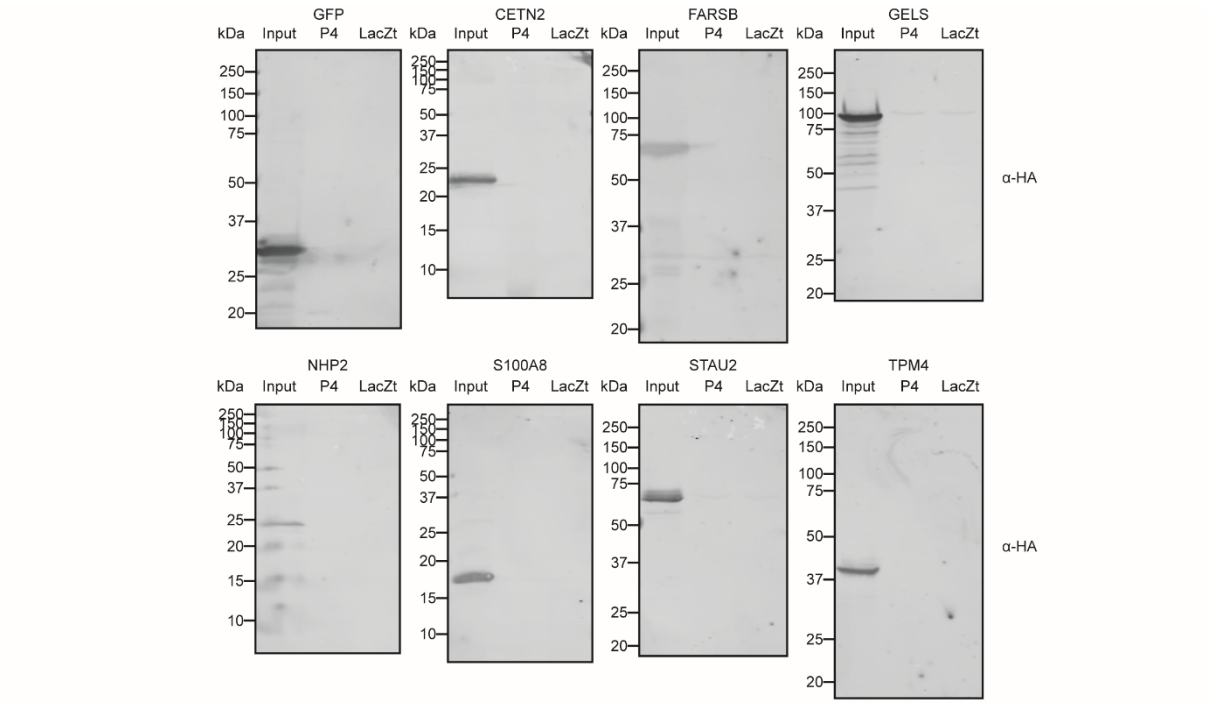

Figure S7: Western blots of aptamer-based pulldowns for validation of putative *P4* protein interactors. Hardly any of the FLAG/HA- or 3xHA-tagged proteins can be detected by an HA-directed antibody in the pulldown fractions except for GELS and STAU2, however those demonstrate similar band intensities in the *P4*-aptamer (P4) and the control *LacZt*-aptamer (LacZt) pulldown samples.

9.2 List of sequences

Table 34: List of *P4*-related and control nucleotide sequences relevant to this work

Name	Sequence (5' to 3')
P4 full-length exon 1	GCCTCAGCCAACAGCTATCTGCAGCTCATTTCCTGCTTTCTGGCCATCTTATCTCTG TCTTCAAGCATTCCTCAGCTTTCTCTTTCCAG
P4 full-length exon 2	AACAGGATTATGAACCGACACCATACAGAGGTATTTGTAAGAAAGAAGGTGGATGCC GGAATCCTTTCTTCAAACAGAAGCTTACCAGTAAGTGCAGACTAATACAACAGG
P4 full-length exon 3	CGGTAAAGAGAAGAACAGAGAAAGCATCCTGCCCCAGCCCTGCCCCAGAGCTAAACG TCATTCTAGAGAATGAAAAATTCCATCTCCACCCAGTGGGTTCTCAGAA
P4 full-length exon 4	TTGCAGAGAGATTGGAACTACAGCAAAGGTATGAACAGGTGTCACGGGGACACAGAA GAAAGAGCAGTTACTCTTCCGGAAGGTTGGAGAAGATTTTGTGAAGGTGGGGATGTT TGATTTGAACCTTGAAGAACAAGCAGAGACCCAAGAAGTACAGAAGAGGGGAGGTGG AAATAGCATGAACGAGGTGGGGCATG
P4 full-length exon 5	CAAATTCACTTTCAATTGATACAATCTTTCACGTCAGAGCTGCTTCTTGTAACACAG AAGTTTTCAGATTCTATGAAAAGGTATTGAATGAATTGAAGGCTCTGTTAAGGGGGC AACTATCTCCCCTCCCCATTCTCCTATCAGCCCATAAAACAGGAACTGACAACCTCT TGGAAGAATTGGGAAGGAACTTTTCGATTTTCTCTGTACAATCTTCACTGGTTCCTC TCTGTGAGAGGAGGAGGGACCTCTTGGATTGGTGTCGTTGGGAAAAGGGTATCAAGT GTGCATGGCTCAGCCTGTTCCTGGCTCTCTCTCTGGGACTGACCTGACTGCAAGCAG CATGTTCTCTGTCTGCTCCTGCCTCCTCCAGGCAATGAGCACCAGGGCGGGTCCAGC CCTTGCTTGGGAGGACTTCAATAGTCCAGCTGCTCTGCCGCGAGTGGGTGAGTGAGT TCAAGTCAGAGGAGAAGACACAGAAAGCTCATTTGGGCCTTGGGTCTTAGCCACATC CTCCAGTCCATCTGGACTAGCAATAAAGCTGACATTTTAATCCCTA

Name	Sequence (5' to 3')
P4 gRNA array 1	AACCCCTACCAACTGGTCGGGGTTTGAAACGGTAAGCTTCTGTTTGAAGAAAGGATT CCGAACCCCTACCAACTGGTCGGGGTTTGAAACTCTCTGTTCTTCTCTTTACCGCCT GTTGTAAACCCCTACCAACTGGTCGGGGTTTGAAAC
P4 gRNA array 2	AACCCCTACCAACTGGTCGGGGTTTGAAACTTCTTGGGTCTCTGCTTGTTCTTCAAG GTTAACCCCTACCAACTGGTCGGGGTTTGAAACTTTGCATGCCCCACCTCGTTCATG CTATTTAACCCCTACCAACTGGTCGGGGTTTGAAAC
P4 MST exon 1+2	TGCCTCAGCCAACAGCTATCTGCAGCTCATTTCCTGCTTTCTGGCCATCTTATCTCT GTCTTCAAGCATTCCTCAGCTTTCTCTTTCCAGAACAGGATTATGAACCGACACCAT ACAGAGGTATTTGTAAGAAAGAAGGTGGATGCCGGAATCCTTTCTTCAAACAGAAGC TTACCAGTAAGTGCAGACTAATACAACAGG
P4 MST exon 3+4	CGGTAAAGAGAAGAACAGAGAAAGCATCCTGCCCCAGCCCTGCCCCAGAGCTAAACG TCATTCTAGAGAATGAAAAATTCCATCTCCACCCAGTGGGTTCTCAGAATTGCAGAG AGATTGGAACTACAGCAAAGGTATGAACAGGTGTCACGGGGACACAGAAGAAAGAGC AGTTACTCTTCCGGAAGGTTGGAGAAGATTTTGTGAAGGTGGGGATG
P4 MST exon 5-1	TTTGATTTGAACCTTGAAGAACAAGCAGAGACCCAAGAAGTACAGAAGAGGGGAGGT GGAAATAGCATGAACGAGGTGGGGCATGCAAATTCACTTTCAATTGATACAATCTTT CACGTCAGAGCTGCTTCTTGTAACACAGAAGTTTTCAGATTCTATGAAAAGGTATTG AATGAATTGAAGGCTCTGTTAAGGGGGCAACTATCTCCCCTCCCC
P4 MST exon 5-2	ATTCTCCTATCAGCCCATAAAACAGGAACTGACAACCTCTTGGAAGAATTGGGAAGG AACTTTTCGATTTTCTCTGTACAATCTTCACTGGTTCCTCTCTGTGAGAGGAGGAGG GACCTCTTGGATTGGTGTCGTTGGGAAAAGGGTATCAAGTGTGCATGGCTCAGCCTG TTCCTGGCTCTCTCTCTGGGACTGACCTGACTGCAAGCAGCAT
P4 MST exon 5-3	GTTCTCTGTCTGCTCCTGCCTCCTCCAGGCAATGAGCACCAGGGCGGGTCCAGCCCT TGCTTGGGAGGACTTCAATAGTCCAGCTGCTCTGCCGCGAGTGGGTGAGTGAGTTCA AGTCAGAGGAGAAGACACAGAAAGCTCATTTGGGCCTTGGGTCTTAGCCACATCCTC CAGTCCATCTGGACTAGCAATAAAGCTGACATTTTAATCCCTA
P4 nanopore read #1	CTCAGCCATAGCAACTTGCAGCTCATTTCCTGCTTTCTGGCACATCTTATTTCCACT GTTTCGATACTCCTAGCTCTTCTCTTCCAGAACAGATACGATTCGTTACTGCATCCA ACCAAGAGGTATTGTAAGTAGAAGGTGGATGCCGGAAACCACTTTCATCAAACAGAA GCTTACCAAAGTTGTAAGACTAATTTCAACAGGCGGTAAAAGAGAAGAACAGAGAAG CATCCTGCCCAGCCTGCTCCAGAGCTAAACGTCAACTCTAGAATGAAAAAAATTCCT TACATCTCCACGAAGTGGGTTTCAGAATTCCAGAGATTGGAACTCAAATCTGATGAC TGCAGGTGTCACGGGGACACAGAAGAAAGAATGGTTCACTTCCAAAGAAGGTTAGAA GATAGATTTTGCAACTAAGGTGGGGATGCTTGACTTGAACCTTGAAGAAGAACAAAG AGACCCAAAGAAGTACAGAAGGTGGAAATAGCTGTTGAACGAAGGTGGGGCATGCAA TTCTTTATGATACAATTCTTACGCAAGAGCTGCTCTTCTTGTAACACAGAAGTCTTC AGATTTCATGCTGAAAAGGTATTGAATGAATTGAAGAATCTGTTAAGGGCAACTATC TCCCCTCCCCATTCCTATCAGCCCAAAACAGGAACTGATACTCCTCTGGAAGAGAAT TGGGAAGGAACTTTTGATTCTTGTCGTTTCACTGGTTCCTCACACCGTGAGAGGAAT CCCTTCTTGGTTGGTGTATTGGGAAAGGGTAACAAGTGTGGCTCAGCCAGTTCCAAG GCTTCATCAAAAGCTTGGACCTGACTGCAAGCAGCTCGTTTTGTCTGCTCCTGCCTC CAGGCAATGAGCACCAGGCGGGTCCAACAGCCTCACTGCTTGGGAGGACTCTTAGCG GTCCGGCTGCTCTGCCGCCGAGTGGTGAGTGAGTTCCAAGTCAGAGGAGCACACAGA AAGCTCATACTGGGCCTTGTCTTGCACACCCAGTCCACTTGACTGCAATAGCTGCGC
P4 nanopore read #2	GCCAACAGCTAAACATCTGCAGCTCATTTTTCCTGCTCTTCTGGCCATCTTATCTCT GTCTTCTGACTCCTCAGCTTTTCCAGAACAGGATTATGATCGACACCATACAGAGGT ATTGTAAGAAAGAAGGTGGATGCCGGAATCCTCTCTTCAAACAGAAGCTACCAGTAA GTGCAGACTAAATACAACAGGCGGTAAAGAGAAGAACAGAGAAAGCATCCTGCCCAG CCCTGCCCCAGAGCTAAACGTCACTCAAGAGAATGAAAAATTCCATCTCCACCCAGT GGGTTCTCAGAATTCCAGAGATTGGAACTACAGCAAAGGATATGAACAGGTGTCAGG GACCAGAAGAAAGAGCAGTTACTCACAGAAGGTTGGAGAAGATTTGTGAAGGTGGGG ATGTTTGATTTGAACCTTGAAGAACAAGCAGAGACCCAAGAAGTACCGGAGAGGGAG

Name	Sequence (5' to 3')
P4 nanopore read #3	GTGGAAATAGCATGAACGAGGTGGGGCATGCAATATTTCTTTTTCAATTGATACAAT CTTACGTCAGAGCTGCTTTTGTAACACAGAAGTTTCAGATTATGAAAAGGTATTGAA TGAATTGAATCTGTTAAGGGGCATTATACCCTCCCCATTCTCCTATCGGCCCATAAA CAGGAACTGACAACCTTCTTGGAAGAATACTGGGAAGGAACATGATCTTTCTGTACA ATTTCACTGATCCTCTGTGAGAAGGAAGGTCCCTTGGATTGGTGTCGTTGGAAAAGG GTATCAAGTGTGCTGGCTCAGCCTGTTCAGGCTCTCTCACTGGACTGACCTGACTGC AAGCAGCATGCTTTTAGTCGCTCCTGCCTCCAGGCAATGAGCACCAGGGCGGGTCCA GCCCTTGCTTGGGAAGAGCATTCAGCAGTCCAGCTGCTCTGCCGCGAGTGAGTGAGT GAGATCAAGTCAGAAGAGGAGAAGACACAGAGCTCATTTGGGCCTTAGGTCTTAGCC ACTCCAAGTCCATCTGGACTAGCAATAAAGCTGACATTTTGC
P4 nanopore read #4	AGCTATCTGCAGCTTACTCCTGCTTTGGCCATCTATCTCTGTCAAGCATTCCTCAGC TCTCTCTTCCAGAACAGGATTATGATCGACACCATACAGAGGTATTTGTAAGAAGGA AGGTGGATGCCGGAATCCTCTTCAAACAGAAGCTACCAGTAAGCGACTAATAACAGG CCGGTAAGAGAAGAACAGAGAAAGCATCCTGCCCCAGCCCTGCCCCCCAGAGCTAAA CGTCATCTAGAGAATGAAAAATTCACTACTCCACCCGGTGGGTTCTCCTAGAATTCC AGAGAGATTGGAACTACAGCAAAGGTATGAACAGGTGTCACAGGACACAGAAGAAAG AGCAGTTACTCTTCCGGAAGGTTGAAGATTTGAAGGTGGGGATGTTTGATTTGAACC TTGAAGAACAAGCAGAGACACCAAGAAGTACAGAAGAGGGAGGTGGAAATAGCCGAA CGAGGTGGGCATGCAATTCACTTTCAATTGATACAATTCTTCACGTCAGAGCTGCTT TGTAACACAGAAGTTTTCAGATTCATGAAAAGGTATTGAATGAATTGAAGGCTCTGT AAGGGTTACTATCTCCCTCCCCATTCTCCATCAGCCCAAAACAGGAACTGACAACCT CTTTGGAAGAATTGGGAAGGAACTTCGATTCTTTTGTTCAATCTCACTGGTTCCTCT GTGAGAGGAGGAGGGTCCTCTTGGATTGGTGTCGTTGGGAAAGGGTATCAAGTGTGC GTGGCTCAGCCTGTTTCAGGCCTCTCTGGGACATTGACCAGCACTGCAAGCAGCATG TTCTCTGTCTGCTCCGCCTCCAGGCAATGAGCACCAGGCGGGTCCAGCCCACTGCTG GGACCAATAGTCCAGCTGCTCTGCCGCGAGTGGTGAGTGAGTTCAAGTCAGAGGAGA AGAAGACACAGAAAGCTCATTAAGGCCTTGGGTCTTAGTTCCATCAGCATTAGCAAT AAAGCTGACG
P4 nanopore read #5	AGCTCATTTCCTGCTTTCTGGCCATTTATCTCTGTCTTCAAGCATTCCTCTCAGCTT CTCTTTCCAGAACGGATTATGATCGACACCATACAGAGGTATTTGTGGGAGAAGGAA GTTGGATGCGGAATCCTTTTCTTCAAACAGAAGTTACCAGTAAGTGCAGACTAAATA CAACAGGCGGTAAAAGAGAAGAACAGAGAAAGCAACCCTGCCCAGCCCTGCCCCAGA GCTAAACGTCATTCTAGAGAAAAATCTCCATCCACCCAGTGGTTCAAGAATTCCAGA GAGATTGGAACTACAGCAAAGGTATGAACAGGTGCTTACGGGGACACAGAAGAAAGA GCAGAGTTACTCACAGAAGGTTGGAAGGAAGATTTTGCGAAGGTAGGATGTTTGATT TGAACCTTGAAGAACAAGCAGAGACCCAAGAAGTACAGAAGAGGGAGGTGGAAAATA GCATGAGGTGGGCATGCAATACTTCAATTGATACAATCTTTACGTCAGAGCTGCTTC TGTAACACAAGAAGTTACAAGATTTTATGAAAAGGTATTGAATGAATTGGAAGGCTG TTAAGGGCAACTATCTCCCCTCCCATTCCTATCAGCCCAACAAAACAGGAACTGACA ACCTCACTTGGAAGAATTGGGAAGGAACTTTTCGATTTCTGTCTGTTTACTAGCACA TCTGTGAGAGGCACCTTCTTGGATTGGTGTCGTTGGGAAAAGGGTATCAGTGTGCAA TGGCTCAGCCTGTTCCTGGCTCCACTGGGACCCATTTGCTGCAAGCAGCCGTTCTGT CTGCTCCTGCCTCCAGGCAATGAGCACAAGGGCGGGTCCAGCCCTTGCTAAGGGGAC CTTTGTATGGTCCAGCTGCTCTGCCGCGAGTGGGTGAGTGAGATCAAGAAGTCAGAA GGAAGACACAGAAAGCTCATTTGGGCCTTGGTCTTAGCCACATCCGGGGACTAG
P4 nanopore read #5	TCTGGCCATTTATCTGTCTTCAAGCATTCCTAGCTTTTTCTCTCCAGAACAGGATTA TGATCGACATCAAGAGGTATTTGTAAGAAGGAAGGTGGATGCCGGAATCCTTTCTTC AAACAGAAGCTACCAGTAAGTGCAGACTAAATACAACAGGCGGTAAAGAGAAGAACA GAGAAAGCATCCTGCCCAGCCCTGCCCCAGAGCTAAACGTCATTTTAGAGAATGAAA AATTCCATCTCCACCCAGTGGGTTCTCAGAATCCAGAGAGATTGGAACTCAGCAAAG GTATGAACAGGTGTCACAGGGACACAGAAGAAAGAGCAGTTACTTTCCGGAAGGTTG GAGAAGATTTGTGAAGGTGGGATGTTTTGATTTGAACCTTGAAGAACCAGAGACCAA GAAGTACACAGAAGAGGGAGGTGGAAATAGCATGAACGAGGTGGGCATGCAATATTC

Name	Sequence (5' to 3')
	ACTTCAATTGATACCGTTACATCAGAGCTGCTTTGTAACACAGAAGTTTCAAGATTC TATGAAAAGGTATTGAATGAATCGATTCTGTTAAGGGGCAACTATCTCCCTCCCCAT TCTCCTATCAGCCCATAAAACAGGAACTGACAACCTCTTGGAAGAATTGGGAAGGTA TTTTTTCGATTTCACTGTCCAATTTCACTGGTTCCTCTGTGAGAGGAGGGTCCTCTT GGATTGGGTGTCGTTGGGAAAAGGGTATCAAGTGTGCATGGCTCAGCCTGTTCCTGG CTCTACCACCTTTGGTCTGACCTGACTGCGAAGCAGCATGCTCTGTCTGCTCCTGCC TCCTCCAGGCAATGAGCACCAGGCGGGTCCAGCCTCCATTGCTTGGGAAGCTCTTTA ATAGTCCAGCTGCTCTGCCGCGAGTAAGTGAGAAGGATCAAGTCAGAGGAAGACACA GAAAGCTCATTTGGGCCTTAGGTCTTAGCCACATCCAGTCCATCTGGACTAGACTAA GTTCCAATCCTAACCCATTATCAATTAATTAACTAAACATCCTCTGCTCCAATTCAA AT
P4 nanopore read #6	TATCTGTCACCAAGATACTCCTCAGCTTTCTCCAGATCAGGATTATGAACCGACACC ATACAGTTATTGTAAGAAAGAAGGTGGATGCCGGAATCCTTTCAATGGCTTACCAGC GGTAAGAGAAGAACAGAGAAAGCATCCTGCCCAGCCCTGCCCCAGAGCTAAACGTCA TTCTAGAATGAAAAATACTTCCACCACCCAGTGGGTTCCCAGAATTCCAGAGATTGG AACTACAGCAAAGGTATGAACAGGTGTCACGGGGACACAGAAGAAAGAGCAGTTACT CTTCCGGAAGGCTGGAGAAGATTTGTGAAGGTTGGATGTTTGATTTGAACCTGAAGA ACAAGCAGAGACCCAAGAAGTACAGAAGAGGAGGTGGAAATAGCATGAACGAGGTGG GGGCATGCAAATTCACTTTCAATTGATACAATCTTACGTCAGAGCTGCTTTGTATCA GAAGTTTCAGATTCTATGAAAAGGTATTGAATGAATTGAAGGCTCTGTTAAGGGGCA TTATCTTCCCTCCCCATTCTCCTATGTCCCAAACAGGAACTGACAACCTCTTGGAAG AATTGGGAAGGAACCGATTTCTCTGTACAATCTTCTGGTATCCTGTGAGAGAGGTCC TTGGATTGGTGTCGTTGGGAAAAGGGTATCAAGTGTGCGTGGCTCAGCCTGTTCCTG GCTTCACCTCTGGGTCTGACCTGACTGCGGCAGCATGTCTCTGTCTGCTCCTGCCTC CAGGCAATGAGCACCAGGCGGGTTCCAGCCTCATTGCTTGGGAGGACTTCAATGGTC CAGCTGCTGCCGCGAGTGGGTGAGTGAGTTCAAGTCAGAGGAGAAGACACAGAAAGC TCATTGGGCCTTGGTCTTAGCCACTCCAGTCCATCTGGACTAGCAATAAGCTGACAT TTTGCCCTGACT
P4 nanopore read #7	GTTCAAGCATTCCTAGCTTCTCTTTCCCAGAGATTGGATTCTCCAGCAAAGGTATGA ACAGGTGTCACAGGACACAGAAGAAAGAAAATAGTTACTTTCCGGAAGGTTGGAGAA GATTTGTGAAGGTGGGATGTTTGATTTGAACCTTGGAAGAACAAGCAGAGACCAAGA AGTACAGGAGGTGGAAATAGCATATGAACGAGGTGGGGCATGTAAATATCTTCGCTG ATACAATCTCGCAAGAGCTATTTTGAACATCAGAGTGGTTCAGATTCCTTTATGAAA AGGTATTGAATGAATTGAAGGCATCTGTTAAGGGCAACTATACCTCATCCCTTCCCA TTTTCCTATCAGCCCATAAAACAGGAACTGACAACCCTTGGAAGAATTGGGAAGGAA CATGATTTCCCTTGTACGTTTCTGGTTCCTCTTGTGTGAGAGGGGACCTCTTGGATC GGTGTGCTGGGAAAAGGTCAAGTGCGCATGGCTCAGCCTGGTTTCCTGGCTCAAAGC TGACCTGACTGCAAGCAGCGCTTCTGTCTGTCCTGGCCTCCTCCAGGCAAATGAGCA CCAGGCGGGTCCAGCCCACTGCCTGGGAGGACCAATGGTCCAGCTCTGCCAACGGTG GGTGAGTGAGTTCAAGTCAGAGGAGAAGACACAGAAAGCTTTGGCCTTGAGGTCTTG CACATCCAAGCCATCTGGACTAGCAGCTG
P4 nanopore read #8	CCCAGTGGGTTTCAGAATTCCAGAGATTGGAACTACAGCAAAGGTATGATAGGTGTC GCGGGACACAGAAGAAAGAGCAGTTACTCTTCCGGAAAGTTGAGAAGATTTGTGAAG GTGGGATGTTTGATTTGAACCTTGAAGAACAGAGACCCAAGAAGTGCAGAAGAGGGA GGTGGAAATAGCCGAACGAGGTGGGGGCATGCAATCTCAATTGATACAATCTTTTCA CAGAGCTGCTTCTTGTATCAAGAAGTTTCAGATATGAAAAGGTATTGAATGAATTAA AGAAATCTGCTAAGGGCAACTATCTCCCTCCCCATTCTCCATCAGCCTCCATAAAAA CAGGAACTGACAACCTCTTGGAAGAATTGGGAAGGAACCGATTTCTGTACAATTTCA GCTCCTCTCTGTGAGAGGAGGGACCTCTTGGACTGGTGTCGTTGGGAAAAGGGTATC AAGTGTGCTGGCTCAGCCTGTTCCTGGCTCTACCACCTCTGTATTGACCTGACTGCA AGCAGCATGTTCTGTCTGCTCCTGCCTCCAGGCAATGAGCACCAGGCGGGTCCAGCC CACTGCTTGGGGGAGGCTTATAGTCCAGCTGCTCGCCAAGTGGTGAGTGAGATCAAG

Name	Sequence (5' to 3')
	TCAGAGGAAGACACAGAAAAAGCTCATTGGGCCTAAGGTCTTAGCCTTTACACCAGT CCACTTGGACTAGCAAAGCTG
S1-aptamer *LacZt*	ATGATAGATCCCGTCGTTTTACAACGTCGTGACTGGGAAAACCCTGGCGTTACCCAA CTTAATCGCCTTGCAGCACATCCCCCTTTCGCCAGCTGGCGTAATAGCGAAGAGGCC CGCACCGATCGCCCTTCCCAACAGTTGCGCAGCCTGAATGGCGAATGGCGCTTTGCC TGGTTTCCGGTACCAGAAGCGGTGCCGGAAAGCTGGCTGGAGTGCGATCTTCCTGAG GCCGATACTGTCGTCGTCCCCTCAAACTGGCAGATGCACGGTTACGATGCGCCCATC TACACCAACGTAACCTATCCCATTACGGTCAATCCGCCGTTTGTTCCCACGGAGAAT CCGACGGGTTGTTACTCGCTCACATTTAATGTTGATGAAAGCTGGCTACAGGAAGGC CAGACGCGAATTATTTTTGATGGCGTTAACTCGGCGTTTCATCTGTGGTGCAACGGG CGCTGGGTCGGTTACGGCCAGGACAGTCGTTTGCCGTCTGAATTTGACCTGAGCGCA TTTTTACGCGCCGGAGAAAACCGCCTCGCGGTGATGGTGCTGCGTTGGAGTGACGGC AGTTATCTGGAAGATCAGGATATGTGGCGGATGAGCGGCATTTTCCGTGACGTCTCG TTGCTGCATAAACCGACTACACAAATCAGCGATTTCCATGTTGCCACTCGCTTTAAT GATGATTTCAGCCGCGCTGTACTGGAGGCTGAAGTTCAGATGTGCGGCGAGTTGCGT GACTACCTACGGGTAACAGTTTCTTTATGGCAGGGTGAAACGCAGGTCGCCAGCGGC ACCGCGCCTTTCGGCGGTGAAATTATCGATGAGCGTGGTGGTTATGCCGATCGCGTC ACACTACGTCTGAACGTCGAAAACCCGAAACTGTGGAGCGCCGAAATCCCGAATCTC TATCGTGCGGTGGTTGAACTGCACACCGCCGACGGCACGCTGATTGAAGCAGAAGCC TGCGATGTCGGTTTCCGCGAGGTGCGGATTGAAAATGGTCTGCTGCTGCTGAACGGC AAGCCGTTGCTGATTCGAGGCGTTAACCGTCACGAGCGGATCCATGGGACCGACCAG AATCATGCAAGTGCGTAAGATAGTCGCGGGCCGGGCCATG
S1-aptamer *mCherry*	ATGGTGAGCAAGGGCGAGGAGGATAACATGGCCATCATCAAGGAGTTCATGCGCTTC AAGGTGCACATGGAGGGCTCCGTGAACGGCCACGAGTTCGAGATCGAGGGCGAGGGC GAGGGCCGCCCCTACGAGGGCACCCAGACCGCCAAGCTGAAGGTGACCAAGGGTGGC CCCCTGCCCTTCGCCTGGGACATCCTGTCCCCTCAGTTCATGTACGGCTCCAAGGCC TACGTGAAGCACCCCGCCGACATCCCCGACTACTTGAAGCTGTCCTTCCCCGAGGGC TTCAAGTGGGAGCGCGTGATGAACTTCGAGGACGGCGGCGTGGTGACCGTGACCCAG GACTCCTCCCTGCAGGACGGCGAGTTCATCTACAAGGTGAAGCTGCGCGGCACCAAC TTCCCCTCCGACGGCCCCGTAATGCAGAAGAAGACCATGGGCTGGGAGGCCTCCTCC GAGCGGATGTACCCCGAGGACGGCGCCCTGAAGGGCGAGATCAAGCAGAGGCTGAAG CTGAAGGACGGCGGCCACTACGACGCTGAGGTCAAGACCACCTACAAGGCCAAGAAG CCCGTGCAGCTGCCCGGCGCCTACAACGTCAACATCAAGTTGGACATCACCTCCCAC AACGAGGACTACACCATCGTGGAACAGTACGAACGCGCCGAGGGCCGCCACTCCACC GGCGGCATGGACGAGCTGTACAAGTAAGGATCCATGGGACCGACCAGAATCATGCAA GTGCGTAAGATAGTCGCGGGCCGGGCCATG
S1-aptamer *P4*	TGCCTCAGCCAACAGCTATCTGCAGCTCATTTCCTGCTTTCTGGCCATCTTATCTCT GTCTTCAAGCATTCCTCAGCTTTCTCTTTCCAGAACAGGATTATGAACCGACACCAT ACAGAGGTATTTGTAAGAAAGAAGGTGGATGCCGGAATCCTTTCTTCAAACAGAAGC TTACCAGTAAGTGCAGACTAATACAACAGGCGGTAAAGAGAAGAACAGAGAAAGCAT CCTGCCCCAGCCCTGCCCCAGAGCTAAACGTCATTCTAGAGAATGAAAAATTCCATC TCCACCCAGTGGGTTCTCAGAATTGCAGAGAGATTGGAACTACAGCAAAGGTATGAA CAGGTGTCACGGGGACACAGAAGAAAGAGCAGTTACTCTTCCGGAAGGTTGGAGAAG ATTTTGTGAAGGTGGGGATGTTTGATTTGAACCTTGAAGAACAAGCAGAGACCCAAG AAGTACAGAAGAGGGGAGGTGGAAATAGCATGAACGAGGTGGGGCATGCAAATTCAC TTTCAATTGATACAATCTTTCACGTCAGAGCTGCTTCTTGTAACACAGAAGTTTTCA GATTCTATGAAAAGGTATTGAATGAATTGAAGGCTCTGTTAAGGGGGCAACTATCTC CCCTCCCCATTCTCCTATCAGCCCATAAAACAGGAACTGACAACCTCTTGGAAGAAT TGGGAAGGAACTTTTCGATTTTCTCTGTACAATCTTCACTGGTTCCTCTCTGTGAGA GGAGGAGGGACCTCTTGGATTGGTGTCGTTGGGAAAAGGGTATCAAGTGTGCATGGC TCAGCCTGTTCCTGGCTCTCTCTCTGGGACTGACCTGACTGCAAGCAGCATGTTCTC TGTCTGCTCCTGCCTCCTCCAGGCAATGAGCACCAGGGCGGGTCCAGCCCTTGCTTG GGAGGACTTCAATAGTCCAGCTGCTCTGCCGCGAGTGGGTGAGTGAGTTCAAGTCAG

Name	Sequence (5' to 3')
	AGGAGAAGACACAGAAAGCTCATTTGGGCCTTGGGTCTTAGCCACATCCTCCAGTCC ATCTGGACTAGCAATAAAGCTGACATTTTAATCCCTAGGATCCATGGGACCGACCAG AATCATGCAAGTGCGTAAGATAGTCGCGGGCCGGGCCATG
Scrambled MST 44	CTTCTCGACAGCATTTCTTTTTTCAGAATGATATGCACACAAGTGCTAATCGAGTAC ACACGACGTTCTCCCCTGCAATCAAGTGGGGGTTCAGATTACTTCATACCAGTCTTT TAGTGCGGACGTCGTTAACATCGAGGCGAATTGTAATTGATTCCGCATGACATGTAA CGATTGTAGGTATCAGTACGGGAATAAGTCCCTATCTCTCC
Scrambled MST 49	CGACGTGGAGCTTAACTCTCCTGAGTCGGGGCTCATATACGGGAATAGCTCTATGGA ATTAAGTTGGAAAAGAATGCAATCCATGCGGTAGCACTTAGGAGCCGCTGATACCTA CCATCACGGAGAGTTCTAAGCGCCTAAGAAAGTTATCAATGAACCCAGAGCCTTAAG AACGCAATGACGGCTGGCGTATGTACCACACTCGGAGGATC

9.3 List of protein interactor candidates

Table 35: List of identified proteins putatively interacting with *P4*

UniProt identifier	Method of identification	UniProt identifier	Method of identification
ACON_HUMAN	ChIRP-MS	DNM1L_HUMAN	ChIRP-MS
ACSL6_HUMAN	S1-aptamer pulldown	DTNB_HUMAN	S1-aptamer pulldown
ACTB_HUMAN	CARPID	DX39B_HUMAN	ChIRP-MS
ACTBL_HUMAN	CARPID, S1-aptamer pulldown	E41L5_HUMAN	S1-aptamer pulldown
ACTC_HUMAN	CARPID	EHD4_HUMAN	ChIRP-MS
ACTG_HUMAN	CARPID	EIF3B_HUMAN	ChIRP-MS
ACTZ_HUMAN	ChIRP-MS	EMAL2_HUMAN	ChIRP-MS
AMPB_HUMAN	ChIRP-MS	FCF1_HUMAN	S1-aptamer pulldown
ANXA6_HUMAN	ChIRP-MS	FGFP1_HUMAN	CARPID
AP2B1_HUMAN	CARPID	FILA2_HUMAN	S1-aptamer pulldown
ATPA_HUMAN	ChIRP-MS	FXR1_HUMAN	S1-aptamer pulldown
ATPB_HUMAN	ChIRP-MS	GDS1_HUMAN	ChIRP-MS
BAG3_HUMAN	ChIRP-MS	GELS_HUMAN	CARPID
BCLF1_HUMAN	S1-aptamer pulldown	GRAH_HUMAN	S1-aptamer pulldown
C8AP2_HUMAN	S1-aptamer pulldown	H14_HUMAN	S1-aptamer pulldown
CAC1D_HUMAN	S1-aptamer pulldown	H2A2C_HUMAN	CARPID
CALD1_HUMAN	ChIRP-MS	HMCS1_HUMAN	ChIRP-MS
CALM1_HUMAN	CARPID	HNRH1_HUMAN	ChIRP-MS
CAN1_HUMAN	ChIRP-MS	HNRPF_HUMAN	S1-aptamer pulldown
CAVN1_HUMAN	ChIRP-MS	HNRPQ_HUMAN	ChIRP-MS
CAVN3_HUMAN	CARPID	HS105_HUMAN	ChIRP-MS
CD180_HUMAN	S1-aptamer pulldown	HSP76_HUMAN	S1-aptamer pulldown
CETN2_HUMAN	S1-aptamer pulldown	HXK1_HUMAN	ChIRP-MS
CL071_HUMAN	S1-aptamer pulldown	HYOU1_HUMAN	ChIRP-MS
COLL2_HUMAN	S1-aptamer pulldown	ICAL_HUMAN	ChIRP-MS
COR1C_HUMAN	CARPID	IF2B2_HUMAN	ChIRP-MS, S1-aptamer pulldown
CTTB2_HUMAN	S1-aptamer pulldown		
CYTSA_HUMAN	CARPID	IF2GL_HUMAN	CARPID
DAXX_HUMAN	CARPID	IF2P_HUMAN	CARPID
DGKA_HUMAN	ChIRP-MS	IGKC_HUMAN	ChIRP-MS
DHX15_HUMAN	S1-aptamer pulldown	IMDH2_HUMAN	ChIRP-MS
DKC1_HUMAN	S1-aptamer pulldown	K22O_HUMAN	S1-aptamer pulldown

UniProt identifier	Method of identification	UniProt identifier	Method of identification
K2C75_HUMAN	S1-aptamer pulldown	RL18A_HUMAN	CARPID
KPYM_HUMAN	CARPID	RL30_HUMAN	CARPID
KR111_HUMAN	S1-aptamer pulldown	RL31_HUMAN	CARPID
KRA22_HUMAN	S1-aptamer pulldown	RL35_HUMAN	CARPID
KRA31_HUMAN	S1-aptamer pulldown	RL36_HUMAN	CARPID
KRA32_HUMAN	S1-aptamer pulldown	RL4_HUMAN	CARPID
KRA33_HUMAN	S1-aptamer pulldown	RL7_HUMAN	CARPID
KRA46_HUMAN	S1-aptamer pulldown	RL8_HUMAN	CARPID
KRT35_HUMAN	S1-aptamer pulldown	RS15A_HUMAN	CARPID
KRT38_HUMAN	S1-aptamer pulldown	RS16_HUMAN	CARPID
KRT83_HUMAN	S1-aptamer pulldown	RS17_HUMAN	CARPID
KRT85_HUMAN	S1-aptamer pulldown	RS29_HUMAN	CARPID
KRT86_HUMAN	S1-aptamer pulldown	RS9_HUMAN	CARPID
KT33A_HUMAN	S1-aptamer pulldown	RTN4_HUMAN	ChIRP-MS
KT33B_HUMAN	S1-aptamer pulldown	S10A8_HUMAN	S1-aptamer pulldown
LLPH_HUMAN	CARPID	SEPT2_HUMAN	ChIRP-MS
LRC47_HUMAN	ChIRP-MS	SF3B1_HUMAN	S1-aptamer pulldown
MARCS_HUMAN	ChIRP-MS	SPEF2_HUMAN	S1-aptamer pulldown
MBB1A_HUMAN	CARPID	SRC8_HUMAN	ChIRP-MS
MCM7_HUMAN	ChIRP-MS	SRSF6_HUMAN	S1-aptamer pulldown
ML12A_HUMAN	CARPID	SSBP_HUMAN	ChIRP-MS
ML12B_HUMAN	CARPID	STAU2_HUMAN	S1-aptamer pulldown
MYH10_HUMAN	CARPID	SVIL_HUMAN	CARPID
MYH9_HUMAN	CARPID	SYAC_HUMAN	ChIRP-MS
MYL6_HUMAN	CARPID	SYFB_HUMAN	ChIRP-MS
MYO1C_HUMAN	CARPID	SYNC_HUMAN	ChIRP-MS
MYO1D_HUMAN	S1-aptamer pulldown	SYWC_HUMAN	ChIRP-MS
MYO5A_HUMAN	CARPID	TAF1A_HUMAN	S1-aptamer pulldown
NAT10_HUMAN	CARPID	TAF1D_HUMAN	S1-aptamer pulldown
NEC2_HUMAN	S1-aptamer pulldown	TCPA_HUMAN	S1-aptamer pulldown
NHP2_HUMAN	S1-aptamer pulldown	TCPZ_HUMAN	ChIRP-MS
NOX4_HUMAN	S1-aptamer pulldown	TDRD6_HUMAN	S1-aptamer pulldown
NUCL_HUMAN	CARPID	TES_HUMAN	S1-aptamer pulldown
OAT_HUMAN	ChIRP-MS	TGM1_HUMAN	S1-aptamer pulldown
OLA1_HUMAN	ChIRP-MS	TIF1B_HUMAN	ChIRP-MS
PAI2_HUMAN	ChIRP-MS	TM219_HUMAN	S1-aptamer pulldown
PARVA_HUMAN	ChIRP-MS	TMOD3_HUMAN	CARPID
PCNT_HUMAN	S1-aptamer pulldown	TNPO1_HUMAN	ChIRP-MS
PDIA3_HUMAN	ChIRP-MS	TPM2_HUMAN	CARPID
PFKAP_HUMAN	ChIRP-MS	TPM3_HUMAN	CARPID
PI42C_HUMAN	CARPID	TPM4_HUMAN	CARPID
PIWL1_HUMAN	S1-aptamer pulldown	TRA2B_HUMAN	S1-aptamer pulldown
PK1IP_HUMAN	S1-aptamer pulldown	TRBP2_HUMAN	S1-aptamer pulldown
PRS7_HUMAN	ChIRP-MS	TRI37_HUMAN	S1-aptamer pulldown
PSMD4_HUMAN	ChIRP-MS	TTF1_HUMAN	S1-aptamer pulldown
PUF60_HUMAN	S1-aptamer pulldown	VATH_HUMAN	S1-aptamer pulldown
RABL6_HUMAN	CARPID	WDR7_HUMAN	S1-aptamer pulldown
REPS1_HUMAN	CARPID	WDR87_HUMAN	S1-aptamer pulldown
RFIP5_HUMAN	CARPID	XRCC6_HUMAN	ChIRP-MS

9.4 List of abbreviations

Table 36: List of used abbreviations with respective meanings

Symbol	Meaning	Symbol	Meaning
+	Positive	Ca^{2+}	Calcium cation
°C	Degree Celsius	CALML5	Calmodulin-like 5
µ-	Micro	CARPID	CRISPR-assisted detection of RNA-protein interaction detection
2D	Two-dimensional		
7SL	Signal recognition particle RNA	Cas	CRISPR-associated
A	Adenine	CCHCR1	Coiled-coil α-helical rod protein 1
-A	Ampere	Ccr7	C-C chemokine receptor type 7
A/A	Antibiotic-Antimycotic	cDNA	Complementary DNA
aa	Amino acids	CDS	Coding sequence
ACTBL2	Actin β-like 2	CDSN	Corneodesmosin
ACTL6A	Actin-like 6A	CETN2	Centrin-2
adj.	Adjusted	ChIP	Chromatin immunoprecipitation
AEBSF	4-(2-aminoethyl)benzenesulfonyl fluoride hydrochloride	ChIRP	Chromatin isolation by RNA purification
AGO	Argonaute	CHR	Cell cycle genes homology region
AGO2	Argonaute RISC catalytic component 2	CMV	Cytomegalovirus
Airn	Antisense of IGF2R non protein coding RNA	c-Myc	Myelocytomatosis viral oncogene homolog
ALKBH5	Alkylation B homolog 5	CNIT	Coding-Non-coding Identifying Tool
AMP	Adenosine monophosphate	COPA	COPI coat complex subunit α
Amp	Ampicillin	CPAT	Coding-Potential Assessment Tool
ANCR	Antidifferentiation noncoding RNA	CPC2	Coding-Potential Calculator 2
ANXA6	Annexin A6	Cq	Quantification cycle
AP-1	Activator protein 1	CRISPR	Clustered regularly interspaced short palindromic repeats
apopt.	Apoptosis		
APS	Ammonium persulfate	cSCC	Cutaneous squamous cell carcinoma
AS	Antisense	C-terminus	Carboxyl-terminus
ATP	Adenosine triphosphate	CTNNB1	Catenin β1
ATP2A2	ATPase sarcoplasmic/endoplasmic reticulum Ca2+ transporting 2	CTP	Cytidine triphosphate
		CX26	Connexin 26
ATP2C1	ATPase secretory pathway Ca2+ transporting 1	Cy5	Cyanine-5
		d	Day
ATPase	Adenine triphosphatase	d-	Deoxyribonucleotide
ATXN1	Ataxin 1	DAPI	4',6-diamidino-2-phenylindole
BAF	BRG1- or BRM-associated factors	DAVID	Database for Annotation, Visualization and Integrated Discovery
BASU	Bacillus subtilis biotin ligase		
BCL2	B-cell lymphoma 2	dCas	Dead Cas
BCS	Bovine calf serum	Dlx5	Distal-less homeobox 5
blast	Basic Local Alignment Search Tool	Dlx6	Distal-less homeobox 6
BLNCR	β1-adjacent long non-coding RNA	DMEM	Dulbecco's modified Eagle medium
BMP	Bone morphogenetic protein	DMSO	Dimethyl sulfoxide
bp	Basepairs	DNA	Deoxyribonucleic acid
BrdU	Bromodeoxyuridine	DNase1L2	Deoxyribonuclease 1-like 2
BRG1	Brahma-related gene 1	DNase2	Deoxyribonuclease 2, lysosomal
C	Cytosine	DPBS	Dulbecco's phosphate-buffered saline
c	Concentration	dT	Thymidine

Symbol	Meaning	Symbol	Meaning
DTT	Dithiothreitol	GADD45A	Growth arrest and DNA damage-inducible α
dWAT	Dermal white adipose tissue		
DWORF	Dwarf open reading frame	GAPDH	Glycerinaldehyde-3-phosphate dehydrogenase
DZIP3	DAZ interacting zinc finger protein 3		
E2F1	E2F transcription factor 1	GELS	Gelsolin
ECACC	European Collection of Authenticated Cell Cultures	GFP	Green fluorescent protein
		GLI	Glioma-associated oncogene
ECM	Extracellular matrix	GO	Gene ontology
EDC	Epidermal differentiation complex	G-protein	Guanine nucleotide-binding protein
EDTA	Ethylenediaminetetraacetic acid	GRCh38	Genome reference consortium human build 38
eEF2	Eukaryotic translation elongation factor 2		
		gRNA	Guide RNA
EGFP	Enhanced green fluorescent protein	GTP	Guanosine triphosphate
EGFR	Epidermal growth factor receptor	h	Hour
EGOT	Eosinophil granule ontogeny transcript	H3K9me3	Trimethylation of lysine 9 of histone H3
EMBL-EBI	European Molecular Biology Laboratory-European Bioinformatics Institute		
		HA	Human influenza hemagglutinin
		HCl	Hydrochloric acid
emPAI	Exponentially modified protein abundance index	HDAC1	Histone deacetylase 1
		HDAC2	Histone deacetylase 2
EMT	Epithelial-to-mesenchymal transition	hEGF	Human epidermal growth factor
ERK	Extracellular-signal regulated kinase	HEK293T	Human embryonic kidney 293T
Evf2	Embryonic ventral forebrain-2	HEPES	4-(2-hydroxyethyl)-1-piperazineethanesulfonic acid
EZH2	Enhancer of Zeste 2 homolog 2		
F/H	FLAG/HA	HK2	Hexokinase 2
FABP5P3	Fatty acid-binding protein 5 pseudogene 3	HLA	Human leukocyte antigen
		HLA-C	Human leukocyte antigen C
FACS	Fluorescence activated cell sorting	hnRNPH1	Heterogeneous nuclear ribonucleoprotein H1
FANTOM5	Functional annotation of the mammalian genome 5		
		hnRNP-K	Heterogeneous nuclear ribonucleoprotein K
FARSA	Phenylalanyl-tRNA synthetase subunit α		
		HOTAIR	HOX transcript antisense RNA
FARSB	Phenylalanyl-tRNA synthetase subunit β	HOXC13	Homeobox C13
		HOXD	Homeobox D
FBS	Fetal bovine serum	hPGK	Human phosphoglycerate kinase 1
FFPE	Formalin-fixed paraffin-embedded	HPLC	High pressure liquid chromatography
FGF	Fibroblast growth factor	iBAQ	Intensity-based absolute quantification
FGF7	Fibroblast growth factor 7	IF	Immunofluorescence
FGFR1	Fibroblast growth factor receptor 1	IGF	Insulin-like growth factor
FGFR2	Fibroblast growth factor receptor 2	IGF1R	Insulin-like growth factor 1 receptor
Firre	Functional intergenic repeating RNA element	Igf2	Insulin-like growth factor 2
		IGF2BP2	Insulin-like growth factor 2 mRNA-binding protein
FITC	Fluorescein isothiocyanate		
FLG	Filaggrin	Igf2r	Insulin-like growth factor 2 receptor
FOXM1	Forkhead box M1	IGFBP4	Insulin-like growth factor-binding protein 4
G	Guanine		
-g	Gram	IL-17	Interleukin-17
G1 phase	Gap 1 phase	IL-22	Interleukin-22
G2 phase	Gap 2 phase	IP	Immunoprecipitation

Symbol	Meaning	Symbol	Meaning
IPTR1	Mammalian target of rapamycin complex 1	MDM2	Mouse double minute 2 homolog
		Meg3	Maternally expressed 3
ITGB1	Integrin subunit β1	MEX3B	Mex-3 RNA-binding family member B
JAK	Janus kinase	min	Minute
K1	Keratin 1	miR	MicroRNA
K10	Keratin 10	MIR31HG	MIR31 host gene
K14	Keratin 14	miRNA	MicroRNA
K5	Keratin 5	-mol	Mole
kb	Kilobase	MOPS	3-(N-morpholino)propanesulfonic acid
kcal	Kilocalorie	mRNA	Messenger RNA
KD	Knockdown	MS	Mass spectrometry
K_D	Dissociation constant	MST	Microscale thermophoresis
kDa	Kilodalton	mTORC1	Mammalian target of rapamycin complex 1
KGM	Keratinocyte growth medium		
KLF4	Krüppel-like factor 4	MTT	3-(4,5-dimethylthiazol-2-yl)-2,5-diphenyltetrazolium bromide
KLHDC7B-DT	Kelch domain-containing 7B divergent transcript		
		N	Number of replicates
KRT1	Keratin 1	n-	Nano
KRT10	Keratin 10	NaOH	Sodium hydroxide
KRT14	Keratin 14	NBP	Non-binding protein
KRT5	Keratin 5	NCBI	National Center for Biotechnology Information
KRT80	Keratin 80		
KS	Kozak sequence	ncRNA	Non-coding RNA
-L	Liter	Neat1	Nuclear paraspeckle assembly transcript 1
LacZt	LacZ truncated		
LB	Lysogeny broth	NFAT	Nuclear factor of activated T-cells
LCE1E	Late cornified envelope 1E	NF-κB	Nuclear factor κ-light-chain-enhancer of activated B-cells
LDHA	Lactate dehydrogenase A		
LDS	Lithium dodecyl sulfate	NHP2	H/ACA ribonucleoprotein complex subunit 2
LGC	ORF Length and GC content		
LINC	Long intergenic non-coding RNA	NKC	Primary neonatal foreskin keratinocytes
lncRNA	Long non-coding RNA		
LOR	Loricrin	NLS	Nuclear localization sequence
m-	Milli	NMIA	N-methylisatoic anhydride
-m	Meter	Nono	Non-POU domain containing octamer-binding
-M	Molar		
M phase	Mitotic phase	NORAD	Non-coding RNA activated by DNA damage
m^6A	N^6-Methyladenosine		
m^7G	7-methylguanosine	NOTCH1	Notch receptor 1
MAF	Musculoaponeurotic fibrosarcoma oncogene homolog	NP-40	Nonidet P-40
		NRON	Non-coding repressor of NFAT
MAFB	Musculoaponeurotic fibrosarcoma oncogene homolog B	ns	Not significant
		nt	Nucleotides
MAFFT	Multiple Alignment using Fast Fourier Transform	N-terminus	Amino-terminus
		NTP	Nucleoside triphosphate
MAL	Megakaryocytic acute leukemia protein	NUMA1	Nuclear mitotic apparatus protein 1
		OD	Optical density
MALAT1	Metastasis-associated lung adenocarcinoma transcript 1	OE	Overexpression
		ORF	Open reading frame
MAPK	Mitogen-activated protein kinase	p	Probability value

Symbol	Meaning	Symbol	Meaning
p53	Tumor protein 53	SDWB	Semi-dry western blot
p63	Tumor protein 63	sec	Second
PAGE	Polyacrylamide gel electrophoresis	SERCA	Sarcoplasmic/endoplasmic reticulum calcium ATPase
PBS	Phosphate-buffered saline		
PCR	Polymerase chain reaction	SFM	Serum-free medium
PDK1	Pyruvate dehydrogenase kinase 1	Sfpq	Splicing factor proline and glutamine rich
PE	Phosphatidylethanolamine		
PFA	Paraformaldehyde	SHAPE	Selective 2' hydroxyl acylation analyzed by primer extension
pH	Potential of hydrogen		
Phe	Phenylalanine	Shp	Small heterodimer partner
PI3K	Phosphoinositide-3-kinase	siRNA	Small interfering RNA
PICSAR	P38-inhibited cutaneous squamous cell carcinoma-associated lincRNA	SMRT-2	SCC misregulated transcript-2
		SNAI2	Snail family transcriptional repressor 2
piRNA	Piwi-interacting RNA	snoRNA	Small nucleolar RNA
PRANCR	Progenitor renewal associated non-coding RNA	snRNA	Small nuclear RNA
		SNUPN	Snurportin 1
PRC2	Polycomb repressive complex 2	SPRR2C	Small proline-rich protein 2C
PRINS	Psoriasis-associated RNA induced by stress	SSC	Saline sodium citrate
		SSRTool	RNA secondary structure prediction ranking tool
Pspc1	Paraspeckle component 1		
PTEN	Phosphatase and tensin homolog	STAT3	Signal transducer and activator of transcription 3
PTENP1	Phosphatase and tensin homolog pseudogene 1		
		STAU1	Staufen double-stranded RNA-binding protein 1
P-value	Probability value		
qPCR	Quantitative PCR	STAU2	Staufen double-stranded RNA-binding protein 2
r-	Ribonucleotide		
RACE	Rapid amplification of cDNA ends	SUMO	Small ubiquitin-related modifier
Ras	Rat sarcoma	T	Thymine
RBP	RNA-binding protein	T2T	Telomere-to-telomere
rcf	Relative centrifugal force	TAE	Tris-acetate-EDTA
RCK	DEAD-box helicase 6	TAZ	Transcriptional coactivator with PDZ-binding motif
RFU	Relative fluorescence unit		
RISC	RNA-induces silencing complex	TBE	Tris-borate-EDTA
RNA	Ribonucleic acid	TBS-T	Tris-buffered saline with Tween20
RNAP	RNA polymerase	T-cell	Thymus derived cell
RNase7	Ribonuclease A family member 7	TEMED	Tetramethylethylenediamine
RPL32	Ribosomal protein L32	TFBI	Transformation buffer I
rpm	Revolutions per minute	TFBII	Transformation buffer II
RPMI	Roswell Park Memorial Institute	TG1	Transglutaminase 1
rRNA	Ribosomal RNA	TG5	Transglutaminase 5
RT	Room temperature	TGF-β	Transforming growth factor β
RT-qPCR	Real-time quantitative PCR	TGS	Tris-glycine-SDS
S	Svedberg	THOR	Testis-associated highly-conserved oncogenic long non-coding RNA
S phase	Synthetic phase		
S100A8	S100 calcium-binding protein A8	TINCR	Terminal differentiation-induced noncoding RNA
S100A9	S100 calcium-binding protein A9		
SATB1	Special AT-rich sequence-binding protein 1	Tns4	Tensin 4
		TPM4	Tropomyosin 4
SCC	Squamous cell carcinoma	TREX2	Three prime repair exonuclease 2
SDS	Sodium dodecyl sulfate	Tris	Tris(hydroxymethyl)aminomethane

Symbol	Meaning	Symbol	Meaning
tRNA	Transfer RNA	WAKMAR 1	Wound and keratinocyte migration-associated lncRNA 1
TTP	Thymidine triphosphate		
U	Uracil	WAKMAR 2	Wound and keratinocyte migration-associated lncRNA 2
-U	Unit		
UCSC	University of California, Santa Cruz	WAT	White adipose tissue
UTP	Uridine triphosphate	WB	Western blot
UTR	Untranslated region	WNT	Wingless-related integration site
UV	Ultraviolet	Xist	X-inactive specific transcript
UVB	Ultraviolet B radiation	XPC	Xeroderma pigmentosum, complementation group C
-V	Volt		
v/v	Volume per volume	YAP1	Yes-associated protein 1
VSV-G	G-glycoprotein of the vesicular stomatitis virus	YFP	Yellow fluorescent protein
		YT++	Yeast extract tryptone
-W	Watt	ZEB1	Zinc finger E-box-binding homeobox 1
w/v	Weight per volume	ZNF750	Zinc finger protein 750

9.5 List of figures

9.6 List of tables

10. References

(1) Schrodinger, E. *What Is Life?: With Mind and Matter and Autobiographical Sketches*; Canto Classics; Cambridge University Press: Cambridge, 2012. https://doi.org/10.1017/CBO9781107295629.
(2) Knaysi, G. On the Existence, Morphology, Nature, and Functions of the Cytoplasmic Membrane in the Bacterial Cell. *J Bacteriol* **1946**, *51* (1), 113–121.
(3) Tyler, S. Epithelium--the Primary Building Block for Metazoan Complexity. *Integr Comp Biol* **2003**, *43* (1), 55–63. https://doi.org/10.1093/icb/43.1.55.
(4) Thowfeequ, S.; Srinivas, S. Embryonic and Extraembryonic Tissues during Mammalian Development: Shifting Boundaries in Time and Space. *Philosophical Transactions of the Royal Society B: Biological Sciences* **2022**, *377* (1865), 20210255. https://doi.org/10.1098/rstb.2021.0255.
(5) Blanpain, C.; Fuchs, E. Epidermal Homeostasis: A Balancing Act of Stem Cells in the Skin. *Nat Rev Mol Cell Biol* **2009**, *10* (3), 207–217. https://doi.org/10.1038/nrm2636.
(6) Kanitakis, J. Anatomy, Histology and Immunohistochemistry of Normal Human Skin. *Eur J Dermatol* **2002**, *12* (4), 390–399; quiz 400–401.
(7) Driskell, R. R.; Jahoda, C. A. B.; Chuong, C.-M.; Watt, F. M.; Horsley, V. Defining Dermal Adipose Tissue. *Exp Dermatol* **2014**, *23* (9), 629–631. https://doi.org/10.1111/exd.12450.
(8) Lynch, M. D.; Watt, F. M. Fibroblast Heterogeneity: Implications for Human Disease. *J Clin Invest* **2018**, *128* (1), 26–35. https://doi.org/10.1172/JCI93555.
(9) Rognoni, E.; Watt, F. M. Skin Cell Heterogeneity in Development, Wound Healing, and Cancer. *Trends Cell Biol* **2018**, *28* (9), 709–722. https://doi.org/10.1016/j.tcb.2018.05.002.
(10) Dekoninck, S.; Blanpain, C. Stem Cell Dynamics, Migration and Plasticity during Wound Healing. *Nat Cell Biol* **2019**, *21* (1), 18–24. https://doi.org/10.1038/s41556-018-0237-6.
(11) Breitkreutz, D.; Koxholt, I.; Thiemann, K.; Nischt, R. Skin Basement Membrane: The Foundation of Epidermal Integrity—BM Functions and Diverse Roles of Bridging Molecules Nidogen and Perlecan. *Biomed Res Int* **2013**, *2013*, 179784. https://doi.org/10.1155/2013/179784.
(12) Blanpain, C.; Fuchs, E. Epidermal Stem Cells of the Skin. *Annu Rev Cell Dev Biol* **2006**, *22*, 339–373. https://doi.org/10.1146/annurev.cellbio.22.010305.104357.
(13) Maeda, K. New Method of Measurement of Epidermal Turnover in Humans. *Cosmetics* **2017**, *4* (4), 47. https://doi.org/10.3390/cosmetics4040047.
(14) Hsu, Y.-C.; Fuchs, E. Building and Maintaining the Skin. *Cold Spring Harb Perspect Biol* **2022**, *14* (7), a040840. https://doi.org/10.1101/cshperspect.a040840.
(15) Guerrero-Juarez, C. F.; Plikus, M. V. Emerging Nonmetabolic Functions of Skin Fat. *Nat Rev Endocrinol* **2018**, *14* (3), 163–173. https://doi.org/10.1038/nrendo.2017.162.
(16) Candi, E.; Schmidt, R.; Melino, G. The Cornified Envelope: A Model of Cell Death in the Skin. *Nat Rev Mol Cell Biol* **2005**, *6* (4), 328–340. https://doi.org/10.1038/nrm1619.
(17) Feingold, K. R.; Elias, P. M. Role of Lipids in the Formation and Maintenance of the Cutaneous Permeability Barrier. *Biochim Biophys Acta* **2014**, *1841* (3), 280–294. https://doi.org/10.1016/j.bbalip.2013.11.007.
(18) Proksch, E.; Brandner, J. M.; Jensen, J.-M. The Skin: An Indispensable Barrier. *Experimental Dermatology* **2008**, *17* (12), 1063–1072. https://doi.org/10.1111/j.1600-0625.2008.00786.x.
(19) Brandner, J. M. Importance of Tight Junctions in Relation to Skin Barrier Function. *Curr Probl Dermatol* **2016**, *49*, 27–37. https://doi.org/10.1159/000441541.
(20) Anderton, H.; Alqudah, S. Cell Death in Skin Function, Inflammation, and Disease. *Biochem J* **2022**, *479* (15), 1621–1651. https://doi.org/10.1042/BCJ20210606.
(21) Ishida-Yamamoto, A.; Igawa, S. The Biology and Regulation of Corneodesmosomes. *Cell Tissue Res* **2015**, *360* (3), 477–482. https://doi.org/10.1007/s00441-014-2037-z.
(22) Lippens, S.; Denecker, G.; Ovaere, P.; Vandenabeele, P.; Declercq, W. Death Penalty for Keratinocytes: Apoptosis versus Cornification. *Cell Death Differ* **2005**, *12* (2), 1497–1508. https://doi.org/10.1038/sj.cdd.4401722.
(23) Milstone, L. M. Epidermal Desquamation. *J Dermatol Sci* **2004**, *36* (3), 131–140. https://doi.org/10.1016/j.jdermsci.2004.05.004.
(24) Box, K.; Joyce, B. W.; Devenport, D. Epithelial Geometry Regulates Spindle Orientation and Progenitor Fate during Formation of the Mammalian Epidermis. *eLife* **2019**, *8*, e47102. https://doi.org/10.7554/eLife.47102.
(25) Raghavan, S.; Bauer, C.; Mundschau, G.; Li, Q.; Fuchs, E. Conditional Ablation of B1 Integrin in Skin: Severe Defects in Epidermal Proliferation, Basement Membrane Formation, and Hair Follicle Invagination. *Journal of Cell Biology* **2000**, *150* (5), 1149–1160. https://doi.org/10.1083/jcb.150.5.1149.
(26) Williams, S. E.; Beronja, S.; Pasolli, H. A.; Fuchs, E. Asymmetric Cell Divisions Promote Notch-Dependent Epidermal Differentiation. *Nature* **2011**, *470* (7334), 353–358. https://doi.org/10.1038/nature09793.

(27) Aragona, M.; Sifrim, A.; Malfait, M.; Song, Y.; Van Herck, J.; Dekoninck, S.; Gargouri, S.; Lapouge, G.; Swedlund, B.; Dubois, C.; et al. Mechanisms of Stretch-Mediated Skin Expansion at Single-Cell Resolution. *Nature* **2020**, *584* (7820), 268–273. https://doi.org/10.1038/s41586-020-2555-7.
(28) Rognoni, E.; Walko, G. The Roles of YAP/TAZ and the Hippo Pathway in Healthy and Diseased Skin. *Cells* **2019**, *8* (5), 411. https://doi.org/10.3390/cells8050411.
(29) Ning, W.; Muroyama, A.; Li, H.; Lechler, T. Differentiated Daughter Cells Regulate Stem Cell Proliferation and Fate through Intra-Tissue Tension. *Cell Stem Cell* **2021**, *28* (3), 436-452.e5. https://doi.org/10.1016/j.stem.2020.11.002.
(30) Sadagurski, M.; Yakar, S.; Weingarten, G.; Holzenberger, M.; Rhodes, C. J.; Breitkreutz, D.; LeRoith, D.; Wertheimer, E. Insulin-Like Growth Factor 1 Receptor Signaling Regulates Skin Development and Inhibits Skin Keratinocyte Differentiation. *Molecular and Cellular Biology* **2006**, *26* (7), 2675–2687. https://doi.org/10.1128/MCB.26.7.2675-2687.2006.
(31) Wang, J.; Eming, S. A.; Ding, X. Role of mTOR Signaling Cascade in Epidermal Morphogenesis and Skin Barrier Formation. *Biology (Basel)* **2022**, *11* (6), 931. https://doi.org/10.3390/biology11060931.
(32) Khavari, T. A.; Rinn, J. Ras/Erk MAPK Signaling in Epidermal Homeostasis and Neoplasia. *Cell Cycle* **2007**, *6* (23), 2928–2931. https://doi.org/10.4161/cc.6.23.4998.
(33) Hudson, L. G.; McCawley, L. J. Contributions of the Epidermal Growth Factor Receptor to Keratinocyte Motility. *Microsc Res Tech* **1998**, *43* (5), 444–455. https://doi.org/10.1002/(SICI)1097-0029(19981201)43:5<444::AID-JEMT10>3.0.CO;2-C.
(34) de Araújo, R.; Lôbo, M.; Trindade, K.; Silva, D. F.; Pereira, N. Fibroblast Growth Factors: A Controlling Mechanism of Skin Aging. *Skin Pharmacology and Physiology* **2019**, *32* (5), 275–282. https://doi.org/10.1159/000501145.
(35) Yang, J.; Meyer, M.; Müller, A.-K.; Böhm, F.; Grose, R.; Dauwalder, T.; Verrey, F.; Kopf, M.; Partanen, J.; Bloch, W.; et al. Fibroblast Growth Factor Receptors 1 and 2 in Keratinocytes Control the Epidermal Barrier and Cutaneous Homeostasis. *J Cell Biol* **2010**, *188* (6), 935–952. https://doi.org/10.1083/jcb.200910126.
(36) Li, X.; Xie, R.; Luo, Y.; Shi, R.; Ling, Y.; Zhao, X.; Xu, X.; Chu, W.; Wang, X. Cooperation of TGF-β and FGF Signalling Pathways in Skin Development. *Cell Prolif* **2023**, e13489. https://doi.org/10.1111/cpr.13489.
(37) Ito, Y.; Sarkar, P.; Mi, Q.; Wu, N.; Bringas, P.; Liu, Y.; Reddy, S.; Maxson, R.; Deng, C.; Chai, Y. Overexpression of Smad2 Reveals Its Concerted Action with Smad4 in Regulating TGF-Beta-Mediated Epidermal Homeostasis. *Dev Biol* **2001**, *236* (1), 181–194. https://doi.org/10.1006/dbio.2001.0332.
(38) Veltri, A.; Lang, C.; Lien, W.-H. Concise Review: Wnt Signaling Pathways in Skin Development and Epidermal Stem Cells. *Stem Cells* **2018**, *36* (1), 22–35. https://doi.org/10.1002/stem.2723.
(39) Lim, X.; Tan, S. H.; Koh, W. L. C.; Chau, R. M. W.; Yan, K. S.; Kuo, C. J.; van Amerongen, R.; Klein, A. M.; Nusse, R. Interfollicular Epidermal Stem Cells Self-Renew via Autocrine Wnt Signaling. *Science* **2013**, *342* (6163), 1226–1230. https://doi.org/10.1126/science.1239730.
(40) Pedro, M. P.; Lund, K.; Iglesias-Bartolome, R. The Landscape of GPCR Signaling in the Regulation of Epidermal Stem Cell Fate and Skin Homeostasis. *Stem Cells* **2020**. https://doi.org/10.1002/stem.3273.
(41) Abe, Y.; Tanaka, N. Roles of the Hedgehog Signaling Pathway in Epidermal and Hair Follicle Development, Homeostasis, and Cancer. *J Dev Biol* **2017**, *5* (4), 12. https://doi.org/10.3390/jdb5040012.
(42) Lee, S. E.; Lee, S. H. Skin Barrier and Calcium. *Ann Dermatol* **2018**, *30* (3), 265–275. https://doi.org/10.5021/ad.2018.30.3.265.
(43) Lee, A.-Y. The Role of MicroRNAs in Epidermal Barrier. *Int J Mol Sci* **2020**, *21* (16), 5781. https://doi.org/10.3390/ijms21165781.
(44) Wagner, R. N.; Piñón Hofbauer, J.; Wally, V.; Kofler, B.; Schmuth, M.; De Rosa, L.; De Luca, M.; Bauer, J. W. Epigenetic and Metabolic Regulation of Epidermal Homeostasis. *Exp Dermatol* **2021**, *30* (8), 1009–1022. https://doi.org/10.1111/exd.14305.
(45) Botchkarev, V. A.; Flores, E. R. P53/P63/P73 in the Epidermis in Health and Disease. *Cold Spring Harb Perspect Med* **2014**, *4* (8), a015248. https://doi.org/10.1101/cshperspect.a015248.
(46) Truong, A. B.; Kretz, M.; Ridky, T. W.; Kimmel, R.; Khavari, P. A. P63 Regulates Proliferation and Differentiation of Developmentally Mature Keratinocytes. *Genes Dev.* **2006**, *20* (22), 3185–3197. https://doi.org/10.1101/gad.1463206.
(47) Moltrasio, C.; Romagnuolo, M.; Marzano, A. V. Epigenetic Mechanisms of Epidermal Differentiation. *Int J Mol Sci* **2022**, *23* (9), 4874. https://doi.org/10.3390/ijms23094874.
(48) Eckhart, L.; Lippens, S.; Tschachler, E.; Declercq, W. Cell Death by Cornification. *Biochim Biophys Acta* **2013**, *1833* (12), 3471–3480. https://doi.org/10.1016/j.bbamcr.2013.06.010.
(49) Sotiropoulou, G.; Zingkou, E.; Pampalakis, G. Reconstructing the Epidermal Proteolytic Cascades in Health and Disease. *The Journal of Pathology* **2022**, *257* (4), 545–560. https://doi.org/10.1002/path.5888.
(50) Foggia, L.; Hovnanian, A. Calcium Pump Disorders of the Skin. *Am J Med Genet C Semin Med Genet* **2004**, *131C* (1), 20–31. https://doi.org/10.1002/ajmg.c.30031.

(51) Savignac, M.; Edir, A.; Simon, M.; Hovnanian, A. Darier Disease : A Disease Model of Impaired Calcium Homeostasis in the Skin. *Biochim Biophys Acta* **2011**, *1813* (5), 1111–1117. https://doi.org/10.1016/j.bbamcr.2010.12.006.
(52) Cialfi, S.; Le Pera, L.; De Blasio, C.; Mariano, G.; Palermo, R.; Zonfrilli, A.; Uccelletti, D.; Palleschi, C.; Biolcati, G.; Barbieri, L.; et al. The Loss of ATP2C1 Impairs the DNA Damage Response and Induces Altered Skin Homeostasis: Consequences for Epidermal Biology in Hailey-Hailey Disease. *Sci Rep* **2016**, *6*, 31567. https://doi.org/10.1038/srep31567.
(53) Richard, M. a.; Paul, C.; Nijsten, T.; Gisondi, P.; Salavastru, C.; Taieb, C.; Trakatelli, M.; Puig, L.; Stratigos, A.; Team, E. burden of skin diseases project. Prevalence of Most Common Skin Diseases in Europe: A Population-Based Study. *Journal of the European Academy of Dermatology and Venereology* **2022**, *36* (7), 1088–1096. https://doi.org/10.1111/jdv.18050.
(54) Nestle, F. O.; Kaplan, D. H.; Barker, J. Psoriasis. *N Engl J Med* **2009**, *361* (5), 496–509. https://doi.org/10.1056/NEJMra0804595.
(55) Orsmond, A.; Bereza-Malcolm, L.; Lynch, T.; March, L.; Xue, M. Skin Barrier Dysregulation in Psoriasis. *Int J Mol Sci* **2021**, *22* (19), 10841. https://doi.org/10.3390/ijms221910841.
(56) Boch, K.; Langan, E. A.; Kridin, K.; Zillikens, D.; Ludwig, R. J.; Bieber, K. Lichen Planus. *Front Med (Lausanne)* **2021**, *8*, 737813. https://doi.org/10.3389/fmed.2021.737813.
(57) Zieman, A. G.; Coulombe, P. A. Pathophysiology of Pachyonychia Congenita-Associated Palmoplantar Keratoderma: New Insights into Skin Epithelial Homeostasis and Avenues for Treatment. *Br J Dermatol* **2020**, *182* (3), 564–573. https://doi.org/10.1111/bjd.18033.
(58) Evtushenko, N. A.; Beilin, A. K.; Kosykh, A. V.; Vorotelyak, E. A.; Gurskaya, N. G. Keratins as an Inflammation Trigger Point in Epidermolysis Bullosa Simplex. *Int J Mol Sci* **2021**, *22* (22), 12446. https://doi.org/10.3390/ijms222212446.
(59) Jaffar, H.; Shakir, Z.; Kumar, G.; Ali, I. F. Ichthyosis Vulgaris: An Updated Review. *Skin Health Dis* **2023**, *3* (1), e187. https://doi.org/10.1002/ski2.187.
(60) Nishifuji, K.; Yoon, J. S. The Stratum Corneum: The Rampart of the Mammalian Body. *Veterinary Dermatology* **2013**, *24* (1), 60-e16. https://doi.org/10.1111/j.1365-3164.2012.01090.x.
(61) Moosbrugger-Martinz, V.; Leprince, C.; Méchin, M.-C.; Simon, M.; Blunder, S.; Gruber, R.; Dubrac, S. Revisiting the Roles of Filaggrin in Atopic Dermatitis. *Int J Mol Sci* **2022**, *23* (10), 5318. https://doi.org/10.3390/ijms23105318.
(62) Sroka-Tomaszewska, J.; Trzeciak, M. Molecular Mechanisms of Atopic Dermatitis Pathogenesis. *Int J Mol Sci* **2021**, *22* (8), 4130. https://doi.org/10.3390/ijms22084130.
(63) de Oliveira, E. C. V.; da Motta, V. R. V.; Pantoja, P. C.; Ilha, C. S. de O.; Magalhães, R. F.; Galadari, H.; Leonardi, G. R. Actinic Keratosis - Review for Clinical Practice. *Int J Dermatol* **2019**, *58* (4), 400–407. https://doi.org/10.1111/ijd.14147.
(64) Fernandez Figueras, M. T. From Actinic Keratosis to Squamous Cell Carcinoma: Pathophysiology Revisited. *J Eur Acad Dermatol Venereol* **2017**, *31 Suppl 2*, 5–7. https://doi.org/10.1111/jdv.14151.
(65) Winge, M. C. G.; Kellman, L. N.; Guo, K.; Tang, J. Y.; Swetter, S. M.; Aasi, S. Z.; Sarin, K. Y.; Chang, A. L. S.; Khavari, P. A. Advances in Cutaneous Squamous Cell Carcinoma. *Nat Rev Cancer* **2023**, *23* (7), 430–449. https://doi.org/10.1038/s41568-023-00583-5.
(66) Naik, P. P.; Desai, M. B. Basal Cell Carcinoma: A Narrative Review on Contemporary Diagnosis and Management. *Oncol Ther* **2022**, *10* (2), 317–335. https://doi.org/10.1007/s40487-022-00201-8.
(67) Droll, S.; Bao, X. Oh, the Mutations You'll Acquire! A Systematic Overview of Cutaneous Squamous Cell Carcinoma. *Cell Physiol Biochem* **2021**, *55* (S2), 89–119. https://doi.org/10.33594/000000433.
(68) Guo, A.; Liu, X.; Li, H.; Cheng, W.; Song, Y. The Global, Regional, National Burden of Cutaneous Squamous Cell Carcinoma (1990–2019) and Predictions to 2035. *European Journal of Cancer Care* **2023**, *2023*, e5484597. https://doi.org/10.1155/2023/5484597.
(69) Jaiswal, A.; Singh, R. Loss of Epidermal Homeostasis Underlies the Development of Squamous Cell Carcinoma. *Stem Cell Rev and Rep* **2023**, *19* (3), 667–679. https://doi.org/10.1007/s12015-022-10486-x.
(70) Phillips, R. Schrödinger's What Is Life? At 75. *cels* **2021**, *12* (6), 465–476. https://doi.org/10.1016/j.cels.2021.05.013.
(71) Crick, F. H. C.; Watson, J. D.; Bragg, W. L. The Complementary Structure of Deoxyribonucleic Acid. *Proceedings of the Royal Society of London. Series A. Mathematical and Physical Sciences* **1954**, *223* (1152), 80–96. https://doi.org/10.1098/rspa.1954.0101.
(72) Watson, J. D.; Crick, F. H. Molecular Structure of Nucleic Acids; a Structure for Deoxyribose Nucleic Acid. *Nature* **1953**, *171* (4356), 737–738. https://doi.org/10.1038/171737a0.
(73) Crick, F. H. On Protein Synthesis. *Symp Soc Exp Biol* **1958**, *12*, 138–163.
(74) ENCODE Project Consortium. An Integrated Encyclopedia of DNA Elements in the Human Genome. *Nature* **2012**, *489* (7414), 57–74. https://doi.org/10.1038/nature11247.

(75) Moss, T.; Langlois, F.; Gagnon-Kugler, T.; Stefanovsky, V. A Housekeeper with Power of Attorney: The rRNA Genes in Ribosome Biogenesis. *Cell Mol Life Sci* **2007**, *64* (1), 29–49. https://doi.org/10.1007/s00018-006-6278-1.
(76) Phizicky, E. M.; Hopper, A. K. The Life and Times of a tRNA. *RNA* **2023**, *29* (7), 898–957. https://doi.org/10.1261/rna.079620.123.
(77) Ding, Z.; Meng, Y.-R.; Fan, Y.-J.; Xu, Y.-Z. Roles of Minor Spliceosome in Intron Recognition and the Convergence with the Better Understood Major Spliceosome. *WIREs RNA* **2023**, *14* (1), e1761. https://doi.org/10.1002/wrna.1761.
(78) Wajahat, M.; Bracken, C. P.; Orang, A. Emerging Functions for snoRNAs and snoRNA-Derived Fragments. *Int J Mol Sci* **2021**, *22* (19), 10193. https://doi.org/10.3390/ijms221910193.
(79) Dueck, A.; Meister, G. Assembly and Function of Small RNA – Argonaute Protein Complexes. *Biological Chemistry* **2014**, *395* (6), 611–629. https://doi.org/10.1515/hsz-2014-0116.
(80) Neumeier, J.; Meister, G. siRNA Specificity: RNAi Mechanisms and Strategies to Reduce Off-Target Effects. *Front Plant Sci* **2021**, *11*, 526455. https://doi.org/10.3389/fpls.2020.526455.
(81) Ozata, D. M.; Gainetdinov, I.; Zoch, A.; O'Carroll, D.; Zamore, P. D. PIWI-Interacting RNAs: Small RNAs with Big Functions. *Nat Rev Genet* **2019**, *20* (2), 89–108. https://doi.org/10.1038/s41576-018-0073-3.
(82) Mattick, J. S.; Amaral, P. P.; Carninci, P.; Carpenter, S.; Chang, H. Y.; Chen, L.-L.; Chen, R.; Dean, C.; Dinger, M. E.; Fitzgerald, K. A.; et al. Long Non-Coding RNAs: Definitions, Functions, Challenges and Recommendations. *Nat Rev Mol Cell Biol* **2023**, *24* (6), 430–447. https://doi.org/10.1038/s41580-022-00566-8.
(83) Statello, L.; Guo, C.-J.; Chen, L.-L.; Huarte, M. Gene Regulation by Long Non-Coding RNAs and Its Biological Functions. *Nat Rev Mol Cell Biol* **2021**, *22* (2), 96–118. https://doi.org/10.1038/s41580-020-00315-9.
(84) Derrien, T.; Johnson, R.; Bussotti, G.; Tanzer, A.; Djebali, S.; Tilgner, H.; Guernec, G.; Martin, D.; Merkel, A.; Knowles, D. G.; et al. The GENCODE v7 Catalog of Human Long Noncoding RNAs: Analysis of Their Gene Structure, Evolution, and Expression. *Genome Res.* **2012**, *22* (9), 1775–1789. https://doi.org/10.1101/gr.132159.111.
(85) Hezroni, H.; Koppstein, D.; Schwartz, M. G.; Avrutin, A.; Bartel, D. P.; Ulitsky, I. Principles of Long Noncoding RNA Evolution Derived from Direct Comparison of Transcriptomes in 17 Species. *Cell Rep* **2015**, *11* (7), 1110–1122. https://doi.org/10.1016/j.celrep.2015.04.023.
(86) Melé, M.; Mattioli, K.; Mallard, W.; Shechner, D. M.; Gerhardinger, C.; Rinn, J. L. Chromatin Environment, Transcriptional Regulation, and Splicing Distinguish lincRNAs and mRNAs. *Genome Res* **2017**, *27* (1), 27–37. https://doi.org/10.1101/gr.214205.116.
(87) Nojima, T.; Proudfoot, N. J. Mechanisms of lncRNA Biogenesis as Revealed by Nascent Transcriptomics. *Nat Rev Mol Cell Biol* **2022**, *23* (6), 389–406. https://doi.org/10.1038/s41580-021-00447-6.
(88) Zuckerman, B.; Ron, M.; Mikl, M.; Segal, E.; Ulitsky, I. Gene Architecture and Sequence Composition Underpin Selective Dependency of Nuclear Export of Long RNAs on NXF1 and the TREX Complex. *Mol Cell* **2020**, *79* (2), 251-267.e6. https://doi.org/10.1016/j.molcel.2020.05.013.
(89) Carlevaro-Fita, J.; Rahim, A.; Guigó, R.; Vardy, L. A.; Johnson, R. Cytoplasmic Long Noncoding RNAs Are Frequently Bound to and Degraded at Ribosomes in Human Cells. *RNA* **2016**, *22* (6), 867–882. https://doi.org/10.1261/rna.053561.115.
(90) Chillón, I.; Marcia, M. The Molecular Structure of Long Non-Coding RNAs: Emerging Patterns and Functional Implications. *Critical Reviews in Biochemistry and Molecular Biology* **2020**, *55* (6), 662–690. https://doi.org/10.1080/10409238.2020.1828259.
(91) Sigova, A. A.; Mullen, A. C.; Molinie, B.; Gupta, S.; Orlando, D. A.; Guenther, M. G.; Almada, A. E.; Lin, C.; Sharp, P. A.; Giallourakis, C. C.; et al. Divergent Transcription of Long Noncoding RNA/mRNA Gene Pairs in Embryonic Stem Cells. *Proceedings of the National Academy of Sciences* **2013**, *110* (8), 2876–2881. https://doi.org/10.1073/pnas.1221904110.
(92) Chen, L.-L. Linking Long Noncoding RNA Localization and Function. *Trends in Biochemical Sciences* **2016**, *41* (9), 761–772. https://doi.org/10.1016/j.tibs.2016.07.003.
(93) Noh, J. H.; Kim, K. M.; McClusky, W. G.; Abdelmohsen, K.; Gorospe, M. Cytoplasmic Functions of Long Noncoding RNAs. *WIREs RNA* **2018**, *9* (3), e1471. https://doi.org/10.1002/wrna.1471.
(94) Schmitz, S. U.; Grote, P.; Herrmann, B. G. Mechanisms of Long Noncoding RNA Function in Development and Disease. *Cell Mol Life Sci* **2016**, *73*, 2491–2509. https://doi.org/10.1007/s00018-016-2174-5.
(95) Cajigas, I.; Leib, D. E.; Cochrane, J.; Luo, H.; Swyter, K. R.; Chen, S.; Clark, B. S.; Thompson, J.; Yates, J. R.; Kingston, R. E.; et al. Evf2 lncRNA/BRG1/DLX1 Interactions Reveal RNA-Dependent Inhibition of Chromatin Remodeling. *Development* **2015**, *142* (15), 2641–2652. https://doi.org/10.1242/dev.126318.
(96) Hacisuleyman, E.; Goff, L. A.; Trapnell, C.; Williams, A.; Henao-Mejia, J.; Sun, L.; McClanahan, P.; Hendrickson, D. G.; Sauvageau, M.; Kelley, D. R.; et al. Topological Organization of Multichromosomal Regions by the Long Intergenic Noncoding RNA Firre. *Nat Struct Mol Biol* **2014**, *21* (2), 198–206. https://doi.org/10.1038/nsmb.2764.

(97) Huarte, M.; Guttman, M.; Feldser, D.; Garber, M.; Koziol, M. J.; Kenzelmann-Broz, D.; Khalil, A. M.; Zuk, O.; Amit, I.; Rabani, M.; et al. A Large Intergenic Noncoding RNA Induced by P53 Mediates Global Gene Repression in the P53 Response. *Cell* **2010**, *142* (3), 409–419. https://doi.org/10.1016/j.cell.2010.06.040.

(98) Latos, P. A.; Pauler, F. M.; Koerner, M. V.; Şenergin, H. B.; Hudson, Q. J.; Stocsits, R. R.; Allhoff, W.; Stricker, S. H.; Klement, R. M.; Warczok, K. E.; et al. Airn Transcriptional Overlap, But Not Its lncRNA Products, Induces Imprinted Igf2r Silencing. *Science* **2012**, *338* (6113), 1469–1472. https://doi.org/10.1126/science.1228110.

(99) Rinn, J. L.; Kertesz, M.; Wang, J. K.; Squazzo, S. L.; Xu, X.; Brugmann, S. A.; Goodnough, L. H.; Helms, J. A.; Farnham, P. J.; Segal, E.; et al. Functional Demarcation of Active and Silent Chromatin Domains in Human HOX Loci by Noncoding RNAs. *Cell* **2007**, *129* (7), 1311–1323. https://doi.org/10.1016/j.cell.2007.05.022.

(100) Brannan, C. I.; Dees, E. C.; Ingram, R. S.; Tilghman, S. M. The Product of the H19 Gene May Function as an RNA. *Molecular and Cellular Biology* **1990**, *10* (1), 28. https://doi.org/10.1128/mcb.10.1.28.

(101) Leighton, P. A.; Ingram, R. S.; Eggenschwiler, J.; Efstratiadis, A.; Tilghman, S. M. Disruption of Imprinting Caused by Deletion of the H19 Gene Region in Mice. *Nature* **1995**, *375* (6526), 34–39. https://doi.org/10.1038/375034a0.

(102) Brockdorff, N.; Bowness, J. S.; Wei, G. Progress toward Understanding Chromosome Silencing by Xist RNA. *Genes Dev* **2020**, *34* (11–12), 733–744. https://doi.org/10.1101/gad.337196.120.

(103) Zhang, X.; Wang, W.; Zhu, W.; Dong, J.; Cheng, Y.; Yin, Z.; Shen, F. Mechanisms and Functions of Long Non-Coding RNAs at Multiple Regulatory Levels. *Int J Mol Sci* **2019**, *20* (22), 5573. https://doi.org/10.3390/ijms20225573.

(104) Xu, S.; Wang, P.; Zhang, J.; Wu, H.; Sui, S.; Zhang, J.; Wang, Q.; Qiao, K.; Yang, W.; Xu, H.; et al. Ai-lncRNA EGOT Enhancing Autophagy Sensitizes Paclitaxel Cytotoxicity via Upregulation of ITPR1 Expression by RNA-RNA and RNA-Protein Interactions in Human Cancer. *Mol Cancer* **2019**, *18*, 89. https://doi.org/10.1186/s12943-019-1017-z.

(105) Zhang, S.; Zhao, B. S.; Zhou, A.; Lin, K.; Zheng, S.; Lu, Z.; Chen, Y.; Sulman, E. P.; Xie, K.; Bögler, O.; et al. The m6A Demethylase ALKBH5 Maintains Tumorigenicity of Glioblastoma Stem-Like Cells by Sustaining FOXM1 Expression and Cell Proliferation Program. *Cancer Cell* **2017**, *31* (4), 591-606.e6. https://doi.org/10.1016/j.ccell.2017.02.013.

(106) Zhang, L.; Yang, Z.; Trottier, J.; Barbier, O.; Wang, L. LncRNA MEG3 Induces Cholestatic Liver Injury by Interaction with PTBP1 to Facilitate Shp mRNA Decay. *Hepatology* **2017**, *65* (2), 604–615. https://doi.org/10.1002/hep.28882.

(107) Yoon, J.-H.; Abdelmohsen, K.; Srikantan, S.; Yang, X.; Martindale, J. L.; De, S.; Huarte, M.; Zhan, M.; Becker, K. G.; Gorospe, M. LincRNA-P21 Suppresses Target mRNA Translation. *Mol Cell* **2012**, *47* (4), 648–655. https://doi.org/10.1016/j.molcel.2012.06.027.

(108) Wang, K. C.; Chang, H. Y. Molecular Mechanisms of Long Noncoding RNAs. *Mol Cell* **2011**, *43* (6), 904–914. https://doi.org/10.1016/j.molcel.2011.08.018.

(109) West, J. A.; Mito, M.; Kurosaka, S.; Takumi, T.; Tanegashima, C.; Chujo, T.; Yanaka, K.; Kingston, R. E.; Hirose, T.; Bond, C.; et al. Structural, Super-Resolution Microscopy Analysis of Paraspeckle Nuclear Body Organization. *J Cell Biol* **2016**, *214* (7), 817–830. https://doi.org/10.1083/jcb.201601071.

(110) Willingham, A. T.; Orth, A. P.; Batalov, S.; Peters, E. C.; Wen, B. G.; Aza-Blanc, P.; Hogenesch, J. B.; Schultz, P. G. A Strategy for Probing the Function of Noncoding RNAs Finds a Repressor of NFAT. *Science* **2005**, *309* (5740), 1570–1573. https://doi.org/10.1126/science.1115901.

(111) Yoon, J.-H.; Abdelmohsen, K.; Kim, J.; Yang, X.; Martindale, J. L.; Tominaga-Yamanaka, K.; White, E. J.; Orjalo, A. V.; Rinn, J. L.; Kreft, S. G.; et al. Scaffold Function of Long Non-Coding RNA HOTAIR in Protein Ubiquitination. *Nat Commun* **2013**, *4*, 2939. https://doi.org/10.1038/ncomms3939.

(112) Lee, S.; Kopp, F.; Chang, T.-C.; Sataluri, A.; Chen, B.; Sivakumar, S.; Yu, H.; Xie, Y.; Mendell, J. T. Noncoding RNA NORAD Regulates Genomic Stability by Sequestering PUMILIO Proteins. *Cell* **2016**, *164* (1–2), 69–80. https://doi.org/10.1016/j.cell.2015.12.017.

(113) Poliseno, L.; Salmena, L.; Zhang, J.; Carver, B.; Haveman, W. J.; Pandolfi, P. P. A Coding-Independent Function of Gene and Pseudogene mRNAs Regulates Tumour Biology. *Nature* **2010**, *465* (7301), 1033–1038. https://doi.org/10.1038/nature09144.

(114) Tanis, S. E. J.; Köksal, E. S.; van Buggenum, J. A. G. L.; Mulder, K. W. BLNCR Is a Long Non-Coding RNA Adjacent to Integrin Beta-1 That Is Rapidly Lost during Epidermal Progenitor Cell Differentiation. *Sci Rep* **2019**, *9* (1), 31. https://doi.org/10.1038/s41598-018-37251-w.

(115) Cai, P.; Otten, A. B. C.; Cheng, B.; Ishii, M. A.; Zhang, W.; Huang, B.; Qu, K.; Sun, B. K. A Genome-Wide Long Noncoding RNA CRISPRi Screen Identifies PRANCR as a Novel Regulator of Epidermal Homeostasis. *Genome Res* **2020**, *30* (1), 22–34. https://doi.org/10.1101/gr.251561.119.

(116) Ziegler, C.; Graf, J.; Faderl, S.; Schedlbauer, J.; Strieder, N.; Förstl, B.; Spang, R.; Bruckmann, A.; Merkl, R.; Hombach, S.; et al. The Long Non-coding RNA LINC00941 and SPRR5 Are Novel Regulators of Human Epidermal Homeostasis. *EMBO Rep* **2019**, *20* (2), e46612. https://doi.org/10.15252/embr.201846612.

(117) Morgenstern, E.; Kretz, M. The Human Long Non-Coding RNA LINC00941 and Its Modes of Action in Health and Disease. *Biol Chem* **2023**. https://doi.org/10.1515/hsz-2023-0183.
(118) Kretz, M.; Webster, D. E.; Flockhart, R. J.; Lee, C. S.; Zehnder, A.; Lopez-Pajares, V.; Qu, K.; Zheng, G. X. Y.; Chow, J.; Kim, G. E.; et al. Suppression of Progenitor Differentiation Requires the Long Noncoding RNA ANCR. *Genes Dev* **2012**, *26* (4), 338–343. https://doi.org/10.1101/gad.182121.111.
(119) Lopez-Pajares, V.; Qu, K.; Zhang, J.; Webster, D. E.; Barajas, B. C.; Siprashvili, Z.; Zarnegar, B. J.; Boxer, L. D.; Rios, E. J.; Tao, S.; et al. A LncRNA-MAF:MAFB Transcription Factor Network Regulates Epidermal Differentiation. *Dev Cell* **2015**, *32* (6), 693–706. https://doi.org/10.1016/j.devcel.2015.01.028.
(120) Shefler, A.; Patrick, M. T.; Wasikowski, R.; Chen, J.; Sarkar, M. K.; Gudjonsson, J. E.; Tsoi, L. C. Skin-Expressing lncRNAs in Inflammatory Responses. *Front Genet* **2022**, *13*, 835740. https://doi.org/10.3389/fgene.2022.835740.
(121) Li, C.; Li, H.; Huang, L.; Kong, Y.; Chen, F.; Liang, J.; Yu, H.; Yao, Z. H19 lncRNA Regulates Keratinocyte Differentiation by Targeting miR-130b-3p. *Cell Death Dis* **2017**, *8* (11), e3174–e3174. https://doi.org/10.1038/cddis.2017.516.
(122) He, Y.; Yin, X.; Yan, J.; Li, X.; Sun, Q. The lncRNA H19/miR-766-3p/S1PR3 Axis Contributes to the Hyperproliferation of Keratinocytes and Skin Inflammation in Psoriasis via the AKT/mTOR Pathway. *Mediators Inflamm* **2021**, *2021*, 9991175. https://doi.org/10.1155/2021/9991175.
(123) Zhang, W.; Zhou, K.; Zhang, X.; Wu, C.; Deng, D.; Yao, Z. Roles of the H19/microRNA-675 Axis in the Proliferation and Epithelial-mesenchymal Transition of Human Cutaneous Squamous Cell Carcinoma Cells. *Oncol Rep* **2021**, *45* (4), 39. https://doi.org/10.3892/or.2021.7990.
(124) Zhang, L.; Piipponen, M.; Liu, Z.; Li, D.; Bian, X.; Niu, G.; Geara, J.; Toma, M. A.; Sommar, P.; Xu Landén, N. Human Skin Specific Long Noncoding RNA HOXC13-AS Regulates Epidermal Differentiation by Interfering with Golgi-ER Retrograde Transport. *Cell Death Differ* **2023**, *30* (5), 1334–1348. https://doi.org/10.1038/s41418-023-01142-z.
(125) Panatta, E.; Lena, A. M.; Mancini, M.; Smirnov, A.; Marini, A.; Delli Ponti, R.; Botta-Orfila, T.; Tartaglia, G. G.; Mauriello, A.; Zhang, X.; et al. Long Non-Coding RNA Uc.291 Controls Epithelial Differentiation by Interfering with the ACTL6A/BAF Complex. *EMBO Rep* **2020**, *21* (3), e46734. https://doi.org/10.15252/embr.201846734.
(126) Mancini, M.; Cappello, A.; Pecorari, R.; Lena, A. M.; Montanaro, M.; Fania, L.; Ricci, F.; Di Lella, G.; Piro, M. C.; Abeni, D.; et al. Involvement of Transcribed lncRNA Uc.291 and SWI/SNF Complex in Cutaneous Squamous Cell Carcinoma. *Discov Oncol* **2021**, *12* (1), 14. https://doi.org/10.1007/s12672-021-00409-6.
(127) Fierro, C.; Gatti, V.; La Banca, V.; De Domenico, S.; Scalera, S.; Corleone, G.; Fanciulli, M.; De Nicola, F.; Mauriello, A.; Montanaro, M.; et al. The Long Non-Coding RNA NEAT1 Is a ΔNp63 Target Gene Modulating Epidermal Differentiation. *Nat Commun* **2023**, *14*, 3795. https://doi.org/10.1038/s41467-023-39011-5.
(128) Gong, Z.; Zhang, Y.; Jiang, Y.; Chen, P.; Ji, J. LncRNA NEAT1 Targets miR-342-3p/CUL4B to Inhibit the Proliferation of Cutaneous Squamous Cell Carcinoma Cells. *J Oncol* **2022**, *2022*, 8145129. https://doi.org/10.1155/2022/8145129.
(129) Lee, C. S.; Mah, A.; Aros, C. J.; Lopez-Pajares, V.; Bhaduri, A.; Webster, D. E.; Kretz, M.; Khavari, P. A. Cancer-Associated Long Noncoding RNA SMRT-2 Controls Epidermal Differentiation. *J Invest Dermatol* **2018**, *138* (6), 1445–1449. https://doi.org/10.1016/j.jid.2018.01.003.
(130) Kretz, M.; Siprashvili, Z.; Chu, C.; Webster, D. E.; Zehnder, A.; Qu, K.; Lee, C. S.; Flockhart, R. J.; Groff, A. F.; Chow, J.; et al. Control of Somatic Tissue Differentiation by the Long Non-Coding RNA TINCR. *Nature* **2013**, *493* (7431), 231–235. https://doi.org/10.1038/nature11661.
(131) Hazawa, M.; Lin, D.-C.; Handral, H.; Xu, L.; Chen, Y.; Jiang, Y.-Y.; Mayakonda, A.; Ding, L.-W.; Meng, X.; Sharma, A.; et al. ZNF750 Is a Lineage-Specific Tumour Suppressor in Squamous Cell Carcinoma. *Oncogene* **2017**, *36* (16), 2243–2254. https://doi.org/10.1038/onc.2016.377.
(132) Sun, B. K.; Boxer, L. D.; Ransohoff, J. D.; Siprashvili, Z.; Qu, K.; Lopez-Pajares, V.; Hollmig, S. T.; Khavari, P. A. CALML5 Is a ZNF750- and TINCR-Induced Protein That Binds Stratifin to Regulate Epidermal Differentiation. *Genes Dev* **2015**, *29* (21), 2225–2230. https://doi.org/10.1101/gad.267708.115.
(133) Eckhart, L.; Lachner, J.; Tschachler, E.; Rice, R. H. TINCR Is Not a Non-coding RNA but Encodes a Protein Component of Cornified Epidermal Keratinocytes. *Exp Dermatol* **2020**, exd.14083. https://doi.org/10.1111/exd.14083.
(134) Nita, A.; Matsumoto, A.; Tang, R.; Shiraishi, C.; Ichihara, K.; Saito, D.; Suyama, M.; Yasuda, T.; Tsuji, G.; Furue, M.; et al. A Ubiquitin-like Protein Encoded by the "Noncoding" RNA TINCR Promotes Keratinocyte Proliferation and Wound Healing. *PLoS Genet* **2021**, *17* (8), e1009686. https://doi.org/10.1371/journal.pgen.1009686.
(135) Morgado-Palacin, L.; Brown, J. A.; Martinez, T. F.; Garcia-Pedrero, J. M.; Forouhar, F.; Quinn, S. A.; Reglero, C.; Vaughan, J.; Heydary, Y. H.; Donaldson, C.; et al. The TINCR Ubiquitin-like Microprotein Is a

Tumor Suppressor in Squamous Cell Carcinoma. *Nat Commun* **2023**, *14* (1), 1328. https://doi.org/10.1038/s41467-023-36713-8.

(136) Breunig, S.; Wallner, V.; Kobler, K.; Wimmer, H.; Steinbacher, P.; Streubel, M. K.; Bischof, J.; Duschl, J.; Neuhofer, C.; Gruber, W.; et al. The Life in a Gradient: Calcium, the lncRNA SPRR2C and Mir542/Mir196a Meet in the Epidermis to Regulate the Aging Process. *Aging (Albany NY)* **2021**, *13* (15), 19127–19144. https://doi.org/10.18632/aging.203385.

(137) Zhang, L.; Hu, J.; Meshkat, B. I.; Liechty, K. W.; Xu, J. LncRNA MALAT1 Modulates TGF-B1-Induced EMT in Keratinocyte. *Int J Mol Sci* **2021**, *22* (21), 11816. https://doi.org/10.3390/ijms222111816.

(138) Elamir, A. M.; Shaker, O. G.; El-Komy, M. H.; Mahmoud Sharabi, M.; Aboraia, N. M. The Role of LncRNA MALAT-1 and MiRNA-9 in Psoriasis. *Biochem Biophys Rep* **2021**, *26*, 101030. https://doi.org/10.1016/j.bbrep.2021.101030.

(139) Zhang, Y.; Gao, L.; Ma, S.; Ma, J.; Wang, Y.; Li, S.; Hu, X.; Han, S.; Zhou, M.; Zhou, L.; et al. MALAT1-KTN1-EGFR Regulatory Axis Promotes the Development of Cutaneous Squamous Cell Carcinoma. *Cell Death Differ* **2019**, *26* (10), 2061–2073. https://doi.org/10.1038/s41418-019-0288-7.

(140) Zhang, L.; Hung, G. C.-C.; Meng, S.; Evans, R.; Xu, J. LncRNA MALAT1 Regulates Hyperglycemia Induced EMT in Keratinocyte via miR-205. *Noncoding RNA* **2023**, *9* (1), 14. https://doi.org/10.3390/ncrna9010014.

(141) He, L.; Zhu, C.; Jia, J.; Hao, X.-Y.; Yu, X.-Y.; Liu, X.-Y.; Shu, M.-G. ADSC-Exos Containing MALAT1 Promotes Wound Healing by Targeting miR-124 through Activating Wnt/β-Catenin Pathway. *Biosci Rep* **2020**, *40* (5), BSR20192549. https://doi.org/10.1042/BSR20192549.

(142) Li, D.; Kular, L.; Vij, M.; Herter, E. K.; Li, X.; Wang, A.; Chu, T.; Toma, M.-A.; Zhang, L.; Liapi, E.; et al. Human Skin Long Noncoding RNA WAKMAR1 Regulates Wound Healing by Enhancing Keratinocyte Migration. *Proc Natl Acad Sci U S A* **2019**, *116* (19), 9443–9452. https://doi.org/10.1073/pnas.1814097116.

(143) Herter, E. K.; Li, D.; Toma, M. A.; Vij, M.; Li, X.; Visscher, D.; Wang, A.; Chu, T.; Sommar, P.; Blomqvist, L.; et al. WAKMAR2, a Long Noncoding RNA Downregulated in Human Chronic Wounds, Modulates Keratinocyte Motility and Production of Inflammatory Chemokines. *J Invest Dermatol* **2019**, *139* (6), 1373–1384. https://doi.org/10.1016/j.jid.2018.11.033.

(144) Tu, Y.; Wang, L.; Wang, X.; Wu, W.; Tu, Y.; Zou, D.; Deng, Y.; Qi, J.; Cao, C.; Xu, D.; et al. LncRNA-WAKMAR2 Regulates Expression of CLDN1 to Affect Skin Barrier through Recruiting c-Fos. *Contact Dermatitis* **2023**, *88* (3), 188–200. https://doi.org/10.1111/cod.14256.

(145) Hall, J. R.; Messenger, Z. J.; Tam, H. W.; Phillips, S. L.; Recio, L.; Smart, R. C. Long Noncoding RNA lincRNA-P21 Is the Major Mediator of UVB-Induced and P53-Dependent Apoptosis in Keratinocytes. *Cell Death Dis* **2015**, *6* (3), e1700. https://doi.org/10.1038/cddis.2015.67.

(146) Sonkoly, E.; Bata-Csorgo, Z.; Pivarcsi, A.; Polyanka, H.; Kenderessy-Szabo, A.; Molnar, G.; Szentpali, K.; Bari, L.; Megyeri, K.; Mandi, Y.; et al. Identification and Characterization of a Novel, Psoriasis Susceptibility-Related Noncoding RNA Gene, PRINS. *J Biol Chem* **2005**, *280* (25), 24159–24167. https://doi.org/10.1074/jbc.M501704200.

(147) Ghosh, D.; Ganguly, T.; Chatterjee, R. Emerging Roles of Non-Coding RNAs in Psoriasis Pathogenesis. *Funct Integr Genomics* **2023**, *23* (2), 129. https://doi.org/10.1007/s10142-023-01057-5.

(148) Shi, R.; Ma, R.; Jiang, X.; Tang, X.; Gong, Y.; Yu, Z.; Shi, Y. Implications of LncRNAs and CircRNAs in Psoriasis: A Review. *RNA Biol* **2023**, *20* (1), 334–347. https://doi.org/10.1080/15476286.2023.2223486.

(149) Luo, L.; Pasquali, L.; Srivastava, A.; Freisenhausen, J. C.; Pivarcsi, A.; Sonkoly, E. The Long Noncoding RNA LINC00958 Is Induced in Psoriasis Epidermis and Modulates Epidermal Proliferation. *Journal of Investigative Dermatology* **2023**, *143* (6), 999–1010. https://doi.org/10.1016/j.jid.2022.12.011.

(150) Wang, Y.; Sun, B.; Wen, X.; Hao, D.; Du, D.; He, G.; Jiang, X. The Roles of lncRNA in Cutaneous Squamous Cell Carcinoma. *Front Oncol* **2020**, *10*, 158. https://doi.org/10.3389/fonc.2020.00158.

(151) Garofoli, M.; Volpicella, M.; Guida, M.; Porcelli, L.; Azzariti, A. The Role of Non-Coding RNAs as Prognostic Factor, Predictor of Drug Response or Resistance and Pharmacological Targets, in the Cutaneous Squamous Cell Carcinoma. *Cancers (Basel)* **2020**, *12* (9), 2552. https://doi.org/10.3390/cancers12092552.

(152) Hon, C.-C.; Ramilowski, J. A.; Harshbarger, J.; Bertin, N.; Rackham, O. J. L.; Gough, J.; Denisenko, E.; Schmeier, S.; Poulsen, T. M.; Severin, J.; et al. An Atlas of Human Long Non-Coding RNAs with Accurate 5′ Ends. *Nature* **2017**, *543* (7644), 199–204. https://doi.org/10.1038/nature21374.

(153) Kent, W. J.; Sugnet, C. W.; Furey, T. S.; Roskin, K. M.; Pringle, T. H.; Zahler, A. M.; Haussler, and D. The Human Genome Browser at UCSC. *Genome Res.* **2002**, *12* (6), 996–1006. https://doi.org/10.1101/gr.229102.

(154) Sayers, E. W.; Bolton, E. E.; Brister, J. R.; Canese, K.; Chan, J.; Comeau, D. C.; Connor, R.; Funk, K.; Kelly, C.; Kim, S.; et al. Database Resources of the National Center for Biotechnology Information. *Nucleic Acids Res* **2021**, *50* (D1), D20–D26. https://doi.org/10.1093/nar/gkab1112.

(155) Cunningham, F.; Allen, J. E.; Allen, J.; Alvarez-Jarreta, J.; Amode, M. R.; Armean, I. M.; Austine-Orimoloye, O.; Azov, A. G.; Barnes, I.; Bennett, R.; et al. Ensembl 2022. *Nucleic Acids Research* **2022**, *50* (D1), D988–D995. https://doi.org/10.1093/nar/gkab1049.

(156) Fishilevich, S.; Nudel, R.; Rappaport, N.; Hadar, R.; Plaschkes, I.; Iny Stein, T.; Rosen, N.; Kohn, A.; Twik, M.; Safran, M.; et al. GeneHancer: Genome-Wide Integration of Enhancers and Target Genes in GeneCards. *Database (Oxford)* **2017**, *2017*, bax028. https://doi.org/10.1093/database/bax028.

(157) Ram, O.; Goren, A.; Amit, I.; Shoresh, N.; Yosef, N.; Ernst, J.; Kellis, M.; Gymrek, M.; Issner, R.; Coyne, M.; et al. Combinatorial Patterning of Chromatin Regulators Uncovered by Genome-Wide Location Analysis in Human Cells. *Cell* **2011**, *147* (7), 1628–1639. https://doi.org/10.1016/j.cell.2011.09.057.

(158) Li, Z.; Liu, L.; Feng, C.; Qin, Y.; Xiao, J.; Zhang, Z.; Ma, L. LncBook 2.0: Integrating Human Long Non-Coding RNAs with Multi-Omics Annotations. *Nucleic Acids Research* **2023**, *51* (D1), D186–D191. https://doi.org/10.1093/nar/gkac999.

(159) Tate, J. G.; Bamford, S.; Jubb, H. C.; Sondka, Z.; Beare, D. M.; Bindal, N.; Boutselakis, H.; Cole, C. G.; Creatore, C.; Dawson, E.; et al. COSMIC: The Catalogue Of Somatic Mutations In Cancer. *Nucleic Acids Research* **2019**, *47* (D1), D941–D947. https://doi.org/10.1093/nar/gky1015.

(160) Bazzini, A. A.; Johnstone, T. G.; Christiano, R.; Mackowiak, S. D.; Obermayer, B.; Fleming, E. S.; Vejnar, C. E.; Lee, M. T.; Rajewsky, N.; Walther, T. C.; et al. Identification of Small ORFs in Vertebrates Using Ribosome Footprinting and Evolutionary Conservation. *EMBO J* **2014**, *33* (9), 981–993. https://doi.org/10.1002/embj.201488411.

(161) The Genotype-Tissue Expression (GTEx) Project. *Nat Genet* **2013**, *45* (6), 580–585. https://doi.org/10.1038/ng.2653.

(162) Uhlén, M.; Fagerberg, L.; Hallström, B. M.; Lindskog, C.; Oksvold, P.; Mardinoglu, A.; Sivertsson, Å.; Kampf, C.; Sjöstedt, E.; Asplund, A.; et al. Tissue-Based Map of the Human Proteome. *Science* **2015**, *347* (6220), 1260419. https://doi.org/10.1126/science.1260419.

(163) Kundaje, A.; Meuleman, W.; Ernst, J.; Bilenky, M.; Yen, A.; Heravi-Moussavi, A.; Kheradpour, P.; Zhang, Z.; Wang, J.; Ziller, M. J.; et al. Integrative Analysis of 111 Reference Human Epigenomes. *Nature* **2015**, *518* (7539), 317–330. https://doi.org/10.1038/nature14248.

(164) Yang, B.; Zhang, L.; Cao, Y.; Chen, S.; Cao, J.; Wu, D.; Chen, J.; Xiong, H.; Pan, Z.; Qiu, F.; et al. Overexpression of lncRNA IGFBP4-1 Reprograms Energy Metabolism to Promote Lung Cancer Progression. *Mol Cancer* **2017**, *16* (1), 154. https://doi.org/10.1186/s12943-017-0722-8.

(165) Li, C.; Cao, Y.; Zhang, L.; Li, J.; Wu, H.; Ling, F.; Zheng, J.; Wang, J.; Li, B.; He, J.; et al. LncRNA IGFBP4-1 Promotes Tumor Development by Activating Janus Kinase-Signal Transducer and Activator of Transcription Pathway in Bladder Urothelial Carcinoma. *Int J Biol Sci* **2020**, *16* (13), 2271–2282. https://doi.org/10.7150/ijbs.46986.

(166) Zhang, L.; Zhang, Z.; Li, E.; Xu, P. C-Myc-Regulated lncRNA-IGFBP4 Suppresses Autophagy in Cervical Cancer-Originated HeLa Cells. *Dis Markers* **2022**, *2022*, 7240646. https://doi.org/10.1155/2022/7240646.

(167) Lai, J.; Chen, B.; Zhang, G.; Li, X.; Mok, H.; Liao, N. Molecular Characterization of Breast Cancer: A Potential Novel Immune-Related lncRNAs Signature. *J Transl Med* **2020**, *18*, 416. https://doi.org/10.1186/s12967-020-02578-4.

(168) Tang, C.; Qu, G.; Xu, Y.; Yang, G.; Wang, J.; Xiang, M. An Immune-Related lncRNA Risk Coefficient Model to Predict the Outcomes in Clear Cell Renal Cell Carcinoma. *Aging (Albany NY)* **2021**, *13* (24), 26046–26062. https://doi.org/10.18632/aging.203797.

(169) Liang, D.; Hu, M.; Tang, Q.; Huang, M.; Tang, L. Nine Pyroptosis-Related lncRNAs Are Identified as Biomarkers for Predicting the Prognosis and Immunotherapy of Endometrial Carcinoma. *Int J Gen Med* **2021**, *14*, 8073–8085. https://doi.org/10.2147/IJGM.S338298.

(170) Yu, Y.; Chen, X.; Cang, S. Cancer-Related Long Noncoding RNAs Show Aberrant Expression Profiles and Competing Endogenous RNA Potential in Esophageal Adenocarcinoma. *Oncol Lett* **2019**, *18* (5), 4798–4808. https://doi.org/10.3892/ol.2019.10808.

(171) Li, M.; Long, S.; Hu, J.; Wang, Z.; Geng, C.; Ou, S. Systematic Identification of lncRNA-Based Prognostic Biomarkers for Glioblastoma. *Aging (Albany NY)* **2019**, *11* (21), 9405–9423. https://doi.org/10.18632/aging.102393.

(172) Ye, J.; Wu, S.; Pan, S.; Huang, J.; Ge, L. Risk Scoring Based on Expression of Long Non-Coding RNAs Can Effectively Predict Survival in Hepatocellular Carcinoma Patients with or without Fibrosis. *Oncol Rep* **2020**, *43* (5), 1451–1466. https://doi.org/10.3892/or.2020.7528.

(173) Xie, J.; Li, H.; Chen, L.; Cao, Y.; Hu, Y.; Zhu, Z.; Wang, M.; Shi, J. A Novel Pyroptosis-Related lncRNA Signature for Predicting the Prognosis of Skin Cutaneous Melanoma. *Int J Gen Med* **2021**, *14*, 6517–6527. https://doi.org/10.2147/IJGM.S335396.

(174) Schneider, V. A.; Graves-Lindsay, T.; Howe, K.; Bouk, N.; Chen, H.-C.; Kitts, P. A.; Murphy, T. D.; Pruitt, K. D.; Thibaud-Nissen, F.; Albracht, D.; et al. Evaluation of GRCh38 and de Novo Haploid Genome Assemblies Demonstrates the Enduring Quality of the Reference Assembly. *Genome Res* **2017**, *27* (5), 849–864. https://doi.org/10.1101/gr.213611.116.

(175) Nurk, S.; Koren, S.; Rhie, A.; Rautiainen, M.; Bzikadze, A. V.; Mikheenko, A.; Vollger, M. R.; Altemose, N.; Uralsky, L.; Gershman, A.; et al. The Complete Sequence of a Human Genome. *Science* **2022**, *376* (6588), 44–53. https://doi.org/10.1126/science.abj6987.

(176) Smits, J. P. H.; Niehues, H.; Rikken, G.; van Vlijmen-Willems, I. M. J. J.; van de Zande, G. W. H. J. F.; Zeeuwen, P. L. J. M.; Schalkwijk, J.; van den Bogaard, E. H. Immortalized N/TERT Keratinocytes as an Alternative Cell Source in 3D Human Epidermal Models. *Sci Rep* **2017**, *7* (1), 11838. https://doi.org/10.1038/s41598-017-12041-y.

(177) Deamer, D.; Akeson, M.; Branton, D. Three Decades of Nanopore Sequencing. *Nat Biotechnol* **2016**, *34* (5), 518–524. https://doi.org/10.1038/nbt.3423.

(178) Wang, L.; Park, H. J.; Dasari, S.; Wang, S.; Kocher, J.-P.; Li, W. CPAT: Coding-Potential Assessment Tool Using an Alignment-Free Logistic Regression Model. *Nucleic Acids Res* **2013**, *41* (6), e74. https://doi.org/10.1093/nar/gkt006.

(179) Sun, K.; Chen, X.; Jiang, P.; Song, X.; Wang, H.; Sun, H. iSeeRNA: Identification of Long Intergenic Non-Coding RNA Transcripts from Transcriptome Sequencing Data. *BMC Genomics* **2013**, *14 Suppl 2* (Suppl 2), S7. https://doi.org/10.1186/1471-2164-14-S2-S7.

(180) Kang, Y.-J.; Yang, D.-C.; Kong, L.; Hou, M.; Meng, Y.-Q.; Wei, L.; Gao, G. CPC2: A Fast and Accurate Coding Potential Calculator Based on Sequence Intrinsic Features. *Nucleic Acids Res* **2017**, *45* (W1), W12–W16. https://doi.org/10.1093/nar/gkx428.

(181) Guo, J.-C.; Fang, S.-S.; Wu, Y.; Zhang, J.-H.; Chen, Y.; Liu, J.; Wu, B.; Wu, J.-R.; Li, E.-M.; Xu, L.-Y.; et al. CNIT: A Fast and Accurate Web Tool for Identifying Protein-Coding and Long Non-Coding Transcripts Based on Intrinsic Sequence Composition. *Nucleic Acids Res* **2019**, *47* (W1), W516–W522. https://doi.org/10.1093/nar/gkz400.

(182) Wang, G.; Yin, H.; Li, B.; Yu, C.; Wang, F.; Xu, X.; Cao, J.; Bao, Y.; Wang, L.; Abbasi, A. A.; et al. Characterization and Identification of Long Non-Coding RNAs Based on Feature Relationship. *Bioinformatics* **2019**, *35* (17), 2949–2956. https://doi.org/10.1093/bioinformatics/btz008.

(183) Camargo, A. P.; Sourkov, V.; Pereira, G. A. G.; Carazzolle, M. F. RNAsamba: Neural Network-Based Assessment of the Protein-Coding Potential of RNA Sequences. *NAR Genom Bioinform* **2020**, *2* (1), lqz024. https://doi.org/10.1093/nargab/lqz024.

(184) Ramos, T. A. R.; Galindo, N. R. O.; Arias-Carrasco, R.; da Silva, C. F.; Maracaja-Coutinho, V.; do Rêgo, T. G. RNAmining: A Machine Learning Stand-Alone and Web Server Tool for RNA Coding Potential Prediction. *F1000Res* **2021**, *10*, 323. https://doi.org/10.12688/f1000research.52350.2.

(185) Madeira, F.; Pearce, M.; Tivey, A. R. N.; Basutkar, P.; Lee, J.; Edbali, O.; Madhusoodanan, N.; Kolesnikov, A.; Lopez, R. Search and Sequence Analysis Tools Services from EMBL-EBI in 2022. *Nucleic Acids Res* **2022**, *50* (W1), W276–W279. https://doi.org/10.1093/nar/gkac240.

(186) Johnson, M.; Zaretskaya, I.; Raytselis, Y.; Merezhuk, Y.; McGinnis, S.; Madden, T. L. NCBI BLAST: A Better Web Interface. *Nucleic Acids Research* **2008**, *36* (suppl_2), W5–W9. https://doi.org/10.1093/nar/gkn201.

(187) Marchler-Bauer, A.; Derbyshire, M. K.; Gonzales, N. R.; Lu, S.; Chitsaz, F.; Geer, L. Y.; Geer, R. C.; He, J.; Gwadz, M.; Hurwitz, D. I.; et al. CDD: NCBI's Conserved Domain Database. *Nucleic Acids Research* **2015**, *43* (D1), D222–D226. https://doi.org/10.1093/nar/gku1221.

(188) Schneider-Poetsch, T.; Ju, J.; Eyler, D. E.; Dang, Y.; Bhat, S.; Merrick, W. C.; Green, R.; Shen, B.; Liu, J. O. Inhibition of Eukaryotic Translation Elongation by Cycloheximide and Lactimidomycin. *Nat Chem Biol* **2010**, *6* (3), 209–217. https://doi.org/10.1038/nchembio.304.

(189) Rodríguez-Jiménez, P.; Fernández-Messina, L.; Ovejero-Benito, M. C.; Chicharro, P.; Vera-Tomé, P.; Vara, A.; Cibrian, D.; Martínez-Fleta, P.; Jiménez-Fernández, M.; Sánchez-García, I.; et al. Growth Arrest and DNA Damage-Inducible Proteins (GADD45) in Psoriasis. *Sci Rep* **2021**, *11*, 14579. https://doi.org/10.1038/s41598-021-93780-x.

(190) Yu, B.; Shan, G. Functions of Long Noncoding RNAs in the Nucleus. *Nucleus* **2016**, *7* (2), 155–166. https://doi.org/10.1080/19491034.2016.1179408.

(191) Yang, T.-H.; Lin, Y.-C.; Hsia, M.; Liao, Z.-Y. SSRTool: A Web Tool for Evaluating RNA Secondary Structure Predictions Based on Species-Specific Functional Interpretability. *Comput Struct Biotechnol J* **2022**, *20*, 2473–2483. https://doi.org/10.1016/j.csbj.2022.05.028.

(192) Brázda, V.; Kolomazník, J.; Lýsek, J.; Bartas, M.; Fojta, M.; Šťastný, J.; Mergny, J.-L. G4Hunter Web Application: A Web Server for G-Quadruplex Prediction. *Bioinformatics* **2019**, *35* (18), 3493–3495. https://doi.org/10.1093/bioinformatics/btz087.

(193) Low, J. T.; Weeks, K. M. SHAPE-Directed RNA Secondary Structure Prediction. *Methods* **2010**, *52* (2), 150–158. https://doi.org/10.1016/j.ymeth.2010.06.007.

(194) Reuter, J. S.; Mathews, D. H. RNAstructure: Software for RNA Secondary Structure Prediction and Analysis. *BMC Bioinformatics* **2010**, *11* (1), 129. https://doi.org/10.1186/1471-2105-11-129.

(195) Wang, J.; Wang, J.; Huang, Y.; Xiao, Y. 3dRNA v2.0: An Updated Web Server for RNA 3D Structure Prediction. *Int J Mol Sci* **2019**, *20* (17), 4116. https://doi.org/10.3390/ijms20174116.

(196) Sandberg, R.; Ernberg, I. Assessment of Tumor Characteristic Gene Expression in Cell Lines Using a Tissue Similarity Index (TSI). *Proc Natl Acad Sci U S A* **2005**, *102* (6), 2052–2057. https://doi.org/10.1073/pnas.0408105102.
(197) Kaur, G.; Dufour, J. M. Cell Lines. *Spermatogenesis* **2012**, *2* (1), 1–5. https://doi.org/10.4161/spmg.19885.
(198) Nelson, B. R.; Makarewich, C. A.; Anderson, D. M.; Winders, B. R.; Troupes, C. D.; Wu, F.; Reese, A. L.; McAnally, J. R.; Chen, X.; Kavalali, E. T.; et al. A Peptide Encoded by a Transcript Annotated as Long Noncoding RNA Enhances SERCA Activity in Muscle. *Science* **2016**, *351* (6270), 271–275. https://doi.org/10.1126/science.aad4076.
(199) Zhang, H.; Zhang, C.; Li, Z.; Li, C.; Wei, X.; Zhang, B.; Liu, Y. A New Method of RNA Secondary Structure Prediction Based on Convolutional Neural Network and Dynamic Programming. *Frontiers in Genetics* **2019**, *10*.
(200) Merino, E. J.; Wilkinson, K. A.; Coughlan, J. L.; Weeks, K. M. RNA Structure Analysis at Single Nucleotide Resolution by Selective 2'-Hydroxyl Acylation and Primer Extension (SHAPE). *J. Am. Chem. Soc.* **2005**, *127* (12), 4223–4231. https://doi.org/10.1021/ja043822v.
(201) Wilkinson, K. A.; Gorelick, R. J.; Vasa, S. M.; Guex, N.; Rein, A.; Mathews, D. H.; Giddings, M. C.; Weeks, K. M. High-Throughput SHAPE Analysis Reveals Structures in HIV-1 Genomic RNA Strongly Conserved across Distinct Biological States. *PLoS Biol* **2008**, *6* (4), e96. https://doi.org/10.1371/journal.pbio.0060096.
(202) Diederichs, S. The Four Dimensions of Noncoding RNA Conservation. *Trends in Genetics* **2014**, *30* (4), 121–123. https://doi.org/10.1016/j.tig.2014.01.004.
(203) Uroda, T.; Anastasakou, E.; Rossi, A.; Teulon, J.-M.; Pellequer, J.-L.; Annibale, P.; Pessey, O.; Inga, A.; Chillón, I.; Marcia, M. Conserved Pseudoknots in lncRNA MEG3 Are Essential for Stimulation of the P53 Pathway. *Mol Cell* **2019**, *75* (5), 982-995.e9. https://doi.org/10.1016/j.molcel.2019.07.025.
(204) Lu, Z.; Zhang, Q. C.; Lee, B.; Flynn, R. A.; Smith, M. A.; Robinson, J. T.; Davidovich, C.; Gooding, A. R.; Goodrich, K. J.; Mattick, J. S.; et al. RNA Duplex Map in Living Cells Reveals Higher-Order Transcriptome Structure. *Cell* **2016**, *165* (5), 1267–1279. https://doi.org/10.1016/j.cell.2016.04.028.
(205) Kappel, K.; Zhang, K.; Su, Z.; Watkins, A. M.; Kladwang, W.; Li, S.; Pintilie, G.; Topkar, V. V.; Rangan, R.; Zheludev, I. N.; et al. Accelerated Cryo-EM-Guided Determination of Three-Dimensional RNA-Only Structures. *Nat Methods* **2020**, *17* (7), 699–707. https://doi.org/10.1038/s41592-020-0878-9.
(206) Hu, L.; Bikle, D. D.; Oda, Y. Reciprocal Role of Vitamin D Receptor on β-Catenin Regulated Keratinocyte Proliferation and Differentiation. *J Steroid Biochem Mol Biol* **2014**, *144 Pt A*, 237–241. https://doi.org/10.1016/j.jsbmb.2013.11.002.
(207) Chan, J. K. C. The Wonderful Colors of the Hematoxylin-Eosin Stain in Diagnostic Surgical Pathology. *Int J Surg Pathol* **2014**, *22* (1), 12–32. https://doi.org/10.1177/1066896913517939.
(208) Yu, C. C.-W.; Woods, A. L.; Levison, D. A. The Assessment of Cellular Proliferation by Immunohistochemistry: A Review of Currently Available Methods and Their Applications. *Histochem J* **1992**, *24* (3), 121–131. https://doi.org/10.1007/BF01047461.
(209) Rieger, A. M. Flow Cytometry and Cell Cycle Analysis: An Overview. *Methods Mol Biol* **2022**, *2579*, 47–57. https://doi.org/10.1007/978-1-0716-2736-5_4.
(210) Wallberg, F.; Tenev, T.; Meier, P. Analysis of Apoptosis and Necroptosis by Fluorescence-Activated Cell Sorting. *Cold Spring Harb Protoc* **2016**, *2016* (4), pdb.prot087387. https://doi.org/10.1101/pdb.prot087387.
(211) Tomasz, M. Mitomycin C: Small, Fast and Deadly (but Very Selective). *Chem Biol* **1995**, *2* (9), 575–579. https://doi.org/10.1016/1074-5521(95)90120-5.
(212) Kuroki, T.; Kashiwagi, M.; Ishino, K.; Huh, N.; Ohba, M. Adenovirus-Mediated Gene Transfer to Keratinocytes--a Review. *J Investig Dermatol Symp Proc* **1999**, *4* (2), 153–157. https://doi.org/10.1038/sj.jidsp.5640200.
(213) Dagnino, L.; Ho, E.; Chang, W. Y. Expression and Analysis of Exogenous Proteins in Epidermal Cells. *Methods Mol Biol* **2010**, *585*, 93–105. https://doi.org/10.1007/978-1-60761-380-0_8.
(214) Liu, S. J.; Lim, D. A. Modulating the Expression of Long Non-Coding RNAs for Functional Studies. *EMBO reports* **2018**, *19* (12), e46955. https://doi.org/10.15252/embr.201846955.
(215) Gorouhi, F.; Davari, P.; Fazel, N. Cutaneous and Mucosal Lichen Planus: A Comprehensive Review of Clinical Subtypes, Risk Factors, Diagnosis, and Prognosis. *ScientificWorldJournal* **2014**, *2014*, 742826. https://doi.org/10.1155/2014/742826.
(216) Truong, A. B.; Khavari, P. A. Control of Keratinocyte Proliferation and Differentiation by P63. *Cell Cycle* **2007**, *6* (3), 295–299. https://doi.org/10.4161/cc.6.3.3753.
(217) Yao, D.; Alexander, C. L.; Quinn, J. A.; Chan, W.-C.; Wu, H.; Greenhalgh, D. A. Fos Cooperation with PTEN Loss Elicits Keratoacanthoma Not Carcinoma, Owing to P53/p21WAF-Induced Differentiation Triggered by GSK3β Inactivation and Reduced AKT Activity. *Journal of Cell Science* **2008**, *121* (10), 1758–1769. https://doi.org/10.1242/jcs.021147.

(218) Tisack, A.; Fotouhi, A.; Fidai, C.; Friedman, B. J.; Ozog, D.; Veenstra, J. A Clinical and Biological Review of Keratoacanthoma. *Br J Dermatol* **2021**, *185* (3), 487–498. https://doi.org/10.1111/bjd.20389.
(219) Perez-Moreno, M.; Jamora, C.; Fuchs, E. Sticky Business: Orchestrating Cellular Signals at Adherens Junctions. *Cell* **2003**, *112* (4), 535–548. https://doi.org/10.1016/S0092-8674(03)00108-9.
(220) Kashef, J.; Franz, C. M. Quantitative Methods for Analyzing Cell–Cell Adhesion in Development. *Developmental Biology* **2015**, *401* (1), 165–174. https://doi.org/10.1016/j.ydbio.2014.11.002.
(221) Uchida, Y.; Park, K. Ceramides in Skin Health and Disease: An Update. *Am J Clin Dermatol* **2021**, *22* (6), 853–866. https://doi.org/10.1007/s40257-021-00619-2.
(222) Listenberger, L. L.; Han, X.; Lewis, S. E.; Cases, S.; Farese, R. V.; Ory, D. S.; Schaffer, J. E. Triglyceride Accumulation Protects against Fatty Acid-Induced Lipotoxicity. *Proceedings of the National Academy of Sciences* **2003**, *100* (6), 3077–3082. https://doi.org/10.1073/pnas.0630588100.
(223) Brockhoff, G. Dynamische Proliferationsanalysen mittels Durchflusszytometrie. *Biospektrum* **2015**, *21* (3), 285–288. https://doi.org/10.1007/s12268-015-0575-x.
(224) Hwang, Y.; Hidalgo, D.; Socolovsky, M. The Shifting Shape and Functional Specializations of the Cell Cycle During Lineage Development. *WIREs Mech Dis* **2021**, *13* (2), e1504. https://doi.org/10.1002/wsbm.1504.
(225) Raj, D.; Brash, D. E.; Grossman, D. Keratinocyte Apoptosis in Epidermal Development and Disease. *J Invest Dermatol* **2006**, *126* (2), 243–257. https://doi.org/10.1038/sj.jid.5700008.
(226) Hockenbery, D. M.; Zutter, M.; Hickey, W.; Nahm, M.; Korsmeyer, S. J. BCL2 Protein Is Topographically Restricted in Tissues Characterized by Apoptotic Cell Death. *Proc Natl Acad Sci U S A* **1991**, *88* (16), 6961–6965. https://doi.org/10.1073/pnas.88.16.6961.
(227) Ganguli, G.; Abecassis, J.; Wasylyk, B. MDM2 Induces Hyperplasia and Premalignant Lesions When Expressed in the Basal Layer of the Epidermis. *EMBO J* **2000**, *19* (19), 5135–5147. https://doi.org/10.1093/emboj/19.19.5135.
(228) Hirata, H.; Samsonov, M.; Sokabe, M. Actomyosin Contractility Provokes Contact Inhibition in E-Cadherin-Ligated Keratinocytes. *Sci Rep* **2017**, *7*, 46326. https://doi.org/10.1038/srep46326.
(229) Humphries, M. J. Cell Adhesion Assays. *Methods Mol Biol* **2009**, *522*, 203–210. https://doi.org/10.1007/978-1-59745-413-1_14.
(230) Gonzales, K. A. U.; Polak, L.; Matos, I.; Tierney, M. T.; Gola, A.; Wong, E.; Infarinato, N. R.; Nikolova, M.; Luo, S.; Liu, S.; et al. Stem Cells Expand Potency and Alter Tissue Fitness by Accumulating Diverse Epigenetic Memories. *Science* **2021**, *374* (6571), eabh2444. https://doi.org/10.1126/science.abh2444.
(231) Cao, H.; Kapranov, P. Methods to Analyze the Non-Coding RNA Interactome—Recent Advances and Challenges. *Front Genet* **2022**, *13*, 857759. https://doi.org/10.3389/fgene.2022.857759.
(232) Mercer, T. R.; Mattick, J. S. Structure and Function of Long Noncoding RNAs in Epigenetic Regulation. *Nat Struct Mol Biol* **2013**, *20* (3), 300–307. https://doi.org/10.1038/nsmb.2480.
(233) Rinn, J. L.; Chang, H. Y. Genome Regulation by Long Noncoding RNAs. *Annu Rev Biochem* **2012**, *81*, 10.1146/annurev-biochem-051410–092902. https://doi.org/10.1146/annurev-biochem-051410-092902.
(234) Smith, J. M.; Sandow, J. J.; Webb, A. I. The Search for RNA-Binding Proteins: A Technical and Interdisciplinary Challenge. *Biochem Soc Trans* **2021**, *49* (1), 393–403. https://doi.org/10.1042/BST20200688.
(235) Flores, J. K.; Kariawasam, R.; Gimenez, A. X.; Helder, S.; Cubeddu, L.; Gamsjaeger, R.; Ataide, S. F. Biophysical Characterisation and Quantification of Nucleic Acid-Protein Interactions: EMSA, MST and SPR. *Curr Protein Pept Sci* **2015**, *16* (8), 727–734. https://doi.org/10.2174/1389203716666150505230806.
(236) Chu, C.; Chang, H. Y. ChIRP-MS: RNA-Directed Proteomic Discovery. *Methods Mol Biol* **2018**, *1861*, 37–45. https://doi.org/10.1007/978-1-4939-8766-5_3.
(237) Yi, W.; Li, J.; Zhu, X.; Wang, X.; Fan, L.; Sun, W.; Liao, L.; Zhang, J.; Li, X.; Ye, J.; et al. CRISPR-Assisted Detection of RNA–Protein Interactions in Living Cells. *Nat Methods* **2020**, *17* (7), 685–688. https://doi.org/10.1038/s41592-020-0866-0.
(238) Butter, F.; Scheibe, M.; Mörl, M.; Mann, M. Unbiased RNA–Protein Interaction Screen by Quantitative Proteomics. *Proc Natl Acad Sci U S A* **2009**, *106* (26), 10626–10631. https://doi.org/10.1073/pnas.0812099106.
(239) Sherman, B. T.; Hao, M.; Qiu, J.; Jiao, X.; Baseler, M. W.; Lane, H. C.; Imamichi, T.; Chang, W. DAVID: A Web Server for Functional Enrichment Analysis and Functional Annotation of Gene Lists (2021 Update). *Nucleic Acids Res* **2022**, *50* (W1), W216–W221. https://doi.org/10.1093/nar/gkac194.
(240) Perkins, D. N.; Pappin, D. J. C.; Creasy, D. M.; Cottrell, J. S. Probability-Based Protein Identification by Searching Sequence Databases Using Mass Spectrometry Data. *ELECTROPHORESIS* **1999**, *20* (18), 3551–3567. https://doi.org/10.1002/(SICI)1522-2683(19991201)20:18<3551::AID-ELPS3551>3.0.CO;2-2.
(241) Gruber, A. R.; Lorenz, R.; Bernhart, S. H.; Neuböck, R.; Hofacker, I. L. The Vienna RNA Websuite. *Nucleic Acids Res* **2008**, *36* (Web Server issue), W70–W74. https://doi.org/10.1093/nar/gkn188.
(242) Ishihama, Y.; Oda, Y.; Tabata, T.; Sato, T.; Nagasu, T.; Rappsilber, J.; Mann, M. Exponentially Modified Protein Abundance Index (emPAI) for Estimation of Absolute Protein Amount in Proteomics by the Number

of Sequenced Peptides per Protein. *Mol Cell Proteomics* **2005**, *4* (9), 1265–1272. https://doi.org/10.1074/mcp.M500061-MCP200.

(243) Srisawat, C.; Engelke, D. R. Streptavidin Aptamers: Affinity Tags for the Study of RNAs and Ribonucleoproteins. *RNA* **2001**, *7* (4), 632–641.

(244) Bragulla, H. H.; Homberger, D. G. Structure and Functions of Keratin Proteins in Simple, Stratified, Keratinized and Cornified Epithelia. *J Anat* **2009**, *214* (4), 516–559. https://doi.org/10.1111/j.1469-7580.2009.01066.x.

(245) Schwanhäusser, B.; Busse, D.; Li, N.; Dittmar, G.; Schuchhardt, J.; Wolf, J.; Chen, W.; Selbach, M. Global Quantification of Mammalian Gene Expression Control. *Nature* **2011**, *473* (7347), 337–342. https://doi.org/10.1038/nature10098.

(246) Deeb, S. E.; Al-Harrasi, A.; Khan, A.; Al-Broumi, M.; Al-Thani, G.; Alomairi, M.; Elumalai, P.; Sayed, R. A.; Ibrahim, A. E. Microscale Thermophoresis as a Powerful Growing Analytical Technique for the Investigation of Biomolecular Interaction and the Determination of Binding Parameters. *Methods Appl. Fluoresc.* **2022**, *10* (4), 042001. https://doi.org/10.1088/2050-6120/ac82a6.

(247) de Lanerolle, P. Nuclear Actin and Myosins at a Glance. *J Cell Sci* **2012**, *125* (21), 4945–4949. https://doi.org/10.1242/jcs.099754.

(248) Baßler, J.; Hurt, E. Eukaryotic Ribosome Assembly. *Annu Rev Biochem* **2019**, *88*, 281–306. https://doi.org/10.1146/annurev-biochem-013118-110817.

(249) Hodge, K.; Have, S. T.; Hutton, L.; Lamond, A. I. Cleaning up the Masses: Exclusion Lists to Reduce Contamination with HPLC-MS/MS. *J Proteomics* **2013**, *88*, 92–103. https://doi.org/10.1016/j.jprot.2013.02.023.

(250) Moritz, B.; Wahle, E. Simple Methods for the 3′ Biotinylation of RNA. *RNA* **2014**, *20* (3), 421–427. https://doi.org/10.1261/rna.042986.113.

(251) Roy, H.; Ling, J.; Irnov, M.; Ibba, M. Post-Transfer Editing in Vitro and in Vivo by the β Subunit of Phenylalanyl-tRNA Synthetase. *EMBO J* **2004**, *23* (23), 4639–4648. https://doi.org/10.1038/sj.emboj.7600474.

(252) Finarov, I.; Moor, N.; Kessler, N.; Klipcan, L.; Safro, M. G. Structure of Human Cytosolic Phenylalanyl-tRNA Synthetase: Evidence for Kingdom-Specific Design of the Active Sites and tRNA Binding Patterns. *Structure* **2010**, *18* (3), 343–353. https://doi.org/10.1016/j.str.2010.01.002.

(253) Ho, M. T.; Lu, J.; Vazquez-Pianzola, P.; Suter, B. α-Phenylalanyl tRNA Synthetase Competes with Notch Signaling through Its N-Terminal Domain. *PLoS Genet* **2022**, *18* (4), e1010185. https://doi.org/10.1371/journal.pgen.1010185.

(254) Tourbez, M.; Firanescu, C.; Yang, A.; Unipan, L.; Duchambon, P.; Blouquit, Y.; Craescu, C. T. Calcium-Dependent Self-Assembly of Human Centrin 2. *J Biol Chem* **2004**, *279* (46), 47672–47680. https://doi.org/10.1074/jbc.M404996200.

(255) Prosser, S. L.; Morrison, C. G. Centrin2 Regulates CP110 Removal in Primary Cilium Formation. *Journal of Cell Biology* **2015**, *208* (6), 693–701. https://doi.org/10.1083/jcb.201411070.

(256) Khouj, E. M.; Prosser, S. L.; Tada, H.; Chong, W. M.; Liao, J.-C.; Sugasawa, K.; Morrison, C. G. Differential Requirements for the EF-Hand Domains of Human Centrin 2 in Primary Ciliogenesis and Nucleotide Excision Repair. *J Cell Sci* **2019**, *132* (19), jcs228486. https://doi.org/10.1242/jcs.228486.

(257) Nishi, R.; Okuda, Y.; Watanabe, E.; Mori, T.; Iwai, S.; Masutani, C.; Sugasawa, K.; Hanaoka, F. Centrin 2 Stimulates Nucleotide Excision Repair by Interacting with Xeroderma Pigmentosum Group C Protein. *Mol Cell Biol* **2005**, *25* (13), 5664–5674. https://doi.org/10.1128/MCB.25.13.5664-5674.2005.

(258) Klein, U. R.; Nigg, E. A. SUMO-Dependent Regulation of Centrin-2. *J Cell Sci* **2009**, *122* (Pt 18), 3312–3321. https://doi.org/10.1242/jcs.050245.

(259) Resendes, K. K.; Rasala, B. A.; Forbes, D. J. Centrin 2 Localizes to the Vertebrate Nuclear Pore and Plays a Role in mRNA and Protein Export. *Mol Cell Biol* **2008**, *28* (5), 1755–1769. https://doi.org/10.1128/MCB.01697-07.

(260) Heraud-Farlow, J. E.; Sharangdhar, T.; Li, X.; Pfeifer, P.; Tauber, S.; Orozco, D.; Hörmann, A.; Thomas, S.; Bakosova, A.; Farlow, A. R.; et al. Staufen2 Regulates Neuronal Target RNAs. *Cell Rep* **2013**, *5* (6), 1511–1518. https://doi.org/10.1016/j.celrep.2013.11.039.

(261) Sharangdhar, T.; Sugimoto, Y.; Heraud-Farlow, J.; Fernández-Moya, S. M.; Ehses, J.; Ruiz de los Mozos, I.; Ule, J.; Kiebler, M. A. A Retained Intron in the 3′-UTR of Calm3 mRNA Mediates Its Staufen2- and Activity-dependent Localization to Neuronal Dendrites. *EMBO Rep* **2017**, *18* (10), 1762–1774. https://doi.org/10.15252/embr.201744334.

(262) Heber, S.; Gáspár, I.; Tants, J.-N.; Günther, J.; Moya, S. M. F.; Janowski, R.; Ephrussi, A.; Sattler, M.; Niessing, D. Staufen2-Mediated RNA Recognition and Localization Requires Combinatorial Action of Multiple Domains. *Nat Commun* **2019**, *10* (1), 1659. https://doi.org/10.1038/s41467-019-09655-3.

(263) Miki, T.; Yoneda, Y. Alternative Splicing of Staufen2 Creates the Nuclear Export Signal for CRM1 (Exportin 1). *J Biol Chem* **2004**, *279* (46), 47473–47479. https://doi.org/10.1074/jbc.M407883200.

(264) Schieweck, R.; Riedemann, T.; Forné, I.; Harner, M.; Bauer, K. E.; Rieger, D.; Ang, F. Y.; Hutten, S.; Demleitner, A. F.; Popper, B.; et al. Pumilio2 and Staufen2 Selectively Balance the Synaptic Proteome. *Cell Rep* **2021**, *35* (12), 109279. https://doi.org/10.1016/j.celrep.2021.109279.

(265) Ehses, J.; Schlegel, M.; Schröger, L.; Schieweck, R.; Derdak, S.; Bilban, M.; Bauer, K.; Harner, M.; Kiebler, M. A. The dsRBP Staufen2 Governs RNP Assembly of Neuronal Argonaute Proteins. *Nucleic Acids Res* **2022**, *50* (12), 7034–7047. https://doi.org/10.1093/nar/gkac487.

(266) Park, E.; Gleghorn, M. L.; Maquat, L. E. Staufen2 Functions in Staufen1-Mediated mRNA Decay by Binding to Itself and Its Paralog and Promoting UPF1 Helicase but Not ATPase Activity. *Proc Natl Acad Sci U S A* **2013**, *110* (2), 405–412. https://doi.org/10.1073/pnas.1213508110.

(267) Condé, L.; Gonzalez Quesada, Y.; Bonnet-Magnaval, F.; Beaujois, R.; DesGroseillers, L. STAU2 Protein Level Is Controlled by Caspases and the CHK1 Pathway and Regulates Cell Cycle Progression in the Non-Transformed hTERT-RPE1 Cells. *BMC Mol Cell Biol* **2021**, *22* (1), 16. https://doi.org/10.1186/s12860-021-00352-y.

(268) Hlavaty, D.; Lechler, T. Roles for Microtubules in the Proliferative and Differentiated Cells of Stratified Epithelia. *Curr Opin Cell Biol* **2021**, *68*, 98–104. https://doi.org/10.1016/j.ceb.2020.10.002.

(269) Broome, A.-M.; Ryan, D.; Eckert, R. L. S100 Protein Subcellular Localization during Epidermal Differentiation and Psoriasis. *J Histochem Cytochem* **2003**, *51* (5), 675–685. https://doi.org/10.1177/002215540305100513.

(270) Bernerd, F.; Compan, D.; Bernard, B.; Leclaire, J.; Medaisko, C.; Mehul, B.; Seité, S.; Marionnet, C.; Dumas, A.; Verrecchia, F.; et al. Modulation of Gene Expression Induced in Human Epidermis by Environmental Stress In Vivo. *Journal of Investigative Dermatology* **2003**, *121* (6), 1447–1458. https://doi.org/10.1111/j.1523-1747.2003.12629.x.

(271) de Carvalho, G. C.; Domingues, R.; de Sousa Nogueira, M. A.; Calvielli Castelo Branco, A. C.; Gomes Manfrere, K. C.; Pereira, N. V.; Aoki, V.; Sotto, M. N.; Da Silva Duarte, A. J.; Sato, M. N. Up-Regulation of Proinflammatory Genes and Cytokines Induced by S100A8 in CD8+ T Cells in Lichen Planus. *Acta Derm Venereol* **2016**, *96* (4), 485–489. https://doi.org/10.2340/00015555-2306.

(272) Voss, A.; Bode, G.; Sopalla, C.; Benedyk, M.; Varga, G.; Böhm, M.; Nacken, W.; Kerkhoff, C. Expression of S100A8/A9 in HaCaT Keratinocytes Alters the Rate of Cell Proliferation and Differentiation. *FEBS Letters* **2011**, *585* (2), 440–446. https://doi.org/10.1016/j.febslet.2010.12.037.

(273) Nag, S.; Larsson, M.; Robinson, R. C.; Burtnick, L. D. Gelsolin: The Tail of a Molecular Gymnast. *Cytoskeleton (Hoboken)* **2013**, *70* (7), 360–384. https://doi.org/10.1002/cm.21117.

(274) Husen, P.; Tarasov, K.; Katafiasz, M.; Sokol, E.; Vogt, J.; Baumgart, J.; Nitsch, R.; Ekroos, K.; Ejsing, C. S. Analysis of Lipid Experiments (ALEX): A Software Framework for Analysis of High-Resolution Shotgun Lipidomics Data. *PLoS One* **2013**, *8* (11), e79736. https://doi.org/10.1371/journal.pone.0079736.

(275) Davis, M. W.; Jorgensen, E. M. ApE, A Plasmid Editor: A Freely Available DNA Manipulation and Visualization Program. *Frontiers in Bioinformatics* **2022**, *2*.

(276) Waterhouse, A. M.; Procter, J. B.; Martin, D. M. A.; Clamp, M.; Barton, G. J. Jalview Version 2--a Multiple Sequence Alignment Editor and Analysis Workbench. *Bioinformatics* **2009**, *25* (9), 1189–1191. https://doi.org/10.1093/bioinformatics/btp033.

(277) Stothard, P. The Sequence Manipulation Suite: JavaScript Programs for Analyzing and Formatting Protein and DNA Sequences. *Biotechniques* **2000**, *28* (6), 1102, 1104. https://doi.org/10.2144/00286ir01.

(278) Livak, K. J.; Schmittgen, T. D. Analysis of Relative Gene Expression Data Using Real-Time Quantitative PCR and the 2(-Delta Delta C(T)) Method. *Methods* **2001**, *25* (4), 402–408. https://doi.org/10.1006/meth.2001.1262.

(279) *siRNA Design Tool*. https://eurofinsgenomics.eu/de/ecom/tools/sirna-design/ (accessed 2023-08-19).

(280) *siRNA Target Finder*. https://www.genscript.com/tools/sirna-target-finder (accessed 2023-08-19).

(281) Chuang, Y.-F.; Wang, P.-Y.; Kumar, S.; Lama, S.; Lin, F.-L.; Liu, G.-S. Methods for in Vitro CRISPR/CasRx-Mediated RNA Editing. *Frontiers in Cell and Developmental Biology* **2021**, *9*, 1388. https://doi.org/10.3389/fcell.2021.667879.

(282) The UniProt Consortium. UniProt: The Universal Protein Knowledgebase in 2023. *Nucleic Acids Research* **2023**, *51* (D1), D523–D531. https://doi.org/10.1093/nar/gkac1052.

11. Acknowledgements

At the end of this thesis, I would like to thank all the people that helped and supported me on the journey to its completion.

Zuerst möchte ich mich bei meinem Doktorvater Prof. Dr. Markus Kretz bedanken, der es mir ermöglicht hat, an diesem äußerst interessanten Themengebiet zu forschen. Dabei möchte ich nicht nur all die hilfreichen und zielführenden Diskussionen hervorheben, sondern auch die empathische Art und Weise deiner Betreuung, die seinesgleichen sucht und mir im Laufe meiner Doktorandenlaufbahn stets eine positive Grundeinstellung vermittelt hat.

Ein großer Dank gilt auch allen Mitgliedern meines Prüfungsausschusses, insbesondere Prof. Dr. Gunter Meister, welcher mich im Grunde über meine gesamte wissenschaftliche Laufbahn hinweg begleitete und in dessen Institut ich schon vor meinem Doktorstudium sehr viele fachliche Kompetenzen erwerben konnte.

Moreover, I want to thank all the collaborators which helped me during my experiments. I am grateful to the whole AG Meister for access to multiple lab devices and in particular to Kevin Heizler and Michaela Bauer for material and immaterial scientific support. Also, much thanks to the group of Dr. Astrid Bruckmann which performed proteomic mass spectrometric analyses for me. Furthermore, I much appreciate the assistance of Dr. Sébastien Ferreira-Cerca's group with the ribosome fractionation and SHAPE experiments. I would like to thank the departments of Prof. Dr. Armin Kurtz, Prof. Dr. Ernst Tamm and Prof. Dr. Ralph Witzgall for access to diverse lab instruments. Many thanks to the group of Prof. Dr. Gerhard Liebisch for carrying out the lipidomic analyses on such short notice. Flow cytometry experiments would not have been possible without Prof. Dr. Gero Brockhoff's group and particularly Gerhard Piendl who was always patient with my technical questions. I want to highlight the tremendous support of Dr. Ayse-Nur Menevse from the group of Prof. Dr. Philipp Beckhove in enabling me to perform live-cell imaging measurements and also helping me with the corresponding analysis. Finally, I am grateful to the group of Prof. Dr. Gernot Längst and especially Sabrina Babl for instructing and advising me regarding the thermophoretic measurements at their facility.

Einer der grundlegendsten Bausteine dieser Arbeit sind alle ehemaligen und gegenwärtigen Mitglieder der AG Kretz. Hierbei möchte ich zunächst Dr. Sonja Hombach, Dr. Johannes Graf, Bianca Förstl und Michaela Pöppel danken, die bereits vor meiner Zeit im Labor wichtige projektbezogene Experimente durchgeführt hatten. Danke an die studentischen Praktikanten

Manuel Schidlmeier, Anna Niebauer, Kira Mangold und Johanna Gizler, die mich unmittelbar bei meinen Forschungen unterstützt haben. Auf keinen Fall unerwähnt bleiben darf dabei auch Carolin Molthof, welche zuerst während ihrer Masterarbeit und später als geschätzte Doktorandenkollegin wesentliche Entdeckungen zum Projekt beigetragen hat. Die Bürozeit wäre nicht im Entfernesten so unterhaltsam gewesen ohne meine Kollegin Eva, die auf Anhieb mit Energie und Schwung die Gruppendynamik bereichert hat. Tausend Dank für all die interessanten Gespräche und witzigen Situationen, die der Arbeitsalltag seitdem mit sich brachte. Und natürlich: Kuchen! Danni, danke für all die hilfreichen Tipps und Tricks im Laboralltag, deine enorme Mithilfe bei meinem Projekt und selbstverständlich auch für all deine amüsanten Geschichten, die die Zeit im Labor wie im Nu verstreichen ließen.

I would like to thank all present and past members of the Biochemistry I department for a wonderful time and the constant familiar atmosphere that made each day something special. I am particularly grateful to my former supervisors Franzi and Hung who helped me a big deal in becoming an independent and efficient scientist while still maintaining enjoyment and fun in the lab. A massive thank you goes to Jan who was very supportive in my last few months as a doctorate student and enabled healthier circumstances for me writing this dissertation. I also appreciate Birgit's amazing help with multiple administrative and other matters a lot. Moreover, many thanks to Gerhard; especially when times get a little hectic it is great to find calm people that act like an anchor and encourage a change of perspective.

I am very glad that I met so many more fun and aspiring people along my PhD career and hope that, even though I am not part of this univers(ity)um anymore, we will not lose track of each other's life journeys. Special thanks to Alice, Antonia, Catha, Eli, Flo, Jojo, Michi J., Moatl, Nanni, Nicolas, and last but definitely not least Sebi. I will keep fond memories of those years.

Ohne die Vielzahl an Betätigungen und Happenings außerhalb des Doktorandenkosmos wäre es mir äußerst schwer gefallen einen offenen und frischen Geist zu bewahren, gerade auch zu Zeiten der Pandemie. Daher gilt ein großer Dank meinen Boulder- und Spieleabend-Gruppen sowie meinen ältesten Freunden Lisa, Lukas, Ogi und Wollo für eine Menge schöner Events.

Und dann danke ich zu guter Letzt den wichtigsten Menschen in meinem Leben, meiner Familie. Zum einen meiner Oma Frieda, welche zu den gutherzigsten Menschen zählt die diese Welt je gesehen hat und die für mich ein absolutes moralisches Vorbild verkörpert. Dann selbstverständlich meiner Schwester Mona und meinem Schwager Philipp, die immer ein offenes Ohr für meine Problemchen hatten und mir sehr viel über das Leben beigebracht haben.

Schließlich natürlich meinen unglaublich großartigen Eltern, ohne deren bedingungslose emotionale Unterstützung ich wohl schon längst ganz woanders wäre. Ich kann auch gar nicht in Worte fassen, wie dankbar ich euch dafür bin. Mama, Papa, schaut mal! Ich hab's geschafft!

Tomorrow holds such better days